In Vivo Measurement and Visualization of Pelvic Position and Orientation and Changes in Soft Tissue Shape and Thickness with Respect to Changes in Seating Surface Shape

Thomas G. Ault

CMU-RI-TR-05-56

November 9th, 2005

Carnegie Mellon University
Pittsburgh, Pennsylvania 15213

Submitted in partial fulfillment of the requirements for the degree of Doctor of Philosophy in the field of Robotics

Thesis Committee:

Mel Siegel, Robotics Institute (Chair)
David Brienza, University of Pittsburgh
Stephen Garoff, Physics
David Simon, Medtronic Navigation
George Stetten, Robotics Institute

.

Table Of Contents

Chapters

Table Of Contents ..... **i**

List Of Figures ..... **v**

List Of Tables ..... **xiii**

Abstract ..... **xv**

Introduction **1**
1.1 Scope of This Thesis 2
1.2 Thesis Overview 3

Pressure Ulcers **5**
2.1 Incidence and Prevalence 5
2.2 Etiology 7
2.3 Physiopathology 9
2.4 Mortality 10
2.5 Treatment 10
2.6 Prevention 11
2.7 Models of Pressure Ulcer Formation 12
2.7.1 Impaired Microcirculation 13
2.7.2 Reperfusion Injury 14
2.7.3 Interstitial Fluid Loss 14
2.7.4 Impaired Lymphatic Return 14
2.7.5 High Strain Rate Injury 15
2.7.6 Apparent Contradiction Between Formation Mechanisms and Physiopathology 15
2.8 Experimental Analysis of Proposed Mechanisms for Pressure Ulcer Formation 15
2.8.1 Animal Models 16
2.8.2 Finite Element Models 19
2.8.3 Noninvasive External Measurements Indicative of Internal Tissue Shape 23

The System **27**
3.1 Description of Subsystems 29
3.1.1 Motor Subsystem 31
3.1.2 Pressure And Orientation Subsystem 33
3.1.3 Ultrasound Subsystem 39
3.1.4 Position Wand Subsystem 41
3.2 Coordinate Systems 41

3.2.1 The Wand Coordinate System 43
3.2.2 The CASS Coordinate System 43
3.2.3 The Actuator Coordinate Systems 44
3.2.4 The Transducer Coordinate Systems 45
3.2.5 The Pelvis Coordinate System 46
3.3 Experimental Procedure 48
3.3.1 Data Acquisition 50
3.3.1.1 MRI Of Pelvis 50
3.3.1.2 Calibrate Wand 50
3.3.1.3 Flatten CASS 50
3.3.1.4 Measure Transducer Locations 50
3.3.1.5 Load Subject 50
3.3.1.6 Create Contour 52
3.3.1.7 Measure Registration Points 52
3.3.1.8 Make Ultrasound and Pressure Measurements 52
3.3.2 Data Analysis 52
3.3.2.1 Construct Pelvic Model 53
3.3.2.2 Register The Pelvis To The CASS 54
3.3.2.3 Construction Of The Soft Tisue Boundary Meshes 54
3.3.2.4 Measure Bulk Tissue Thickness And Volume 62
3.3.3 Visualization 64
3.4 Error Analysis 66
3.4.1 Registration Accuracy 66
3.4.1.1 The Iterative Closest Point Algorithm 66
3.4.1.2 Accuracy Of The ICP 66
3.4.1.3 Accuracy Of Manual Registration 69
3.4.1.4 How To Obtain Accurate Registration 70
3.4.2 Accuracy Of Soft Tissue Thickness Measurements 70
3.4.3 Accuracy Of Boundary Point Location Measurements 75
3.4.4 Accuracy Of Bulk Tissue Thickness Measurements 76
3.5 Conclusion 76

Pilot Study 77
4.1 Introduction 77
4.2 Methods 78
4.2.1 Subjects 78
4.2.2 Procedure 79
4.2.3 Analysis 80
4.3 Results 81
4.3.1 Subject #1 82
4.3.2 Subject #2 101
4.3.3 Subject #3 121
4.4 Discussion 139
4.4.1 Comparison Across Subjects 139
4.4.2 Comparison With Previous Work 145
4.4.2.1 Related Work On Measuring Pelvic Orientation 145
4.4.2.2 Related Work On Seating Contour Shape 145
4.4.2.3 Related Work On Biomechanical Properties Of Soft Tissue 146
4.4.2.4 Related Work On Measuring Soft Tissue Thickness 147

4.4.3 Strengths And Weaknesses Of Our Approach....152
4.5 Conclusions....153
4.6 Future Work....155
4.6.1 Improvements To The Experimental Procedure To Increase Its Accuracy 155
4.6.2 Improvements To The Experimental Procedure That Will Increase Our Understanding Of Seating Biophysics....156
4.6.3 Improvements To Techniques For Pressure Ulcer Prevention....157

Appendicies

Structure and Mechanical Properties of Soft Tissue....159
A.1 The Planes Of The Body....159
A.2 Anatomy....160
A.2.1 Anatomy of the Skin....160
A.2.2 Anatomy of the Pelvis....162
A.3 Mechanical Properties of Soft Tissue....165

Ultrasonic Measurement....167
B.1 Introduction....167
B.2 The Imaging Model....168
B.2.1 Properties of the Pulse and the Medium....168
B.2.2 Model of Propagation in a Single Layer....171
B.2.2.1 Curved Pulse Paths....173
B.2.3 Multiple Tissue Layers....174
B.2.4 The Resolution Cell....176
B.3 Echo Detection....176
B.4 Error Analysis....177
B.4.1 Uncertainty in Location of the Transducer....178
B.4.2 Uncertainty in Time-of-Flight....178
B.4.3 Uncertainty in the Speed of Sound, Angle of Entry and Tissue Boundary Orientations....178
B.4.3.1 Effects on Thickness Measurements....179
B.4.3.2 Effects on Measurement of Boundary Points....181
B.4.4 Discussion....182
B.5 Conclusions....184

Ultrasonic Tissue Characterization....205
C.1 Introduction....205
C.2 Theory....206
C.2.1 Imaging Model....206
C.2.1.1 Response of a Single Scatterer....207
C.2.1.2 Resolution Cells....209
C.2.1.3 Response of Homogeneous Regularly-Spaced Scatterers....211
C.2.1.4 Response of Homogeneous or Heterogeneous Randomly-Spaced Scatterers....212
C.3 Methods For Tissue Characterization....213
C.3.1 Signal-Based Methods....213
C.3.1.1 Coefficient of Attenuation....214

C.3.1.2 Coefficient of Integrated Backscatter 215
C.3.1.3 Slope And Intercept 217
C.3.1.4 Envelope-Based Methods 219
C.3.1.5 Other Signal-Based Methods 221
C.3.2 Image-Based Methods 222
C.3.3 Discussion 225
C.4 Conclusions 227

The Coordinate System Rotation Distance Metric 229
D.1 Definition of the Metric 231
D.2 Proof of Bounds on Distance Between Corresponding Points 232

Bibliography 239

.

List Of Figures

Chapters

Table Of Contents ..... **i**

List Of Figures ..... **v**

List Of Tables ..... **xiii**

Abstract ..... **xv**

Introduction **1**

Pressure Ulcers **5**

Figure 2.1: The four stages of pressure ulcers. 6

Figure 2.2: Curve (from [108]) showing the relationship between pressure magnitude and time of application required for pressure ulcer formation over bony prominences in human beings. This curve is only a guideline; the exact tolerance of the body to pressure depends upon many factors, including the location the pressure is applied to and the presence of shear, friction, or other contributing risk factors. 7

Figure 2.3: Tissue compaction vs. time predicted by the model of Arthur Mak and his colleagues [147]. The long time required for the tissue to reach a steady-state agrees with the creep response for tension in soft tissue[30] and indentation tests of Cochran, as reported by Reddy *et al* in [104]. 20

Figure 2.4: Agreement (taken from [147]) between pressure and time required for soft tissue damage predicted by Zhang *et al*[147] and clinical observations of Reswick and Rogers[108]. The predicted curve is for an arbitrary threshold of 11.5% loss in volume before tissue damage from interstitial fluid loss occurs. The agreement between this value and reality is not presently known. 21

The System **27**

Figure 3.1: The Computer Automated Seating System (CASS) 28

Figure 3.2: A typical actuator head with a pressure sensor 28

Figure 3.3: An actuator head that has been augmented with ultrasonic transducers 28

Figure 3.4: Block diagram of the CASS, illustrating its subsystems 30

Figure 3.5: The motor controller and driver subsystem of the CASS 31

Figure 3.6:The subsystem of the CASS that measures interface pressure and the orientation of the surfaces of its actuators. 32

Figure 3.7: Typical calibration curve for a pressure sensor 33

Figure 3.8: The two angles - tilt and rotation - that describe the orientation of the actuator head 34

Figure 3.9: Picture, diagram and schematic of the tilt sensors of the CASS. 34

Figure 3.10: Relationship between q and Δh *35*
Figure 3.11: Picture, diagram and schematic for the rotation sensors of the CASS....36
Figure 3.12: Typical calibration curves for the tilt and rotation sensors. The values on the x-axis are the output of the digitizer, which digitizes the voltage output by the sensor with 12 bits of resulution. 37
Figure 3.13: Block diagram of the ultrasonic subsystem of the CASS. 38
Figure 3.14: An actuator augmented with ultrasonic transducers 38
Figure 3.15: Mapping from sensor number to its transducer.....38
Figure 3.16: The position wand 41
Figure 3.17: The coordinate systems of the CASS. The figure on the left shows the relationships between the wand coordinate system (WCS, blue) and the CASS coordinate system (CCS,red). For these coordinate systems, the z-axis comes out of the page. Most of the displacement between the WCS and the CCS occurs along the z-axis. The figure on the right shows the relationship between the actuator coordinate system (ACS) and the transducer coordinate system (TCS).....42
Figure 3.18: Calculation of the Actuator Coordinate System (ACS). Note that the angle ρ illustrated in the figure is negative.....44
Figure 3.19: Calculation of the actuator coordinate system when an orientation sensor is not present. 45
Figure 3.20: Rear (top), side (middle) and top (bottom) views of the pelvic coordinate system. The x-axis is red, the y-axis is green and the z-axis is blue.....47
Figure 3.21: Schema for data acquisition 49
Figure 3.22: The data analysis schema 51
Figure 3.23: The registration points acquired during the data acquisition process conform to the shape of the pelvis, facilitating the match between the registration points measured in the WCS and the surface of the pelvic model, whose vertecies are positioned with respect to the PCS. 53
Figure 3.24: B-mode ultrasonic images of the same region of the buttocks from two slightly different angles of entry into the body. Note how the circled boundary between the biceps femoris and semimembranosus muscles is much brigher than in the right. 55
Figure 3.25: B-mode image in the sagittal plane of the buttocks of a healthy 35 year old male with the different muscle groups labeled. 55
Figure 3.26: The initial segmentation of an ultrasonic echogram. Circled echoes indicate potential soft tissue boundaries. 58
Figure 3.27: The skin, fat and muscle zones of an ultrasonic echogram. 58
Figure 3.28: Using a set-aside echogram to find a soft-tissue boundary. 58
Figure 3.29: Using neighboring echograms to enhance the segmentation process. The four echograms in this figure all come from ultrasonic transducers mounted on the same actuator. Weak echoes circled in red might be ignored were it not for the corresponding striong echoes circled in blue in the neighboring echograms. 59
Figure 3.30: The interpolated surface 62
Figure 3.31: A typical view from the visualization software. 63
Figure 3.32: The color scale used to indicate pressure at each actuator by the visualization software. 64
Figure 3.33: Schema for simulated registration trials. 65

Figure 3.34: Worst-case and best-estimate of the upper bound in measuring the thickness of the skin layer. 72
Figure 3.35: Worst-case and best-estimate of the upper bound in measuring the thickness of the fat layer. 72
Figure 3.36: Worst-case and best-estimate of the upper bound in measuring the thickness of the muscle layer. 73
Figure 3.37: Worst-case and best-estimate of the upper bound in measuring the location of the boundary between the skin and fat layers. 74
Figure 3.38: Worst-case and best-estimate of the upper bound in measuring the location of the boundary between the fat and first muscle layers. 74
Figure 3.39: Worst-case and best-estimate of the upper bound in measuring the location of the boundary between the first and second muscle layers. 75

Pilot Study 77

Figure 4.1: Interface pressure distribution for subject #1 for the flat and pressure-equalized contours. 82
Figure 4.2: Thickness of skin(blue), fat(aqua) and the first muscle layer (yellow) broken down by region for both the flat and equalized contours. Bulk tissue between the last resolved layer and the pelvis is shown by brown bars. Numbers along the x-axis indicate the sensor where the measurements were taken. Each number has two bars associated with it; the bar on the left measures thickness for the flat contour, while the bar on the right measures thickness for the equalized contour. A missing bar indicates that no measurements were available for that combination of sensor and contour. 91
Figure 4.3: Front view of subject #1, flat contour. 92
Figure 4.4: Front view of subject #1, equalized contour. 93
Figure 4.5: Side view of subject #1, flat contour. 94
Figure 4.6: Side view of subject #1, equalized contour. 95
Figure 4.7: View of subject #1, flat contour from the right front corner. 96
Figure 4.8: View of subject #1, equalized contour from the right front corner. 97
Figure 4.9: Boundaries between tissue layers of subject #1 for the flat contour. 98
Figure 4.10: Boundaries between tissue layers of subject #1 for the equalized contour. 99
Figure 4.11: Interface pressure distribution for subject #2 for the flat and pressure-equalized contours. 101
Figure 4.12: Cumulative distribution of soft tissue beneath the left ischial tuberosity (graph on the left) and the right ischial tuberosity (graph on the right) for subject #2. 103
Figure 4.13: Thickness of skin(blue), fat(aqua) and the first muscle layer (yellow) broken down by region for both the flat and equalized contours. Bulk tissue between the last resolved layer and the pelvis is shown by brown bars. Numbers along the x-axis indicate the sensor where the measurements were taken. Each number has two bars associated with it; the bar on the left measures thickness for the flat contour, while the bar on the right measures thickness for the equalized contour. A missing bar indicates that no measurements were available for that combination of sensor and contour. 111
Figure 4.14: Front view of subject #2, flat contour. 112

Figure 4.15:: Front view of subject #2, equalized contour. 113
Figure 4.16: Side view of subject #2, flat contour. 114
Figure 4.17: Side view of subject #2, equalized contour. 115
Figure 4.18: View of subject #2, flat contour from the right front corner. 116
Figure 4.19: View of subject #2, equalized contour from the right front corner. 117
Figure 4.20: Boundaries between tissue layers of subject #2 for the flat contour. 118
Figure 4.21: Boundaries between tissue layers of subject #2 for the equalized contour. 119
Figure 4.22: Interface pressure distribution for subject #2 for the flat and pressure-equalized contours. 121
Figure 4.23: Cumulative distribution of soft tissue beneath the left ischial tuberosity (graph on the left) and the right ischial tuberosity (graph on the right) for subject #3. 123
Figure 4.24: Thickness of skin(blue), fat(aqua) and the first muscle layer (yellow) broken down by region for both the flat and equalized contours. Bulk tissue between the last resolved layer and the pelvis is shown by brown bars. Numbers along the x-axis indicate the sensor where the measurements were taken. Each number has two bars associated with it; the bar on the left measures thickness for the flat contour, while the bar on the right measures thickness for the equalized contour. A missing bar indicates that no measurements were available for that combination of sensor and contour. 129
Figure 4.25: Front view of subject #3, flat contour. 130
Figure 4.26: Front view of subject #3, equalized contour. 131
Figure 4.27: Side view of subject #3, flat contour. 132
Figure 4.28: Side view of subject #3, equalized contour. 133
Figure 4.29: View of subject #3, flat contour from the right front corner. 134
Figure 4.30: View of subject #3, equalized contour from the right front corner. 135
Figure 4.31: Boundaries between tissue layers of subject #3 for the flat contour. 136
Figure 4.32: Boundaries between tissue layers of subject #3 for the equalized contour. 137
Figure 4.33: Cumulative thickness of bulk tissue beneath the left (top) and right (bottom) ischial tuberosities for all three subjects. 142
Figure 4.34: Development of soft tissue stiffness beneath the left (top) and right (bottom) ischial tuberosities over the course of the equalization algorithm for all three subjects. 149

Appendicies

Structure and Mechanical Properties of Soft Tissue 159
Figure A.1: The planes of the body. 159
Figure A.2: The structure of the skin 160
Figure A.3: The front (anterior), side (lateral) and rear (posterior) views of the pelvis with important anatomical landmarks indicated. 161
Figure A.4: Typical force/deformation relationship for the buttocks of a seated able-bodied male (from [15]). The compressive load is measured in grams. 164

Figure A.5: Example of the non-linear force/deformation relationship and hysteresis of porcine tissue (from [145]). Indentation took 5 seconds, the holding interval was 10 seconds, and recovery took 5 seconds. Human tissue has a similar response. 164

Ultrasonic Measurement 167

Figure B.1: A typical echogram of the return echoes for a 7.5 MHz ultrasonic pulse emitted into the buttocks of a 29 year-old healthy human male. The x-axis measures time in ADC samples collected at a rate of one sample every 10^{-8} seconds. The y-axis measures voltage differential across the transducer in ADC bits, where one bit equals 390.625 μV. 167

Figure B.2: Illustration of our model of an ultrasonic pulse. In the left diagram, the intensity of the ultrasonic pulse (equal to the square of the amplitude) at any point is space is represented by the grey level. Maximum intesity is black; minimum is white. The pulse diameter is measured at -3 dB from the maximum intensity of the pulse.... 169

Figure B.3: Imaging model for a single tissue layer whose boundaries are inclined at angles β_0 and β_1 to the x-axis respectively. The pulse enters the tissue layer at (x_0, z_0) at an angle of θ_0 to the normal and reflects from the far side of the layer at (x_1, z_1). The thickness of the layer, L_0, is defined to be the distance from the near side to the far side along the normal to the near side at (x_0, z_0).....172

Figure B.4: Model of pulse-echo imaging for multiple tissue layers- in this case, multiple tissue layers between the transducer and the pelvis- shown with all layers parallel for clarity. The pulse enters the body through a coupling wedge which serves two purposes: (1) its shape gives the angle of entry (θ_1) of the ultrasonic pulse and (2) it matches the acoustic impedance of the skin to the acoustic impedance of the transducer, so that no reflections arise from the skin/transducer interface. The pulse reflects from the pelvis at point P. 174

Figure B.5: The resolution cell concept illustrated in two dimensions. As the pulse propagates through the soft tissue it encounters many discontinuities. A discontinuity encountered at time t/2 will continue to reflect energy until time $t/2+\Delta T$, where ΔT is the duration of the pulse, provided that the acoustic response of the discontinuity ceases quickly after insonuation. Since it takes time t/2 for the scattered energy to return to the transducer, this discontinuity will contribute to the amplitude of the received signal over the interval $[t, t+\Delta T]$. 175

Figure B.6: Amplitude thresholding for echo detection. All echoes above a certain threshold are considered to be echoes from tissue interfaces. The basic technique is illustrated in the figure to the left, and some of the problems with amplitude thresholding are illustrated in the figure to the right. 176

Figure B.7: Difference per unit thickness between the calculated thickness of skin and its actual value as a function of the actual speed of sound and angle of entry in skin. The thickness of the layer was calculated assuming *c1*=1600 m/s and θ_1=0. 187

Figure B.8: Difference per unit thickness between the calculated thickness of the layer of fat and its actual value as a function of the actual speeds of sound in skin and fat and the actual angle of entry in skin with all layer boundaries parallel. The calculated thickness of the fat layer was obtained by assuming *c1*=1600 m/s, c_2=1450 m/s and θ_1=0.....188

Figure B.9: Difference per unit thickness between the calculated thickness of the layer of muscle and its actual value as a function of the actual speeds of sound in skin and muscle and the actual angle of entry in skin with all layer boundaries parallel. The calculated thickness of the muscle layer was obtained by assuming *c1*=1600 m/s, c_3=1580 m/s and θ_1=0. 189
Figure B.10: Difference per unit thickness between the calculated thickness of the skin layer and its actual value as a function of the actual speeds of sound in skin (*c1*) and the orientations of the near and far boundaries of the layer (*b1, b2*) with the angle of entry (*q1*) held constant at zero. The calculated thickness of skin was obtained by assuming *c1*=1600 m/s and β_1=*b2*=0.....190
Figure B.11: Difference per unit thickness between the calculated thickness of the fat layer and its actual value as a function of the actual speed of sound in skin (*c1*) and the orientations of the near and far boundaries of the fat layer (*b2, b3*) with the angle of entry (*q1*) held constant at zero. The calculated thickness of the fat layer was obtained by assuming *c1*=1600 m/s, *c2*=1450 m/s and β_2=*b3*=0.....191
Figure B.12: Difference per unit thickness between the calculated thickness of the fat layer and its actual value as a function of the actual speed of sound (*c2*) and the orientations of the near and far boundaries (*b2, b3*) of the fat layer itself with the angle of entry (*q1*) held constant at zero. The calculated thickness of the fat layer was obtained by assuming *c1*=1600 m/s, *c2*=1450 m/s and β_2=*b3*=0.....192
Figure B.13: Difference per unit thickness between the calculated thickness of the muscle layer and its actual value as a function of the actual speed of sound in skin (*c1*) and the orientations of the near and far boundaries (*b3, b4*) of the muscle layer itself with the angle of entry (*q1*) held constant at zero. The calculated thickness of the fat layer was obtained by assuming *c1*=1600 m/s, *c3*=1580 m/s and *b3*=*b4*=0. 193
Figure B.14: Difference per unit thickness between the calculated thickness of the muscle layer and its actual value as a function of the actual speed of sound (*c2*) and the orientations of the near and far boundaries (*b3, b4*) of the muscle layer itself with the angle of entry (*q1*) held constant at zero. The calculated thickness of the fat layer was obtained by assuming *c1*=1600 m/s, *c2*=1450 m/s and β_3=*b4*=0.....194
Figure B.15: Difference between the calculated location where the ultrasonic pulse intersected the skin/fat boundary its actual value as a function of the actual speed of sound (*c1*) and angle of entry (*q1*) in skin with the boundaries of the layer kept parallel. The thickness of the layer was calculated assuming *c1*=1600 m/s and θ_1=0...195
Figure B.16: Difference between the calculated location where the ultrasonic pulse intersected the fat/muscle boundary and its actual value as a function of the actual speed of sound in fat (*c2*) and skin (*c1*) and the actual angle of entry (*q1*) in skin with the boundaries of the layer kept parallel. The location of the boundary point was calculated assuming *c1*=1600 m/s, c_2=1450 m/s and θ_1=0.....196
Figure B.17: Difference between the calculated location where the ultrasonic pulse intersected the muscle/bone boundary and its actual value as a function of the actual speed of sound in muscle (*c3*) and skin (*c1*) and the actual angle of entry (*q1*) in skin with the boundaries of the layer kept parallel. The location of the boundary point was calculated assuming *c1*=1600 m/s, *c3*=1580 m/s and θ_1=0.....197
Figure B.18: Difference per unit thickness between the calculated location where the ultrasonic pulse intersects the skin/fat boundary and its actual value as a function of

the actual speed of sound in skin (*c1*) and the orientations of the near and far boundaries (*b1*, *b2*) of the skin layer with the angle of entry (*q1*) held constant at zero. The calculated location of the boundary point was obtained assuming *c1*=1600 m/s and β_1=*b2*=0. 198
Figure B.19: Difference per unit thickness between the calculated location where the ultrasonic pulse intersects the fat/muscle boundary and its actual value as a function of the actual speed of sound in skin (*c1*) and the orientations of the near and far boundaries (*b2*, *b3*) of the fat layer with the angle of entry (*q1*) held constant at zero. The calculated location of the boundary point was obtained assuming *c1*=1600 m/s, *c2*=1450 m/s and β_2=*b3*=0.....199
Figure B.20: Difference per unit thickness between the calculated location where the ultrasonic pulse intersects the fat/muscle boundary and its actual value as a function of the actual speed of sound (*c2*) and orientations of the near and far boundaries (*b2*, *b3*) of the fat layer itself with the angle of entry (*q1*) held constant at zero. The calculated location of the boundary point was obtained assuming *c1*=1600 m/s, *c2*=1450 m/s and β_2=*b3*=0.....200
Figure B.21: The individual contours that make up figure B.20 displayed separately for comparison.....201
Figure B.22: Difference per unit thickness between the calculated location where the ultrasonic pulse intersects the muscle/bone boundary and its actual value as a function of the actual speed of sound in fat (*c2*) and the orientations of the near and far boundaries (*b3, b4*) of the muscle layer with the angle of entry (*q1*) held constant at zero. The calculated location of the boundary point was obtained assuming *c2*=1450 m/s, *c3*=1580 m/s and β_3=*b4*=0.....202
Figure B.23: Difference per unit thickness between the calculated location where the ultrasonic pulse intersects the muscle/bone boundary and its actual value as a function of the actual speed of sound (*c3*) and orientations of the near and far boundaries (*b3, b4*) of the muscle layer itself with the angle of entry (*q1*) held constant at zero. The calculated location of the boundary point was obtained assuming *c2*=1450 m/s, *c3*=1580 m/s and β_3=*b4*=0.....203
Figure B.24: The individual contours that make up figure B.23 displayed separately for comparison.....204

Ultrasonic Tissue Characterization 205
Figure C.1: Scattering of an ultrasonic pulse from a rectangular crystal array of circular objects that are much smaller than the wavelength of the pulse.....210

The Coordinate System Rotation Distance Metric 229

Bibliography 239

.

List Of Tables

Chapters

Table Of Contents i

List Of Figures v

List Of Tables xiii

Abstract xv

Introduction 1

Pressure Ulcers 5

The System 27

Table 3.1:Registration Parameters For ICP Algorithm 67
Table 3.2:Registration Accuracy By Region 68

Pilot Study 77

Table 4.1:Contour Depth And Interface Pressure For Subject #1 87
Table 4.2:Position And Orientation Of Pelvis For Subject #1 87
Table 4.3:Bulk Tissue Volume For Subject #1..... 87
Table 4.4:Bulk Tissue Thickness For Subject #1 88
Table 4.5:Thickness Of Individual Tissue Layers For Subject #1 89
Table 4.6:Contour Depth And Interface Pressure For Subject #2 107
Table 4.7:Position And Orientation Of Pelvis For Subject #2 107
Table 4.8:Bulk Tissue Volume For Subject #2..... 107
Table 4.9:Bulk Tissue Thickness For Subject #2 108
Table 4.10:Thickness Of Individual Tissue Layers For Subject #2 109
Table 4.11:Contour Depth And Interface Pressure For Subject #3 125
Table 4.12:Position And Orientation Of Pelvis For Subject #3 125
Table 4.13:Bulk Tissue Volume For Subject #3..... 125
Table 4.14:Bulk Tissue Thickness For Subject #3 126
Table 4.15:Thickness Of Individual Tissue Layers For Subject #3 127
Table 4.16:Distance From Midpoint For All Three Subjects 140

Appendicies

Structure and Mechanical Properties of Soft Tissue 159

Ultrasonic Measurement 167

Ultrasonic Tissue Characterization 205

The Coordinate System Rotation Distance Metric 229

Bibliography 239

.

Abstract

Pressure ulcers are volumes of tissue necrosis that evolve after prolonged exposure of skin and soft tissue to the forces of reclining or sitting. They are serious problems for people confined to beds and wheelchairs. Treating them is expensive, and if untreated fatal infections can evolve, so substantial clinical effort is focussed on prevention. However the precise conditions for and mechanisms of ulcer development and evolution are poorly understood, so prevention is largely ad hoc.

Current models of pressure ulcer formation and evolution postulate that soft tissue distortion is a more important issue than pressure per se. This thesis reports the development and evaluation of a system that uses reclining MRI, non-invasive measurement of pelvic bone position and orientation, external pressure sensing, and ultrasonic soft tissue thickness sensing to measure the distortions and distortion changes of the various soft tissue layers of the buttocks when a subject sits on a surface of dynamically variable shape. This multi-modality system is required because current volumetric imaging scanners cannot accomodate seated subjects, and they certainly cannot accommodate subjects seated on a dynamically shaped surface.

Pressure and thickness data are fused with pelvic bone position and orientation data to yield shapes and thicknesses of skin, fat, and muscle layers as a function of seating contour. Results are rendered on an interactive 3D visual display for qualitative intuition-building by human researchers, and they are analyzed quantitatively to generate functional relationships between subjects and seating contours. The approach is validated by a small pilot study of two healthy subjects and one spinal-cord injured subject. The study concretely explores and evaluates the kinds of comparisons and analyses that can be done. If this pilot study is successfully validated by a large enough future study drawn from a broad enough population, it is apparent that the currently accepted models of soft tissue distortion for seated subjects will need to be revised substantially.

Chapter 1
Introduction

An estimated 250,000 persons suffer from spinal cord injuries in the United States, and there are approximately 7,500-11,000 new cases of spinal cord injury each year[90]. Spinal cord injuries nearly always lead to paralysis; 55% of the spinal cord injured are paraplegic, and 44% are quadriplegic[90]. Because of their confinement to wheelchairs or beds, victims of spinal cord injury (SCI) have a very high risk of developing *pressure ulcers*: ulcerations of the skin or deeper tissues arising from the pressure, shear or friction incurred in normal sitting or reclining for prolonged periods of time. While not fatal in and of themselves, pressure ulcers are painful and can lead to potentially fatal complications (such as infection) if not treated.

The spinal cord injured are not the only ones at risk for developing pressure ulcers. Any person immobilized for a prolonged period has some risk of developing pressure ulcers. The elderly, diabetics, and those in long-term hospital care have a particularly high risk.

Despite considerable research efforts, pressure ulcers remain a significant health care problem. Although much progress has been made over the past 20 years in the treatment and prevention of pressure ulcers, results in both areas are inadequate. While treatments for pressure ulcers are effective, they are still expensive, costing one billion dollars per year in treatment expenses alone[4]. Current preventative measures, while less expensive than current treatments, are not as effective.

Underlying the inability to develop effective preventative measures is an inadequate understanding of the etiology of pressure ulcers. Pressure relief, along with corresponding relief efforts for shear and frictional forces, are the primary components of pressure ulcer prevention. However, although pressure, shear and frictional forces are certainly the primary risk factors, to say that they cause pressure ulcers is an overstatement. Instead, researchers now believe that the soft tissue distortion- rather than pressure, shear and friction- plays the key role in pressure ulcer formation. Pressure relief efforts will be effective when they reduce or eliminate the underlying soft tissue distortion.

However, few studies relating interface pressure, shear and friction to the underlying soft tissue distortion have been done, in part because measuring the distortion of the soft tissues of the body (other than the skin surface) under various loading conditions is a difficult problem. Measuring the soft tissue distortion for subjects reclining on mattresses or pads with different mechanical properties or shapes cut out of them is conceptually straightforward, since these subjects can pass through an MRI machine while reclining on

a mattress or pad. The principal difficulty in measuring the soft tissue distortion for reclining subjects is extracting and modeling the three-dimensional shapes of the different layers of soft tissue from the two-dimensional MRI slices. However, such methods cannot be applied to measuring the relationship between seating surface shape and soft tissue distortion for seated subjects, since seated subjects cannot pass through an MRI machine. Consequently, methods for directly measuring the distortion of the soft tissues in seated subjects have been lacking until now, and researchers have had to make do with indirect measurements of soft tissue shape.

We have constructed a system capable of measuring the shape of the soft tissues of a seated subject in a much more direct fashion than has been done previously. By fusing MRI, ultrasound and pressure data, we compute the position and orientation of the pelvis relative to the seating surface[1] and the shapes of the intervening soft tissues. In addition to producing quantitative, numerical results, we visualize this information on a high-performance graphics display as a "virtual x-ray" that a researcher can manipulate. We can create different seating contours and investigate the relationship between seating surface shape, soft-tissue distortion, and interface pressure. Through the use of this tool, researchers will be better able to assess the role of soft tissue distortion in the development of pressure ulcers and develop better preventative measures for those individuals confined to wheelchairs.

1.1 Scope of This Thesis

The goal of this thesis to develop a system to measure the position and orientation of the pelvis and the shape of the soft tissues of the buttocks between the pelvis and the seating contour. In order to make this goal achievable within a single thesis, we must place reasonable limitations on the scope of our work. The system has been tested with a small pilot study consisting of three subjects, two of which are healthy and one of which suffers from spinal cord injury. This pilot study demonstrates the ability of the technique to measure pelvic position, pelvic orientation and soft tissue distortion and explore how those those quantities are related to measurements of pressure at the interface between the buttocks and the seating surface. However, the pilot study is not sufficiently large enough to draw any clinically significant conclusions about the relationships between pelvic position, pelvic orientation, soft tissue distortion, interface pressure, the shape of the seating surface and the injury status of the subject (e.g. healthy or suffering from spinal cord injury). Larger studies will be needed to draw such conclusions.

Likewise, the system developed in this thesis is intended only for research and is not intended for use in a clinical setting. It's role to help researchers better understand how soft tissue distortion impacts the formation of pressure ulcers, so that knowledge can be

1. As a rigid indenter, the pelvis plays a major role in distorting the soft tissues, and research has strongly implicated its position and orientation in the formation of pressure ulcers for both seated and reclining subjects. Hence, any system that seeks to measure and visualize soft tissue distortion must include measurements of the position, orientation and shape of the pelvis.

used to design better preventative measures. We do not intend that the system developed in this thesis be used by clinicians in a day-in, day-out basis to measure the distortion the soft tissues of a patient's buttocks experiences in preparation for designing or recommending patient-specific preventative measures. For this reason, many of the procedures used in measuring and visualizing the distortion of the soft tissues of the buttocks are not as automatic as they could be.

Because of limitations on time and expense, only part of our seating apparatus is instrumented with the ultrasonic transducers we use to measure the individual soft tissue layers in the buttocks. This part covers the region in the vicinity of the ischial tuberosity of the pelvis, where pressure ulcers that arise from prolonged sitting are most common. In principle, the entire seating surface could be instrumented with ultrasonic transducers (as it is with pressure transducers) to provide complete coverage. Of course, since we measure the position and orientation of the pelvis and know the shape of the seating contour, we can compute the *overall* shape of the soft tissues throughout the buttocks, since these two surfaces constrain those tissues.

1.2 Thesis Overview

Chapter 2 provides background material on pressure ulcers. We discuss the incidence, prevalence and etiology of pressure ulcers and describe the current pathogenic models. We describe (briefly) the current methods for the treatment and prevention of pressure ulcers. The work of other groups relevant to ours is presented here as well.

Chapter 3 describes the expanded Computer-Automated Seating System (CASS) and our experimental methods. Here we describe the structure and function of the components of the CASS system and how we use those components to measure the position and orientation of the pelvis and the shapes of the layers of skin, fat and muscle in the buttocks. We evaluate the accuracy of those measurements using the material developed in the appendices.

Chapter 4 describes a small pilot study that validates the experimental method developed in chapter 3 and demonstrates that procedure produces data and analysis that is useful to researchers seeking to understand the relationship between soft tissue distortion and pressure ulcers. The experimental technique from chapter 3 is applied to four subjects under two different experimental conditions: seated on a flat contour and seated on a pressure-equalized contour. We analyze the data from these experiments and compute the bulk thickness of the soft tissue beneath the pelvis over the entire buttocks and the thicknesses of the individual soft tissue layers in the vicinity of the ischial tuberosity. We also present reconstructed images of the shapes of those soft tissue layers ***in vivo***[2]. We

2. A glossary of medical terms not in common use is provided at the end of the thesis. The first time a term in the glossary appears in the thesis, it is highlighted in bold. The remaining appearances of that term appear in plain text. Note that the terms in vivo and in vitro are traditionally italicized in the medical literature, and so they have been italicized in this thesis. The first use of other terms contained in the glossary will be highlighted only by bold text and will not be italicized also.

analyze these results and draw some very preliminary conclusions about the role of soft tissue distortion in the formation of pressure ulcers that provide direction for future clinical studies. Finally, we propose new directions, both for pressure ulcer research using the current system and for improvements to the current system that will expand its research capabilities.

Appendix A gives a brief introduction to the planes of the body and the anatomy of the buttocks and upper thigh. It also provides a brief discussion of the biomechanics properties of the soft tissues of the body. Those who are unfamiliar with either of these subjects should consult this appendix before reading the rest of the thesis.

Appendix B investigates how common assumptions about the speed of sound and path of the ultrasonic pulse through the tissues of the body affect the accuracy of measurements made with that pulse. The material in this appendix is used in Chapter 3 to estimate the accuracy of the measurements of the thickness of the skin, fat and muscle layers made by the system described in that chapter. Appendix B builds an imaging model that explains the content of a received signal echogram in terms of the properties of emitted ultrasonic pulse and the geometry and mechanical properties of the soft tissues of the buttocks. From this imaging model, an iterative method is constructed to compute the thickness of the soft tissue layers the pulse has passed through and the locations where the pulse intersected the boundaries between those layers. These boundary points are what the procedure in chapter 3 assembles to construct an image of the shapes of the individual soft tissue layers *in vivo*. The appendix then analyzes how assumptions made by this iterative method and uncertainties in its inputs affect the accuracy of the soft tissue thicknesses and boundary point locations it computes.

Appendix C surveys the literature for ultrasonic tissue characterization and describes the current state-of-the-art in this field. We describe its theoretical basis, its ability to differentiate tissue types, and its ability to diagnose various diseases by identifying pathological changes in soft tissue. The material in this appendix is supplemental to the thesis as a whole and the main points of the thesis can be understood without it.

Appendix D derives the distance metric we use to measure the distance between two rotations. The analysis of the accuracy of the registration method described in chapter 3 requires that we compute the distance between two coordinate systems, which can be expressed as the distance between their origins and the distance between their rotations. The metric we use, which we call the coordinate system rotation distance metric, is based on the distance between corresponding axes in the coordinate systems that represent the two rotations. It has the advantage of being independent of how the rotations are represented and of placing an upper bound on the distance between any two corresponding points in the coordinate systems represented by those rotations.

Chapter 2
Pressure Ulcers

Pressure ulcers are regions of tissue **necrosis** caused by long-term exposure of body sufraces to forces sufficient to occlude blood flow. Individuals with compromised sensation and mobility are at highest risk for developing pressure ulcers. Pressure ulcers progress through four stages of increasing seriousness, which are illustrated and defined in figure 2.1. The accurate staging of pressure ulcers is important, since the stage of the ulcer indicates the type of treatment. In general, stage I and II ulcers can be treated using conservative measures, and stage III and IV ulcers require surgery[58].

The visible manifestation of a pressure ulcer on the skin surface occurs up to several days after the insult that caused it. Although a pressure ulcer might appear to begin on the skin surface and proceed inward, in reality, damage may occur in the dermis or deeper soft tissues and spread outwards. This “inside-out” development of pressure ulcers also makes prevention very important- by the time an ulcer becomes visible (and thus, treatable), damage to the underlying soft tissues has already occurred.

2.1 Incidence and Prevalence

The general prevalence of pressure ulcers in Great Britain and Denmark has been estimated to be around 50 individuals with at least one ulcer per 100,000 residents[102]. In the United States, most studies report a prevalence from 3% to 11% in acute care settings [42]. Incidence and prevalence are higher in long-term care settings- a prevalence of 15% to 25% of patients admitted to skilled nursing facilities has been reported[42]. Another study reports that 23% of persons in skilled care or nursing homes have at least one sore[89]. The spinal-cord injured and paraplegics are particularly vulnerable to developing pressure ulcers. Seventy-five percent of those suffering from spinal cord injury will develop at least one ulcer in their lifetime[86], while 50%of paraplegics will develop at least one ulcer in their lifetime[86].

A review of 1604 pressure ulcers in 649 patients in Veteran’s Administration hospitals found that 87% of these pressure ulcers are found over bony prominences of the body[58]. Of these, 28% can be found beneath the ischial tuberosity, 19% beneath the trochanter, 17% beneath the sacrum, 9% beneath the heel, 5% beneath the malleolus, 5% beneath the pretibial, and 4% beneath the patella. This means that 64% of all pressure ulcers are found in close proximity to the pelvis. For patients confined to wheelchairs (as opposed to the bedridden), nearly all pressure ulcers are found in proximity to the pelvis or sacrum, probably because of the prolonged periods of sitting involved.

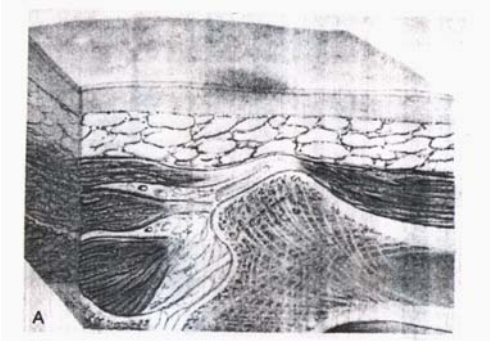

Stage I: Non-blanchable **erythema** of intact skin; this lesion heralds a forthcoming skin ulceration.

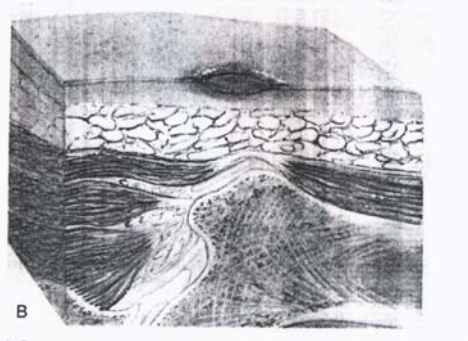

Stage II: Superficial ulcer with partial-thickness skin loss in the dermis, epidermis or both. It may present as an abrasion, blister, or shallow crater.

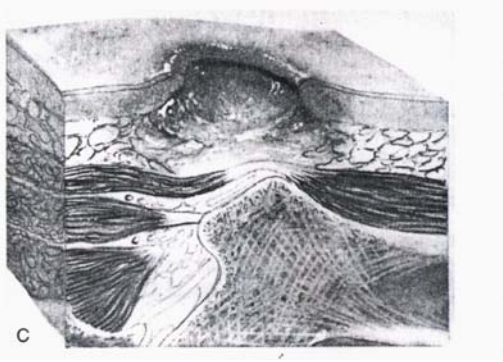

Stage III: Ulcer with tissue loss extending through the dermis and epidermis. The tissue loss may extend all the way down to, but not through, the underlying **fascia**.

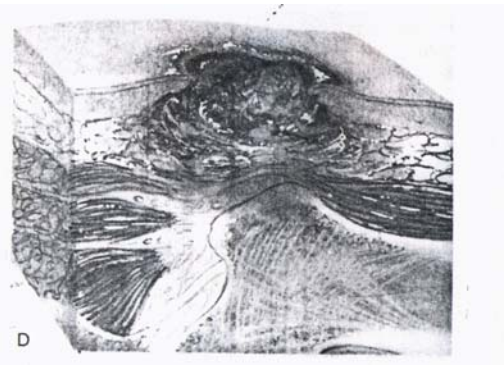

Stage IV: Ulcer with skin loss through the dermis, epidermis and into or through the fascia with possible damage to muscle, bone, or supporting structures. Sinus tracts or undermining of the neighboring tissues may be present.

Figure 2.1: The four stages of pressure ulcers.

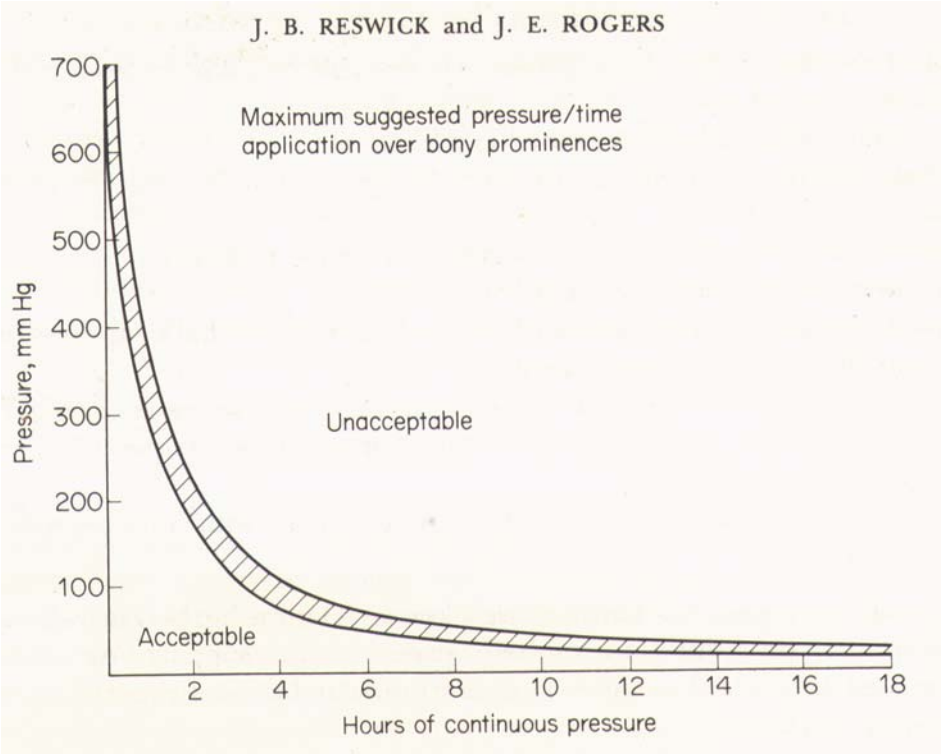

Figure 2.2: Curve (from [108]) showing the relationship between pressure magnitude and time of application required for pressure ulcer formation over bony prominences in human beings. This curve is only a guideline; the exact tolerance of the body to pressure depends upon many factors, including the location the pressure is applied to and the presence of shear, friction, or other contributing risk factors.

2.2 Etiology

Extensive work has been done to identify the risk factors for the development of pressure ulcers in individuals. These factors have been identified as ([86] and [58]):

- Pressure
- Shear
- Friction
- Heat
- Impaired Mobility
- Incontinence
- Neuropathy or Impaired Sensation
- Malnutrition
- Advanced Age
- Chronic Illness
- Altered States of Consciousness (*e.g.* coma)

The first three risk factors are considered *extrinsic* risk factors because they are external to the patient; the remainder are called *intrinsic* risk factors, as they are properties of the patient himself or herself. The distinction between extrinsic and intrinsic risk factors is

important, because, while we can control the extrinsic risk factors, we cannot always control the intrinsic risk factors. For example, while we can control the pressure a patient is exposed to (at least in principle), at present there is nothing we can do about a patient's advanced age or neuropathy.

Pressure ulcer risk factors can also be divided into *essential* and *contributing* factors. Essential risk factors are those that are required for pressure ulcers to form, while contributing risk factors increase the vulnerability of the patient to the essential risk factors, but cannot produce a pressure ulcer by themselves. Pressure, shear and friction applied to the skin surface are the essential risk factors. As a practical matter, pressure is the only of these risk factors that can occur alone. In order to subject the skin to shear or friction without pressure, the force applied to the skin surface would have to be parallel to it at all points of contact. Pressure, on the other hand, can be applied to the skin surface without significant (external) shear or friction, as in the case of an immobile patient lying flat on a bed. Hence, shear and friction, although theoretically capable of giving rise to pressure ulcers on their own, are usually treated as contributing risk factors that increase the vulnerability of the patient to ulceration from the application of pressure.

There is a well-known and clinically-recognized inverse relationship between the magnitude and the duration of the applied pressure; the larger the pressure magnitude, the shorter the soft tissues can tolerate it before breakdown occurs. Kosiak was one of the first to demonstrate this relationship in his experiments on dogs[51], and in their classic paper, Reswick and Rogers demonstrated this pressure/time relationship beneath bony prominences in human beings[108]; the curve from their study is shown in figure 2.2 and is typical of the pressure/time relationship in humans. The exact locus of the curve depends upon the location of the ulcer (thicker areas of tissue tolerate pressure for longer durations than thinner areas) and the presence of shear[113], friction[25] or other contributing risk factors (see below), which reduce the ability of soft-tissue to tolerate pressure.There is most likely a threshold below which applied pressures will not result in ulceration for any duration of application, but the value of such a threshold, or the range of possible values, has not been definitively established.

The remaining risk factors (impaired mobility, incontinence, etc.) are all contributing risk factors. Moisture, typically from incontinence, increases the vulnerability of the skin to mechanical damage and increases the potential for infection[42]. Heat not only moistens the skinthrough increased sweatting, but also alters blood flow and prolonged exposure to temperatures above normal body temperature in an environment where airflow is restricted can cause damage to the skin[50]. Impaired mobility, such as paraplegia or quadriplegia, restricts the ability of the patient to make the normal adjustments people without mobility deficits use to relieve a buildup of pressure during sitting or reclining. Impaired sensation (through neuropathy, spinal cord injury or other nerve damage, or being in an altered state of consciousness) prevents a patient from being aware that such changes need to be made. Malnutrition impairs the body's ability to resist damage and to heal damage once it has occurred. Advanced age or chronic illnesses are likely to predispose the patient to having several other risk factors, especially impaired mobility, impaired sensation, or incontinence. Aging skin is also more vulnerable to damage[62],

and chronically ill patients are more likely to require lengthy hospital stays, which have been positively correlated with the development of pressure ulcers[105].

Several risk assessment tools exist to evaluate a patient's risk for developing pressure ulcers. The most popular are the Norton[95], Braden[6], and Waterlow[138] scales. Risk assessment takes place when the patient is admitted to the hospital or long-term care facility and is periodically repeated to track increasing or decreasing risk over time. By identifying high-risk patients early on, care facilities can initiate preventative measures immediately without wasting time or resources on patients unlikely to develop pressure ulcers.

While much work has been done on assessing pressure ulcer risks for patients admitted to a hospital or nursing home for a long period of time, less work has been done on risk assessment for wheelchair-bound individuals. Separate risk assessment tools may be necessary, as a study by D. Anthony *et al* has shown that the scales used for general patients may not be as effective for wheelchair users[2]. Furthermore, some patients appear to be resistant to developing pressure ulcers despite being in a high-risk group. The factors that give rise to this resistance are presently unknown.

2.3 Physiopathology

In a stage I ulcer, there is significant edema and dilation of the capillaries and venules with striking red blood cell engorgement, platelet **thrombi** and hemorrhage[42]. Degeneration of the subcutaneous fat and sweat glands often occurs. A non-blanchable **erythema** may be visible in the epidermis.

As the ulcer progresses from stage I to stage II, several epidermal responses may be seen[42], including **diffuse eosinophilia** with erosions and crust formation, **focal eosinophilia** and necrosis with possible subepidermal separation, and a **subepidermal bulla**. The follicles may also begin to deteriorate.

In stage II, the epidermis is lost and the **dermal papillae** become identifiable. Acute inflammation of the dermis is present. As the ulcer progresses, a diffuse fibrotic dermis with loss of connective structures and a **hemorrhagic crust** presents[42].

In Stage III and Stage IV, there is full-thickness destruction of the skin[42]. Cellular detail is obliterated and a black **eschar** forms in the wound. Sinus tracts and **osteomyelitis** may be present.

The stages of pressure ulcer formation are defined in terms of the appearance of the ulcer and its visible symptoms. However, the physiological mechanisms that lead to the formation of a pressure ulcer are believed to cause damage to the deeper tissues of the body before they cause damage to the superficial tissues. By the time an ulcer presents itself on the skin as a stage I ulcer, damage to the deeper tissues has already occurred. For this reason, one must keep in mind that the four stages described above gauge the externally-visible development of the pressure ulcer and do not account for damage that

may have occurred to the deeper tissues. The physiological mechanisms that lead to the formation of pressure ulcers are discussed in section 2.7.

2.4 Mortality

Pressure ulcers are not fatal in and of themselves. However, they can lead to potentially fatal complications if left untreated, including infection, **sepsis**, osteomyelitis, and **carcinomas**[42]. The most common of these complications is infection, since pressure ulcers compromise the body's first and best defense against infection: the skin. Sepsis is a particularly dangerous, as it has an estimated mortality rate of 50% to 70% in those with pressure ulcers[42]. Squamous cell carcinoma is another particularly dangerous, if uncommon (estimated incidence rate is 0.5%[42]), complication; when squamous cell carcinoma occurs in melanomas, it behaves aggressively with a metastatic rate of approximately 61%[42]. According to Torai & Chung[125], 7.5% of patients with spinal cord injuries died of complications directly related to their pressure ulcers.

2.5 Treatment

All pressure ulcer treatments are based upon treating the patient so that his or her own natural healing abilities can repair the wound. All treatment methods begin by addressing the risk factors that lead to pressure ulcer development. Unless these factors are controlled, the ulcers will not heal. Some intrinsic risk factors, such as advanced age or neuropathy, cannot be addressed directly.

Pressure ulcer treatments can be divided into conservative and surgical methods. About 80% of pressure ulcers can be treated conservatively[58]; almost all of these are stage I or II ulcers, although sometimes stage III ulcers can be treated by conservative methods. Conservative treatment begins with debriedment of the wound and removal of any necrotic tissue. Then the wound is cleansed and disinfected and antibiotics applied if necessary. Finally, a bandage is used to cover the ulcer so it can heal on its own[57,58]. For ulcers that have progressed far enough for there to be an actual cavity, a gel is used along with the bandage to fill the wound completely. Recent research in conservative measures has also seen the application of human growth hormones to speed healing[58].

Surgical treatment is indicated whenever the ulcer has penetrated all the way through the dermis into the underlying **fascia**[58]. Most surgical techniques use flaps to fill in the dead space, resurface the wound and distribute any applied pressure over a larger area. A good flap will also allow the wound to be closed without tension. This is important because tension increases the chances that scar tissue will form or that the wound will reopen. Once surgical methods have been applied to an ulcer, conservative methods usually follow so that the wound can heal. Some surgical techniques for closing pressure ulcers can be found in [47] and [91].

Treating pressure ulcers is expensive, having been estimated at $120,000 per sore in 1987[111]. The total cost for treating pressure ulcers, including medical and surgical care, hospital bed occupancy, and lost time from work, is believed to be between $3 billion and $7 billion annually.

2.6 Prevention

Since pressure ulcer treatment is so expensive, prevention is preferred to treatment. Current preventative methods involve reducing or removing the risk factors for pressure ulcer development. Pressure relief and pressure reduction form the centerpiece of pressure ulcer prevention. For patients confined to bed (*e.g.* most quadriplegics, those recovering from surgery, some elderly in nursing homes), periodic turning and special pads and mattresses are the primary means of pressure relief. Periodic turning alters which areas of the body are exposed to pressure; guidelines recommend that patients be turned at least once every two hours[7]. Special pads and mattresses, such as high density foam mattresses, air mattresses, water mattresses, alternating pressure pads, redistribute the pressure from high-loading bearing areas to low load-bearing areas and increase the surface area over which external forces are applied. These same devices are also used to provide relief from shear and friction. In addition, patients should be positioned to minimize shear and friction. This means that elevation of the head should be avoided, and neck collars and other support devices should not be allowed to rub against the skin.

For patients in wheelchairs, pressure relief involves periodic weight shifts and the use of seat cushions. Pressure-relieving weight shifts have the same function as periodic rotation of bedridden patients; they provide temporary relief for load bearing areas. It is recommended that patients with spinal-cord injuries shift their weight at least once every fifteen minutes[7]. Strict compliance with this recommendation is difficult to achieve, especially if the patient has impaired sensation that prevents him or her from detecting a dangerous buildup in pressure over time. For this reason, pressure reducing surfaces (*e.g.* seat cushions) play an especially important role in pressure ulcer prevention for wheelchair-bound individuals. Wheelchair seat cushions are highly customized to the individual, but their design is still a hit-or-miss affair guided by various rules of thumb (*e.g.* distribute the pressure evenly over the buttocks, remove pressure from the bony prominences and areas where the tissues are thin, make the cushion envelope the buttocks)[16]. Studies of various designs of seat cushions and their efficacy can be found in [31] and [67].

Joan Sanders and her colleagues have proposed that with proper conditioning, the skin and subcutaneous tissues might adapt to handle the excessive pressure, shear and friction incurred during siting or reclining[111], making the body of a subject with spinal cord injury more able to tolerate sitting or reclining for prolonged periods of time and less likelt to develop pressure ulcers. Such conditioning would not replace seat cushions or pressure-relieving weight shifts, but would augment them. While the body clearly does adapt to mechanical stress, Sanders has yet to demonstrate that such conditioning would have a significant effect on the body’s resistance to pressure ulcer formation.

Skin care is important for all high-risk individuals. A systematic skin inspection should be performed at least once a day. Skin should be kept clean and dry, but excessive dryness should be avoided. For incontinent patients, the skin should be cleansed at the time of soiling; not only is moist skin more vulnerable to pressure-related damage, but the soiled skin serves as a breeding ground for infectious microorganisms that can colonize the pressure sores and invade the body.

Proper nutritional support is also important for all high-risk patients. Studies have suggested a role for nutrition in pressure ulcer prevention[3]. Experts advise providing support for the intake of protein and calories. Malnutrition should be avoided at all costs.

Education of both the patient and caregivers is a must. Patients and caregivers must see pressure ulcers as something controllable and understand the rationale for the different prevention strategies.

2.7 Models of Pressure Ulcer Formation

Current preventative measures are not as effective as we would like. The incidence and prevalence rates quoted in section 2.1 are in spite of the use of preventative devices and practices. Although incorrect or inadequate use of preventative measures accounts for part of the relatively high incidence of pressure ulcers, these current incidence rates cannot be entirely attributed to these factors; the preventative measures currently in use are simply not effective enough.

Current preventative measures are relatively ineffective because we are essentially "shooting in the dark" when it comes to pressure ulcer prevention. Current methods address the risk factors directly without fully understanding how these risk factors operate on the body to create pressure ulcers. If all of the risk factors were eliminated, the possibility of developing pressure ulcers would be eliminated as well, but this is not always feasible. For example, short of suspending the patient in a weightless environment, it is not possible to eliminate pressure. Since we cannot eliminate all, or even the most important risk factors, it is necessary for us to control these risk factors. Effective control requires that we understand the pressure ulcer formation process, so that we can predict what effect lowering a risk factor will have and predict how much of a risk factor can be present and still be "safe." For example, if we do not understand how external pressure leads to tissue breakdown, we cannot predict what magnitude of pressure would be safe for a particular individual, *i.e.* we cannot know the pressure/time relationship curve for that individual. In the absence of an effective model, we are left with trial and error followed by an after-the-fact evaluation of a method's effectiveness.

At present, there is no adequate model for pressure ulcer formation. A good model would explain the pressure/time curve of figure 2.2 and allow us to compute it for a particular individual once all the relevant factors are known. With an effective model, we could predict an individual's vulnerability to pressure ulcers and know what steps needed to be taken to prevent such ulcers from forming.

Although there is no adequate model, there is a clear delineation between what we do know and what we do not know. We know that the prolonged application of pressure, shear, and friction lead to irreversible tissue damage and breakdown, which usually starts in the deeper tissues of the body and spread outwards, manifesting as an ulceration on the skin surface. We also know that the presence of other external (moisture) and internal (aging, malnutrition, etc.) factors increase the vulnerability of the soft tissues to this process. What we do not fully understand are the physiological mechanisms that produce

the soft tissue damage in response to the application of external forces. However, several such mechanisms have been proposed, including:

- Impaired microcirculation
- Reperfusion injury
- **Interstitial fluid** flow
- Impeded lymphatic return
- Cellular damage from high strain rates

Each of these mechanisms is discussed in greater detail below.

2.7.1 Impaired Microcirculation

In the impaired microcirculation model, the application of external forces produces an internal stress tensor whose resulting strain tensor causes the capillaries to occlude or collapse. This results in local **ischemia**, which in turn leads to anoxia and the buildup of toxic waste products, followed by tissue necrosis. As tissue necrosis sets in, the local **collagen** network disintegrates, increasing the load on the neighboring regions, which can lead to mechanical impairment of microcirculation in those regions and start the cycle of degeneration in those regions.

The collapse of the capillaries is said to occur at an internal pressure of 32 mmHg (= 4.26 kPa)[22]. This value is somewhat misleading, however, as it is the mechanical behavior of the soft tissues that causes the collapse of the capillaries, not the pressure itself. In other words, the collapse is the result of the internal strain tensor, not the internal stress tensor. If pressure magnitude alone were all that were required for impaired microcirculation, then scuba divers, who experience isotropic pressures well in excess of 760 mmHg when diving to depths of 30 feet or more, would experience extreme ischemia during such dives. Hence, it is not the application of pressure itself which impairs microcirculation, but the mechanical response of the soft tissues to the application of anisotropic pressure.

Human skin is remarkably resilient to ischemia; it requires twelve hours of normothermic ischemia before irreversible damage sets in[22]. In contrast, muscle is especially vulnerable to ischemia, with irreversible damage setting in four hours after the start of ischemia. This agrees with the theory that pressure ulcers usually start in the deep tissues of the body and proceed outward.

In the early days of pressure ulcer research, researchers attributed pressure ulcer formation entirely to tissue damage from pressure-induced ischemia. This was supported by early animal studies[34,51,25]. Although researchers began to question the proprietary role granted to ischemia as early as 1981, the idea that pressure ulcers can be attributed to ischemia alone persists to this day ([58] and [110]). Modern research has shown that tissue damage occurs earlier than is possible for it to be attributed to ischemia alone[74]. Furthermore, if ischemia alone were responsible for pressure ulcer formation, then the curve of Figure 2.2 should be flat for all pressures above the capillary closing pressure of 32 mmHg. Hence, while ischemia from impaired microcirculation is clearly an important mechanism in pressure ulcer formation, it is clearly not the only mechanism.

2.7.2 Reperfusion Injury

Ironically, soft tissues can incur just as much or more damage after the end of an ischemic episode as during that episode. This damage is called *reperfusion injury* and stems primarily from three sources: free radical formation, **leukocyte** infiltration, and alteration of vascular permeability. During the period of ischemia, complex changes in local tissue chemistry result in the creation of enzymes that favor free-radical production. When blood flow resumes, these enzymes convert molecular oxygen into dangerous free-oxygen radicals, which can cause tissue damage. After the ischemic episode ends, the body also recruits leukocytes to eliminate damaged or dead tissue; in the process of removing dead tissue, the leukocytes may attack healthy cells as well. Finally, mechanical damage to the capillaries and changes in membrane potential during the ischemic period allow toxic waste products to leak from the capillaries into the surrounding tissues (whereas the reverse would normally be true), also producing cellular damage. Although reperfusion injury is usually thought of in the context of surgery, transplantation, and reattaching severed limbs, it is reasonable to believe that it occurs following pressure-induced ischemia. The possible role of reperfusion injury in pressure ulcer formation was suggested by Michel and Gillot[81].

2.7.3 Interstitial Fluid Loss

This mechanism was first proposed by Reddy *et al*[104] and has been the subject of much recent research, including work done by Mak *et al*[75] and Zhang *et al*[147]. In the skin, the flow of the interstitial fluid and **ground substances** combine with the mechanical properties of the collagen and **elastin** matrix to give skin its viscoelastic nature and electromechanical properties[111]. In addition, the interstitial fluid is responsible for nutrient and waste transport between the cells and capillaries of the dermis. Since the interstitial fluid is incompressible at the pressures incurred from sitting or reclining, tissue compression results in the flow of the interstitial fluid out of the compressed region. Significant fluid loss could lead to the compromise of the intercellular transport process as well as the stiffening of the soft tissue in the region, making it more vulnerable to mechanical injury. Compromise of the intercellular transport process would lead to necrosis through hypoxia, malnutrition, and the accumulation of cellular waste products. Furthermore, as fluid volume decreases, cells come into contact with one another, resulting in contact stresses that may damage these cells or inhibit their function. This is of particular concern for the **fibroblasts**, which maintain the collagen network which gives the dermis and subcutaneous tissues their structural strength. So far, interstitial fluid loss has been studied in the skin; its possible role in deeper tissues is unknown.

2.7.4 Impaired Lymphatic Return

The lymphatic system is a separate system of capillaries and larger vessels (called *lymphatics*) which transports lymph from the tissues of the body to the veins near the heart where it mixes with the general mass of blood. Krouskoup *et al*[53] and Reddy *et al*[104,106] have proposed that the same mechanisms which impede the microcirculation of blood would also impede the microcirculation of lymph. Since lymph is responsible for nourishing cells and removing waste and contains leukocytes which fight disease, impairment of the lymphatic flow would lead to cellular malnutrition, the build up of toxic waste products, and increased vulnerability to infection.

2.7.5 High Strain Rate Injury

In 1995, Adam Landesman and his colleagues proposed that a high strain rate (*e.g.* rapid deformation of the soft tissue) could significantly damage or kill soft tissue cells through a buildup of intracellular calcium[55]. They supported this hypothesis by subjecting endothelial cells ***in vitro*** to loads with the same magnitude, but different rates of application, resulting in the same endpoint magnitude of strain for all cells, but different strain rates. Cells subjected to a high strain rate demonstrated elevated intracellular calcium levels, whereas those subjected to a low strain rate did not. Furthermore, senescent cells were shown to be more vulnerable to fatal injury from rapid variations in strain than younger cells, even though they deformed to the same extent when exposed to the same load. Even if high strain rate injury is only applicable to endothelial cells, and not to the soft tissues in general (which is unlikely), this is still a significant finding, since endothelial cells in the capillaries regulate the transport of nutrients and wastes between the blood and the interstitial fluid. High strain rate injury is primarily of concern in places where the soft tissues are exposed to forces that cause rapid deformation, such as the heel of the foot during normal walking, making it important for understanding why diabetics develop ulcers on their feet. It's role in causing pressure ulcers in seated or reclining subjects is presently unknown.

2.7.6 Apparent Contradiction Between Formation Mechanisms and Physiopathology

One might notice an apparent contradiction between some of the proposed mechanisms for pressure ulcer formation, which include both blood and interstitial fluid loss, and the physiopathology of the early stages of pressure ulcers, in which edema and the engorgement of the capillaries with red blood cells occur. However, one must take into account that the physiopathology is that of *visible* legions, whereas the proposed mechanisms are those that are active during the application of external forces when the lesion is not yet visible.

2.8 Experimental Analysis of Proposed Mechanisms for Pressure Ulcer Formation

All of these mechanisms involve internal physiological changes resulting from the application of external forces, and assessing the role each plays in pressure ulcer formation requires the ability to measure these internal physiological changes under controlled conditions. In particular, with the exception of reperfusion injury, all of the proposed mechanisms depend upon the internal mechanical strain tensor (and its time derrivative), and any attempt to assess their role in the pathogenesis and development of pressure ulcers must account for the mechanical deformation in some fashion. Measuring the internal physiological changes proposed by these mechanisms is somewhat difficult, however, and to overcome these difficulties, researchers have taken the following approaches:

(1) Animal models
(2) Finite-element models
(3) Noninvasive external measurements indicative of internal tissue state

2.8.1 Animal Models

From the earliest days of pressure ulcer research, researchers have used animal models to explore the relationship of external pressure, shear, and friction to the pathogenesis of pressure ulcers. Pioneering work done by Groth[34] and Kosiak[51] established the inverse pressure/time relationship for sore formation. Their experiments were flawed, however, in that they used "loose-skin" animals (rabbits in Groth's experiments and dogs in Kosiak's) and pressure-application methods that were later shown to be unreliable in the magnitude of pressure they produced. Hence, some of their conclusions about the magnitude of pressure needed to produce ulcers are of questionable relevance to human beings.

Dinsdale[25] was the first researcher to use pigs, whose skin is much more similar to human beings both structurally and histologically than rabbits or dogs, as his animal model. He applied pressures ranging from 160 mmHg to 1200 mmHg, both with and without accompanying non-normal shear force to achieve friction between the applicator and the skin surface, to the posterior superior illiac spine of paraplegic swine for three hours. These experiments produced superficial (stage II) lesions in four of nine swine without friction and in five of ten swine with friction; less pressure was required to create an ulcer when friction was present. Dinsdale also explored the repeated application of pressures ranging from 25 to 454 mmHg, both with and without accompanying friction, for three hour periods over several days on normal swine and found that pressures as low as 45 mmHg could produce partial-thickness (stage II) ulcers when friction was present, but pressures of 290 mmHg were required when friction was not present. Dinsdale also measured and compared the cutaneous blood flow of the pigs subjected to pressure and friction with those subjected to pressure alone and found no significant difference between the two groups. On the basis of these experiments, Dinsdale concluded that friction significantly reduced the magnitude of pressure applied for a given duration required for an ulcer to form and that the ulcer-enhancing effect could not be attributed to ischemia.

The animal experiments of Daniel *et al*[22] were the first to question the ischemia model of pressure ulcer formation. They subjected thirty paraplegic swine to pressures ranging from 30 mmHg to 1000 mmHg for periods ranging from 2 to 18 hours. In contrast to earlier experiments, they used a force transducer at the point of contact and a computer-controlled negative feedback system to insure that the pressure applied to the experimental subject remained within +/-5 mmHg of the target pressure during the period of application and performed a full-thickness biopsy in addition to a visual inspection of the site where pressure was applied. The results of the experiments divided the pigs into three groups: (1) those with muscle damage only, (2) those with damage to the muscle and deep dermis, and (3) those with full-thickness damage to the muscle, dermis and epidermis; only the third group had visible lesions. The extent of the damage was directly related to the magnitude and duration of the pressure applied; pigs in the first group had been subjected to low pressures for long durations or high pressures for short durations, while pigs in the third group had been subjected to moderate-to-high pressures for very long durations. Daniel *et al*'s results were significant in that (1) they demonstrated that the initial pathologic changes for serious (stage III or higher) ulcers begin in the muscle and spread outwards; and (2) damage to the skin began as early as eight hours with a sufficiently high

magnitude of applied pressure. The latter conclusion is significant, since skin has been demonstrated to withstand normothermic ischemia for up to 12 hours without necrosis([82] quoted in [22]), casting doubt upon the ability of the impaired microcirculation mechanism to account for the entire pathogenesis of pressure ulcers.

Reddy *et al*[105] and Le *et al*[56] explored the relationship between external interface pressure and subcutaneous pressure in Yorkshire pigs. Reddy *et al* used a wick catheter technique to measure the changes in interstitial pressure in the forelimbs of ten pigs to the application of external pressures ranging from 200 to 500 mmHg via a blood-pressure cuff. His results showed that internal pressure approached 72% of the external pressure; with a pre-infusion of excess fluid into the tissue, there was no significant difference between internal and external pressure.

In contrast to Reddy *et al*'s experiments, Le *et al*'s experiments showed a significant difference between internal and external pressure. Le *et al* measured the relationship between internal and external pressures near the greater trochanter of pigs lying horizontally on a clear plexiglass table using a modified "needle method." Unlike Reddy *et al*, Le *et al* found that the internal pressure was not equal to the external pressure, but was three to five times greater when measured near the trochanter; the measured internal pressure fell off as the sensor moved away from the trochanter. Le *et al* concluded that their results were consistent with the fact that pressure ulcers were more likely to be found near bony prominences such as the trochanter.

The apparent contradiction between Reddy *et al*'s and Le *et al*'s results can be resolved by examining how the pressure was applied in each case. In Reddy *et al*'s experiments, the pressure was applied biaxially through a cuff and the resulting compression of the soft tissues was qualitatively observed to be "uniform." In Le *et al*'s experiments, the pressure was applied uniaxially and the resulting compression of the soft tissues was not uniform. This supports the notion that the non-uniform deformation of soft tissue results in higher internal stress in that tissue[1]. However, neither experiment measured soft tissue distortion, so a quantitative relationship between external tissue pressure and internal soft tissue distortion could not be established.

More recent animal experiments have been conducted by Hyodo *et al*[35] and Goldstein and Sanders[32]. In order to investigate the healing rate of pressure ulcers, Hyodo *et al* exposed monoplegic pigs to 800 mmHg of pressure applied to the greater trochanter for 24 hours or longer through a 3 cm diameter plastic disk with a spring and locking collar attached via a cancellous screw; the screw was drilled into the proximal femoral shaft, so as not to disturb the trochanter. Hyodo *et al* chose to use monoplegic pigs instead of paraplegic pigs to avoid the complications and mortality experienced by Daniel *et al*, and

1. The reverse is not necessarily true. Consider a human diving to a depth of 30 feet in water; this person would experience an interface pressure of 760 mmHg across the entire skin surface, with correspondingly high internal soft tissue pressures. However, because the interface pressure is uniform across the entire body, and soft tissue is incompressible at 760 mmHg, there is no significant soft tissue distortion.

unlike Daniel *et al*, they did not wait until significant muscle atrophy had set in before applying pressure. Application of pressure for two days was found to cause sufficient breakdown for a stage IV ulcer to develop. Following their manifestation, the ulcers were debrieded to reveal viable tissue, packed with gauze and bandaged to allow the wounds to heal. The progress of the wound healing was monitored over a three-week period by taking photographs and measuring wound dimensions and volume every other day. Wound area and volume were found to increase briefly after treatment then decrease exponentially; this healing behavior was found to match that reported on human beings ([119] quoted in [35]). Hyodo *et al* concluded that the uniform and predicable wound-healing behavior of their model made it an ideal one for the investigation of pressure ulcer formation and healing.

Goldstein and Sanders[111] developed their animal model to test two hypothesis: (1) the point when tissue breakdown occurs depends upon the magnitude and direction of the load, and (2) tissue subjected to repetitive mechanical stresses will adapt to accommodate those stresses. To test the first hypothesis, they subjected eight normal pigs to several different combinations of normal and shear stresses applied in 10 minute intervals until breakdown (stage I, stage II or reactive hyperemia) started to occur; combinations of normal and shear force that caused slippage were avoided. To test the second hypothesis, Goldstein and Sanders subjected eight other pigs to loads daily for four ten-minute intervals each day; three different combinations of normal and shear stresses were used. In neither case were the investigators attempting to create full-thickness (stage III or IV) ulcers and none manifested. In both experiments, Goldstein and Sanders used a computer-controlled applicator with negative feedback to insure that the application of normal and shear forces remained constant at their nominal values. Unlike previous experiments by other researchers, the applicator could control both the applied pressure and the applied shear force. Following both experiments, tissue samples were excised to the depth of the skeletal muscle and examined both quantitatively and qualitatively by an investigator who had been blinded to the treatment of each sample. Such quantitative analyses proved to be difficult however, as many relevant features of the skin were found to be highly variable between animals even in control tissue samples. Furthermore, whether the tissue samples had been preserved in paraffin or plastic blocks was found to affect measurements of dermal area.

Results from Goldstein and Sanders's analysis confirmed that shear stress significantly reduced the pressure needed for ulcers to form; these results were unique in that the applicator used could control and maintain the magnitude and direction of the shear force as well as the magnitude of the normal force. However, they did not evaluate enough subjects to establish a quantitative relationship between pressure, shear, and ulcer formation. For the pigs subjected to repetitive stresses, analysis also showed that there was no significant difference between control and experimental tissue samples, indicating no detectable adaption. Goldstein and Sanders concluded that observing the progressive change from healthy skin to low grade ulceration was difficult and very subtle and sophisticated analysis would be required to observe and evaluate such changes.

Kokate *et al* used mongrel swine to investigate the effects of temperature on pressure ulcer

development[50]. They designed an applicator that could apply a constant 100 mmHg of presssure at temperatures of 25 degrees, 35 degrees, 40 degrees and 45 degrees Celsius at different locations over the body of the pig. In their experiments, the pressure and temperature of their applicator was applied to the skin of 16 pigs for five hours. Thereafter, they visual tracked changes to the regions of the skin of the animals where the applicators had been applied and obtained histological samples from those regions extending through the subcutaneous fat and into the muscle every seven days. After 28 days, the pigs were killed and deep biopsies of the regions where the heat and pressure had been applied were found. Kokate *et al* found that no damage at all occured in the regions where the applicator had a temperature of 25 degrees Celsius, while those regions whose applicator had been kept at 35 degrees (almost equal to the normal skin temperature for pigs) displayed damage to the muscle but not to the skin. Regions that had been kept at 40 and 45 degrees Celsius displayed damage to both the skin and the muscle, with significantly more damage occuring to both skin and muscle from the latter temperature. They concluded that prolonged exposure to temperatures above the normal surface temperature for skin could accellerate the formation of pressure ulcers, but temperatures below it could inhibit pressure ulcer formation.

In summary, the main result of the animal experiments performed so far has been to establish the relationship between external forces (pressure, shear, and friction) and the development of pressure ulcers[34,51,25,22,32]. So far, quantitative relationships between external pressure and ulcer formation have been established[34,51,25,22,32] and the qualitative effect of shear and friction on pressure ulcer formation[25], although recent work presents the potential to develop a quantitative relationship between shear, pressure and ulcer formation[32]. Recent work has also attempted a quantitative, histological analysis of the progressive physiological changes leading up to pressure ulcer formation[32], attempts at establishing a quantitative relationship between external and internal tissue pressure[56,105] and investigated how the prolonged application of heat affects the development of pressure ulcers[50]. However, no animal studies so far have attempted to observe the progressive changes leading to ulcer formation during the application of pressure or to quantify the relationship between soft tissue *distortion* and ulcer formation.

2.8.2 Finite Element Models

Some researchers have approached the evaluation of the physiopathological process of pressure ulcer formation through finite element modeling. Finite element models have the advantage of providing precise control over the experimental parameters and allow easy examination of any of the model's parameters, even parameters that might be difficult to evaluate in real-world experiments, such as internal tissue deformation. The main disadvantage of finite element models is that the applicability of their results depends upon how well the underlying physiological model used to construct the simulation; if the simulation's model does not match reality, then conclusions drawn from the simulation will be of questionable validity. Of course, this means that the results of real-world experiments can serve as a check on the validity of a finite element model; disagreement between the results of a real-world experiment and a simulation of a finite element model using the same experimental data indicates a flawed model. Agreement between a finite

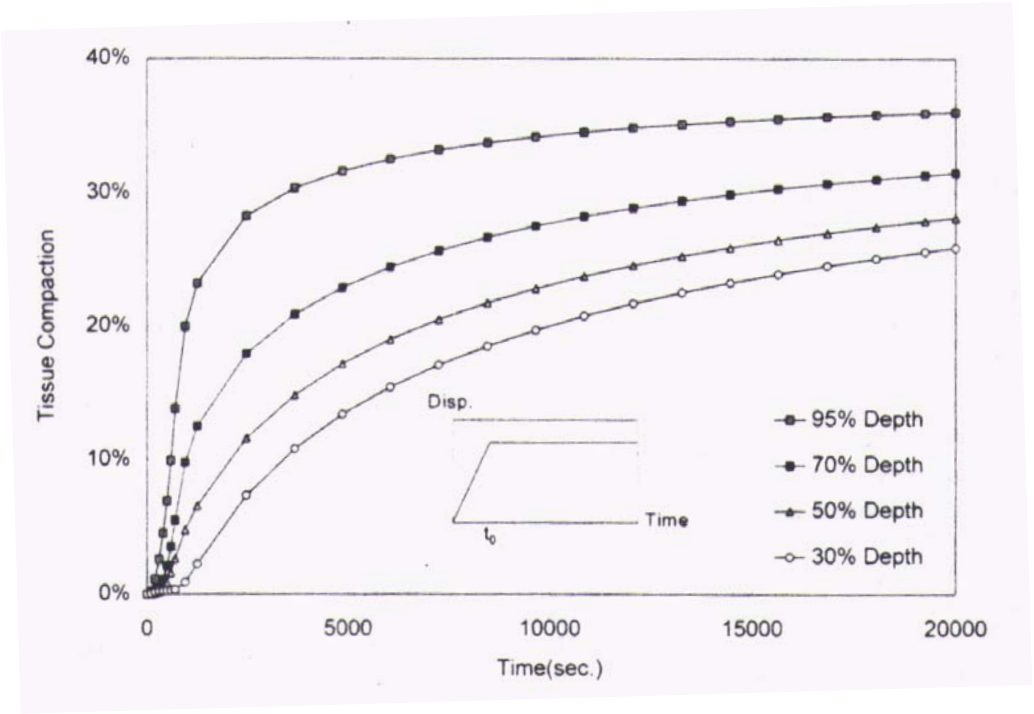

Figure 2.3: Tissue compaction vs. time predicted by the model of Arthur Mak and his colleagues [147]. The long time required for the tissue to reach a steady-state agrees with the creep response for tension in soft tissue[30] and indentation tests of Cochran, as reported by Reddy *et al* in [104].

element model and real-world experiments strengthens, but does not entirely validate, conclusions drawn from that model.

Early attempts at finite element modeling included the work of Chow and Odell[18] and Reddy and his colleagues[104,106]. Chow and Odell used an axisymmetric finite element model to estimate internal stress distributions under various boundary conditions in which large deformations were built up in an incremental manner. Reddy *et al*[106] estimated the internal strain distribution using a two-dimensional physical model for the buttock. The results of both models agreed for small loads. The main weakness of these early works was their simplicity; both were effectively two-dimensional models generalized to three-dimensions. However, while the buttocks are certainly symmetric about the center plane of the body perpendicular to its front (or at least reasonably approximately so), they are not axisymmetric and have significant variation in all three dimensions.

Working from a simple mathematical model, Reddy *et al* were the first to suggest the role of interstitial fluid flow in pressure ulcer formation[104]. Considering a cylinder of tissue with a pressurized region and using Darcy's Law, he and his colleagues showed that an inverse pressure/time relationship existed for the fluid to reach a given fraction of its initial volume. This relationship mirrors that of the pressure/time relationship required for pressure ulcers to form. This work became the basis for the finite-element models of Mak *et al*[75] and Zhang *et al*[147], which have produced rather strong results so far. Using a

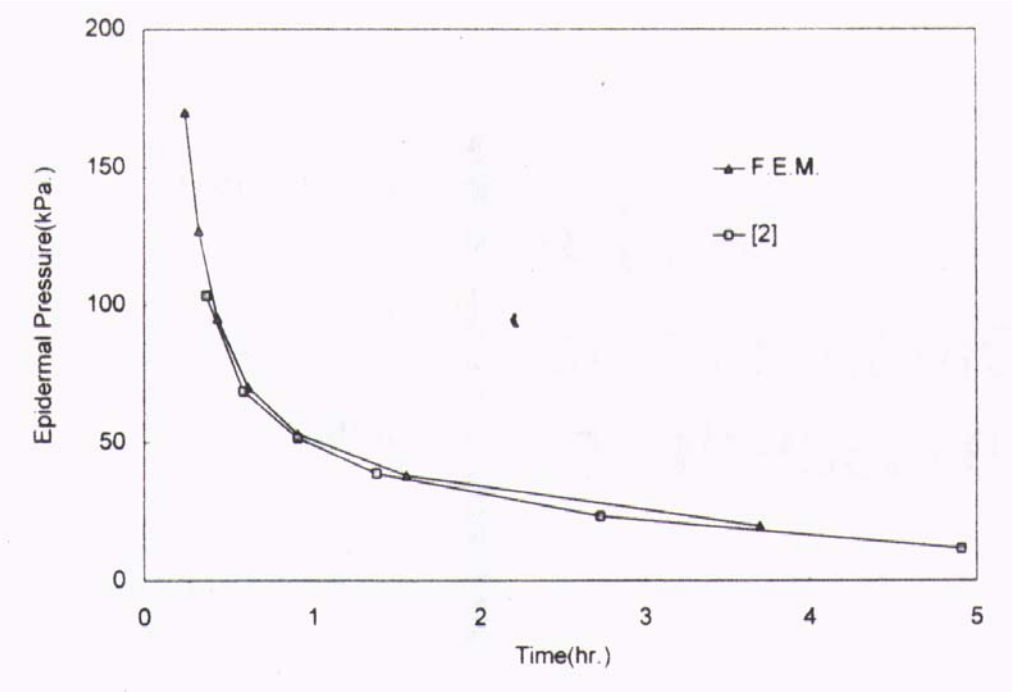

Figure 2.4: Agreement (taken from [147]) between pressure and time required for soft tissue damage predicted by Zhang *et al*[147] and clinical observations of Reswick and Rogers[108]. The predicted curve is for an arbitrary threshold of 11.5% loss in volume before tissue damage from interstitial fluid loss occurs. The agreement between this value and reality is not presently known.

biphasic poroelastic model for the skin and subcutaneous tissues, Zhang *et al*[147] were able to create a pressure/time response curve that agrees well with the experimental results of Reswick and Rogers[108] illustrated in figure 2.2, when an arbitrary threshold of 11.5% loss in interstitial fluid volume was used at the point where soft tissue damage occurred (see figure 2.3). Mak's models have also produced soft tissue indentation creep curves that agree with what is known about indentation creep in human soft tissue (see figure 2.4).

The primary advantage that Mak *et al*'s and Zhang *et al*'s models have over earlier models is the use of more sophisticated mechanical model than has been used previously. Their poroelastic model agrees more with what is known about the viscoelastic properties of human skin and can handle large indentations as well as small ones. However, as Mak *et al* and Zhang *et al* clearly state in their work, the threshold of 11.5% volume loss for tissue damage to occur is arbitrary; whether skin loses this much interstitial fluid volume under seated conditions, or whether this loss is enough to cause damage in reality is not known. Studies that can measure the actual deformation of the skin and subcutaneous tissues and calculate the actual fluid loss under seated conditions are needed.

Another weakness of Mak and his colleagues' model is that it only applies to poroelastic solids like the skin. Muscle and fat are not poroelastic materials, and hence the results of Mak and his colleagues are of validity at those places where the skin lies directly over the

bone. This is not as big a disadvantage as it might appear at first, as it is just these areas where pressure ulcers are likely to appear. Nevertheless, Mak and his colleagues' results cannot be used to estimate interstitial fluid loss in areas where tissues other than skin are present.

Other attempts at finite element modeling of human soft tissue include the work of Todd and Thacker[124] and Vannah and Childress[128]. Todd and Thacker created three-dimensional finite element models of the soft tissues around the ischial tuberosities of one male and one female subject. The geometry of each model was generated from MRI scans taken with the back and thighs of the subjects suspended above the imaging table by foam cushions so that the buttocks were left to hang freely. Four different materials made up each model: bone, soft tissue, cushion and elastic foundation. The mechanical properties of bone were assumed to be average values obtained from the literature; mechanical properties of the other three substances were obtained experimentally for each subject. Todd and Thacker subjected their models to various boundary conditions and computed the resulting interface pressures from the model; these values were then compared to the interface pressures obtained when the experimental subjects were subjected to the same boundary conditions *in vivo*. A 50% discrepancy between computed and measured pressures for reclining subjects was found (results for seated subjects were not available). Todd and Thacker concluded that better estimates of soft tissue mechanical properties were required to make their model a viable one.

Vannah and Childress[128] did not address the development of pressure ulcers directly, but the modeling of bulk muscular tissue *in vivo*. Nevertheless, their results have significance for pressure ulcer research, as Daniel *et al*'s animal experiments demonstrated that stage III and higher pressure ulcers can start with degeneration in the muscular tissue[22]. Vannah and Childress conducted indentation tests on the posterior lower legs of living human subjects and created a materially and geometrically non-linear two-dimensional axisymmetric finite element model to estimate the composite material stiffness of the muscular tissue. The model of Vannah and Childress could accommodate large soft tissue strains and accounted for local and global deformation geometries. The indentation tests revealed that while bulk muscular tissue exhibited hysteresis and a non-linear stress/strain relationship, extensive preconditioning was not needed to gain repeatable results; this contrasts with the behavior of skin, ligaments and tendons, for which extensive preconditioning is needed to produce a repeatable hysteresis curve. Their model showed good agreement between computed and measured force/displacement curves for both indenters of 8 mm and 19 mm diameter for up to 20 mm of indentation. Vannah and Childress also found that the typical composite stiffness of bulk muscular tissue could be represented by the Jamus-Green-Simpson strain energy formulation for elastomers.

Vannah and Childress's model is limited in that it only applies to bulk muscular tissue. Skin, fat, and other body tissues have different mechanical responses, as is seen by the absence of preconditioning in muscular tissue. Hence, Vannah and Childress's results are not directly applicable to pressure ulcer development in the buttocks region, although they are applicable to modeling muscular tissue in that region. Vannah and Childress's method

is also not directly applicable, as, unlike the lower leg, the buttocks cannot be approximated as axisymmetric and the differences in mechanical behavior of the different types of soft tissue cannot be neglected.

2.8.3 Noninvasive External Measurements Indicative of Internal Tissue Shape

A third approach that researchers have taken to assess the physiological response of human soft tissue to external forces is to measure external quantities noninvasively that are believed to be indicative of internal tissue conditions. Some such quantities that investigators have used include:

(1) Interface pressure, shear, and friction
(2) Cutaneous blood-flow
(3) Soft tissue stiffness

Measurements of interface pressure and accompanying shear and frictional forces are as old as the field of modern pressure ulcer research itself. Obviously, if one knows the distribution of mechanical forces applied to the body, the constitutive equations for human soft tissues, and the relevant parameters of those equations (*e.g.* distribution of the elastic moduli, viscoelastic constants, etc.), then one can theoretically compute the mechanical state of the internal soft tissues from measurements of external forces alone. However, not enough is known currently about the mechanical behavior of human soft tissue *in vivo*, nor how that mechanical behavior varies across individuals or between high risk and low risk individuals, for such computations to be feasible. The mechanical behavior of human soft tissue is complex and dependent upon the loading history, and simple assumptions about the relationship between external forces and the internal mechanical state of the soft tissues are not warranted. Furthermore, even if we were able to predict internal mechanical state from measurements of the external forces, we do not know enough at present about how the mechanical state of the soft tissues affects their physiological function. Hence, measurements of external forces are not at present sufficient to characterize the internal physiological state.

When the genesis of pressure ulcers was attributed entirely to tissue necrosis due to ischemia arising from impaired microcirculation, non-invasive measurements of skin blood flow were popular[5,21]. Such measurements were used to relate the magnitude of pressure and shear required to occlude blood flow in the skin and to explore differences in the cutaneous blood flow of subjects at high risk and low risk for developing pressure ulcers. While less popular, noninvasive evaluation of cutaneous blood flow is still used today; an excellent survey of the techniques can be found in Lee and Ostrander's work[59].

As an example, Bogie *et al*[9] used measurements of transcutaneous oxygen tension and transcutaneous carbon dioxide with accompanying interface pressure measurements to evaluate the effectiveness of seat cushions in maintaining the cutaneous blood flow of a total of 42 subjects with traumatic spinal cord injury. Their results showed that patients with a lesions below T6 (*e.g.* paraplegics) showed a progressive decrease in ability to maintain cutaneous blood flow while seated on their prescribed seat cushions, while those with lesions above T6 (*e.g.* quadriplegics) showed progressive improvement in ability to

maintain cutaneous blood flow. On the basis of these results, Bogie *et al* concluded that paraplegics were at greater risk for developing pressure ulcers than quadriplegics.

While cutaneous blood flow measurements are useful for evaluating the role of impaired cutaneous microcirculation in the formation of pressure ulcers, these measurements are not useful for evaluating the role of other mechanisms, such as interstitial fluid loss or impeded lymphatic return. In addition, cutaneous blood flow measurements give no information about blood flow in deeper tissues. Since the skin has been shown to be highly-resistant to ischemia([82] quoted in [22]), the relative utility of cutaneous blood measurements, as opposed to muscle blood flow measurements or soft tissue deformation measurements, is questionable.

Brienza *et al*[11,12] have proposed soft tissue stiffness as a measure of soft tissue distortion. As discussed above, soft tissue is best modeled as a quasi-linear viscoelastic solid. If the indentation is perpendicular to the skin surface and the relaxation of the soft tissue in response to that indentation is neglected, the force/deflection relationship may be written as:

$$F(x) = k(x)(x - x_0) \qquad x \geq x_0 \tag{2.1}$$

where x is distance along the direction of indentation, x_0 is the depth where the skin surface is encountered, and k(x) is a function giving the effective stiffness of the soft tissue at depth x. The form of the function k(x) depends upon the unloaded thickness of the soft tissue; for a given compressive load, thinner tissue will exhibit a stiffer response than thicker tissue[15]. The form will also depend upon the composition and structure of the tissue under the indenter. Hence, measurements of tissue stiffness vs. indentation depth can give a measurement of overall soft tissue distortion. The stiffer the tissue response to indentation, the more relative distortion has taken place.

Brienza *et al* have developed a seating apparatus capable of creating seating contours and measuring the resulting interface pressures and soft-tissue stiffnesses[12,43] and an algorithm that creates seat-cushion contours that distributes pressure in inverse proportion to the soft tissue stiffness[11]. Inasmuch as stiffness characterizes soft tissue thickness, this means that load-bearing is shifted away from thinner tissues to thicker ones, which are believed to be better able to tolerate pressure for longer periods of time[15]. Although data on the effectiveness of seat-cushions designed by this algorithm in preventing pressure ulcers are not yet available, an evaluation by Karg *et al*[44] on 10 able-bodied subjects and 30 elderly subjects demonstrated that use of high-resiliency foam cushions constructed with the stiffness-optimized contour resulted in lower peak pressures than use of cushions of the same material constructed with contours derived from the shape of the seated buttocks alone. Another evaluation by Brienza and Karg[14] on 12 spinal-cord injured and 30 elderly subjects also demonstrated the superiority of cushions designed by this algorithm over flat foam cushions for reducing peak pressures. This same study also showed that changes to the shape of the seating surface produced greater variation in the distribution of interface pressure for subjects with spinal cord injury than the similar

changes to the seating surface shape produced in the variation in interface pressure distribution of the elderly subjects, even though Brienza and Karg could find no significant difference in the stiffness of the soft tissues for the two groups for similar loading conditions.

The main drawback of soft tissue stiffness measurements is that, while they provide a good measurement of overall soft tissue deformation, they cannot measure the distortion of the individual soft tissue layers, *e.g.* the deformation of the skin, fat, and muscle. The deformation of the individual layers could be computed from overall stiffness measurement if the arrangement and mechanical properties of the tissue layers were known, but they are not.

Chapter 3
The System

As discussed in chapter two, researchers who study the origin and prevention of pressure ulcers have great interest in the role that soft tissue distortion plays in their development. This interest includes the role that the pelvis plays as a rigid indenter into the soft tissues of the buttocks, since this indentation is a major cause of such distortion and because pressure ulcers tend to occur beneath the bony surfaces of the body. However, until now, researchers have had to make do with indirect measurements of soft tissue distortion[14] or with finite element models whose ability to reflect reality is unknown[124]. Direct measurements of soft tissue thicknesses for seated subjects using ultrasound, such as those done by Wang[133,136], have so far only measured tissue thickness along a single line but not over an entire areas. Consequently, such measurements cannot be used to measure the shapes of the soft tissues. Likewise, these efforts did not measure the location or orientation of the pelvis with respect to the seating surface and therefore could not analyze the role the pelvis plays as a rigid indenter into the soft tissue.

This thesis extends the Computed Automated Seating System (CASS) developed by Dr. David Brienza and his group at the University of Pittsburgh[43] and used by Jue Wang for her Ph.D. thesis[133] and subsequent work[134,136]. It develops a new methodology for measuring the position and orientation of the pelvis and the shapes of the soft tissues in the right buttock of a seated human subject using the existing hardware of the CASS with new, custom, software. It differs from previous work with the CASS in that its measurements of soft tissue shape are direct, occur over an area rather than a single line, and includes the position and orientation of the pelvis in addition to the shapes of the individual soft tissue shapes. Measuring the position and orientation of the pelvis not only allows the new system to assess its role as a rigid indentor qualitatively, but to compute changes in the volume and shape of the bulk tissue that lies beneath it. This thesis is also focusses on the relationship between the pelvis, the seating surface shape, the interface pressure and the distortion of the soft tissues of the buttocks. This distinguishes it from the work done by Wang or Todd and Thacker[124], who used measurements of soft tissue distortion to compute the parameters of models of soft tissue behavior but did not focus themselves with the observed relationship between soft tissue distortion and seating surface shape.

We begin this chapter with a detailed description of the subsystems that make up the augmented Computed Automated Seating System. We then describe the coordinate systems we use to describe the position and orientation of the rigid objects the system developed in this thesis uses for its measurements, such as the pelvis or the surface of the

Figure 3.1: The Computer Automated Seating System (CASS)

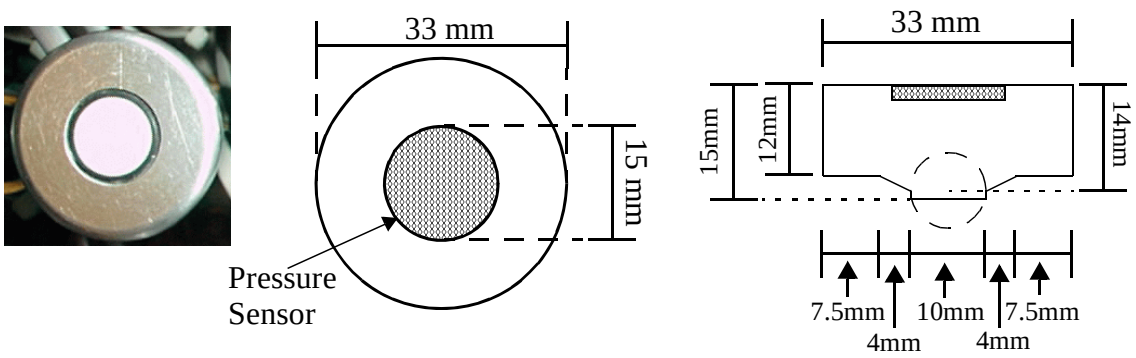

Figure 3.2: A typical actuator head with a pressure sensor

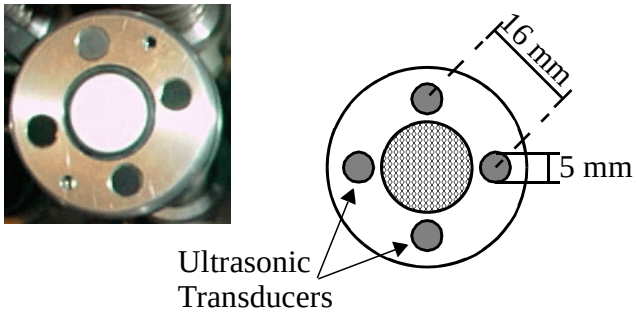

Figure 3.3: An actuator head that has been augmented with ultrasonic transducers

CASS itself. Then we describe the experimental procedure used to acquire data from a subject seated on the CASS and the procedures used to analyze and visualize these data. Finally, we analyze the accuracy of the measurements made and values computed by these procedures.

3.1 Description of Subsystems

Figure 3.1 displays the augmented Computed Aided Seating System. It consists of a 12x11 rectangular array of actuators that can move up and down under the control of a personal computer. Each actuator has a head that swivels easily around a ball bearing and contains at pressure sensor at its center (figure 3.2). The swivelling heads allow the surface of the actuators to conform to the shapes of the buttocks of a seated subject rather than indenting themselves into his or her skin. The pressure sensor measures the pressure at the interface between the buttocks and thighs of the seated subject and the surface of the CASS. A position wand mounted on the right side of the CASS allows the measurement of discrete points in the coordinate frame of the CASS within an approximate 3' radius. The actuators are separated by a mean distance of 42.65 mm, as measured by the position wand.

Nine actuators arranged in a 3x3 grid on the right side of the CASS have been augmented with four ultrasonic transducers each (figure 3.3), for a total of 36 ultrasonic transducers, in addition to the normal pressure sensor. These actuators have also been augmented with sensors to measure the orientation of their surface so that echoes measured by the ultrasonic transducers can be located in space relative to the CASS. These actuators were chosen for augmentation because they cover the right buttock of subjects seated on the CASS. All of the actuators of the CASS were not augmented because the cost would be prohibitive. The work of augmenting these nine actuators with ultrasound and orientation sensors was done primarily by Jue Wang and is described in several of her publications[131,132,135].

The augmented CASS can be divided into five different subsystems:

(1) The **motor** subsystem controls the movement of the actuators up and down over a range of approximately 150 mm.
(2) The **pressure and orientation** subsystem monitors the interface pressure between the seating surface of the CASS and the buttock and thighs of the seated subject. It also monitors the orientation of the nine actuators augmented with ultrasonic transducers.
(3) The **ultrasound subsystem** controls and monitors the 36 ultrasound transducers mounted on the augmented actuators. It selectively excites them one at a time, listens for and amplifies echoes from the transmitted pulse, and digitizes the result. By analyzing these echoes, we can measure the thickness of the layers of skin, fat, and muscle above the transducer. By assembling the results from all 36 transducers, we obtain the shape of those layers in the superficial right buttock of the seated subject.
(4) The **position wand** subsystem measures the location of discrete points within about a 635 mm radius of the right front corner of the CASS. We use the position wand to measure the locations of points on the surface of the pelvis which are

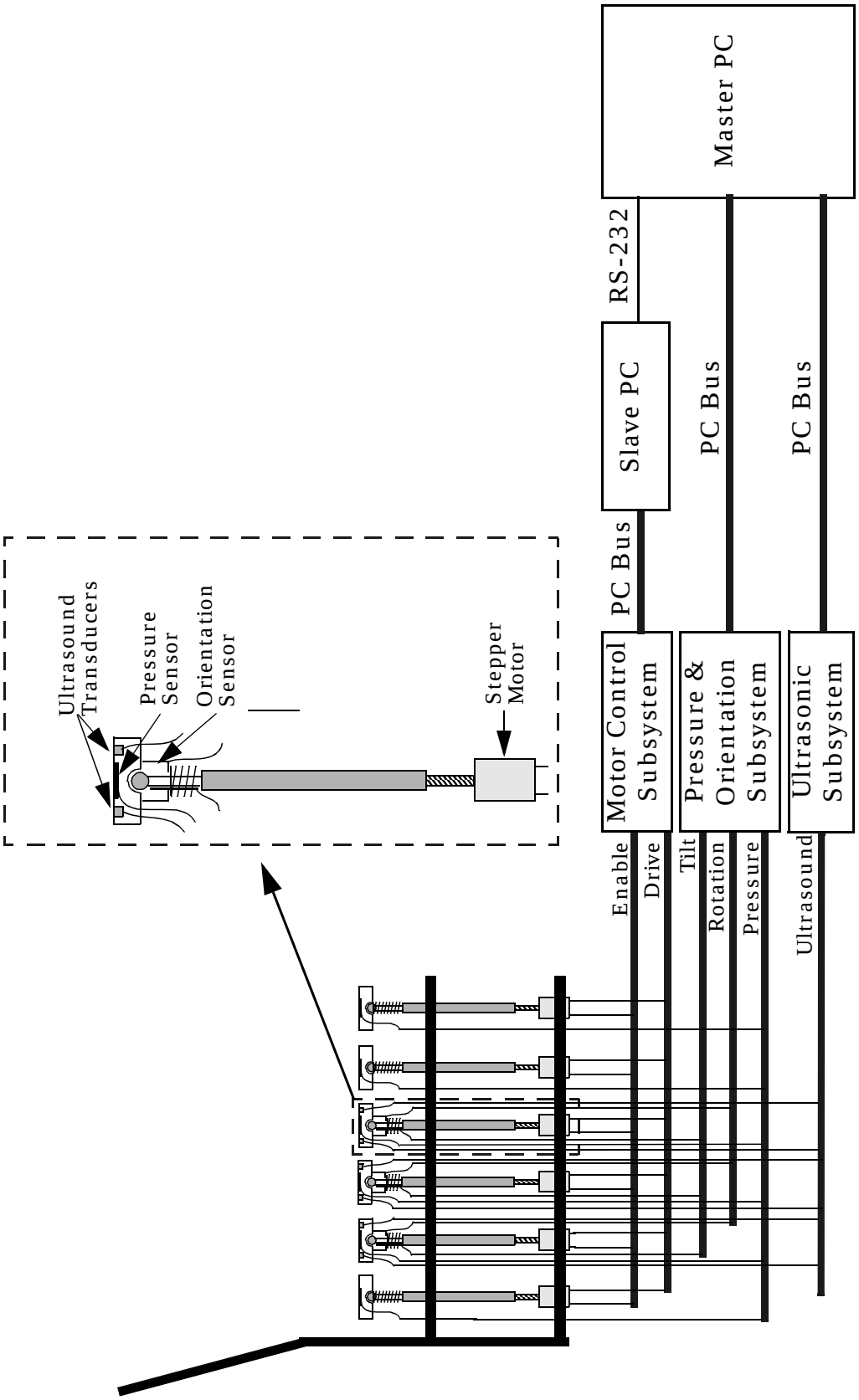

Figure 3.4: Block diagram of the CASS, illustrating its subsystems

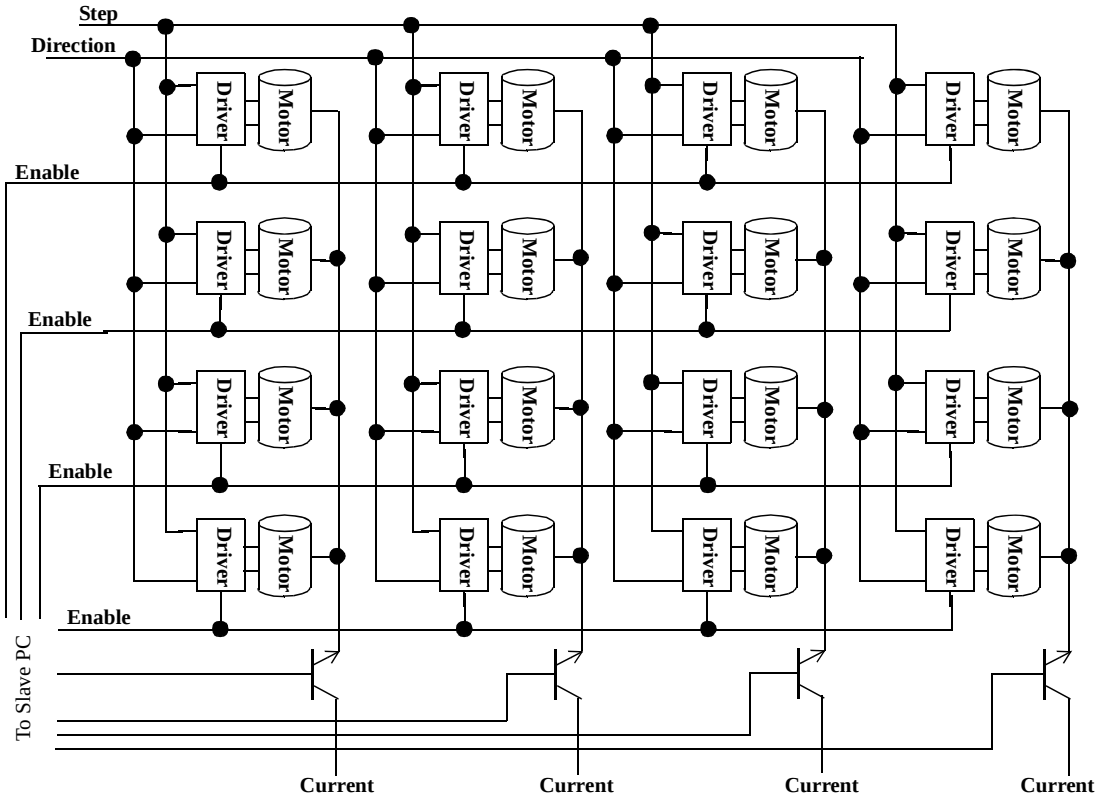

Figure 3.5: The motor controller and driver subsystem of the CASS

then matched to a model of the pelvis through a registration process to measure the position and orientation of the pelvis with respect to the surface of the CASS.

Figure 3.4 shows a block diagram of these subsystems and how they are integrated. Each of these subsystems is discussed in greater detail below. The subsystems are controlled by a pair of PCs, a master and a slave. The master PC controls all of the subsystems except the motors directly, which it controls by issuing orders to the slave over an RS232 serial line using a custom protocol. This arrangement exists to accommodate the limited number of ISA slots available in the master PC.

3.1.1 Motor Subsystem

Figure 3.5 illustrates the block diagram for the motor subsystem. It consists of 128 Superior Electric M601 stepper motors arranged in an 11x12 array; the two actuators in each of the upper- right and upper-left corners of the last row of the array do not have motors connected to them and do not move. The M601 stepper motor has 200 steps per revolution. Each motor is connected to a threaded rod which is screwed into the base of a slotted aluminum cylinder that makes up the base of the actuator. A tiny metal rod firmly attached to the frame of the CASS is inserted into the slot of the cylinder to keep it from rotating. Consequently, when the system drives the motor to turn the threaded rod, the cylinder moves up and down. In this arrangement, the motors can move the actuators over a range of approximately 150 mm. Each stepper motor is controlled by its own Allegro

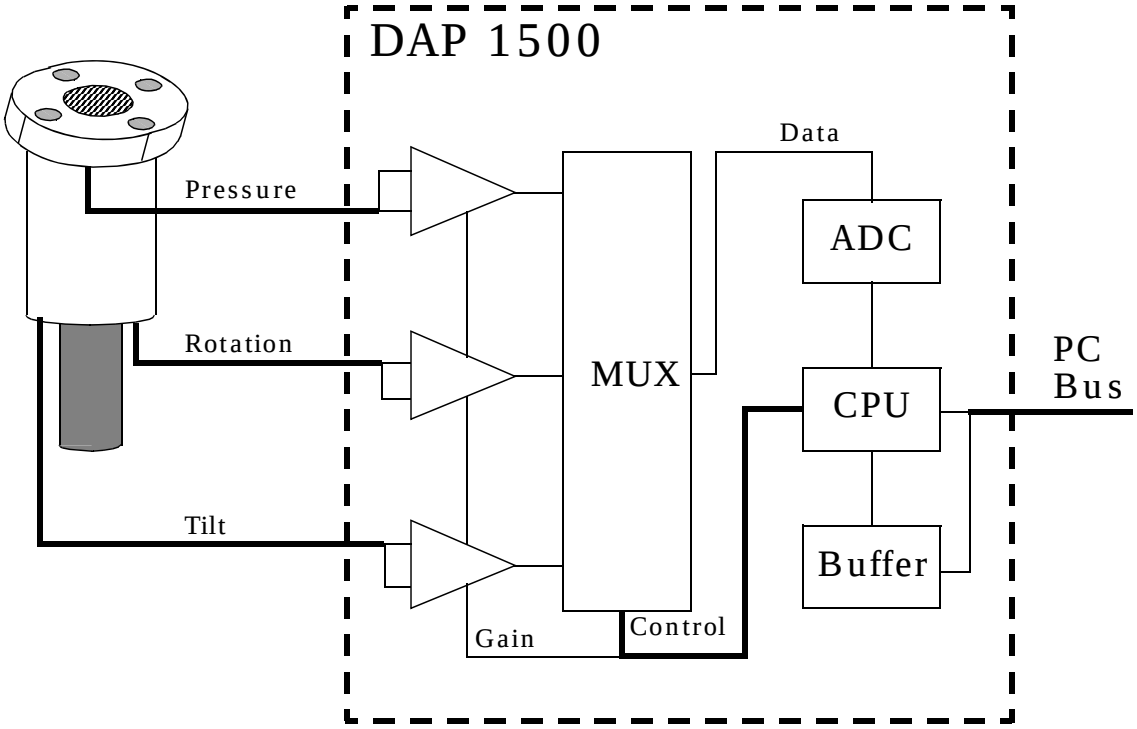

Figure 3.6:The subsystem of the CASS that measures interface pressure and the orientation of the surfaces of its actuators.

UCN-5804B stepper motor translator/driver IC. Because the motors do not have any sort of position feedback attached to them, their heights are calculated using dead reckoning based on the number of steps taken by the motor times the pitch of the screw.

At the time the motor subsystem was designed, no off-the-shelf component could control 128 individual stepper motors, so a custom control system was designed instead that would allow an off-the-shelf 8-axis stepper motor controller card installed in the slave PC to be multiplexed among the 128 motors. Motors are grouped together in sets of 16, with each member of a set sharing the same step input and direction signal from the motor controller card. Within each group of sixteen, each motor belongs to a *primary subgroup* of four motors and a distinct *secondary subgroup* of four motors. Motors within the same primary subgroup share the same current source, which may be selectively enabled or disabled. Motors within the same secondary subgroup have the enable/disable input of their UCN-5804B drivers ICs connected together. Thus, by choosing which current source and driver to enable, the slave PC can select which motor in the group of sixteen will respond to the commands from the motor controller board.

This arrangement allows up to eight motors to be driven simultaneously, provided that they belong to distinct groups. The software in the slave PC has been written to take advantage of this property when it is instructed to create a seating contour rather than just moving an individual motor. When instructed to create a contour, the slave PC computes how far each motor needs to move from its present height. Then, beginning with the first group of sixteen, the slave selects the motor with the farthest to go and instructs the motor

controller card to move that motor towards its destination by a little bit. Then, while that motor is moving, it selects the motor in the next group and instructs it to move towards its destination, and so on for all eight groups. Then it returns to the first group and repeats the entire process until all motors have reached their destinations. The distance moved by the motors in each group is such that it is either sufficient for the motor to reach its goal or for the motor to have completed its motion by the time the slave PC returns to its group, whichever is smaller. This algorithm allows the slave PC to keep as many motors moving as possible.

Tests conducted on the motors have shown that they have a relative error of less than 2% of the distance travelled for both loaded and unloaded conditions[133].

3.1.2 Pressure And Orientation Subsystem

Figure 3.6 shows the block diagram for the pressure and orientation subsystem of the CASS. Although the pressure and orientation sensors measure fundamentally different quantities, the mechanism they use to report changes in the quantities measure - a change in resistance - is essentially the same. Furthermore, both the pressure and orientation sensors are monitored by the same device. Consequently, we consider these two different sensor types to be part of the same subsystem, even though they measure very different quantities.

The pressure sensors of the CASS are Foxboro/ICT 1860-03G-LDN-B silicon pressure sensors. Each sensor has a range of 0-15 PSI with a nominal accuracy of +/-0.15 PSI and best-fit straight-line linearity of +/- 0.02 PSI. The sensors are coupled to the buttocks of the subjects seated on the CASS through a silicon diaphragm 14.6 mm in diameter. The sensors were calibrated using a mercury tube with a thin, flexible diaphragm across the bottom. The diameter of the tube was wide enough to cover the entire sensor, and the diaphragm was coated with ultrasound gel during the calibration process to reduce friction between the pressure sensor and the calibration tube. Calibration data was collected at nine evenly-spaced data points over the range 0.5 to 5 PSI. The accuracy of the pressure sensors after calibration is +/-2.9 mmHg (equal to 0.06 PSI). Figure 3.7 displays a typical calibration curve for one of the sensors.

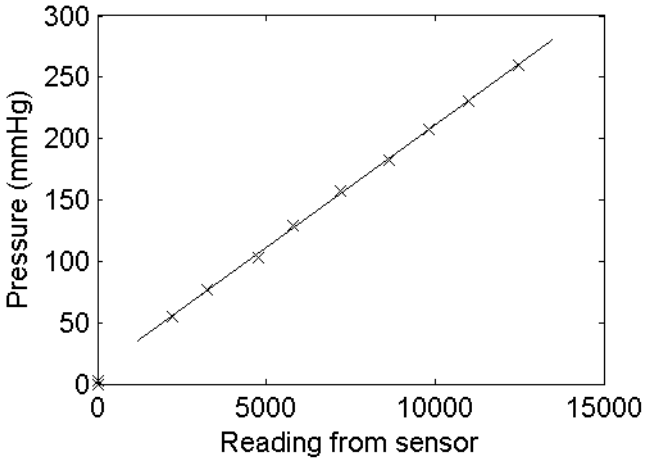

Figure 3.7: Typical calibration curve for a pressure sensor

The CASS has 100 pressure sensors deployed in a 10x10 array across its middle. The rightmost column (u=0), leftmost column (u=11) and row farthest to the rear (v=10) of actuators do not have pressure sensors. Since subjects never sit on this portion of the

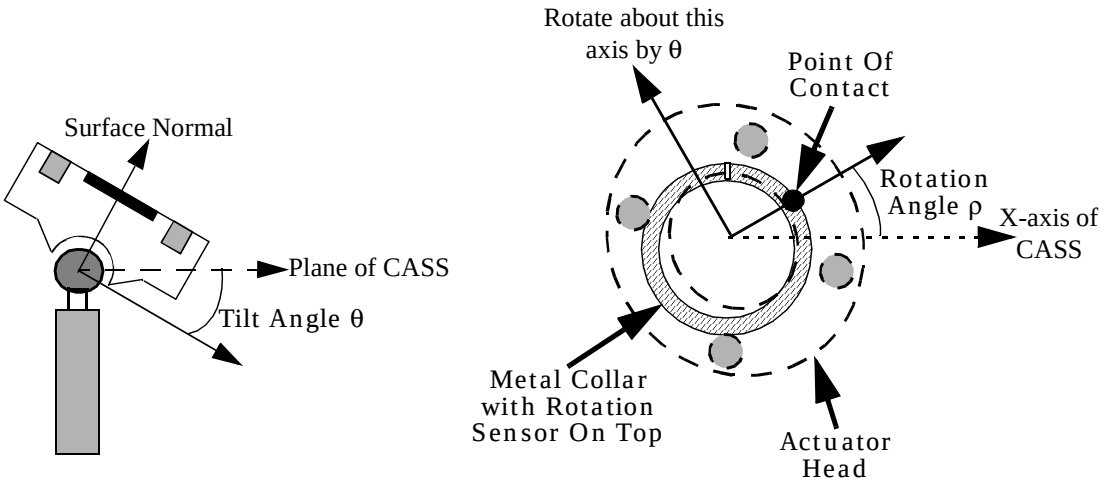

Tilt Angle (Side View) Rotation Angle (Top View)

Figure 3.8: The two angles - tilt and rotation - that describe the orientation of the actuator head

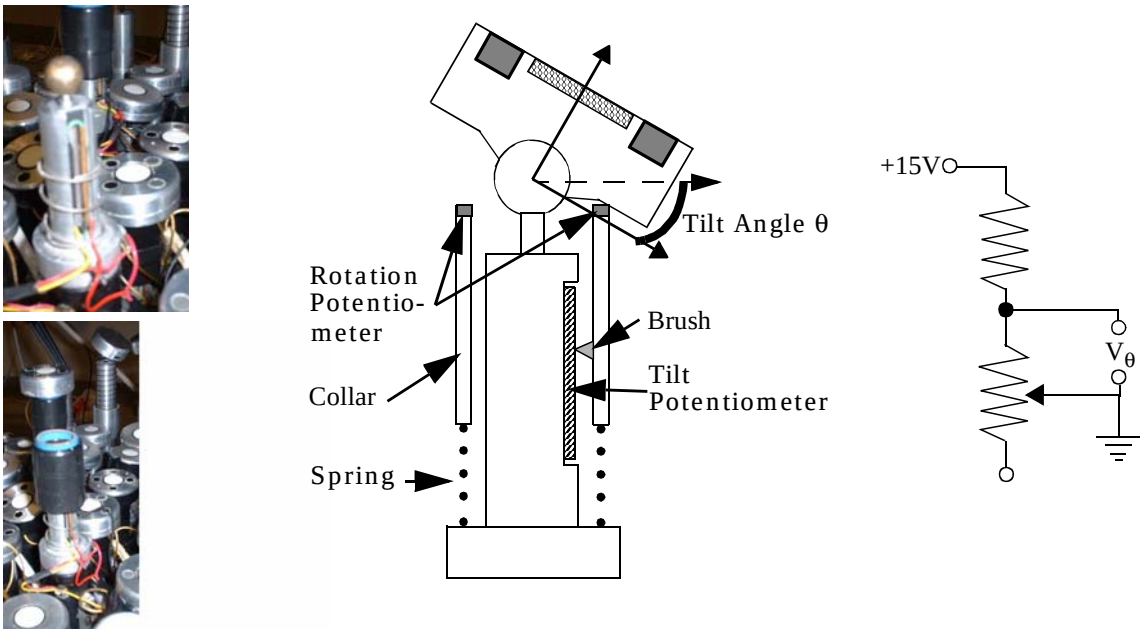

Figure 3.9: Picture, diagram and schematic of the tilt sensors of the CASS.

CASS, these missing sensors are not a problem. Over the years of its operation, a small number of pressure sensors have broken in a manner that cannot be repaired. Since replacement pressure sensors are no longer available, the broken sensors have been moved to the outer corners and edges of the CASS where subjects do not sit on them. The coefficients of the calibration functions for the broken pressure sensors have been set to zero.

The orientation sensors measure the orientation of the actuator surface relative to the surface of the CASS in terms of *tilt* and *rotation* angle, which are illustrated in figure 3.8. The tilt angle measures the declination of the surface with respect to the horizontal xy-plane of the CASS. The rotation sensor measures the direction in the xy-plane of the CASS in which the declination occurs. Taken together, these two quantities are sufficient to compute the normal to the surface of the actuator as:

$$\hat{n}(\rho, \theta) = \left[\cos\rho\sin\theta \;\; \sin\rho\sin\theta \;\; \cos\theta\right] \tag{3.1}$$

where θ is the tilt angle and ρ is the rotation angle. This does, however, leave a third degree of freedom - the rotation about the normal - unmeasured. However, empirical evidence collected during the pilot study conducted as a part of this thesis indicates that very little of such rotation occurs during our experimental procedure. The rotation that does occur is sufficient to leave an approximately 2 mm uncertainty in the location of the ultrasound sensors during the experimental procedure. This uncertainty is confined to the plane of the actuator head.

Each orientation sensor consists of a pair of wire-wound potentiometers and a sliding, spring-mounted collar, as shown in figure 3.9. On the inside of the collar are a metal brush and a pin that fits into a slot on the actuator head to keep it from rotating.The tilt potentiometer is mounted on the shaft of the actuator just beneath the ball bearing that the actuator head swivels about. On the inside of the sliding collar is a metal brush that makes contact with the surface of the tilt potentiometer, shorting the potentiometer at that point. As the actuator head swivels downward from the horizontal, it pushes the collar down, changing its resistance. Since the tilt potentiometer is in series with a larger resistance, this motion causes the voltage across the tilt potentiometer to change as a function of the tilt angle.

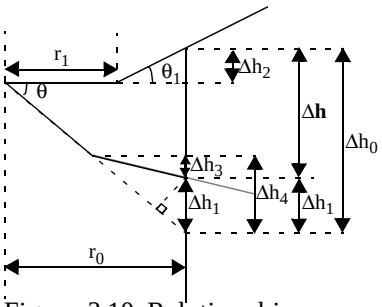

Figure 3.10: Relationship between θ and Δh

The relationship between the vertical deflection of the collar (Δh) and the tilt angle (θ) is shown in figure 3.10. We can use the relationships among the various triangles in figure 3.10 to compute Δh_1, Δh_2, Δh_3, and Δh_4 from Δh and the known geometry of the actuator head (w_1, w_2, θ_1):

$$\Delta h_1 = \Delta h_4 - \Delta h_3 \tag{3.2}$$

$$\Delta h_2 = (w_0 - w_1)\tan\theta_1 \tag{3.3}$$

$$\Delta h_3 = d_1\tan(\theta - \theta_1) \tag{3.4}$$

$$\Delta h_4 = d_1\tan\theta \tag{3.5}$$

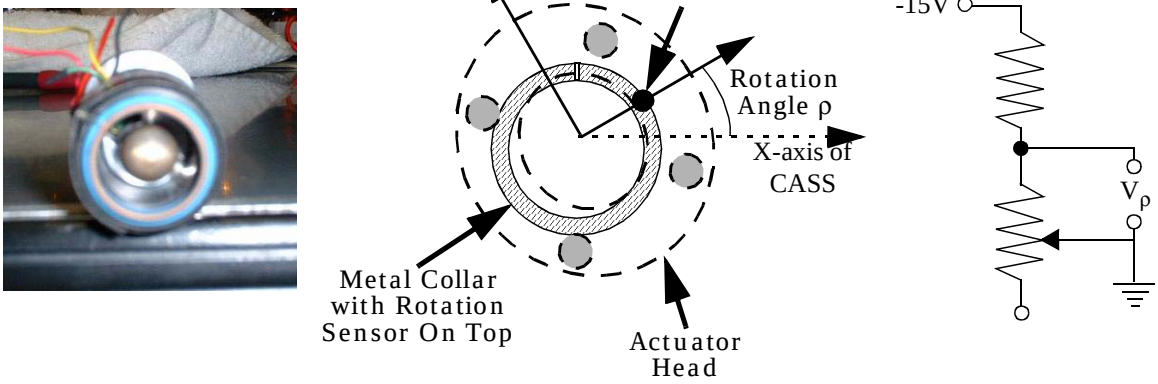

Figure 3.11: Picture, diagram and schematic for the rotation sensors of the CASS

$$d_1 = \frac{w_0 \cos\theta - w_1}{\cos\theta} \tag{3.6}$$

This makes the relationship between θ, Δh, w_1, w_2 and θ_1:

$$\Delta h = \frac{w_0 \cos\theta(\tan\theta_1 + \tan(\theta - \theta_1)) - w_1(\cos\theta\tan\theta_1 + \tan\theta - \tan(\theta - \theta_1))}{\cos\theta} \tag{3.7}$$

The relationship between Δh and the voltage measured across the tilt potentiometer (v_θ) is:

$$v_\theta = \frac{R_1 + R_2\Delta h}{R_0 + R_1 + R_2\Delta h} v_0 \tag{3.8}$$

where v_0 is the voltage used to drive the tilt sensor and R_0 is the constant resistance in the circuit and $R_1+R_2\Delta h$ is the variable resistance of the tilt potentiometer.

As equations (3.7) and (3.8) show, the function that relates θ to v_θ is very complex. However, this function can be well-approximated by a cubic whose coefficients can be computed by careful calibration. To calibrate the tilt sensor, we use an electronic level to tilt the actuator head at a known angle, for which we measure the resulting voltage. For each tilt sensor, we collect twelve voltage measurements at declinations of approximately 0, 2, 4, 6, 8, 10, 13, 16, 20, 25, and 30 degrees. Because a given change in the height of the collar results in a larger change in the tilt angle when the declination is small than when it is large, we sample voltages at smaller increments when the tilt angle is small than we do when it is large. We then fit a cubic to these data points and use it to compute tilt angle from voltage measured across the potentiometer. This process results in an accuracy in measuring the tilt angle of about +/-0.45 degrees.

The operation of the rotation sensor is somewhat simpler. The rotation potentiometer is

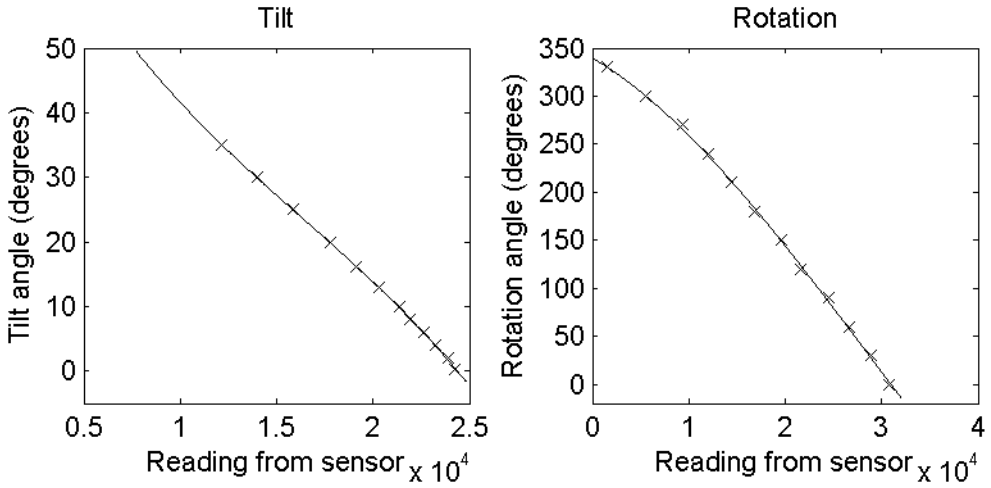

Figure 3.12: Typical calibration curves for the tilt and rotation sensors. The values on the x-axis are the output of the digitizer, which digitizes the voltage output by the sensor with 12 bits of resulution.

mounted on top of the sliding collar. One end of the rotation potentiometer is connected to a -12 V source through a fixed resistance R_3, while the other end is left disconnected. The actuator shaft is grounded, so when a person sits on the actuator head and causes it to tilt away from the horizontal, the head of the actuator makes contact with the point p_1 illustrated in figure 3.11. The weight of the person also forces the actuator head into contact with the ball bearing, which completes the circuit through the actuator shaft. Since the resistance across the potentiometer depends upon the point of contact p_1, the voltage measured across the potentiometer will be a function of the angle between the line from the center of the actuator to the origin of the potentiometer (point p_0 in figure 3.11) and the line from the center of the actuator to the point of contact at p_1. The difference between this value and the rotation angle, which is measured counterclockwise from the x-axis of the CASS, is a constant that can be accounted for during calibration.

The relationship between the rotation angle (ρ) and the voltage measured across the rotation potentiometer (v_ρ) is:

$$v_\rho = \frac{R_4 + R_5(\rho + \rho_0)w_0\pi}{R_3 + R_4 + R_5(\rho + \rho_0)w_0\pi} v_0 \tag{3.9}$$

where v_0 is the voltage used to drive the rotation sensor (and is, in fact, the same voltage used to drive the tilt sensor), w_0 is the radius of the metal collar the rotation potentiometer is attached to, p_0 is the angle between the origin of the rotation potentiometer and the X-axis of the CASS, R_3 is the constant resistance in the rotation sensor circuit, and $R_4 + R_5(\rho + \rho_0)w_0\pi$ is the variable resistance of the rotation potentiometer. Like the relationship between θ and v_θ, the value of ρ as a function of v_ρ implied by equation (3.9) can be well approximated by a cubic whose coefficients can be computed by measuring v_ρ

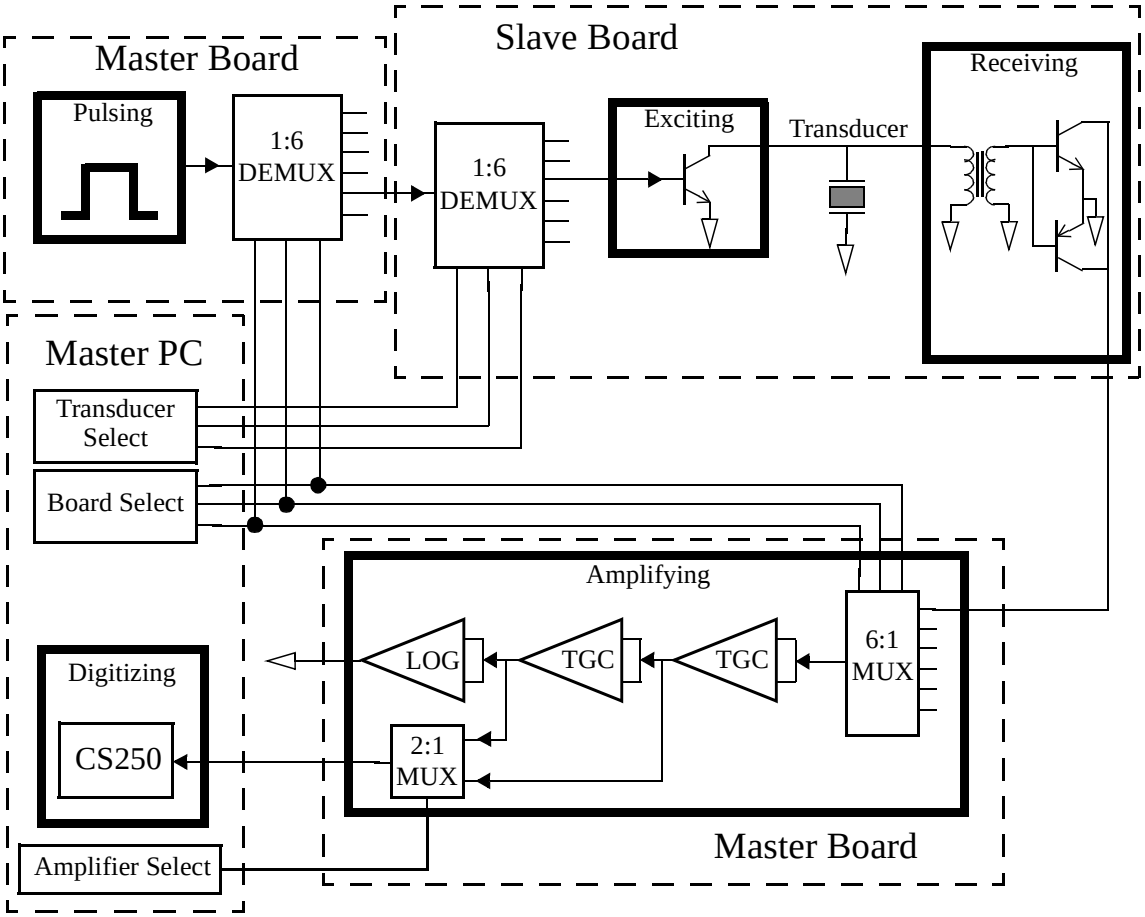

Figure 3.13: Block diagram of the ultrasonic subsystem of the CASS.

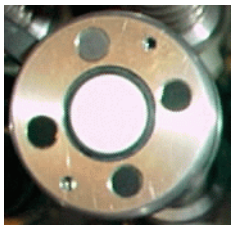

Figure 3.14: An actuator augmented with ultrasonic transducers

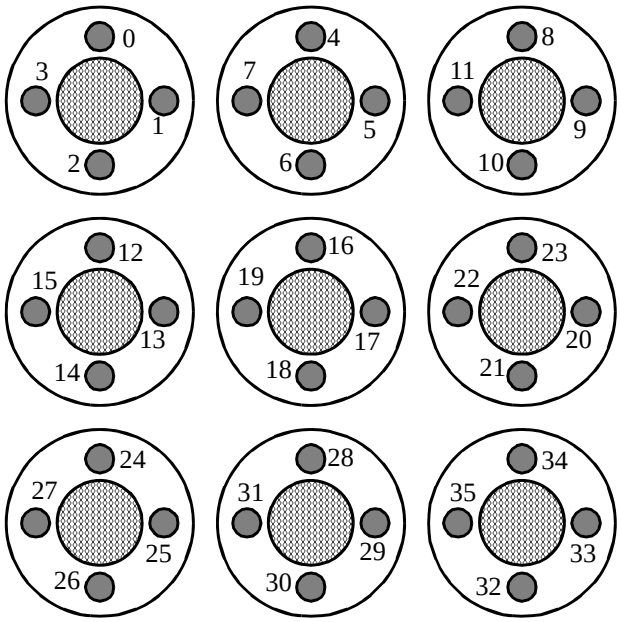

Figure 3.15: Mapping from sensor number to its transducer

at known values of ρ and then computing the coefficients that give the best fit to that data in the least squares sense. Using this procedure, the rotation sensors were calibrated using twelve samples spaced evenly at 30 degrees in the range 0 to 330. The accuracy of the rotation sensors once calibrated is 5.8 degrees. Typical calibration curves for the tilt and rotation sensors are shown in figure 3.12. The x-axis in these figures gives the value output by the digitizer while the y-axis gives the tilt or rotation angle.

The pressure, tilt, and rotation sensors are monitored by a Microstar Laboratories Data Acquisition Processor (DAP) board, model 1200e. The DAP board samples its inputs at a rate of 1kHz with twelve bits of accuracy. Since there are 100 pressure sensors[1], nine tilt potentiometers, and nine rotation potentiometers to sample every cycle, each sensor is sampled at an effective rate just under 10Hz. Although this rate seems somewhat low, it is adequate for the needs of the system developed for this thesis.

3.1.3 Ultrasound Subsystem

Figure 3.13 displays the block diagram for the ultrasound subsystem, which consists of thirty-six ultrasonic transducers and circuits for pulsing, exciting, receiving, amplifying, and digitizing. The transducers are composed of a novel 1-3 ceramic compound with resonant properties, which have been shown to have increased sensitivity (-22 dB in open loop), wider broadband (81% at -3dB) and faster ring-down (0.8 ms at 20 dB) over conventional piezoelectric transducers [135]. The center frequency of the transducers is 7.5MHz and their axial resolution when driven by the circuit in figure 3.13 has been measured to be 0.26 mm in water [133].

There are thirty-six ultrasonic transducers evenly distributed over nine actuators in the region from <3,5> to <5,7>, so that when a subject is seated on the CASS, the transducers will fall underneath the right cheek of the buttocks. Each actuator has four transducers assigned to it, and they are arranged about the actuator head as shown in figure 3.14. Each transducer is identified by a number between zero and thirty-five. Figure 3.15 displays the correspondence between a transducer's number and its location on the CASS.

Each transducer has its own exciting and receiving circuit, but all thirty-six share common pulsing, amplifying and digitization circuits. The thirty-six exciting and receiving circuits are evenly distributed across six circuit boards, while the remaining circuits are all contained on the same board as the first group of six exciting and receiving circuits.

The ultrasound subsystem functions as follows:

(1) The pulsing circuit generates a pulse 1 μs wide at a 1kHz repetition rate. This pulse is sent through a 1:6 analog multiplexor that selects a particular board, and then through another 1:6 analog multiplexor that selects a particular transducer.

1. Broken pressure sensors continue to be sampled by the DAP, even though the coefficients of their functions used to compute pressure from voltage have been set to zero. The update rate of the remaining functional sensors would only be slightly higher if the broken sensors were not sampled.

(2) The exciting circuit uses the pulse as a trigger to generate a pulse of its own, 50 ns long, which is amplified by a IRFF330 power transistor and used to excite the transducer.

(3) The receiving circuit uses a combination of an isolating transformer and a differential pair of transistors to amplify the received echoes. It passes them back through 6:1 analog demultiplexor to the amplification circuit. The control lines of the demultiplexor are connected to the control lines of the multiplexor that selects which board is active, so only signals from the currently-active board are sent to the amplifier. Because only one transducer on a board can be active at a time, the outputs from the six receiving circuits on each board are simply tied together, elminating the need for a second demultiplexor.

(4) The amplification circuit passes the received signal through a pair of AD600 voltage-controlled amplifiers, which are used to implement time gain compensation (TGC), which is used to compensate for the attenuation of ultrasound in soft tissue. The control voltage for these amplifiers is synchronized to the trigger pulse has the form

$$\begin{aligned} V &= V_0 & t < t_0 \\ V &= V_0(1 - e^{-\alpha(t - t_0)}) & t \geq t_0 \end{aligned} \tag{3.10}$$

where t is the time since the last clock pulse, t_0 is a delay of 7.7 μs, and α is an amplification constant approximately equal to 2.14×10^{-2} μs^{-1}. This value of α was chosen to match the average attenuation of ultrasound in soft tissue of 7.5 dB per centimeter for the transducers used by the CASS and assuming that the speed of sound in soft tissue is 1540 m/s.

(5) The output of the AD600 amplifiers passes through an analog demuliplexor whose control is attached to the master PC, allowing the system to select one or two stages of amplification. The output of the second AD600 amplifier is also connected to a series of components that perform logarithmic compression of the received signal, but this functionality is not used in this thesis.

(6) The output of the AD600 amplifiers passes into a GaGe CompuScope 250 dual channel high-speed digitizing board, which is configured to trigger on the positive edge of the pulse generated by the pulsing circuit, so digitization is always synchronized with the transmitted pulse. The DACs on the CompuScope board have eight bits of resolution and a voltage controlled amplifier allows signals to be sampled over a wide variety of ranges, including +/-100mV, +/-500mV, +/-1V, and +/-5V. Likewise, the clocks on the GageScope can be configured to sample at a variety of sampling frequencies ranging from 1kHz to 100MHz.

Although 1 kHz pulse repetition rate theoretically allows us to sample all thirty-six ultrasound transducers at a rate of approximately 28 Hz, in practice, it takes a few seconds to acquire digitized signals from all thirty-six transducers and store them in the computer's

memory. Bugs in the library used to communicate with the GageScope can sometimes result in the corruption of the sampled signal. When such corruption occurs, it is obvious from a simple examination. For this reason, we always collect at least two sets of data from all thirty-six transducers and throw out any corrupted signals.

3.1.4 Position Wand Subsystem

The position wand is a MicroScribe-3DX digitizing wand made by the Immersion corporation, shown in figure 3.16. It is used to locate points in three dimensional space relative to the CASS. Its workspace occupies a sphere approximately 1270 mm in diameter and it can locate points in three dimensional space with a nominal accuracy of 0.3 mm. The position wand communicates with the master PC over an RS-232 serial line at 9600 baud. The position wand is configured to send continuous updates of its joint angles to the master PC as it moves. The software on the master PC computes the location of the tip from these joint angles. The wand also has a pedal that can act like a pushbutton. This pedal signals the software when to acquire a registration point.

Figure 3.16: The position wand

Before it is used in the experimental procedure described in section 3.3, the position wand is calibrated to the large square metal frame at the bottom of the CASS by recording the locations of three marked points, two of which lie along one edge of the frame and one which lies on the surface at a known distance from the edges. The software on the master PC uses these points to compute a coordinate frame whose x- and y-axes lie along the edges of the frame and whose z-axis points straight up and reports the coordinates of points with respect to this frame.The tip of the position wand is quite sharp and was removed during data acquisition to avoid injuring the subject seated on the CASS.

3.2 Coordinate Systems

There are four important coordinate systems that are attached to different components of the CASS system. These are:

(1) The **wand coordinate system** (WCS), which is attached to the large metal frame of the CASS. The software in the master PC computes the location of the position wand tip with respect to this coordinate system, hence its name.

(2) The **CASS coordinate system** (CCS), which is attached to the flat surface of the grid of actuators of the CASS when the actuators are all at their rest height. The CASS coordinate system is distinct from the wand coordinate system, which is attached to the frame of the CASS.

(3) The **actuator coordinate systems** (ACS), which are attached to the centers of

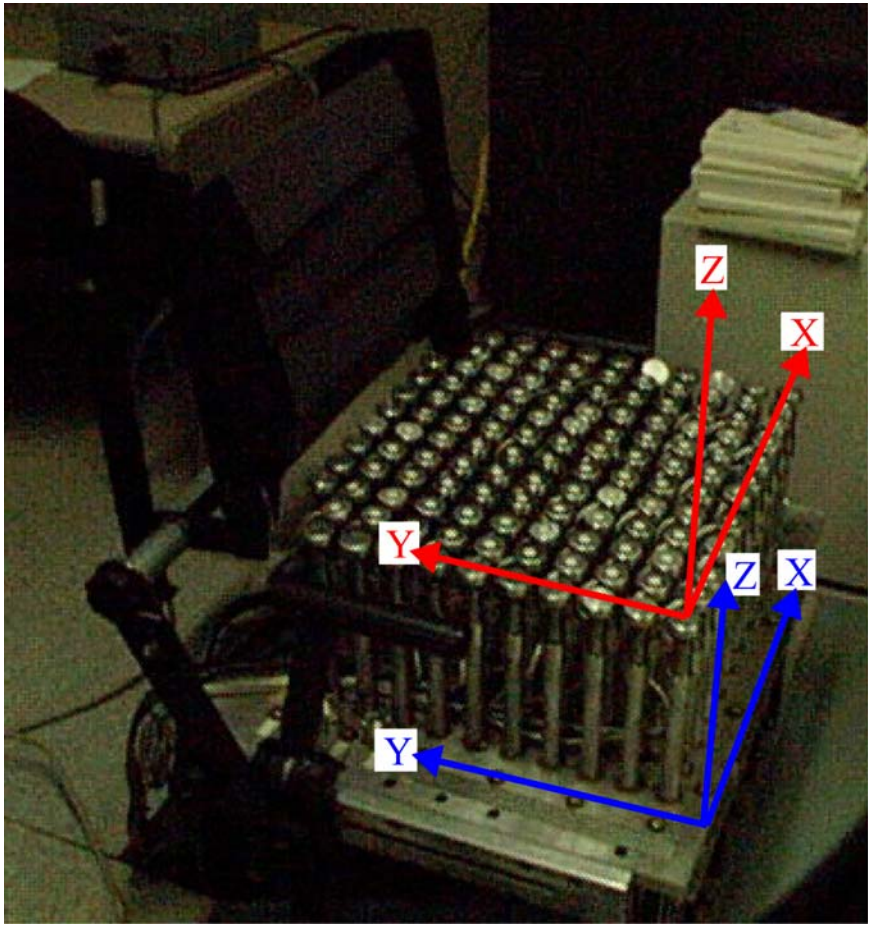

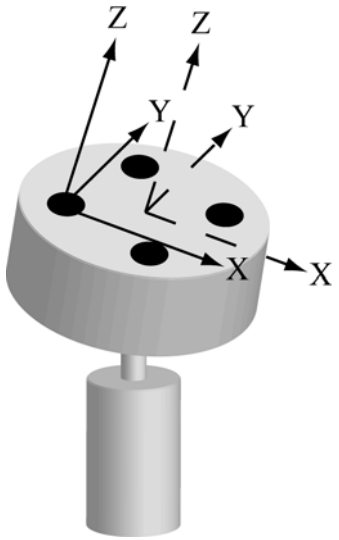

Figure 3.17: The coordinate systems of the CASS. The figure on the left shows the relationships between the wand coordinate system (WCS, blue) and the CASS coordinate system (CCS,red). For these coordinate systems, the z-axis comes out of the page. Most of the displacement between the WCS and the CCS occurs along the z-axis. The figure on the right shows the relationship between the actuator coordinate system (ACS) and the transducer coordinate system (TCS).

the surfaces of each actuator.

(4) The **transducer coordinate systems**, which are attached to the centers of each transducer and have the same orientation as the ACS of the actuator the transducer belongs to.

In addition to these four coordinate systems, there is a fifth coordinate system that is attached to the subject seated on the CASS:

(5) The **pelvis coordinate system** (PCS), which is attached to the center of the subject's pelvis and has its axes pointing in physically meaningful directions.

These coordinate systems and their relationships are illustrated in figure 3.17 and are described in greater detail below.

3.2.1 The Wand Coordinate System

As its name implies, the tip of the position wand is measured relative to this coordinate system. It exists primarily as an intermediary between the pelvis coordinate system and the CASS coordinate system. Its origin is located about 85.725 mm from the front right corner (as one sits on the CASS) along the front edge of the CASS frame. Its x-axis points along the front edge of the frame of the CASS, its y-axis along the right edge from the front to the back of the CASS, and its z-axis point straight up.

The position wand is calibrated to the wand coordinate system by measuring the location of three marked points on the CASS frame. One of these points is the origin of the WCS and is placed 85.725 mm from the right front corner along the front edge of the CASS. The second point is placed 298.45 mm from the right front corner along the front edge and the difference between it and the origin is used to compute the initial direction of the x-axis. The location of the position wand itself on the frame of the CASS prevents us from using the right edge of the CASS frame itself as to compute the y-axis, so the third point is located on the surface of the CASS frame 330.2 mm along the right edge from the origin. The difference between the location of this third point and the origin as measured by the position wand is used to compute the y-axis of the WCS. The z-axis is computed as the cross-product of the initial x- and y-axes, and then the final direction of the x-axis is computed as the cross product of the y- and z-axes. This creates a coordinate system whose axes are all perpendicular and are closely aligned with the frame of the CASS. Because all of the other coordinate systems are calibrated with respect to the WCS, the position and orientation of the WCS are arbitrary, so an exact match to the CASS frame is not necessary.

3.2.2 The CASS Coordinate System

The CASS coordinate system is aligned with the surface of the actuators of the CASS when they are all flat and at the same height. Its origin is placed at the center of actuator <0,0>. Its x-axis runs through the centers of the actuators on the first row, and its y-axis runs through the centers of the actuators on the first column. Its z-axis is computed from the cross-product of the x- and y-axes and points straight up.

Since the motors can be at any height when the system is initialized, the location of the

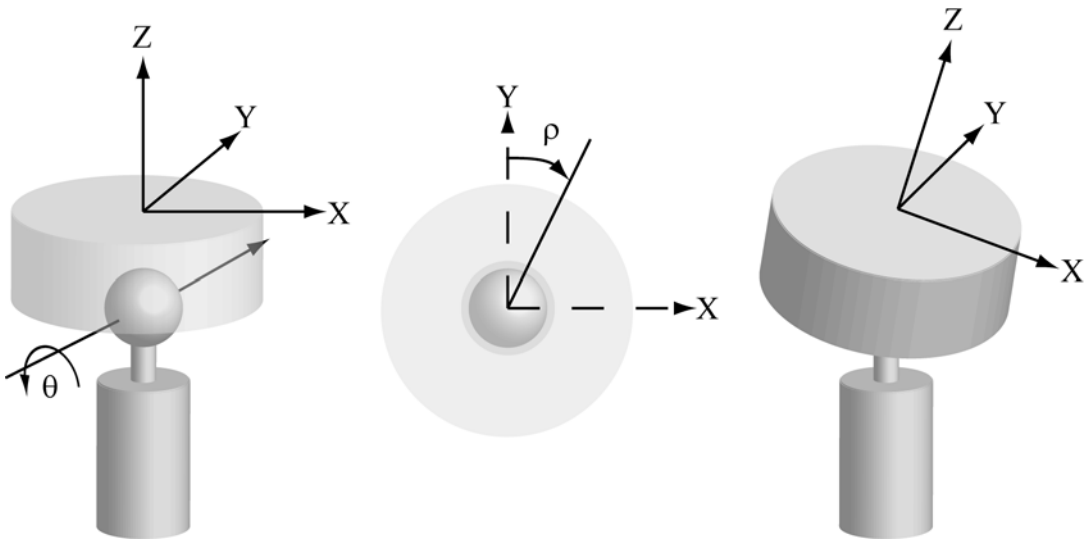

Figure 3.18: Calculation of the Actuator Coordinate System (ACS). Note that the angle ρ illustrated in the figure is negative.

CCS can vary from one use of the system to the next. Consequently, it is necessary to measure the pose of the CCS with respect to the WCS using the position wand after it has been calibrated. The calibration of the CCS to the WCS is performed by measuring the locations of the centers of the actuators at <0,0>, <6,0> and <0,8>, which are the farthest actuators in the first row and column the position wand can reach. These measurements are performed with the surface of the CASS as flat as possible with respect to the xy-plane of the WCS, and the z-coordinates of the second and third points are ignored, meaning that any trivial differences in height between the three actuators are ignored. The measurement of the center of <0,0> is used as the location of the origin of the CCS in the WCS. The initial direction of the x-axis is computed from the difference in the locations of the centers of <6,0> and <0,0> actuators, and the direction of the y-axis is computed from the difference between the centers of the <0,0> and <0,8> actuators. The z-axis is computed from the cross-product of the x- and y-axes, and the final direction of the x-axis is computed from the cross-product of the y- and z-axes. This results in a coordinate system whose axes are mutually perpendicular and is aligned with the surface of the CASS. Once calibrated, the offset between the WCS and the CCS remains until the system is re-initialized.

3.2.3 The Actuator Coordinate Systems

Each actuator has its own coordinate system located at the center of its head, with its x- and y-axes in the plane of the actuator surface and its z-axis pointing along the surface normal. When the actuator head is flat, it's x-, y- and z-axes are aligned with the corresponding axes of the CCS and its origin is located at *(42.65u, 42.65v, 0.0)* mm in CASS coordinates, where *u* and *v* are the components of the actuator's number. When the actuator head is tilted, the origin of the ACS and the directions of its axes are computed by rotating the flat ACS about the center of the ball bearing located at *(42.65u, 42.65v, -14)* mm. The rotation is performed about the axis $\begin{bmatrix}\sin\rho & \cos\rho & 0\end{bmatrix}$ by θ, where θ and ρ are the

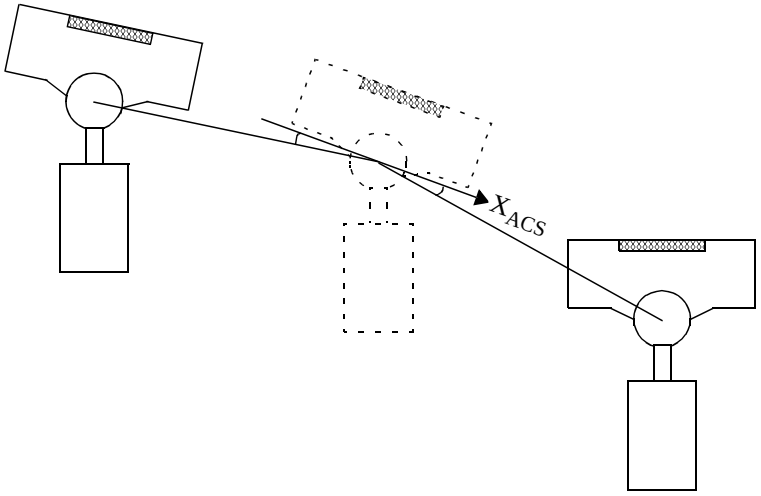

Figure 3.19: Calculation of the actuator coordinate system when an orientation sensor is not present.

tilt and rotation angles for the actuator, as defined in section 3.1.2. This rotation corresponds to the physical motion of the actuator head about the ball bearing and is illustrated in figure 3.18.

For those actuators in the region from <3,5> to <5,7> that have tilt and rotation sensors, we use the values reported by those sensors to compute the pose of the ACS with respect to the CCS. For actuators that do not have pressure and rotation sensors, we compute the tilt and rotation angles from the heights of the neighboring actuators. In this case, the tilt and rotation angles are computed such that the x-axis of the actuator makes an angle with the line drawn from the center of the ball bearing of the actuator's left neighbor to the center of the actuator's own ball bearing that is the same as the angle it makes with the line drawn from the ball bearing of the actuator's right neighbor to its own ball bearing (see figure 3.19). The y-axis is computed similarly, but uses the neighbors to the front and rear rather than to the left and right. The z-axis is computed as the cross product of the two. For actuators on the edges of the CASS that may be missing a neighbor on one side or the other, a phantom neighbor is constructed that has the same height as the actuator whose tilt and rotation angles are being computed.

Comparing the values for tilt and rotation computed by this algorithm to the values measured by the rotation and orientation sensors for the 3x3 array of actuators where such sensors have been mounted reveals that in many cases, the tilt and rotation values computed by this algorithm do not agree well with the measured values. However, for those actuators that do not have orientation sensors, the values computed by this algorithm will be a better approximation to their true orientation than assuming the heads of the actuators are flat.

3.2.4 The Transducer Coordinate Systems

As each actuator has a coordinate system associated with it, so does each ultrasonic

transducer. The coordinate system for an ultrasonic transducer is located at the center of that transducer, with its axes aligned with the axes of the actuator the transducer belongs to. The primary purpose of the transducer coordinate system is to have a coordinate system in which the description of the propagation of the ultrasonic pulse has a simple form. The locations of the echoes from tissue layer boundaries encountered by the pulse are initially calculated in the transducer's TCS and then transformed to the CCS.

The offset between the TCS for a transducer and the ACS of the actuator it belongs to is treated as a constant during the run of an experiment, even though empirical evidence indicates that there is a slight rotation about the surface normal sufficient to move the transducer by about 2 mm in the plane of the actuator surface during the run of an experiment. However, because the actuator heads are free to rotate about the surface normal, and can rotate quite considerably between runs of an experiment, the offset between the TCS and the ACS must be computed anew for each run.

The offset between TCS and ACS is a pure translation that is computed by the following procedure:

(1) After the position wand has been calibrated to the frame of the CASS and the surface of the CASS has been flattened so that it is aligned with the xy-plane of the WCS, the location of the center of each of the thirty-six ultrasonic transducers in the WCS is measured with the position wand and recorded.
(2) The transformations from the WCS to the CCS and the CCS to the ACS of the actuator each transducer belongs to are applied so that the location of each transducer with respect to its ACS is now known.
(3) To correct for any tilt in the actuator head that may exist, we compute the best-fit plane for each group of four transducers that share the same actuator. Then we rotate that plane along with the transducers about the ball bearing of the actuator so that the normal to the plane points straight up along the z-axis. This yields the positions of the ultrasonic transducers relative to the ACS when the actuator head is flat. From this point forward, we consider the locations of the ultrasonic transducers to be fixed at these positions relative to the ACS.

The last step is actually unnecessary, since over the data we have collected so far, the dot product of the normal to the best fit plane and the z-axis of the CCS has always been at least 0.99999, which corresponds to an angle of 0.25 degrees or less between the normal and the z-axis.

3.2.5 The Pelvis Coordinate System

So far, we have defined coordinate systems that are attached to the objects that are part of the CASS. However, there is one rigid object that we are concerned with that is not attached to the CASS at all: the pelvis. Consequently, we need to assign a coordinate system to the pelvis that is physically meaningful but does not reference any object on the CASS. As part of the experimental procedure, we collect registration data that allows us to compute the position and orientation of the pelvis with respect to the CASS.

The pelvis coordinate system is defined with respect to certain anatomical landmarks on

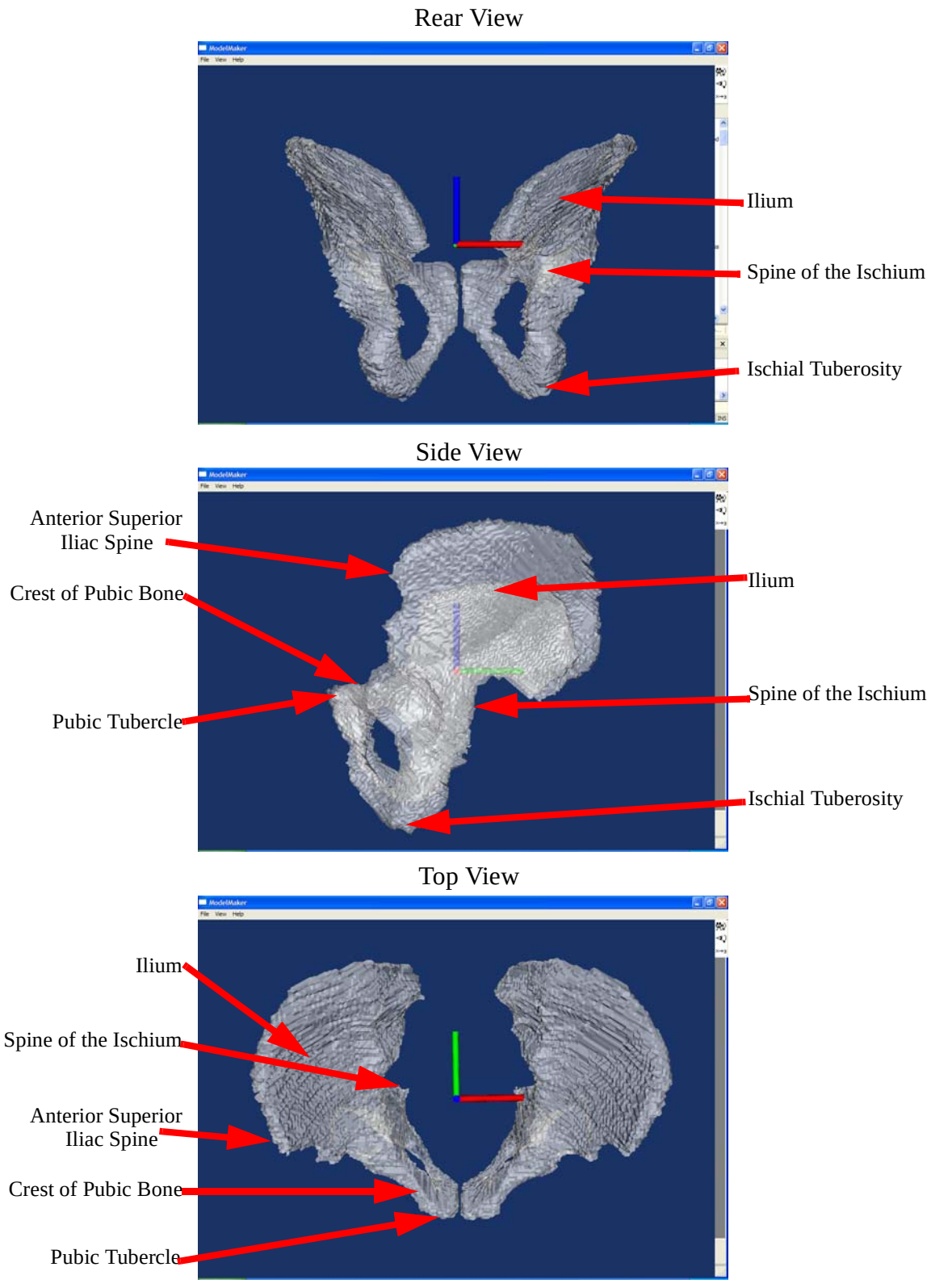

Figure 3.20: Rear (top), side (middle) and top (bottom) views of the pelvic coordinate system. The x-axis is red, the y-axis is green and the z-axis is blue.

the pelvis and readers who are unfamiliar with the anatomy of this region should consult appendix A. The origin of the PCS is placed at the center of its bounding box[2]. Its x-axis points from the right ilium to the left ilium along the line drawn between the two anterior superior iliac spines. The y-axis points from the front of the pelvis to the back along the crest of the pubic bone. If one looks at the pelvis from the side, the y-axis appears to extend from the pubic tubercle towards the spine of the ischium. However, if one looks from above, one can see that the y-axis actually extends from the pubic tubercle to somewhere along the sacrum. The z-axis is computed as the cross product of the x- and y-axes and points more or less along the direction of the spine. Figure 3.20 illustrates the pelvic coordinate system for one of the subjects from chapter 4.

While the axes of the pelvic coordinate system are useful for orienting the pelvis relative to the other four coordinate systems, their raw values can be difficult to interpret. Consequently, we report the orientation of the pelvis with respect to the CCS using pitch, roll and yaw angles, designated as α, β and γ, respectively. The definitions of pitch, roll and yaw that we use are slightly different from their standard meanings and are explained below:

> The **pitch** of the pelvis is the angle between the pelvis -y-axis and the xy-plane of the CCS. Pitch is defined this way so that positive values have the pubic tubercle (which can be thought of as the “nose” of the pelvis) tilted up and away from the CASS, while negative values have the pubic tubercle tilted downwards.
>
> The **roll** of the pelvis is the angle between the pelvis +x-axis and the xy-plane of the CCS. Positive roll tilts the pelvis to the right and negative tilts it to the left.
>
> The **yaw** of the pelvis is the angle between the projection of the pelvis +x-axis onto the xy-plane of the CCS and the +x-axis of the CCS itself, taken counterclockwise about the +z-axis of the CCS. Unlike pitch and yaw, which have ranges between -90 and +90 degrees, the range of the yaw angle goes from 0 to 360 degrees.

Given these definitions, one can see that the pitch angle indicates how much the pelvis is tilted forward and back, the roll angle indicates how much the pelvis is tilted from side to side, and the yaw angle indicates how twisted the pelvis is with respect to the front of the CASS. Since each value of pitch and roll actually corresponds to two distinct orientations of the pelvis, each triple of pitch, roll and yaw angles actually describes four different poses. However, three of the four poses correspond to positions of the subject that are physically impossible, so only the physically-possible pose is considered.

3.3 Experimental Procedure

Having described the subsystems of the CASS and defined the coordinate systems we use, we can now describe our experimental procedure. This procedure is broken into three phases: data acquisition, data analysis and visualization. The current procedure is set up to measure the position and orientation of the pelvis and the shapes of the layers of skin, fat

2. The bounding box is a rectalinear prism whose sides are placed at the farthest extent of the pelvis along the x-, y- and z-axes.

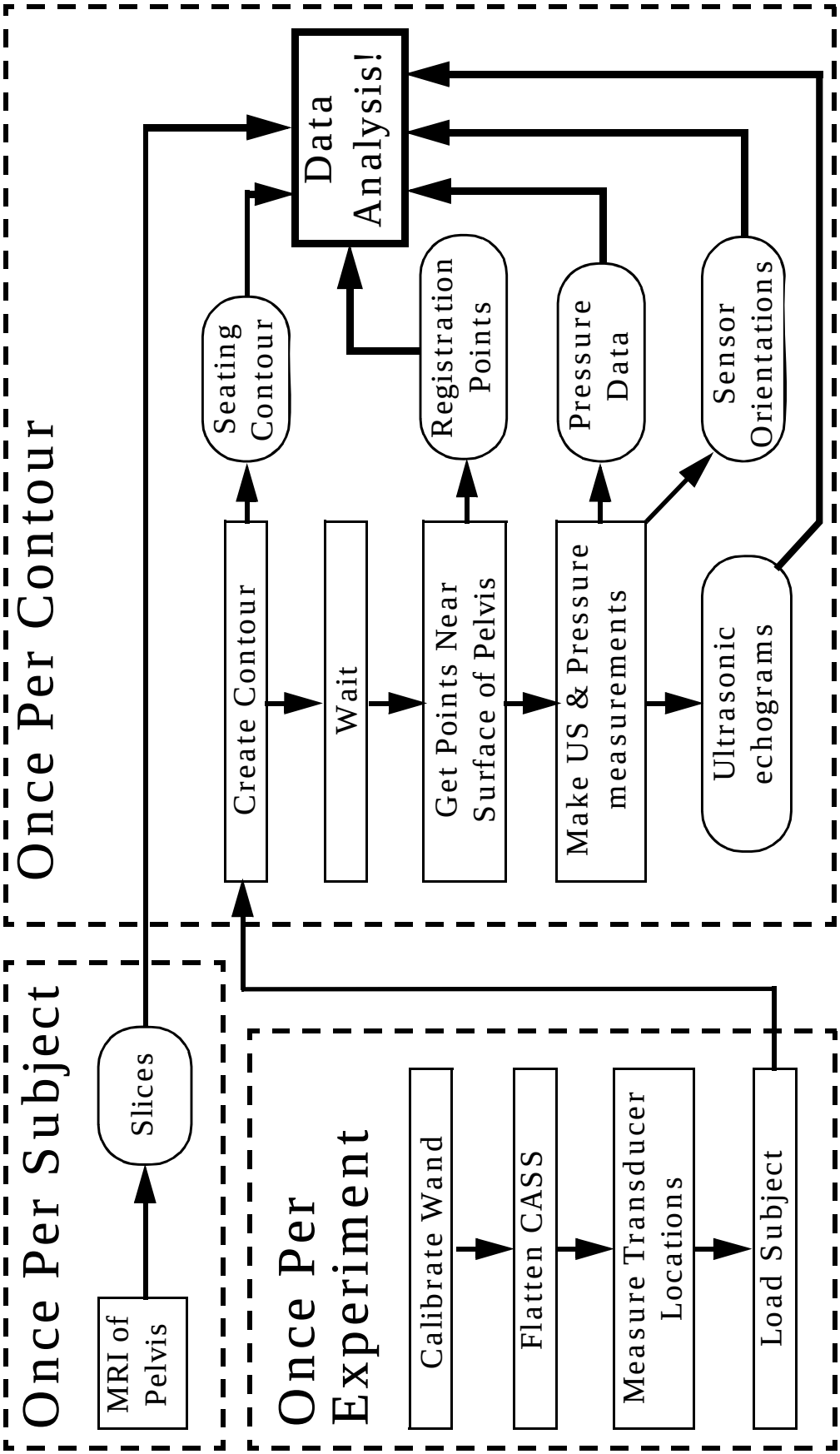

Figure 3.21: Schema for data acquisition

and muscle within the buttocks for two different seating contours: one flat and one shaped to equalize the pressure across the buttocks to within a given tolerance. However, the procedure could be easily adapted to make these measurements for other seating contours.

3.3.1 Data Acquisition

The schema for the data acquisition process is illustrated in figure 3.21.

3.3.1.1 MRI Of Pelvis

Data acquisition begins with an MRI scan of the subject's pelvic region. We acquire cross-sections of the subject's pelvis in the transverse plane of the body (approximately perpendicular to the spine). These images are set aside to build a model of the subject's pelvis during the data analysis phase.

3.3.1.2 Calibrate Wand

Before the subject can be seated on the CASS, the position wand must be calibrated to the wand coordinate system, the surface of the CASS must be flattened, and the poses of the CASS coordinate system and the transducer coordinate systems must be measured. Calibration of the position wand and measurement of the CCS and TCS poses are described in their respective subsections in the section on coordinate systems above.

3.3.1.3 Flatten CASS

To flatten the surface of the CASS, the actuators are driven down approximately 2 cm beyond the lower limit of their range and then raised to the reference height of approximately 14 cm from their lowest point. Because any knowledge of the height of the actuators is lost when the equipment is turned off, driving the actuators down and up in this fashion insures that they are all approximately 14 cm above their lowest point. This produces an approximately flat surface that is flattened further by measuring the heights of as many actuators as the position wand will reach and adjusting the heights of any actuators that do not fall within 1 mm of the reference height. Finally, the remaining actuators are flattened by placing a long, flat object across the rows and columns of the CASS and adjusting the heights of the actuators so that the object lies flat on top of the CASS. This produces a flat surface such that the xy-plane of the CCS is closely aligned to the xy-plane of the WCS. Any slight differences between the two will have negligible impact on the results of this procedure.

3.3.1.4 Measure Transducer Locations

The final step in the preparatory process is to measure the initial locations of the ultrasonic transducers with the position wand and then coat them with ultrasound gel so that they can couple to the skin of the subject more easily.

3.3.1.5 Load Subject

After the setup of the CASS is complete, the subject can be seated on the CASS. Healthy subjects can seat themselves on the CASS with the help of detachable armrests located on either side. However, subjects with spinal cord injuries need assistance transfering on and off the CASS. This transfer is accomplished by trained personnel with the help of a pivot transfer device. Once the subject is seated on the CASS, the back and armrests are

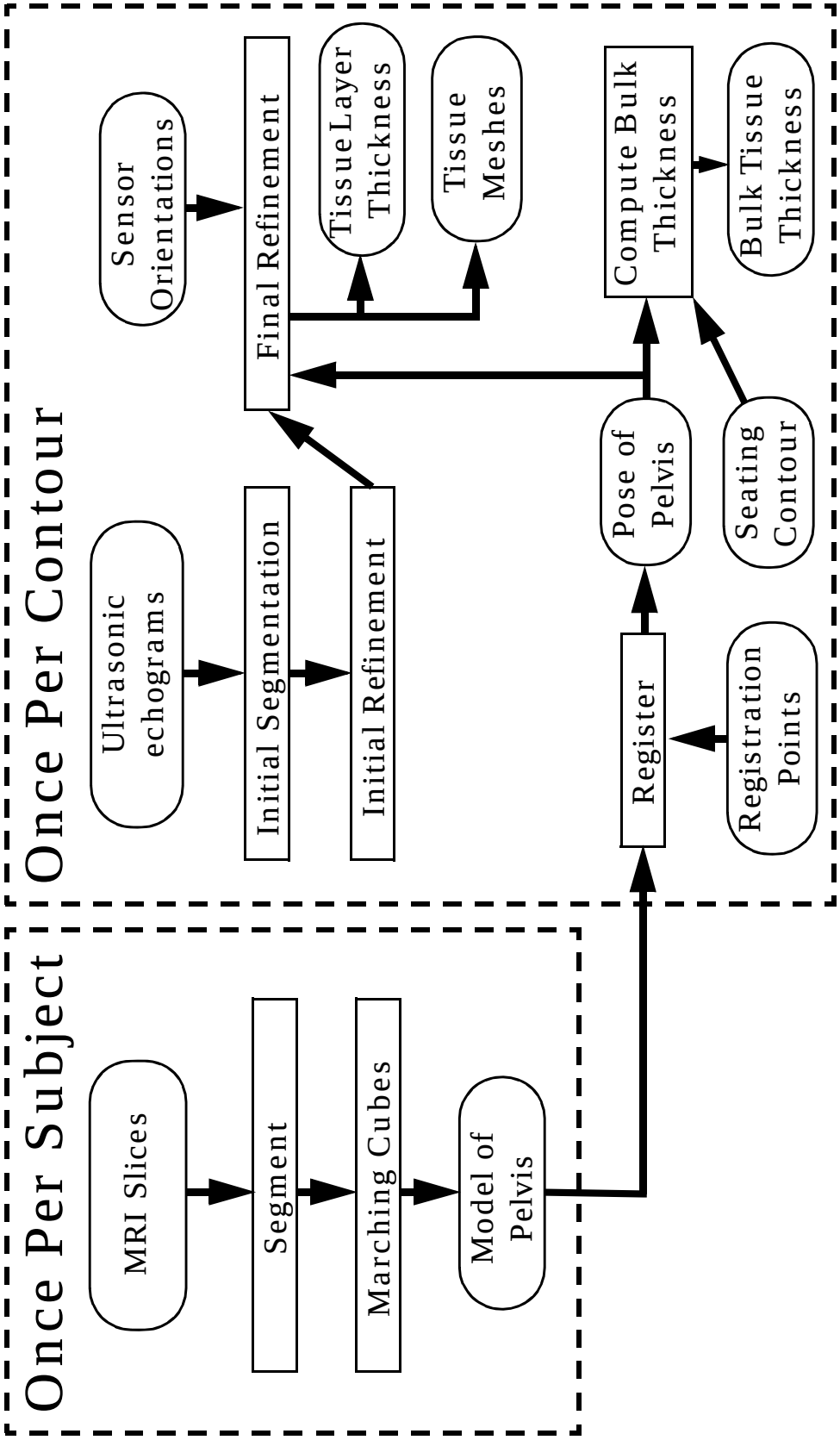

Figure 3.22: The data analysis schema

adjusted to make them feel comfortable. Leg rests are placed beneath the subject's feet and adjusted so that the top of the subject's thighs are approximately horizontal.

3.3.1.6 Create Contour

After the subject is seated and comfortable, we move the actuators downward to create the seating contour for which we wish to make measurements and wait for a few minutes to allow the soft tissues to settle.

3.3.1.7 Measure Registration Points

We use the position wand to acquire and record twenty-five to thirty points on the skin above the anterior superior iliac spine and the crest of the ilium. The skin is very thin at this point and directly above the bone, with at most 5 mm of tissue between the surface of the skin and the pelvis. Furthermore, even obese subjects do not exhibit significant amounts of fat in this region. During the data analysis phase, these points will be matched to a model of the pelvis built from the subject's MRI scans to compute the position and orientation of the pelvis with respect to the surface of the CASS.

3.3.1.8 Make Ultrasound and Pressure Measurements

Once we have acquired enough registration points, we acquire and store two sets of pressure, orientation and ultrasonic measurements. Each set consists of the measurements from all 100 pressure sensors, all nine orientation sensors, and the capture of a echogram of the return echoes for each of the thirty-six ultrasonic transducers. For each transducer, we capture a sequence of four echograms, one right after the other. The first two echograms are captured at low amplification, and the second two at high amplification. The first and third echograms in the sequence are captured with a scale of +/- 500 mV, while the second and fourth are acquired with a scale of +/- 100 mV. This procedure allows us to avoid resorting to logarithmic compression to overcome the limited dynamic range of the digitizing board. An empirical comparison of the echograms in the sequence reveals no significant difference between them. It takes about 30 seconds to acquire a complete set of 144 echograms (4 echograms from each sensor), most of which is spent acquiring, compressing and storing the ultrasound data.

For the most part, there are no significant differences between the pressure measurements, orientation measurements and ultrasonic echoes in both data sets. Occasionally, there are significant differences between the two sets of ultrasonic echoes for each sensor that arise because the subject shifts position slightly in between the acquisition of the first and second data sets. Such shifts are unavoidable in human subjects. The differences between the sets of echograms can be useful in segmenting these echograms into different tissue layers. We discuss phenomenon more in the section on data analysis below.

3.3.2 Data Analysis

Figure 3.22 shows the data analysis schema. The inputs to the data analysis process are the transverse MRI cross-sections of the gluteal region and the two sets of pressure, orientation and ultrasound data collected for one contour. The outputs are:

(1) A triangular mesh model of the subject's pelvis.

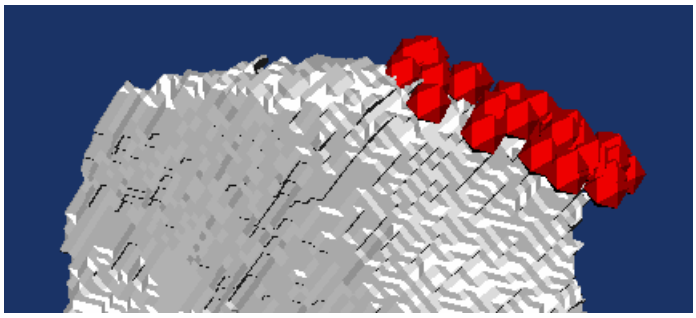

Figure 3.23: The registration points acquired during the data acquisition process conform to the shape of the pelvis, facilitating the match between the registration points measured in the WCS and the surface of the pelvic model, whose vertecies are positioned with respect to the PCS.

(2) The position and orientation of the subject's pelvis relative to the surface of the CASS.
(3) The thickness of the layer of skin, the layer of subcutaneous fat, and the first muscle layer above each of the thirty-two functional ultrasonic transducers.
(4) Triangular mesh models of the boundary surfaces between the skin and subcutaenous fat, between the subcutaenous fat and the first muscle layer, and between the first and second muscle layer.
(5) The thickness and volume of the bulk tissue between the pelvis and the seating contour.

For the most part, the "first muscle layer" mentioned in the third and fourth items is the gluteus maximus, but it may include portions of the semitendinosus or biceps femoris muscles where these emerge from the beneath the gluteus maximus in the upper thigh. We do not have a sufficient density of ultrasound transducers to distinguish between them. The "second muscle layer" may be the semitendinosus, the biceps femoris (in the gluteal region where these muscles fall beneath the gluteus maximus), the semimembranous (in the upper thigh where the semitendinosus and biceps femoris form the most superficial layer of muscle), the aductor magnus, or any of smaller the muscles that connect the pelvis to the femur.

3.3.2.1 Construct Pelvic Model

The transverse MRI cross sections of the gluteal region and upper thighs for each subject are manually segmented into voxels that belong to the pelvis and voxels that do not. Then the marching cubes algorithm is applied to the segmented images to create a surface model of the pelvis for each subject. Normally a triangle decimation algorithm is applied at this point to reduce the number of triangles in the model. However, because modern graphics hardware can easily handle the large number of triangles that make up the surface model, and because past experience with triangle decimation algorithms has shown that they tend to produce an unacceptable number of slivers - triangles that have one angle close to zero and are almost degenerate - triangle decimation was not applied to the models.

3.3.2.2 Register The Pelvis To The CASS

We analyze the data acquired for each contour separately through the procedure described below. We begin by registering the points acquired by the position wand to the surface of the pelvis model to compute the position and orientation of the pelvis relative to the CASS. During the data acquisition process, the position wand was used to acquire a set of 30 or so registration points that have a spatial relationship to both the CASS and to the pelvis. The locations of the registration points with respect to the WCS (and hence the CCS, since the offset between the two is a constant whose value is measured by calibrating the CCS to the WCS using the procedure described in section 3.2.2) is recorded during the data acquistion phase, but the precise locations of the registration points with respect to the pelvis is not known. However, as shown in figure 3.23, the number and arrangement of the registration points is such that they capture the shape of the right anterior superior iliac spine, and this makes it possible to match the registration points to the pelvic model built in section 3.3.2.1 above in such a way that the original relationship between the registration points and the pelvis of the subject that existed during the data acquistion phase can be recovered. Performing this match is called "registering the pelvis to the CASS" and computes the relationship between the PCS and the CCS.

Registration is performed manually using the visualization software described in section 3.3.3, which displays a scene like the one shown in figure 3.31 on page 63. This software has controls that move the origin of the PCS relative to the CCS and controls that rotate the pelvic model about each of the three axes of the PCS independently of the other two axes. These controls allow the pelvic model to be positioned and oriented arbitrarily with respect to the CASS. The visualization software also has controls that allow the relationship between the pelvic model and the registration points to be examined from any angle and that allow the pelvic model to be made solid or transparent, as suits the needs of the researcher. The researcher uses these controls to align the pelvic model to the registration points until the best match between them, as judged by the researcher after assessing the match from several angles, is obtained.

Once the researcher has found what he or she considers to be the best match, he or she uses the controls to jiggle the pelvic model by a few degrees around each axis or to move the origin of the pelvic model in space along each axis by 2 or 3 mm. If the during the jiggling process, a better match between the pelvic model and the registration points is obtained, then that match is used as the alignment between pelvic model and the registration points and the researcher repeats the jiggling process using the new match as the starting point. Registration terminates once the researcher finds a match that cannot be improved by jiggling, and the position and orientation of the PCS with respect to the CCS that produced this match is recorded.

3.3.2.3 Construction Of The Soft Tisue Boundary Meshes

Once we have registered the pelvis to the CASS, we can segment the ultrasonic echograms. Segmenting these echograms is not an easy task and is not simply a matter of looking for large echoes, calling them tissue layer boundaries, and assigning them to skin, fat and muscle layers based on the order in which they occur. The strong specularity of the reflections from tissue layers means that an echo from a layer boundary may be much

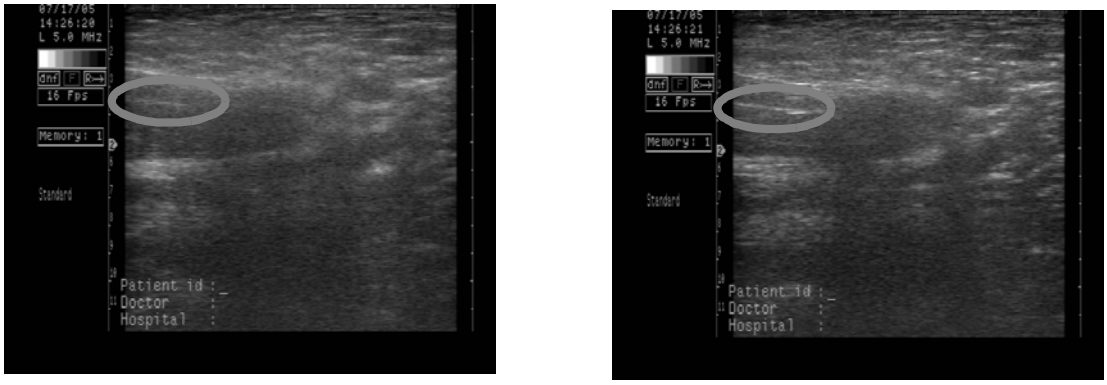

Figure 3.24: B-mode ultrasonic images of the same region of the buttocks from two slightly different angles of entry into the body. Note how the circled boundary between the biceps femoris and semimembranosus muscles is much brigher than in the right.

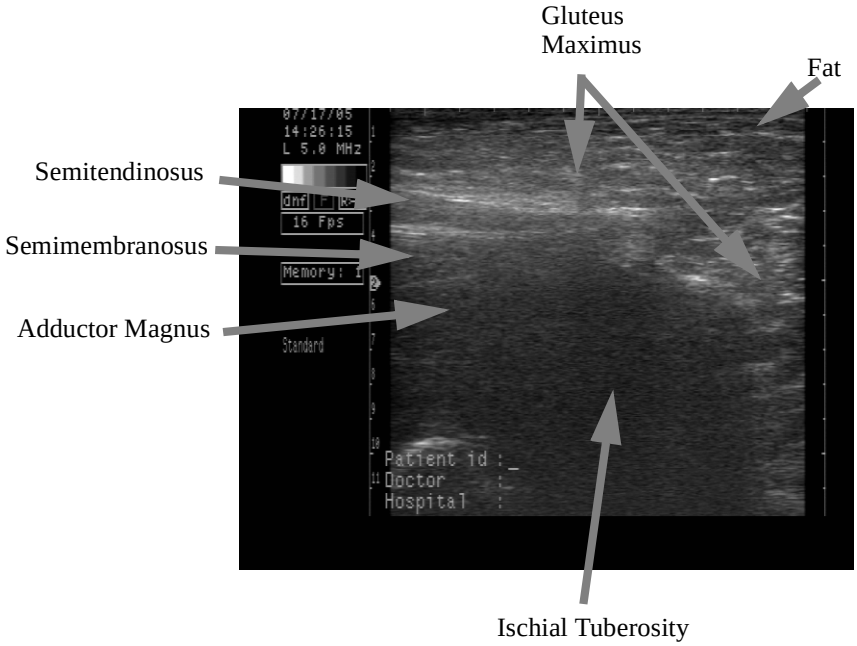

Figure 3.25: B-mode image in the sagittal plane of the buttocks of a healthy 35 year old male with the different muscle groups labeled.

diminished (because only part of the reflected energy returns to the transducer) or absent entirely from the A-mode echogram. The farther a boundary is from the transducer, the more perpendicular it must be to the path of the ultrasonic pulse for its reflection to reach the transducer. We illustrate these problems in the discussion below, then describe our solution to these problems.

Figure 3.24 shows two B-mode[3] ultrasonic images of the same region in the body but taken at two slightly different angles. At one location, the interfaces between the different tissue layers are bright and easily distinguished, but at the other location, these same boundaries have become indistinct.

Figure 3.25 illustrates a further complication. Here, we have identified the different tissue layers visible in a B-mode image taken from the underside of the right buttock in the vicinity of the ischial tuberoisity of a seated subject with one cheek hanging off of a chair. The transducer was oriented so that the image was taken in a sagittal[4] plane of the body. Segmenting the image into the different tissue layers required not only knowledge of where the transducer was located, but also required knowledge of the anatomy of the body in this region acquired from various atlases such as *Gray's Anatomy*[33], the *Atlas of Human Anatomy*[92], and the *Anatomy Coloring Book*[5][46]. Identification of the layers began by identifying anatomical landmarks within the image, such as the tip of the iscial tuberosity and then applying knowledge about what muscles connect to the tip of the iscial tuberosity and the location of the transducer to identify the semitendinosus muscle. Then knowledge about what muscles lie next to the semitendinosus was used to identify the other muscle layers in the image. To distinguish the semitendinosus muscle from the biceps femoris, the transducer had to be moved down the length of the leg to determine whether the muscle connected to the medial or lateral side of the knee.

The point of this discussion is that identifying tissue layers within a B-mode ultrasonic image is not a trivial task and requires knowledge beyond just the contents of the image itself. Furthermore, if segmenting B-mode images into different tissue layers is difficult, then segmenting the 32 A-mode signals we obtain as part of our data acquisition process is going to be even more difficult, since they lack the contextual and visual clues present in the B-mode image. In this manner, the problem we face in segmenting our A-mode echograms is very different from the work done by other researchers such as Wang[133] or Agner[1]. These researchers used a single transducer and could position their subjects in such a way to obtain good echoes. Because we are attempting to measure the shape of

3. There are three different "modes" of operation for ultrasonic imaging: A-mode, B-mode and the rarely-used C-mode. A-mode images are a time line of echoes received by a single transducer that is fixed in space and are typically displayed as amplitude vs. time waveforms. B-mode images are obtained by mechanically or electronically scanning a transducer across a region to create a cross-sectional image of that region and are what people typically think of when they think of "ultrasound" in the context of medical examinations.
4. A sagittal plane divides the body into left and right halves.
5. In spite of its frivolous-sounding name, this is not a child's text, but a serious work that uses the coloring of black-and-white anatomical images to stimulate visual memory.

the soft tissues for subjects as they sit naturally on the CASS, we cannot reposition the subjects to obtain strong echoes. Furthermore, what may be a good position for one contour may be a very poor position for another. Consequently, we must develop a process for segmenting the ultrasonic images that takes into account the fact that the echoes from the interfaces between tissue layers may be very large or small and that large echoes do not necessarily correspond to tissue layer boundaries.

To surmount this problem, we have conducted a series of examinations of a thirty-five year-old healthy male subject in which we compared A-mode and B-mode images from the same regions of the body. We also conducted a B-mode examination of the subject's posterior right buttock and thigh with those regions hanging off of a chair, both to understand how the anatomy in this region appears under ultrasonic imaging and to get a rough idea of differences in the way the fat and muscle layers respond to compression of different depths. From the results of this examination, we constructed the following process to segment the echograms we acquire from the thirty-two ultrasonic transducers into layers of skin, fat and muscle:

The initial segmentation

(1) We group all of the echograms by sensor number in all of the data sets we acquired for the contour under consideration. We remove any spoiled or corrupted echograms. For each sensor, we pick the most representative echogram from among all the remaining echograms for that sensor. The most representative echogram is generally the one with the strongest set of echoes, although is most cases, all of the echograms acquired for the same sensor are very similar and the choice of which echogram is most "representative" is an arbitrary one.

(2) We scan through the set of representative echograms and identify potential echoes from tissue layer boundaries. At this stage, we are as generous as possible in considering what may or may not be an echo, and we mark almost any disturbance as a boundary echo unless there is a good reason not to. Figure 3.26 shows an example of identifying echoes for this step. We call the set of echoes identified in this step the set of potential boundaries.

(3) We establish three zones on the representative echogram for each transducer: the skin zone, the fat zone and the muscle zone. Because the skin is generally between 1 and 3 mm thick, the skin zone occupies the first 4 μsec of the echogram, which is equal to 3 mm of tissue at 1540 m/s, the average speed of sound in soft tissue. The boundary between skin and fat is assigned to the first large echo in the skin zone.

To compute the width of the fat zone, we examine the transverse MRI cross sections we obtained for the subject and compute an average thickness for the layer of fat beneath the skin in the vicinity of the ischial tuberosity. Call this thickness L_f. The fat zone occupies the region on the echogram that corresponds to the interval $[3+L_f/2, 3+L_f]$ mm, which is another way of saying that, when the subject is seated, his layer of subcutaneous fat will be compressed to no less than

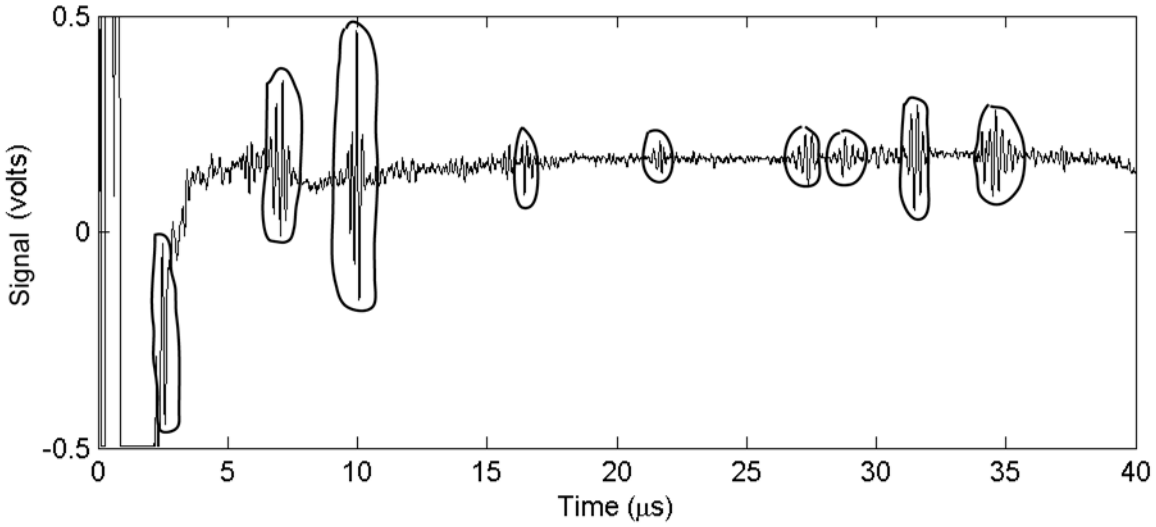

Figure 3.26: The initial segmentation of an ultrasonic echogram. Circled echoes indicate potential soft tissue boundaries.

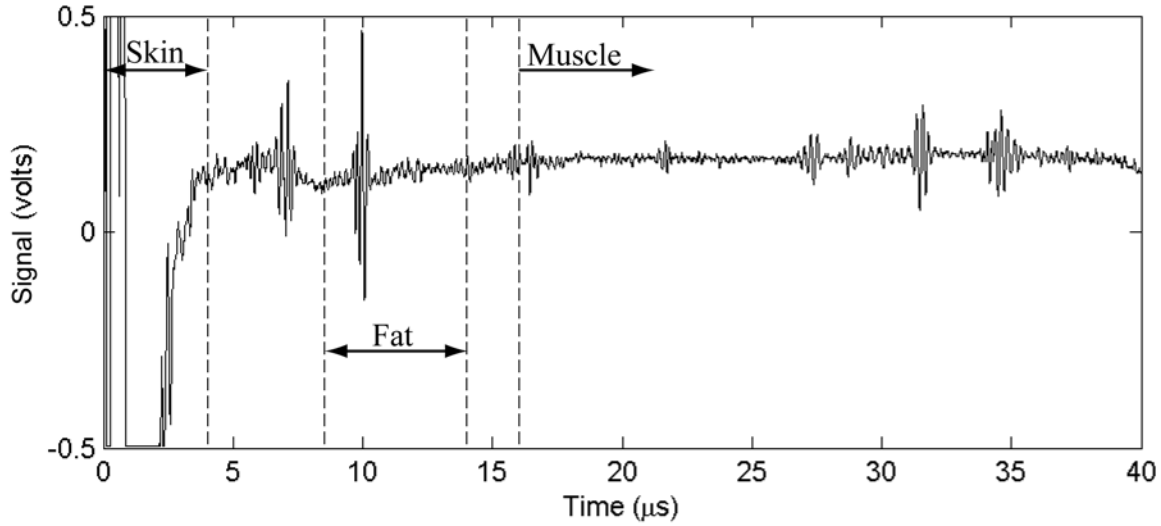

Figure 3.27: The skin, fat and muscle zones of an ultrasonic echogram.

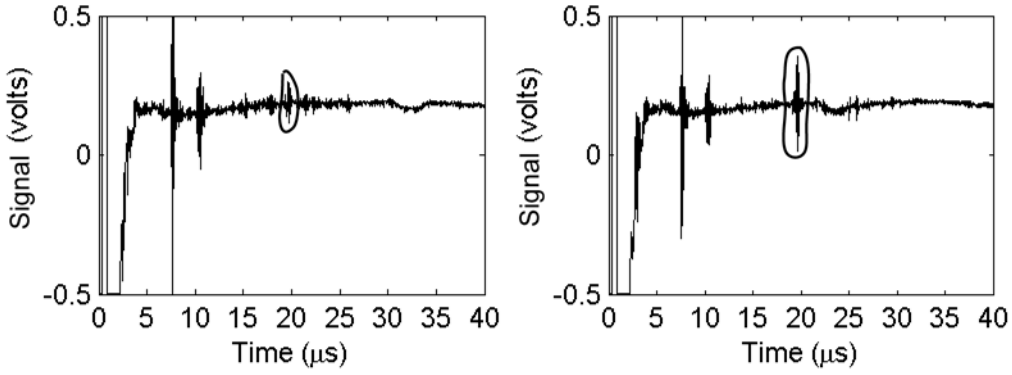

Figure 3.28: Using a set-aside echogram to find a soft-tissue boundary.

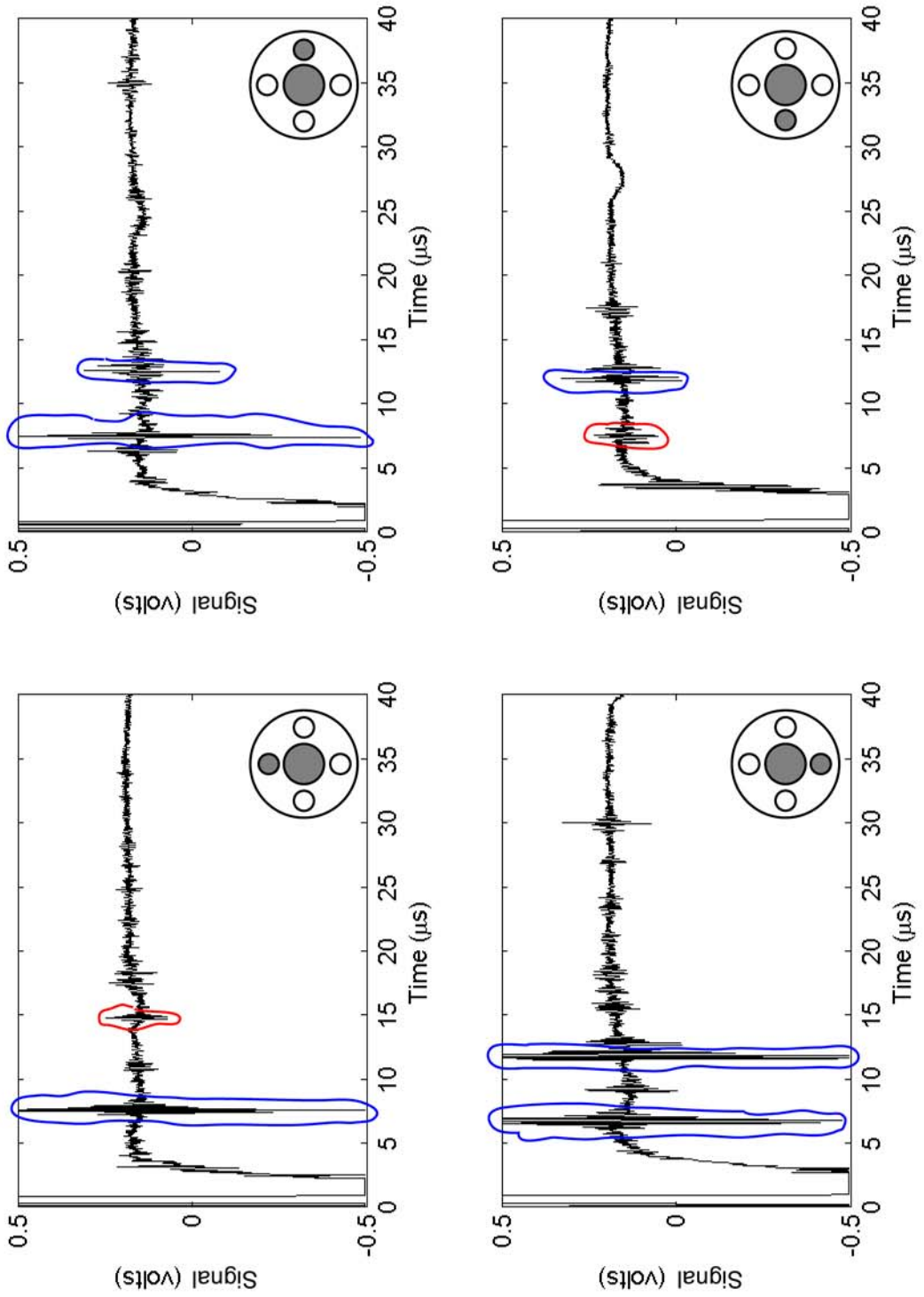

Figure 3.29: Using neighboring echograms to enhance the segmentation process. The four echograms in this figure all come from ultrasonic transducers mounted on the same actuator. Weak echoes circled in red might be ignored were it not for the corresponding striong echoes circled in blue in the neighboring echograms.

half of its thickness when he is lying down. The constant “3” comes from the upper bound on the thickness of the skin layer. The boundary between the layer of subcutaneous fat and the first muscle layer is assigned to the first large echo that appears in the fat zone.

The muscle zone begins 1-5 mm after the echo after the echo identified as the fat/muscle boundary and extends to the end of the echogram. The exact location where the muscle zone begins depends on the relationship between the transducer and the pelvis and corresponds to our prior belief about the minimum thickness of the first muscle layer beneath the subcutaneous fat. Transducers beneath the ischial tuberosity or descending public ramus will be assigned smaller minimum thicknesses than sensors that do not fall beneath the pelvis at all. The boundary between the first and second muscle layers is assigned to the first large echo in this region.

Figure 3.27 illustrates the skin, fat and muscle zones for an example echogram. When boundaries between the skin, fat, and first and second muscle layers have been placed by steps (1)-(3) for all thirty-two transducers, the initial segmentation of the echograms is complete and we proceed with the initial refinement.

The Initial Refinement

(4) We refine the segmentation for each transducer by considering the segmentations of the other transducers that share the same actuator, since these transducers are relatively close by and point in the same direction. For example, in figure 3.29, although the echoes circled in red are quite weak, the echoes at the same location for the other transducers that belong to the actuator are quite strong. It is unlikely that the boundary between the first and second muscle layers dips down just at this once transducer, so we assign the boundary to the echoes circled in red.

We also examine the echograms we set aside in step (1) as not being representative and use them to refine the segmentation for the representative echogram. Although these “non-representative” echograms are often very similar to the representative echogram, occassionally they can be used to filter out transient effects, such as a momentary distubance causing the pulse to intersect a boundary at an oblique angle, resulting in a weak echo in the representative echogram. This process is shown in figure 3.28.

The Final Refinement

(5) At this point, we assemble all the refined boundary points computed in step (4) that belong to the same boundary into a triangular mesh that represents that boundary. We do this for all three boundaries: skin/fat, fat/first-muscle and first-muscle/second-muscle. We render the pelvis, the CASS, and the tissue meshes using the techniques described in section 3.3.3 on data visualization. We also render all of the potential boundary points for each transducer along with the boundary meshes.

(6) Once the scene is rendered and we can see the relationship between the tissue

meshes and the pelvis, we use our knowledge of the anatomy of the gluteal region and upper thigh to refine the segmentation further. For the most part, we refine the shape of the boundary between the first and second muscle layers during this step. The shapes of the skin/fat and fat/first-muscle boundaries are generally well-established by the preceeding steps.

As an example of the kind of refinement that takes place during this step, we know that the region behind the ischial tuberosity is occupied by almost entirely by the gluteus maximus, so we would favor deeper echoes over shallower ones for transducers located in this region. We know that the gluteus maximus, the biceps femoris, the semitendinosus, and the semimembranous muscles must all pass beneath the ischial tuberosity, so for transducers located beneath the ischial tuberosity, we expect the first muscle layer to be very thin, and so on.

Once the final refinement is complete, we have the final shapes of the boundaries between skin and fat, fat and the first muscle layer, and the first and second muscle layers. We can also compute the thicknesses of the skin, the subcutaneous fat, and the first muscle layer above the transducers.

The segmenting procedure does not always find a boundary for every soft tissue layer above every transducer. Sometimes this occurs because the missing layer does not lie above the transducer. For example, when the contour is flat, it is entirely possible for the fat layer to be squeezed out entirely from beneath the ischial tuberosity. Sometimes a boundary is missing because the individual layers are squeezed together so tightly that the boundaries between them become blurred. This can occur beneath the ischial tuberosity when the biceps femoris, semitendinosus and semimembranous muscles are squeezed together so tightly that it becomes impossible to distinguish between them. But most often, the segmentation procedure fails to find a boundary above a transducer because the reflection from that boundary, whether due to attenuation or non-normal incidence, was not received by the transducer or because the amplitude of the reflection is too small to distinguish it from the surrounding noise.

Whatever the cause, the missing boundary creates a hole in the triangular mesh for that boundary. If enough of the transducer’s neighbors have points on the boundary, the missing boundary is simply ignored and the neighbors are connected together to create the triangular mesh, in effect “papering over” the missing boundary. If the missing boundary occurs on the edge of the mesh, the triangles it would be connected to are simply omitted and the mesh will cover less area than it normally would. Only if a large group of neighboring points on the boundary between two tissue layers are missing is the hole left in the mesh for that boundary. If too many boundary points are missing to create a coherent mesh, then that mesh is simply omitted. In practice, missing boundary points almost never occur for the boundary between skin and fat, seldom occur for the boundary between fat and the first muscle layer, but occur quite often for the boundary between the first and second muscle layers.

3.3.2.4 Measure Bulk Tissue Thickness And Volume

The final step in our data analysis process is to compute the thickness and volume of the bulk tissue between the pelvis and the surface of the CASS. Although the data from the ultrasonic transducers allows us to measure the thickness of the individual layers of skin, fat and muscle, they only provide this information over a limited area and for a small number of sites. By computing the bulk tissue thickness and volume, we can observe how the overall shape of the soft tissues changes from one seating contour to other or varies from one subject to another. Furthermore, the bulk tissue thickness measurements can serve as a substitute for the thicknesses of the individual tissue layers above the transducers for certain comparisons when these individual thickness measurements could not be made because the boundary between two neighboring tissue layers that lies above that transducer could not be located for the reasons described at the end of section 3.3.2.3.

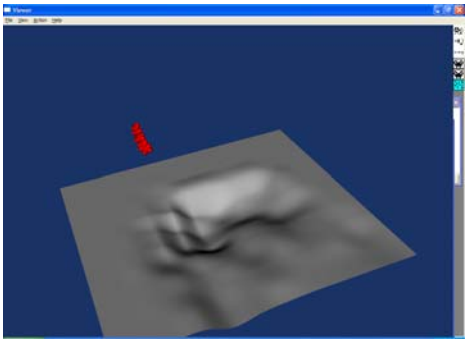

Figure 3.30: The interpolated surface

We interpolate a continuous surface for the CASS using bicubic interpolation over the grid of actuators, using the normal to each actuator surface to compute the first derrivatives along the x- and y-axes of the surface shape at the grid points. Figure 3.30 shows the interpolated surface for a pressure-equalized contour.

We compute the bulk thickness of soft tissue by sampling the interpolated surface at regular intervals and computing the distance between the interpolated surface and the pelvis. We compute the volume of bulk tissue by summing the thickness measurements and multiplying by the square of the sampling interval; this treats the bulk tissue above each sample as a rectilinear solid, which is a close approximation for sampling intervals that are small enough. The sampling interval must be chosen carefully. If it is too coarse, the bulk tissue thickness and volume measurements will not accurately reflect the distribution of bulk tissue beneath the pelvis. If it is too fine, the computation of bulk thickness will take much longer than it should. To choose a sampling interval, we compared the histograms of bulk tissue thickness measurements for sampling intervals of 1.07 mm, 2.13 mm, and 4.27 mm, which correspond to 40, 20 and 10 samples per actuator, to each other. Each histogram plotted the fraction of the total number of thickness measurements that fell within bins that were 10 mm wide. Histograms were compared by plotting them on the same figure and examining them visually. The shape of the histogram using a 1.07 mm sampling interval differed significantly from the shapes of the histograms that used sampling intervals of 2.13 mm 4.27 mm. However, the shapes of the histograms that used sampling intervals of 2.13 mm and 4.27 mm did not differ significantly from one another. Consequently, we chose to use a sampling interval of 2.13 mm to compute bulk tissue thickness for all the results reported in this thesis.

When it comes to the direction along which we make our bulk tissue thickness

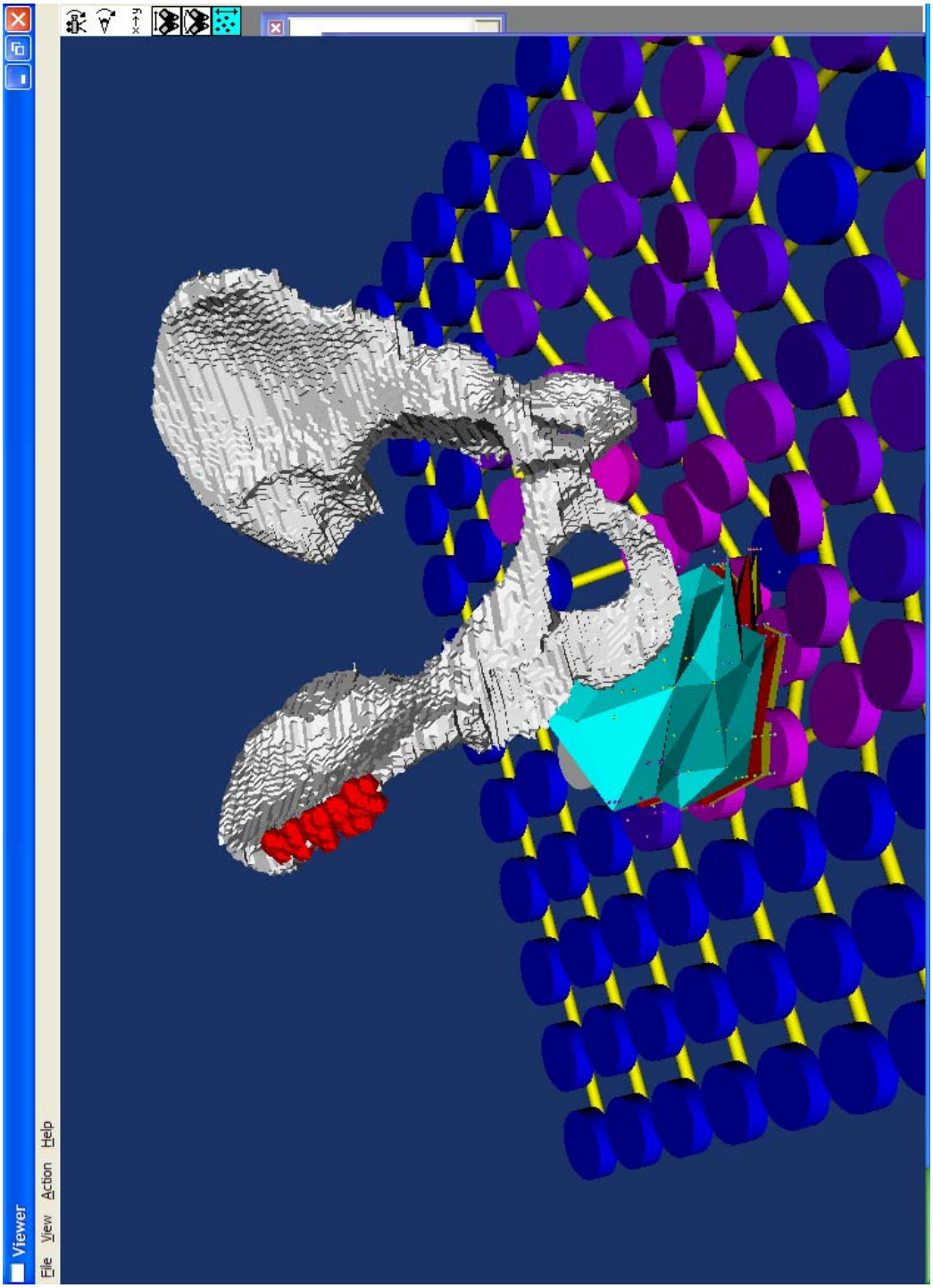

Figure 3.31: A typical view from the visualization software.

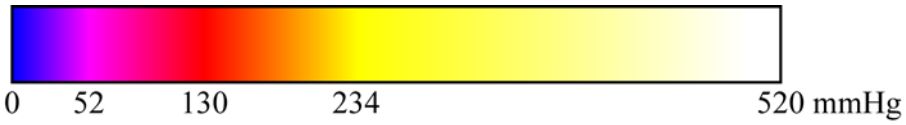

Figure 3.32: The color scale used to indicate pressure at each actuator by the visualization software.

measurements, there are two sensible choices: straight up along the z-axis of the CASS or along the normal to the surface. The latter is appropriate for measuring the amount of bulk tissue that contributes to the weight, and thus the pressure, felt by each actuator. The former is appropriate for measuring the thickness of bulk tissue above a transducer, since the direction indicated by the surface normal is an approximation to the path of the ultrasonic pulse. Which direction is chosen depends on what our needs are. Since we are primarily interested in the relationship between bulk tissue thickness, interface pressure, and the pelvic position and orientation, we measure bulk thickness along the z-axis in almost all cases, since this yields the height of the column of tissue above each point on the seating surface. We only measure bulk thickness along the normal when we need to measure the thickness of bulk tissue above a transducer beyond what can be measured by the ultrasound itself.

3.3.3 Visualization

Once the data collected for a contour have been analyzed, the results of the analysis need to be displayed so they can be evaluated qualitatively by researchers. The visualization software is written in C++ using a combination of OpenGL and the Visualization Toolkit[76] and can be run on any PC that has modern graphics hardware and runs Microsoft Windows.

The visualization software displays a scene like the one in figure 3.31. The scene depicts a perspective view of the pelvis, the CASS and the soft tissue boundary meshes all rendered in their correct relative locations. The CASS is rendered as a grid of disks whose dimensions are the same as the actuator heads they represent. Each disk is drawn at the height and orientation it would be in the real world, so that taken together, the disks represent a faithful representation of the surface of the CASS. Each disk is colored using the scale shown in figure 3.32 to represent the pressure measured at the actuator it represents. Disks on the edges of the CASS whose actuators do not have pressure sensors are colored blue. The pelvis is colored white to reflect the bone that composes it, and the tissue meshes are colored to indicate their identity. The boundary between skin and fat is colored yellow, while the boundary between fat and the first muscle layer is colored red and the boundary between the first and second muscle layers is colored aqua. The registration points are represented by tiny red spheres. A simple set of controls allows the researcher to navigate the camera through the scene using an intuitive interface. All of the objects in the scene can be made invisible or transparent to allow the researcher to see parts of the scene that might otherwise be obscured. The scene is lit by a light source that is positioned behind the camera at infinity and follows the camera as it moves through the scene so that the light source remains positioned behind the camera at infinity.

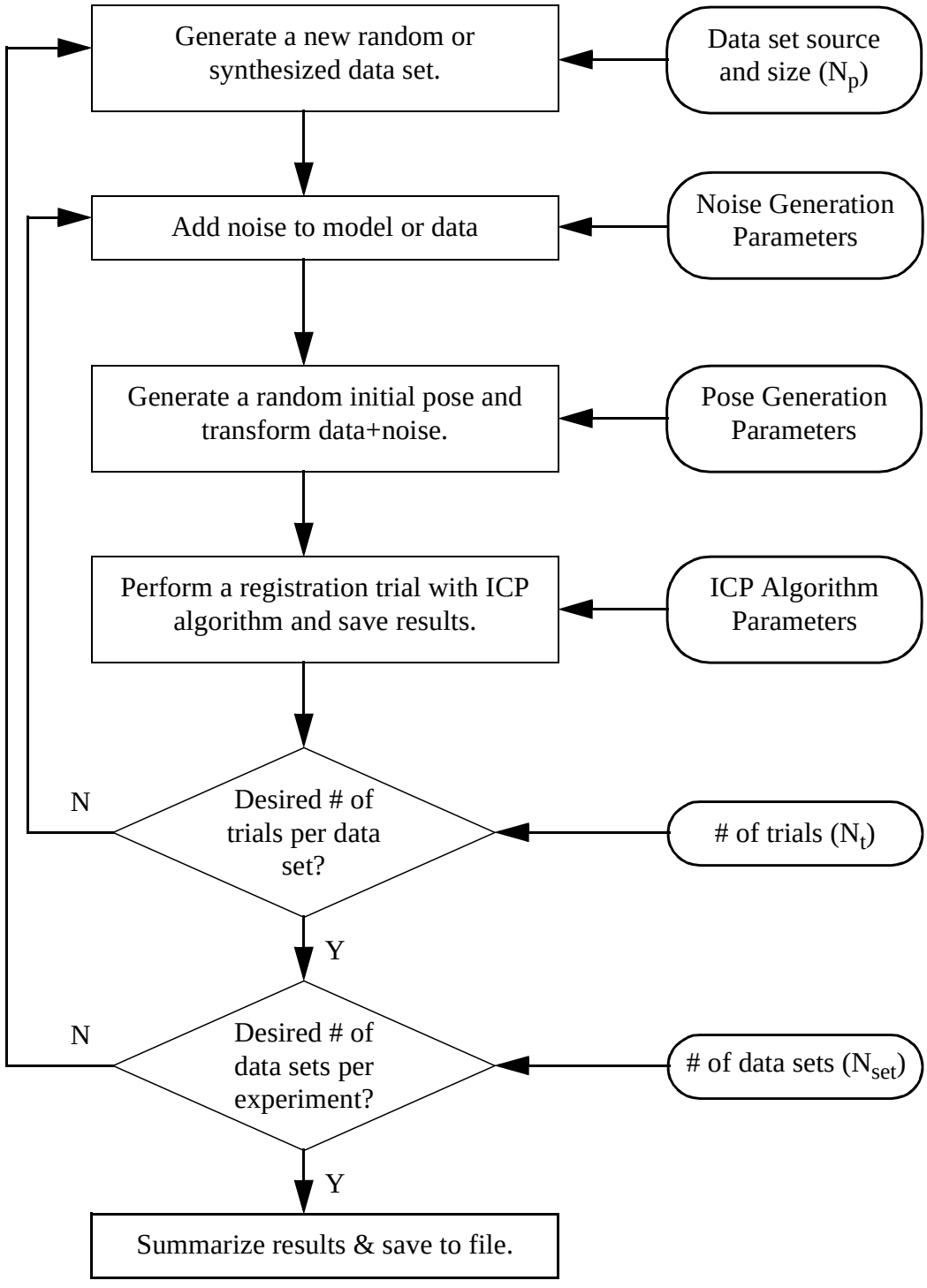

Figure 3.33: Schema for simulated registration trials.

3.4 Error Analysis

In order for the results of the data analysis procedure described in section 3.3.2 to be meaningful, we need to know how accurate they are. In the following sections, we identify different sources of error and analyze how they affect the accuracy of the result.

3.4.1 Registration Accuracy

The accuracy of the registration process used to compute the position and orientation of the pelvis with respect to the CASS is affected by the uncertainty in the locations of the registration points and our choice of where on the pelvis we obtain those points. As of this writing, the accuracy of the manual registration algorithm has not been validated and for reasons explained below, the position and orientation of the PCS with respect to the CCS computed by this algorithm may have large errors. In fact, given the restriction that the position wand can only measure points near the surface of the right anterior iliac spine, no shape-based registration algorithm will be able to compute the transformation between the PCS and the CCS accurately. In the following paragraphs, we explain why this is so and provide a simple fix to the current system so that will ensure accurate registration in the future.

3.4.1.1 The Iterative Closest Point Algorithm

We begin by considering an automated registration algorithm - the Iterative Closest Point (ICP) registration algorithm developed by Besl and McCay[8] and applied by David Simon to surgical registration tasks in his Ph.D. thesis[117]. The ICP algorithm functions by searching the space of possible transformations between the pelvic model and the registration points for the transformation that minimizes the distance between the registration points and the model. At each iteration, the ICP computes the closest point on the the surface of the pelvic model to each registration point, computes the transformation between the PCS and the CCS that minimizes the Euclidean distance between each registration point and its corresponding closest point on the surface of the pelvic model, and then applies this transformation to the pelvic model. In the next iteration, the transformed model will be used to compute the set of closest points on the model. Iteration continues until the transformation computed during the current iteration differs only slightly from the transformation computed during the previous iteration, or until a maximum limit on the number of iterations is exceeded. Modifications made to the ICP algorithm made by David Simon as part of his Ph.D. work allowed the ICP to avoid becoming trapped in local minima of the search space and to ignore outlier registration points.

3.4.1.2 Accuracy Of The ICP

We originally used the ICP algorithm to compute the transformation between the PCS and the CCS, and so we sought to measure its accuracy using a series of simulated registration trials that were similar to the simulated registration trials David Simon used for the same purpose in his PhD work. Figure 3.33 shows the schema for these simulated registration trials. For each set of experimental conditions, we generate N_{set} sets of N_p data points by selecting them randomly from the surface of the pelvic model in the vicinity of the right anterior superior iliac spine. The steps performed for each registration experiment are illustrated by the flowchart in figure 3.33. For each set of registration points, we perform

Table 3.1: Registration Parameters For ICP Algorithm

Parameter	Meaning	Value
Termination Thresholds e_{Tr} and e_{Rr}	Difference in pose from the last to the current iteration must be less than these values for the ICP to terminate.	$e_{Tr}= e_{Rr}=10^{-4}$
k_{max}	Maximum ICP iteration count	1000
Minima Suppression	Whether minima suppression is enabled or not	Enabled
$\theta_{p\text{-}max}$	Maximum value of the angle used in the uniformly-distributed random perturbation of the minima-suppression phase of the ICP.	5 degrees
$\tau_{p\text{-}max}$	Maximum value of the translation used in the uniformly-distributed random perturbation of the minima-suppression phase of the ICP	$\tau_{imax}/2$
I_p	Number of iterations without improvement required for termination of minima-suppression phase of the ICP algorithm.	6
Data size, N_p	Number of points in the data set	30
N_t	Number of trials per set	1000
N_{set}	Number of data sets per simulation	1
τ_{imax}	Maximum translation distance for randomly-generated initial pose	30 mm
θ_{imax}	Maximum rotation angle of each axis for randomly-generated initial pose	30 degrees
μ_{mag}	Mean magnitude of Gaussian measurement errors used to corrupt data points.	5 mm
σ_{mag}	Variance of magnitude of Gaussian measurement errors used to corrupt data points.	2.5 mm

Table 3.2: Registration Accuracy By Region

	Translation Error (mm)		Rotation Error (CSRDM)	
Region	Mean	StdDev	Mean	StdDev
Right ASIS only	57.6	33.7	1.20	0.70
Right PSIS only	53.3	29.3	1.92	0.83
Right ASIS and PSIS	14.8	11.2	0.44	0.36
Both ASIS	13.4	8.8	0.55	0.33
Both PSIS	31.0	23.7	0.93	0.69
Both PSIS+ASIS	4.4	4.7	0.14	0.14

N_t registration trials. For each registration trial, we corrupt the registration points with gaussian measurement errors and then apply a randomly-generated transform between the registration points and the model. The simulator generates the transform by choosing a random translation from a uniform distribution over the interval $[0, t_{max}]$ and a random rotation. The simulator generates the random rotation by rotating about a random vector $\hat{v}$ by a random angle drawn from a uniform distrubtion over the interval $[0, \theta_{max}]$. The vector $\hat{v}$ is selected by generating a random point on the unit sphere. Corruption of the randomly-selected registration points is performed by adding a vector $\hat{e}$ to each registration point whose magnitude is drawn from a normal distribution with mean μ_{mag} and variance σ_{mag} and whose direction is chosen by generating a random point on the unit sphere. The error vector $\hat{e}$ is chosen separately for each registration point. Once the data points have been corrupted by measurement errors and had the random transform applied to them, the simulator feeds the data and the model to the ICP algorithm, which attempts to compute the transformation between them. When the ICP algorithm completes, the simulator records the results of the trial - whether the ICP algorithm converged and the transformation it computed - and proceeds with the next trial. When all trials for a data set are complete, the simulator proceeds to the next set of registration points. When the results of an experiment are analyzed, the difference between the true pose of the registration data points with respect to the model and the pose recovered by the ICP is used as a measure of registration quality.

Table 3.1 shows the parameters for the simulated registration trials of the ICP algorithm and the first line of table 3.2 shows the results. As shown in the table, when restricted to registration points acquired from the right anterior superior iliac spine, the ICP algorithm performs quite poorly, with a mean translation error of 57.6 mm and a mean rotation error of 1.20. The rotation error measures the mean distance between the orientation of the PCS as computed by the ICP and its true orientation using the coordinate system rotation distance metric described in appendix D, and its value is unitless. To get a feel for how far the mean distance between the true and computed orientations is, the mean rotation error

of 1.20 corresponds to an average angle of 40.6 degrees between the x-, y-, and z-axes of the PCS as computed by the ICP and the corresponding axes of the true PCS when their origins are coincident.

There are two reasons for the poor performance of the ICP algorithm:

(1) Sometimes the ICP algorithm gets sidetracked by a poor initial guess at the transformation between the PCS and the CCS. This guess places the registration points in a physically impossible location (e.g. somewhere inside the pelvis) or someplace on the surface of the pelvis far from the right anterior superior iliac spine.

(2) When the registration points are drawn from the right anterior superior iliac spine alone, there are many transformations between the PCS and the CCS that place the points on the surface of the pelvic model in the vincinity of the right anterior superior iliac spine in similar locations but that differ wildly in where they place the points on the left side of the model. To see this, imagine that registration points were acquired along the crest of the right anterior superior iliac spine. By careful manipulation of the roll angle and origin of the PCS, it is possible to keep the registration points close to the crest of the right anterior superior iliac spine, but move the left side of the pelvis up and down quite a bit. In other words, for all practical purposes, acquiring registration points only from the right anterior iliac spine does not constrain the registration problem enough to permit an accurate solution.

3.4.1.3 Accuracy Of Manual Registration

Because of its poor performance under the restrictions imposed by the configuration of the CASS equipment on where the position wand can obtain registration points, the manual registration algorithm described in section 3.3.2.2 was used instead of the ICP. Using a human to perform the registration between the PCS and the CCS allows us to eliminate the first problem *but not the second*. While the points on the pelvic model in the vicinity of the right anterior superior iliac spine are probably close to their true locations, the farther away one moves from the right anterior superior iliac spine, the larger the potential difference between the location of a point on the pelvic model computed by the manual registration algorithm and its true location becomes.

However, while the possibility of the manual registration algorithm producing large errors in measuring the position and orientation of the PCS with respect to the CCS should not be understated, neither should it be overstated. While item (2) represents a *potential* source of large error in computing the transformation between the PCS and the CCS with the manual registration algorithm, its *actual* impact on that algorithm is presently unknown. Consequently, the most accurate statement that can be made about the manual registration algorithm is that it has yet to be validated and its accuracy is unknown. Therefore, any of the results in this thesis that depend upon the position and orientation of the PCS with respect to the CCS computed by that algorithm or conclusions drawn from those results should be treated with extreme caution until future studies are conducted using improvements to the data acquisition procedure to ensure accurate registration and

validate those conclusions. Given the small size of the pilot study conducted in chapter 4, such studies are needed anyway to avoid drawing conclusions from a non-representative sample.

3.4.1.4 How To Obtain Accurate Registration

Fortunately, a simple modification to the data acquisition process will ensure accurate registration for future studies. Although the current configuration of the CASS equipment limits us to obtain registration points from the right anterior superior iliac spine, the right anterior superior iliac spine is not the only place where only a thin layer of skin separates us from the pelvis. The left superior anterior iliac spine and both posterior superior iliac spines are also suitable places to obtain registration points. As the data in table 3.2 show, if we were to obtain a second position wand so that we could acquire registration points on both sides of the pelvis, and alter the configuration of the CASS so that registration points could be acquired from the anterior and posterior superior iliac spines (called “ASIS” and “PSIS” respectively in table 3.2), then registration using the ICP algorithm with registration points obtained from all four superior iliac spines would have a mean translation accuracy of 4.4 mm and rotation accuracy of 0.14. This rotation accuracy corresponds to an average angle of 4.6 degrees between the x-, y-, and z-axes of the PCS as computed by the ICP and the corresponding axes of the true PCS when their origins are coincident. The accuracy of the manual registration algorithm will be similar.

3.4.2 Accuracy Of Soft Tissue Thickness Measurements

Our ability to measure the thicknesses of the skin, fat, and first muscle layer accurately is affected by the following quantities:

(1) **Misidentification of Tissue Type Interfaces**
The difference between which echoes in the ultrasonic echogram we believe correspond to tissue layer boundaries and which echoes actually correspond to tissue layer boundaries.

(2) **Time-Of-Flight Measurement Uncertainty**
The differences between the measured time-of-flight of the ultrasonic pulse to the boundaries identified in (1) and the actual time-of-flight.

(3) **Departure From Normal Of Ultrasonic Pulse Launch Direction**
The difference between the assumed angle of entry of the pulse into the body of zero degrees and the actual angle of entry.

(4) **Uncertainty In Speed-Of-Sound In The Different Tissue Layers**
The difference between the assumed speed of sound in each of the layers of soft tissue and the actual speed of sound.

(5) **Uncertainty In The Orientation Of The Tissue Layer Boundaries**
The difference between our assumption that the tissue layer boundaries are perpendicular to the path of the ultrasonic pulse and the actual orientations of those boundaries.

The first item has a huge potential impact on the accuracy of our thickness measurements, as the difference between the actual echo from the boundary and where we believe the

boundary lies can be quite large. However, at present we have no way of estimating the probability that we have misidentified an echo as being a reflection from a tissue layer boundary. Given the large number of candidate echoes that could be assigned to a boundary, exhaustive enumeration of all the possible assignments of a set of boundaries to a set of echoes followed by an evaluation of their probabily of being the correct assignment is impractical. Sincewe cannot quantitatively evaluate the impact of mischaracterizing an echo as a reflection from a boundary, we ignore this source of potential error until we can run a study comparing the boundaries identified by the process in section 3.3.2.3 to a known configuration of skin, fat and muscle layers *in vivo*.

The impact of the remaining sources of uncertainty is analyzed in appendix B, and so we apply the results of that analysis to our ultrasonic thickness measurements. As discussed in that appendix, the impact of the angle of entry of the ultrasonic pulse into the body has little effect on the accuracy of our tissue thickness measurements. Furthermore, because we couple the transducers directly to the skin through a coupling gel, the difference between the angle of entry of the pulse into the body is unlikely to differ significantly from zero, so we can ignore this potential source of error. Likewise, as discussed in appendix B, any reasonable method of measuring the time-of-flight of the ultrasonic pulse between neighboring tissue layers is going to have little impact on the accuracy of the tissue thickness measurements.

To compute the thicknesses of the soft tissue layers, we assume the speed of sound in each layer is equal to its textbook value of 1600 m/s for skin, 1450 m/s for fat and 1580 m/s in muscle[77]. We have no way of knowing how accurate these values are for the individual subjects we examine with our system. However, we can assume that the true speeds of sound lie within 100 m/s of these values, since even variation this large would correspond to extreme changes in the mechanical properties of soft tissue.

We also assume that the path of the pulse is straight, which is equivalent to assuming that all of the boundaries between tissue layers are normal to the path of the pulse. This assumption clearly does not hold for all tissue layers within the buttocks. However, reflection at the tissue layer boundaries is highly specular and both the transducer and the pulse have a finite, non-zero width, so the greater the angle of reflection, the more likely it is that the reflected pulse will miss the transducer completly. Indeed, we only need to worry about angles of reflection that are significantly different from zero for tissue layers close to the transducer.

According to Jue Wang[133], the diameter of the crystal in the ultrasound transducers for the CASS is 3 mm. The pulse grows wider as it propagates through the body. The width of the pulse at -3dB in mm as a function of distance travelled in mm can be approximated by:

$$W = 1 + \frac{4d}{70} \tag{3.11}$$

This approximation can be used to compute the maximum angle between the normal to the tissue layer and the path of the pulse that will allow the reflected pulse to overlap the

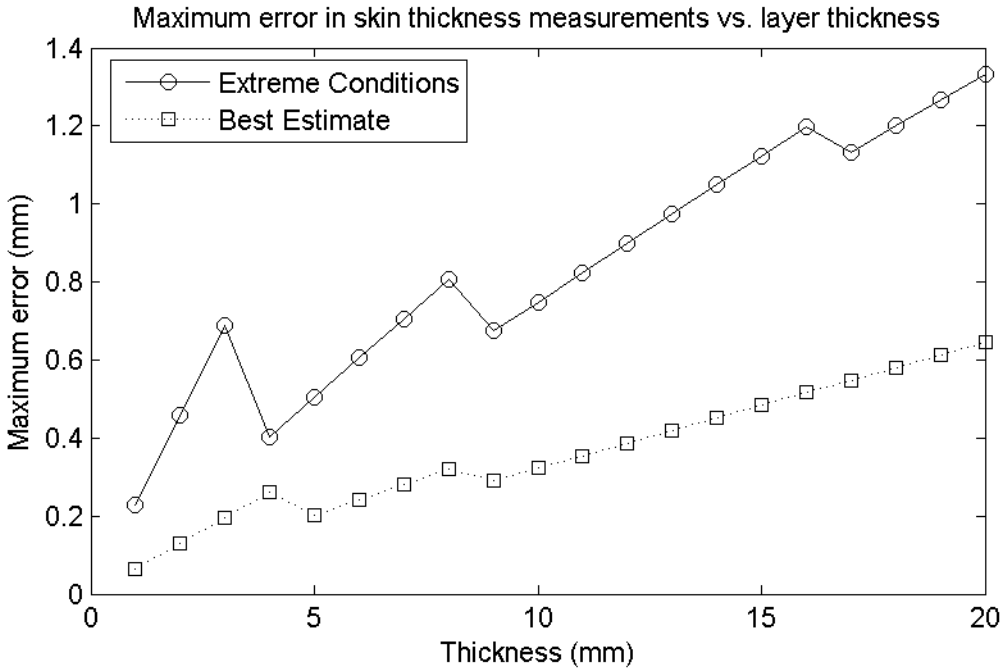

Figure 3.34: Worst-case and best-estimate of the upper bound in measuring the thickness of the skin layer.

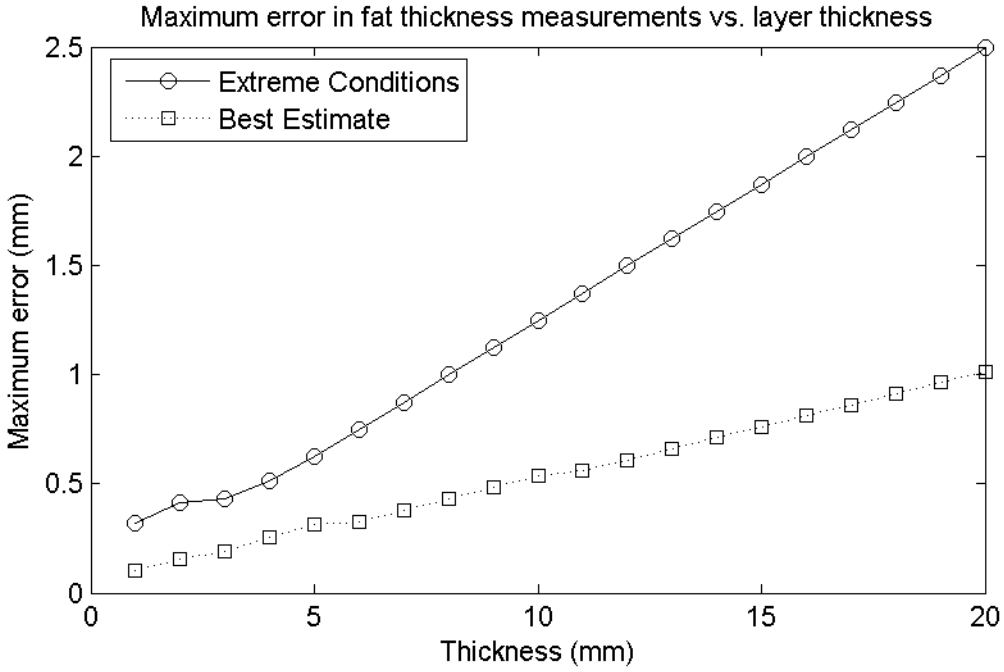

Figure 3.35: Worst-case and best-estimate of the upper bound in measuring the thickness of the fat layer.

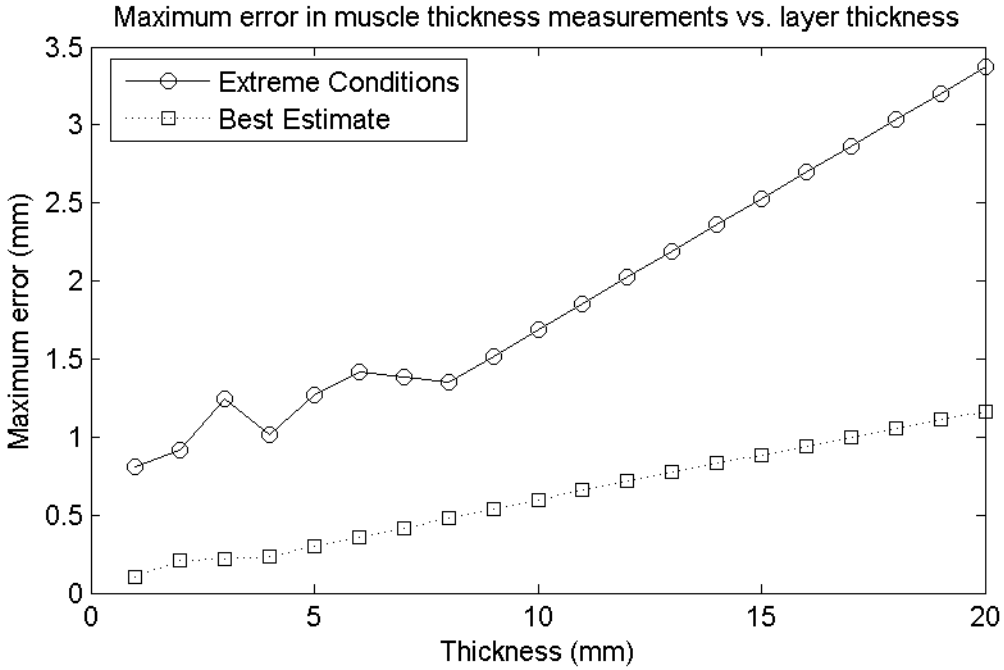

Figure 3.36: Worst-case and best-estimate of the upper bound in measuring the thickness of the muscle layer.

transducer. By combining this maximum with the upper bound on the uncertainty in the speed of sound for each layer of 100 m/s and using the material in Appendix B, we can compute an upper bound on the error in measuring the thickness of the layers of skin, fat and muscle. The solid lines in figures 3.34, 3.35 and 3.36 show this “worst-case” upper bound as a function of tissue layer thickness. In these figures, the upper bound for the fat layer is computed assuming a skin layer that is 3 mm thick and the upper bound for the muscle layer is computed assuming a skin layer 3 mm thick and a fat layer 5 mm thick. Within realistic bounds, other layer thicknesses will produce similar error curves. The large relative errors in these figures are the result of extreme conditions, such as an angle of incidence of 20 degrees at the skin/fat boundary and the assumption that any overlap between the reflected pulse and the transducer produces a visible echo. While such conditions are possible, they are not likely to occur. In the same figures, the dotted lines show the upper bound on measurement error for a more realistic set of conditions that assumes that the maximum angle of incidence for any layer is 10 degrees and that the speed of sound lies within 50 m/s of its textbook value. This more moderate set of conditions also requires that at least half of the width of the reflected pulse overlap the transducer before a noticable echo will appear. This figure shows a much smaller relative error in the thickness measurements ranging from 10% for thinner tissue to about 2-5% for thicker tissues. The values shown by the dotted lines constitute our best estimate of the upper bound of measurement error in the thickness measurements made by the ultrasonic transducer.

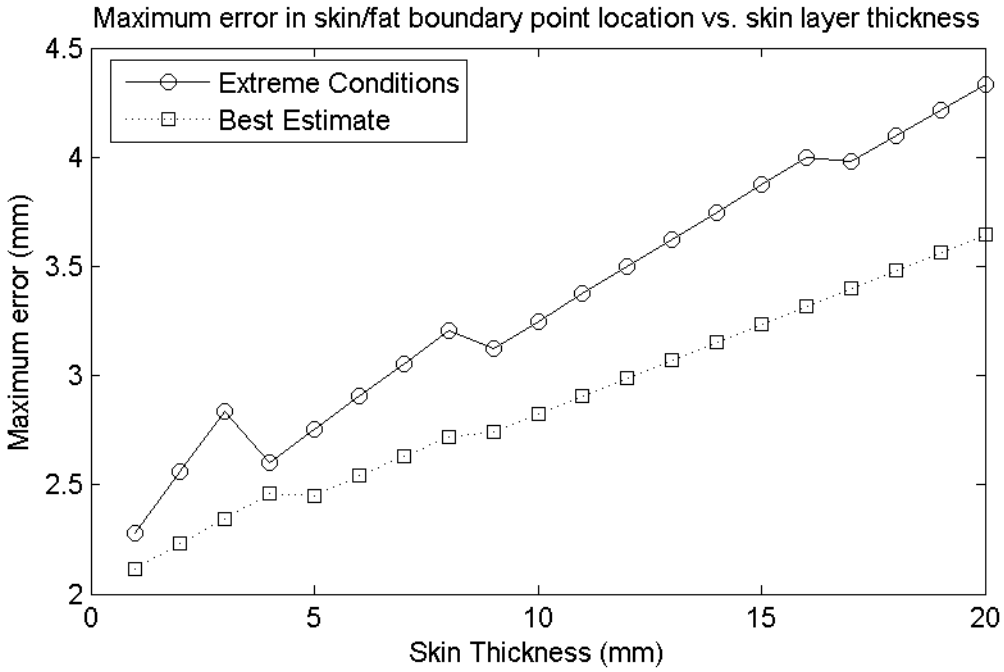

Figure 3.37: Worst-case and best-estimate of the upper bound in measuring the location of the boundary between the skin and fat layers.

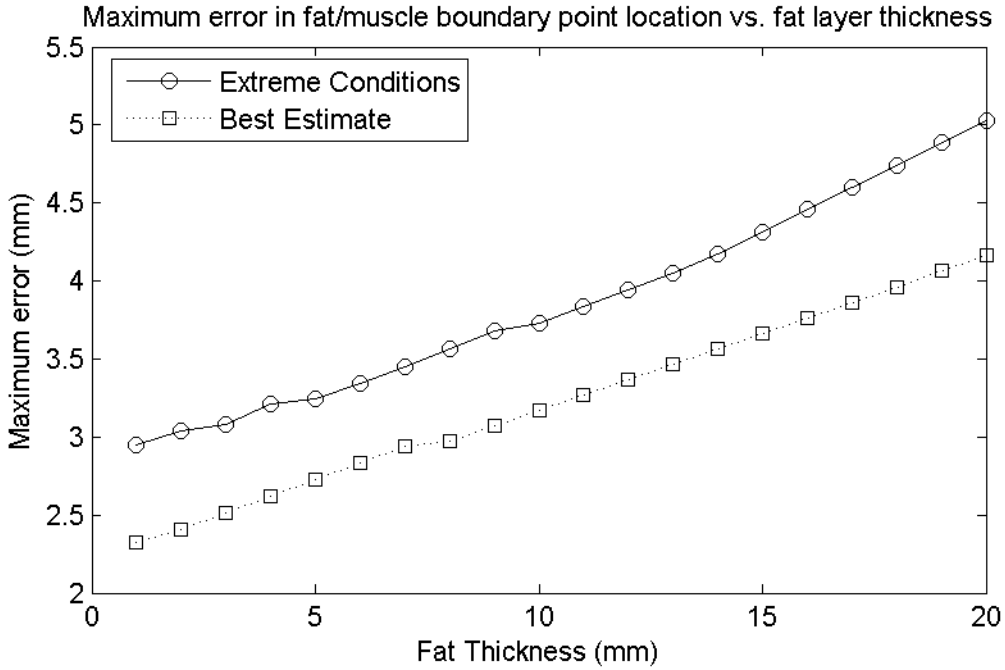

Figure 3.38: Worst-case and best-estimate of the upper bound in measuring the location of the boundary between the fat and first muscle layers.

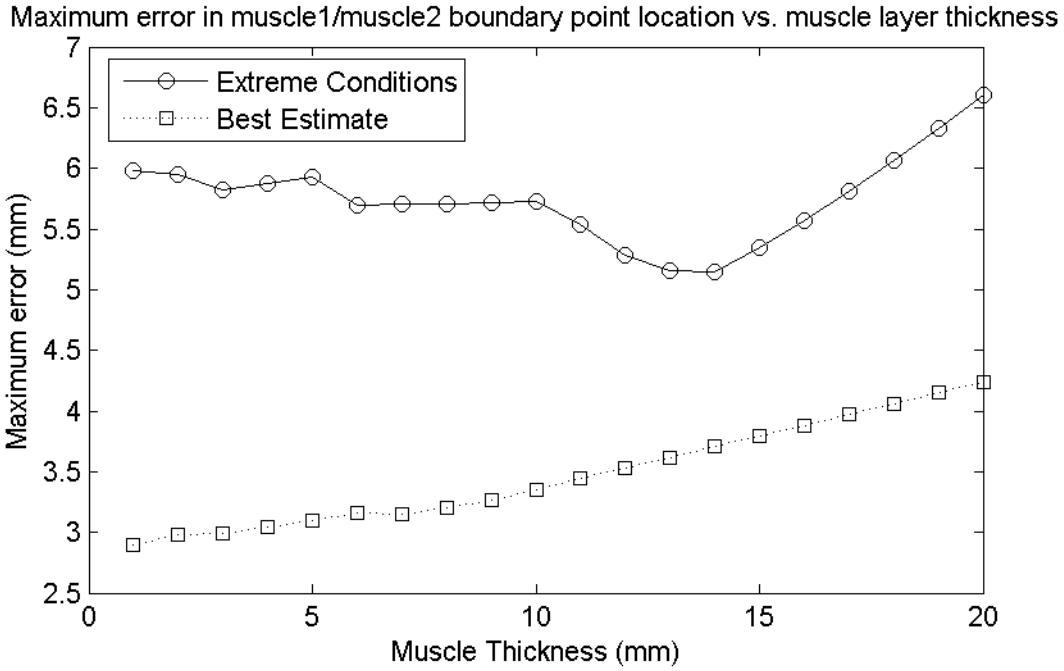

Figure 3.39: Worst-case and best-estimate of the upper bound in measuring the location of the boundary between the first and second muscle layers.

3.4.3 Accuracy Of Boundary Point Location Measurements

Our ability to measure the locations where the ultrasonic pulse intersects the boundaries between the layers of skin, fat and muscle is affected by the same quantities as the layer thickness measurements plus the uncertainty in our ability to measure the location of the transducer and the normal to its surface. The uncertainty in the transducer location is a function of the uncertainty in measuring the initial location of the transducer accurately (equal to the accuracy of the position wand, which is about 0.3 mm and can be considered neglidible), the uncertainty in the measurement of the tilt and rotation angles for the actuator the transducer is attached to (about 0.5 degrees for the tilt angle and about 5 degrees for the rotation angle), and the uncertainty in the location of the transducer that occurs because of the rotation of the actuator about its own normal during the measurement process (about 2 mm). The uncertainty in the transducer normal depends only on the uncertainty in the tilt and rotation angles.

By using the material in Appendix B to compute the effect that the uncertainty in speed of sound and orientation of the tissue layer boundaries has on the uncertainty in the boundary point locations and combining this uncertainty linearly with the uncertainty in the boundary point locations generated by the uncertainty in the transducer location and normal, we can compute an upper bound on the total uncertainty. The solid lines in figures 3.37, 3.38 and 3.39 show this upper bound as a function of layer thickness for extreme conditions (the “worst-case scenario”), while the dotted lines show this upper bound for more realistic conditions and constitute our best estimate of the upper bound on the measurement error. The extreme and moderate conditions are the same as those in the

preceeding section. The extreme conditions assume no limit on the orientation of the tissue layer boundaries and a variation in the speed of sound of up to 100 m/s from its textbook value. The more moderate conditions limit the orientation of the tissue layer boundaries so that the angle of incidence the pulse makes with the boundary is no more than 10 degrees and that the speed of sound lies within 50 m/s of its textbook value. If the uncertainties seem large for thin tissue layers, it is because these are upper bounds.

3.4.4 Accuracy Of Bulk Tissue Thickness Measurements

The accuracy of the bulk tissue thickness measurements is affected by the ability to accurately compute the position and orientation of the pelvis. The accuracy in the bulk volume measurements will be proportional to this value. Because the accuracy of the manual registration algorithm is unknown, the accuracy of the bulk thickness measurements is likewise unknown. For this reason, the reader should treat the bulk thickness measurements reported in this thesis and any conclusions drawn from them with caution until a future study with improvements made to the data acquisition process that guarantee accurate registration can be conducted to validate those conclusions.

3.5 Conclusion

In this chapter, we developed a procedure that uses the computer automated seating system developed at the University of Pittsburgh by David Brienza and Jue Wang to directly measure both the position and orientation of the pelvis and the thickness and shape of the soft tissues of the buttocks for a seated subject. We also analyzed the accuracy of the measurements computed by the system and found them to be of sufficient accuracy for this task. Until now, direct measurements of pelvic position, pelvic orientation and soft tissue shape have not been possible. Researchers who wanted to study the relationship between soft tissue distortion and pressure ulcer formation previously had to make do with finite element models or indirect measurements of soft tissue shape. The development of this procedure represents a significant step forward in understanding the development of pressure ulcers.

Because this procedure is still in the prototype stage, it must still be demonstrated to yield data and results that are meaningful to researchers seeking to understand pressure ulcer development. For this reason, we conducted a small pilot study to validate the procedure developed in this chapter and to demonstrate its usefulness. That study and its results are the subject of the next chapter.

Chapter 4
Pilot Study

4.1 Introduction

In the previous chapter, we developed a system that allows us to measure and visualize how the soft tissues of the buttocks of a human subject deform as the subject sits on seating surfaces of different shapes. The seating surface is instrumented with pressure and ultrasonic sensors and its shape can be varied under computer control, allowing us to explore how those changes in soft tissue shape relate to the shape of the seating contour or the interface pressure between the seat and the buttocks. In this chapter, we report the results of a small pilot study on three human subjects - two able-bodied and one paraplegic with spinal cord injury - to demonstrate the usefulness of that system. Each subject in the study sat on two different seating contours, one flat and the other custom-designed to equalize the pressure across the buttocks. For each contour, data were collected and analyzed using the procedures described in chapter 3 to measure:

- The position and orientation of the subject's pelvis with respect to the seating surface
- The thickness and volume of the bulk soft tissue beneath the pelvis
- The shape and thickness of the skin, fat and first muscle layer in right buttock in the vicinity of the ischial tuberosity

Relationships between these values and the seating contour shape and interface pressure were explored, and comparisons of these values both between contours for the same subject and between subjects for the same contour were made. Although the small size of the study and the potentially large registration errors prevent us from generalizing its conclusions to the populations of healthy subjects and those with spinal cord injury at large, its results do suggest some interesting directions for future research as well as improvements that could be made to the current procedure. The most important potential discoveries suggested by the pilot study are:

(1) When seated on a pressure-equalized contour, the orientation of the pelvis aligns it with the seating contour, whereas when seated on a flat contour, the orientation of the pelvis may have a large tilt or roll.

(2) The distribution of soft tissue beneath the left and right halves of the body is not symmetric, and the two sides did not respond in the same manner as the contour changed from the flat shape to the pressure-equalized shape.

(3) There was no obvious difference between the healthy subjects and the subject with spinal-cord injury in way the pelvis moved or the soft tissues changed shape as the contour changed from its flat shape to its pressure-equalized shape.

Current models for the behavior of the soft tissues of the buttocks when seated on a surface of a particular shape treat the pelvis as a rigid cylindrical core with a spherical cap suspended in elastic or viscoelastic goo that bears the weight of the upper body and is free to move up and down under the influence of gravity. However, these models cannot account by themselves for the asymmetry in response between the left and right halves of the buttocks noted in point (2), since the measurements made in the pilot study tend to rule out a difference in mechanical properties between the two sides of the buttocks. Likewise, because earlier studies strongly suggest that the mechanical properties of the soft tissues of subjects with spinal-cord injury differ from those of healthy subjects, these current models cannot explain point (3) either. While points (2) and (3) may simply be the result of the small subject population used in the pilot study or the potentially large errors in the manual registration process described in section 3.4.1, future studies can be designed to rule these causes out. Should such improvements validate the results of this pilot study, then the current, simple models of the interaction between the pelvis and the soft tissues of the buttocks will need to be extended, possibly to take into account the interaction between the pelvis and the femurs or the pelvis and the spine.

We begin this chapter by describing the experimental methodology of the study and the subjects that took part in it. We then present the results for each subject separately and make comparisons between the flat and equalized contour. Then we discuss the similarties and differences in the response of the pelvis and the soft tissues between the three subjects when exposed to the flat and pressure-equalized seating contours. This is followed by a comparison of our results with those published in the current literature. Finally, we draw conclusions about the usefulness of the system as a whole, enumerate the contributions made by this thesis, and describe how others may build upon our work in the future.

4.2 Methods

4.2.1 Subjects

Three subjects took part in the pilot study. Subjects #1 and #2 were healthy, able-bodied men aged 40 and 35 respectively. Subject #3 was a paraplegic man of age 62 with a spinal cord injury at the 9th thorasic veritbrae. It has been more than 20 years since he was injured. Subjects #1 and #2 weigh about 74 and 77 kg respectively, while subject #3 is a bit heavier at about 90kg. The MRI scans of subject #3's pelvis reveal that he has quite a bit more body fat than subjects #1 and #2.

To be inlcuded in the study, subject #3 had to meet the following criteria:

- Be male between the ages of 20 and 64
- Have a spinal cord injury with lesions between the fourth cervical and twelth thorasic vertebrae.
- Suffer from paraplegia with little or no injury below the waist
- Be free of sitting-induced pressure ulcers for at least one month prior to the study
- Be medically stable with no active illnesses
- Be at least one year from the onset of the spinal cord injury, so that his body and tissues will be in a medically stable condition.

4.2.2 Procedure

After informed consent was obtained, the following procedure was performed on each subject to acquire data:

(1) An MRI scan in the transverse plane of the body was performed on the subject's pelvis, starting just above the ilium and finishing approximately 1-2 cm beneath the ischial tuberosities, as described in chapter 3, section 3.3.1.

(2) The Computer-Automated Seating System was prepared and calibrated as described in chapter 3, section 3.3.1. The initial locations of the ultrasonic transducers were measured using the position wand.

(3) The subject was seated on a flat contour and interface pressures, ultrasound echoes and registration points were recorded using the procedure described in chapter 3, section 3.3.1.

(4) The actuators of the CASS were moved to form a custom seating contour for the subject that distributed the pressure evenly across the buttocks through the following algorithm:

(4a) Find the actuator with the highest pressure. If this describes more than one actuator, use the one whose motor number <u,v> has the lower value for "v." If this still describes more than one actuator, use the one with the lowest value for "u." Consider only actuators with a pressure equal to or greater than 10 mmHg, as actuators with pressures less than this value tend to have no contact or only incidental contact with the subject's body. If no actuator has a pressure equal to or greater than 10 mmHg, terminate.

(4b) Move the actuator found in step (4a) down 0.5 mm.

(4c) Repeat steps (4a) and (4b) until among all actuators with a pressure greater than or equal to 10 mmHg, the difference between the highest and lowest pressure is equal to or less than 25 mmHg for at least five iterations. This is the contour that equalizes pressure across the buttocks of the subject. The tolerance of 25 mmHg was chosen as a compromise between equalizing the pressure distribution over the buttocks and having an acceptable running time for the equalization algorithm.

The algorithm is allowed to proceed for a maximum of 10,000 iterations before terminating without convergence. In this case, the resulting contour would be considered an approximation to the equalized contour and used in place of the equalized contour for the remainder of the study. However, the algorithm converged for all three subjects, so use of an approximate contour was not necessary.

(5) The contour shape, interface pressures, ultrasound echoes and registration points measurements were recorded for the equalized contour, again following the procedure described in chapter 3, section .

(6) The subject was unloaded from the CASS and the final locations of the ultrasonic transducers were recorded. The difference between the initial and final locations of the ultrasonic transducers gives an indication of how much rotation

about the normal to the actuator surface occurred during the procedure. As described in section 3.1.2, the orientation sensors cannot measure this rotation about the actuator surface normal, and so it becomes a source of error in the calcuation of the locations of the ultrasonic transducers during the experimental procedure. By measuring the difference between the initial and final locations of the transducers, we can quantify the magnitude of this error.

4.2.3 Analysis

Data acquired for each subject and contour is analyzed off-line using the procedure described in chapter 3, section 3.3.2 to obtain the following values:

- The position and orientation of the subject's pelvis
- The thickness and volume of the bulk tissue beneath the pelvis
- The thickness of the skin, the fat, and the first muscle layer above each of the 32 ultrasound transducers beneath the subject's right buttock

We also calculate the thickness of bulk tissue above each pressure sensor that falls beneath the pelvis and check whether there is a correlation between interface pressure and that thickness. We also test to see if interface pressure for the flat contour can predict absolute bulk thickness, the change in bulk thickness, or the depth of the equalized contour.

We summarize the thickness measurements for bulk tissue by reporting minimum, maximum, mean and standard deviation values for the entire pelvis. We do the same for the individual soft tissue layers in the right buttock. However, because the pelvis covers such a large area above the CASS, reporting these statistics over the whole pelvis can disguise important trends. For example, soft tissue volume beneath the pelvis as a whole might decrease slightly in going from the flat to the equalized contour, but still increase beneath the ischial tuberosities. Consequently, we divide the area beneath the pelvis into eight regions and report statistics for each individual region in addition to the statistics for the pelvis as a whole. These regions are:

Beneath The Ischial Tuberosities: This region includes all the tissue that falls beneath either the left or right ischial tuberosity plus a small portion of the descending pubic ramus. The areas beneath the left and right tuberosities are treated as two separate regions. Because sitting-induced pressure ulcers commonly occur beneath the ischial tuberosity, we focus our analysis on the behavior of the soft tissue in these regions. For this reason, the remaining regions are defined by their relation to the ischial tuberosities.

Behind The Ischial Tuberosities: Each of this pair of regions includes all the tissue that falls beneath the pelvis and behind the plane that touches the back of the ischial tuberosity and runs parallel to the x-axis of the pelvis. The areas behind the left and right tuberosities are separate regions the plane that defines each region is defined with respect to the appropriate tuberosity. For the most part, these regions are occupied by the gluteus maximus muscles.

Beside The Ischial Tuberosities: These regions include all the tissue that falls beneath the pelvis either to the left of the left ischial tuberosity or to the right of the right tuberosity, with the left and right sides being considered separate regions. It

does not include any tissue that falls behind the ischial tuberosities.

In Front Of The Ischial Tuberosities: These regions include all the tissue that falls more-or-less directly in front of the ischial tuberosity on either side, with the left and right sides being considered separate regions, that does not belong to any other region. Since only a small part of the descending pubic ramus is contained within these regions, the bulk tissue thickness measurements are generally not of interest. However, because the first muscle layer in this region is likely to be the biceps femoris or semitendinosus muscles, as opposed to the gluteus maximus muscle found in the other six regions, it is useful for our analysis to segregate the thickness measurements of the individual tissue layers in this region from the other regions.

These regions do not cover the entire space beneath the pelvis. In particular, there are areas beneath the descending pubic ramii on either side of the pubic tubercle that do not belong to any region. Since the tissue in this region falls on the inside of the thigh, occupies a relatively small part of the surface area beneath the pelvis, and pressure ulcers do not normally occur here, the behavior of the bulk tissue in this region is not interesting and we do not report statistics for it as a separate region.

4.3 Results

In this section, we report the results of our study for each of the subjects individually and analyze the changes that occur as the subject moves from a flat to an equalized contour. The large volume of tabular data is captured by six color images that illustrate the pelvis and soft tissue layers from several different angles. To better enable comparisons between the flat and equalized contours, pictures generated from the same viewpoint for the flat and equalized contour are shown on facing pages, with the flat contour on the left and the equalized contour on the right. With the exception of some small figures, the tables and images for each subject are presented at the end of the analysis for that subject. Following the analysis for the individual subjects is a comparison between the three subjects of the behavior of their pelvises and soft tissues.

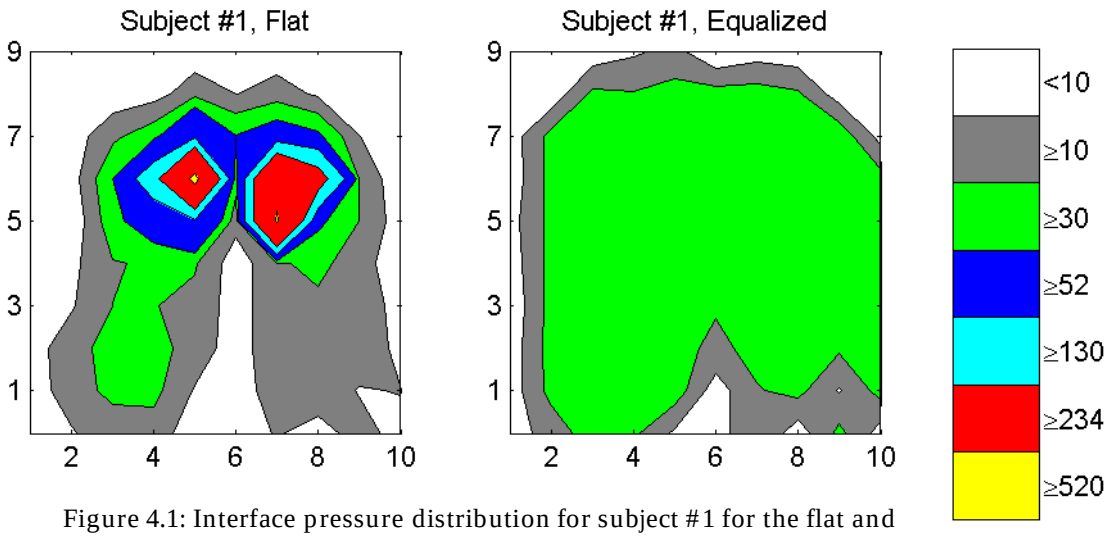

Figure 4.1: Interface pressure distribution for subject #1 for the flat and pressure-equalized contours.

4.3.1 Subject #1

The statistics in table 4.1 describe the flat and equalized contours and their respective interface pressures. Statistics are provided both for the entire contour and separately for the left and right sides. Figure 4.1 illustrates the pressure distribution for both contours graphically. The equalized contour for subject #1 is quite deep and its left and right halves are symmetric. Peak pressure is someone higher on the right side than on the left, but the high pressure zone on the left side is larger than the zone on the right, resulting in a higher mean pressure. The difference between the minimum and maximum pressure for the equalized contour is slightly higher than the 25 mmHg needed for the equalization algorithm to converge. This discrepancy occurred because there is a delay between the termination of the equalization algorithm and the measurement of the interface pressure for the equalized contour during which the registration points were measured. Unavoidable shifts that occurred during this period increased the peak pressure for the equalized contour slightly. It took approximately 3000 iterations for the equalization algorithm to converge.

As shown in table 4.2, the pelvis of subject #1 moves a considerable distance - more than 60 mm - in between the flat and equalized contours. Most of this movement is downwards and matches the change in maximum contour depth from 0 to 64 mm. His pelvis also assumes a more neutral orientation with respect to the CASS surface when subject #1 is seated on the pressure equalized contour than when he is seated on the flat contour. Subject #1's pelvis has a large roll of 12.5 degrees and a moderate downward pitch of -6 degrees when the surface of the CASS is flat, which diminish to 6 and -1.3 degrees when the surface assumes its pressure-equalized shape.

Table 4.4 summarizes the thickness of bulk tissue beneath the pelvis for the flat and equalized contours, both for the whole pelvis and broken down by region, while table 4.3 shows the volume. Both the mean bulk tissue thickness and volume decrease when moving from the flat contour to the equalized one and the tissue distribution becomes

more uniform, as shown by the decrease in standard deviation for the bulk tissue thickness. Surface area beneath the pelvis, which is proportional to the number of thickness measurements[1], changes only slightly between the two contours. Provided that this decrease in thickness and volume is not the result of measurement error, the overall decrease in thickness and volume shows a redistribution of soft tissue from underneath the pelvis. From an examination of the portion of the seating contour that does not fall beneath the pelvis, this redistribution is probably towards the legs, but without the ability to measure bulk tissue volume in this region we cannot be sure.

The change in the thicknesses of the individual layers beneath the right buttock shown in table 4.5 follows the expected pattern. The skin layer does not change thickness very much, while the thicknesses of the fat and first muscle layer increase. Although this may appear to contradict the findings in the previous paragraph, the increase in the thickness of the fat layer is slight (~1.7 mm), albeit significant at the $p<0.0005$ level, while the increase in the muscle layer is not significant ($p<0.08$). The difference in significance levels arises from the difficulty in resolving the boundary between the first and second muscle layers for the equalized contour; this boundary could be resolved above only 16 transducers for the equalized contour, as opposed to 23 transducers for the flat contour. Furthermore, the measurements for the deeper muscle layers indicate a significant decrease in thickness that is consistent with the decrease in bulk tissue thickness across the entire pelvis.

The decrease in bulk tissue thickness and volume is not uniform among all the regions beneath the pelvis. The minimum, mean and maximum bulk tissue thickness beneath the right ischial tuberosity both increase, with the minimum thickness increasing by more than 14 mm and the maximum increasing by more than 17 mm. Bulk tissue volume remains about the same, but this is probably either an artefact of the decrease in the number of measurements beneath the right ischial tuberosity between the flat and equalized contours[2], which corresponds to a reduction in surface area of about 2.8 cm^2. Since a corresponding change does not occur beneath the left ischial tuberosity, this decrease is probably not the result of the change in the orientation of the pelvis but is more likely the result of an imperfect manual segmentation. If the number of measurements beneath the right ischial tuberosity had remained constant at 390, the volume of bulk tissue in this

1. As described in section 3.3.2.4, bulk tissue thickness is computed by measuring the distance between the pelvis and the seating surface along the z-axis of the CASS coordinate system at regularly-spaced intervals. Since the total volume of bulk tissue beneath the pelvis is equal to the sum of the rectangular columns of tissue at each of these sampling points, and the cross-section of each column is a 2 mm by 2 mm square, the volume of bulk tissue beneath the pelvis will be proportional to the number of grid points (aka the “number of measurements”) that fall beneath the pelvis.
2. Both the change in orientation of the pelvis and unavoidable variation in the placement of boundaries between the different regions beneath the pelvis (e.g. the boundaries that separate the region beneath the right ischial tuberosity from the region behind it) between the flat and equalized contours can produce changes in the number of bulk tissue thickness measurements that fall within a particular region. Since bulk tissue volume is proportional to the number of measurements, a change in bulk tissue volume within a region may correspond either to a genuine shift in the amount of tissue within that region or a shift in the boundaries. Careful analysis is needed to distinguish between the two cases.

region would have increased by 12.2 cm^3, a relative increase of 20.6%. This increase is more consistant with the increase in minimum, maximum and mean thickness beneath the right ischial tuberosity than the volume remaining constant.

A different and unexpected pattern occurs beneath the left ischial tuberosity. Here, the minimum bulk tissue thickness *decreases* significantly, while the mean thickness, maximum thickness and volume decrease only slightly. Since presumably the body is trying to relieve the very high pressure that occurs in this region when sitting on the flat contour, one would expect the tissue to increase in thickness, not decrease. This decrease in bulk tissue thickness and volume can be attributed to the large roll of the pelvis that occurs when subject #1 is seated on the flat contour. Because of this roll, the left side of the pelvis starts with a considerable amount of tissue beneath it that decreases as the roll goes away during the movement to the equalized contour.

However, what cannot be explained at present is the fact that the mean thickness of bulk tissue beneath the left ischial tuberosity decreases only slightly while the pressure in this region decreases all the way from 533 mmHg to 43 mmHg. If the body redistributes pressure by moving the pelvis from above areas with thinner tissue to regions with thicker tissue, or by shifting tissue from low-pressure areas to high-pressure areas, then we would expect to see an *increase* in bulk tissue thickness beneath the left ischial tuberosity as subject #1 goes from the flat to the equalized contour, just as we observed with the tissue beneath the right ischial tuberosity. The simplest explanation is that the large roll in subject #1's pelvis is the result of an error in measuring the orientation of subject #1's pelvis. In this case, the roll is not quite as large as we have reported and the tissue beneath the left ischial tuberosity thickens between the flat and equalized contours as we would expect. However, if the measurement of the roll in subject #1's pelvis when seated on the flat contour is accurate, this decrease in bulk thickness cannot be explained as the result of , the body is relieving pressure through a mechanism whose behavior we did not measure, such as by shifting the center of gravity of the upper torso or by changing the composition of the soft tissues in this region (e.g. substituting fat for muscle or changing which muscles bear the load of the pelvis) without changing the overall thickness of tissue. The lack of ultrasonic sensors in this area prevents us from obtaining a clearer picture.

In any case, this behavior of the tissue beneath the left ischial tuberosity illustrates in a dramatic fashion a principle that we will observe for all three subjects: *provided that the position and orientation measurements of the pelvis are accurate, there is no correlation between interface pressure at some point on the buttocks and the thickness of soft tissue above that point*. To test this principle, we computed for subject #1 the mean thickness of bulk tissue above the 16 pressure sensors that fall beneath the pelvis for the flat contour and the 18 pressure sensors that fall beneath the equalized contour and computed correlation coefficients between the bulk tissue thickness and the interface pressure. In neither case was a statistically significant correlation found. Furthermore, interface pressure for the flat contour did not predict bulk tissue thickness for the equalized contour, nor did it predict the change in bulk tissue thickness or the depth of the seating contour for the actuator the pressure sensor was attached to.

Behind the left and right ischial tuberosities, we see a different pattern. Mean bulk tissue thickness behind both ischial tuberosities decreases significantly. Bulk tissue volume behind the right ischial tuberosity decreases significantly by 18.5% while volume behind the left ischial tuberosity increases slightly by 1.3%. However, the surface area behind the left ischial tuberosity increases by more than 40% as the 12.5 degree roll to the right side disappears. Since the minimum, maximum and mean thickness of bulk tissue in this region all decrease as the contour moves from the flat to the equalized condition, this increase in surface area is probably disguising a net decrease in bulk tissue volume.

If the measurements of the position and orientation of subject #1's pelvis are accurate, the decrease in bulk tissue volume and thickness behind the ischial tuberosities and increase beneath them probably indicates a shift of tissue as the contour changes from flat to equalized. An examination of the individual thickness measurements supports this hypothesis. An examination of table 4.5 shows that while the thickness of the skin layer remains relatively constant, the fat and first muscle layers increase in mean thickness beneath the right ischial tuberosity by approximately 4.8 mm and 9.5 mm respectively. In contrast, while the thickness of the fat layer behind the right ischial tuberosity increases by about 2 mm, the thickness of the first muscle layer decreases by about 7.5 mm. Since the first muscle layer in both of these regions is almost certainly the gluteus maximus, these measurements suggest that pressure relief is achieved in part by shifting more fat beneath the pelvis and shifting more of the gluteus maximus from behind the ischial tuberosity to beneath it. The system was not able to resolve the other muscle layers beneath the ischial tuberosity, so we cannot ascertain how much of the load imposed by the pelvis is being borne by the gluteus maximus and how much by the other muscles.

Table 4.1: Contour Depth And Interface Pressure For Subject #1

	Minimum		Mean		Maximum	
	Flat	Eq	Flat	Eq	Flat	Eq
Contour Depth (mm)	0.0	0.0	0.0	17.3	0.0	64.5
Right Side	0.0	0.0	0.0	23.2	0.0	64.5
Left Side	0.0	0.0	0.0	17.3	0.0	58.5
Interface Pressure (mmHg)	10.3	16.6	71.1	35.8	571.0	43.5
Right Side	19.5	16.6	67.0	35.9	571.0	43.5
Left Side	10.3	28.5	79.6	36.5	533.0	43.4

Table 4.2: Position And Orientation Of Pelvis For Subject #1

Contour	Position (mm)			Orientation (degrees)		
	X	Y	Z	Pitch	Roll	Yaw
Flat	268.9	276.4	126.4	-6.39	12.53	-1.84
Equalized	249.4	288.7	69.1	-1.27	6.02	2.56
Change	-19.5	12.3	-57.3	5.12	-6.51	4.40

Table 4.3: Bulk Tissue Volume For Subject #1

Region		Flat	Equalized	% Change
Whole Pelvis		2643.3	2175.0	-17.7
Beneath Ischial Tuberosity	Right	59.1	58.8	-0.4
	Left	56.7	53.6	-5.4
Behind Ischial Tuberosity	Right	950.8	775.2	-18.5
	Left	715.6	724.9	1.3
Beside Ischial Tuberosity	Right	331.3	178.8	-46.0
	Left	207.3	167.8	-19.0
In Front Of Ischial Tuberosity	Right	63.7	19.3	-69.7
	Left	46.4	26.3	-43.3

Table 4.4: Bulk Tissue Thickness For Subject #1

Side	Contour	N	Min	Mean	StdDev	Max
Whole Pelvis						
N/A	Flat	5300	8.8	124.7	50.3	220.0
	Equalized	5341	15.5	101.8	37.7	180.5
	(% Change)	0.8	76.1	-18.4	-25.0	-18.0
Beneath Ischial Tuberosity						
Right	Flat	390	8.71	37.9	28.6	107.8
	Equalized	322	22.9	45.6	27.6	124.9
	(% Change)	-17.4	162.9	20.3	-3.5	15.9
Left	Flat	293	24.5	48.4	31.6	133.1
	Equalized	302	15.5	44.4	28.6	127.5
	(% Change)	3.1	-36.7	-8.3	-9.5	-4.2
Behind Ischial Tuberosity						
Right	Flat	1638	58.1	145.1	25.6	145.1
	Equalized	1790	55.2	108.3	23.2	156.9
	(% Change)	9.3	-5.0	-25.4	-9.4	8.1
Left	Flat	1092	69.3	163.8	33.9	220.0
	Equalized	1545	60.2	117.3	25.8	117.4
	(% Change)	41.5	-13.1	-39.6	-23.9	-46.6
Left of Left Ischial Tuberosity or Right of Right Ischial Tuberosity						
Right	Flat	655	62.5	126.5	29.5	177.4
	Equalized	351	51.7	127.4	27.1	169.8
	(% Change)	-46.4	-17.3	0.7	-8.1	-4.3
Left	Flat	323	49.8	160.4	41.6	218.0
	Equalized	311	50.8	134.9	27.7	180.5
	(% Change)	3.9	2.0	-15.9	-33.4	-17.2
In Front Of Ischial Tuberosity						
Right	Flat	172	81.6	92.6	4.5	92.6
	Equalized	46	96.5	104.8	6.4	119.8
	(% Change)	-73.3	18.3	13.2	42.2	29.4
Left	Flat	102	100.5	113.8	9.9	132.2
	Equalized	60	100.2	109.7	6.5	124.9
	(% Change)	-41.2	-0.3	-3.6	-34.3	-5.5

Table 4.5: Thickness Of Individual Tissue Layers For Subject #1

Tissue Layer	Contour	N	Min	Mean	StdDev	Max
Entire Right Buttock						
Skin	Flat	32	1.56	2.67	0.46	3.35
	Equalized	32	1.84	2.56	0.42	3.45
	(% Change)	0	17.95	-3.99	-8.76	2.86
Fat	Flat	31	0.00	2.32	1.37	5.61
	Equalized	30	0.91	4.01	2.34	11.1
	(% Change)	-3.23	N/A	73.32	69.97	97.8
First Muscle Layer	Flat	23	2.88	10.90	10.50	45.24
	Equalized	16	5.07	15.67	10.28	40.30
	(% Change)	-30.43	75.89	43.76	-2.1	-10.93
Remaining Muscle	Flat	8	70.56	102.55	28.07	146.40
	Equalized	8	15.74	39.16	31.06	111.78
	(% Change)	0	-77.70	-61.82	10.63	-23.65
Beneath Right Ischial Tuberosity						
Skin	Flat	2	2.70	2.90	0.28	3.10
	Equalized	8	1.89	2.48	0.41	3.10
	(% Change)	300.00	-29.97	-14.30	43.78	0
Fat	Flat	2	0.00	0.30	0.42	0.60
	Equalized	8	0.91	5.16	2.60	7.89
	(% Change)	300.00	27.27	1634.76	518.45	1226.83
First Muscle Layer	Flat	2	4.48	5.42	1.34	6.37
	Equalized	2	14.53	14.97	0.63	15.42
	(% Change)	0	224.34	176.11	-52.72	142.18
Remaining Muscle	Flat	0	N/A	N/A	N/A	N/A
	Equalized	3	15.74	21.24	6.60	28.55
	(% Change)	N/A	N/A	N/A	N/A	N/A
Behind Right Ischial Tuberosity						
Skin	Flat	10	1.56	2.45	0.53	3.14
	Equalized	8	2.00	2.41	0.33	2.94
	(% Change)	-20.00	28.21	-1.77	-38.20	-6.36
Fat	Flat	10	1.44	3.19	1.53	5.61
	Equalized	6	1.83	5.05	3.48	11.1
	(% Change)	-40.00	27.27	58.48	126.77	97.80

Table 4.5: Thickness Of Individual Tissue Layers For Subject #1

Tissue Layer	Contour	N	Min	Mean	StdDev	Max
First Muscle Layer	Flat	3	28.46	36.09	8.50	45.24
	Equalized	4	13.23	28.55	12.78	40.30
	(% Change)	33.33	-53.50	-20.91	50.36	-10.93
Remaining Muscle	Flat	7	70.56	105.16	29.27	146.40
	Equalized	4	21.42	54.38	39.69	111.78
	(% Change)	-42.86	-69.64	-48.28	35.62	-23.65
To The Right Of The Right Ischial Tuberosity						
Skin	Flat	16	1.94	2.80	0.45	3.35
	Equalized	14	1.84	2.72	0.47	3.45
	(% Change)	-12.50	-4.96	-2.88	3.67	2.86
Fat	Flat	16	1.05	2.20	0.93	4.25
	Equalized	14	1.05	2.92	1.13	5.07
	(% Change)	-12.50	0	32.76	21.98	19.28
First Muscle Layer	Flat	15	2.88	7.21	2.36	11.97
	Equalized	9	5.07	11.12	4.49	17.51
	(% Change)	-40.00	75.89	54.33	90.58	46.33
Remaining Muscle	Flat	0	N/A	N/A	N/A	N/A
	Equalized	0	N/A	N/A	N/A	N/A
	(% Change)	N/A	N/A	N/A	N/A	N/A
In Front Of The Right Ischial Tuberosity						
Skin	Flat	4	2.44	2.54	0.10	2.65
	Equalized	2	2.18	2.34	0.22	2.50
	(% Change)	-50.00	-10.49	-7.95	132.31	-5.74
Fat	Flat	3	0.00	1.36	1.37	2.73
	Equalized	2	3.71	3.95	0.35	4.20
	(% Change)	-33.33	27.27	190.41	-74.49	53.58
First Muscle Layer	Flat	3	6.89	7.85	1.56	9.65
	Equalized	1	6.57	6.57	0.00	6.57
	(% Change)	-66.67	-4.70	-16.40	-100.00	-6.42
Remaining Muscle	Flat	1	84.34	84.34	0.00	84.34
	Equalized	1	32.04	32.04	0.00	32.04
	(% Change)	0	-62.01	-62.01	N/A	-62.01

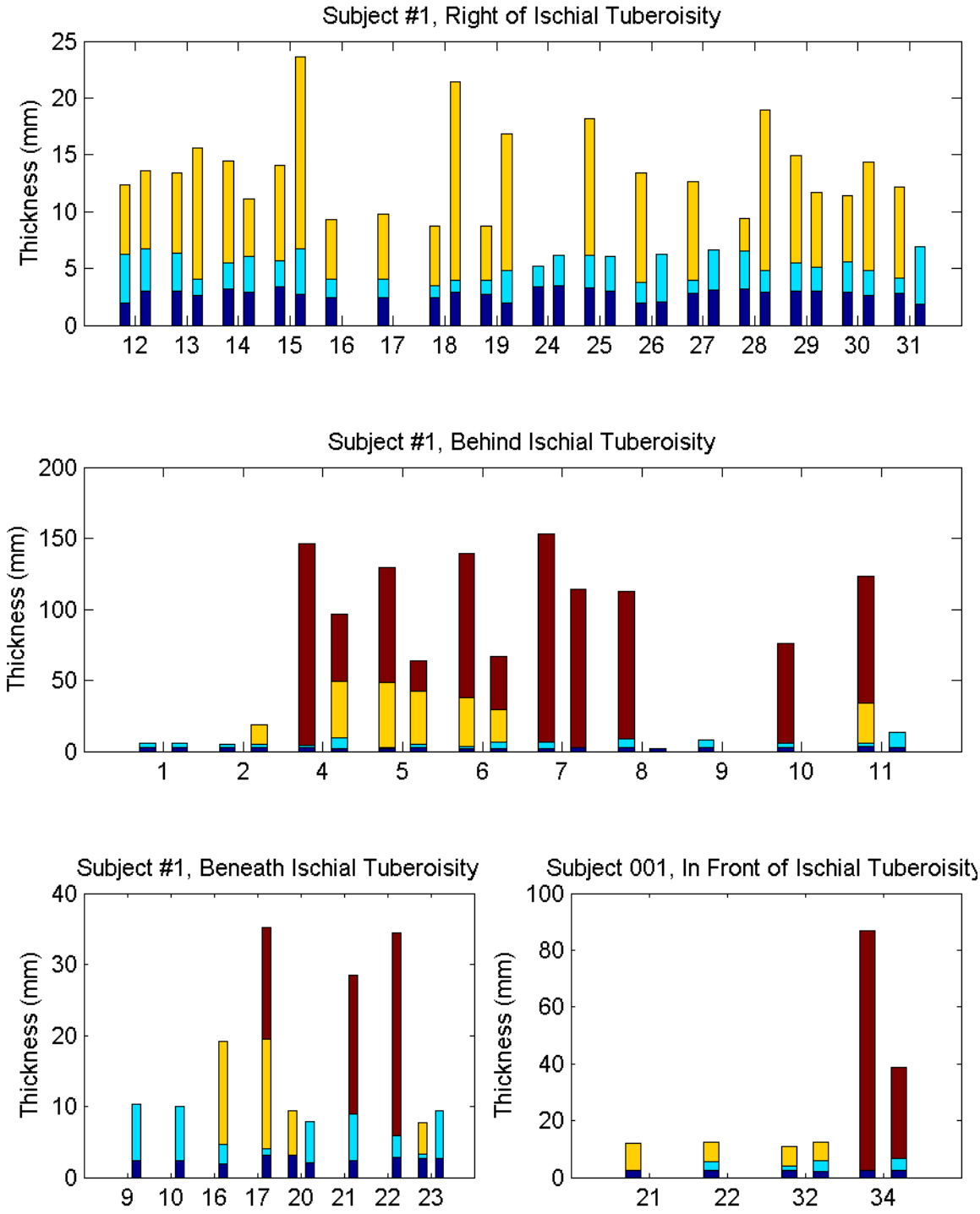

Figure 4.2: Thickness of skin(blue), fat(aqua) and the first muscle layer (yellow) broken down by region for both the flat and equalized contours. Bulk tissue between the last resolved layer and the pelvis is shown by brown bars. Numbers along the x-axis indicate the sensor where the measurements were taken. Each number has two bars associated with it; the bar on the left measures thickness for the flat contour, while the bar on the right measures thickness for the equalized contour. A missing bar indicates that no measurements were available for that combination of sensor and contour.

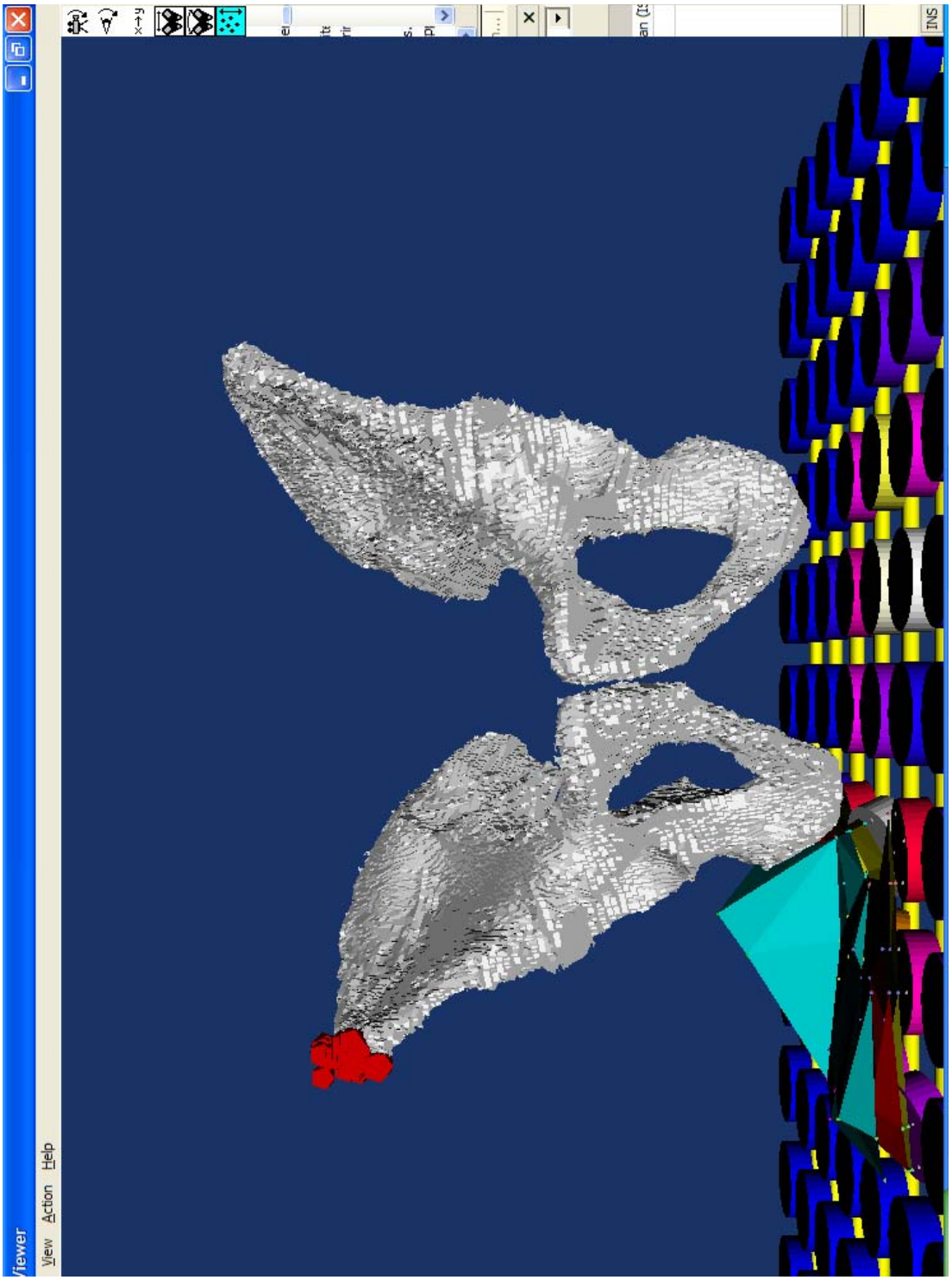

Figure 4.3: Front view of subject #1, flat contour.

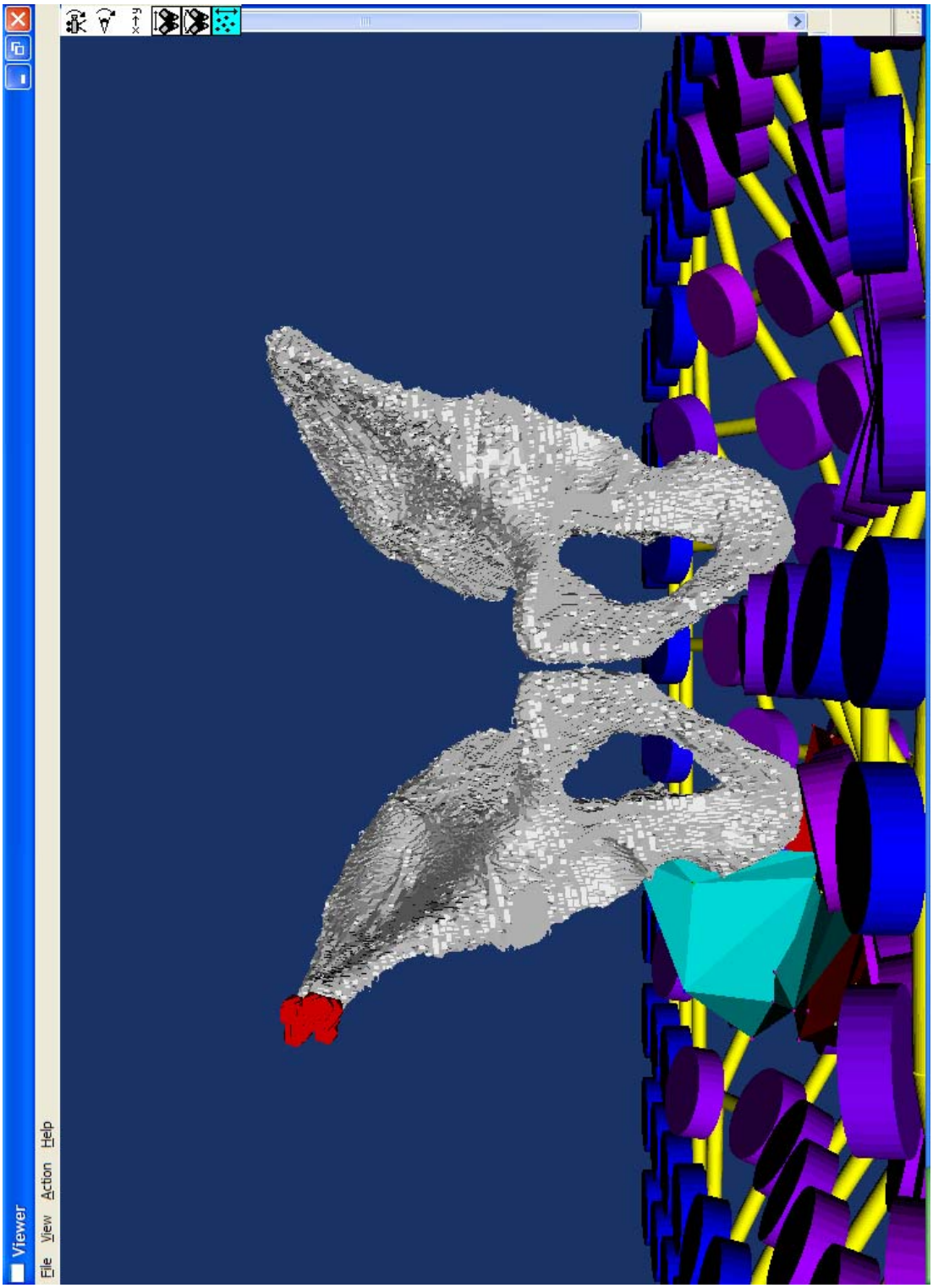

Figure 4.4: Front view of subject #1, equalized contour.

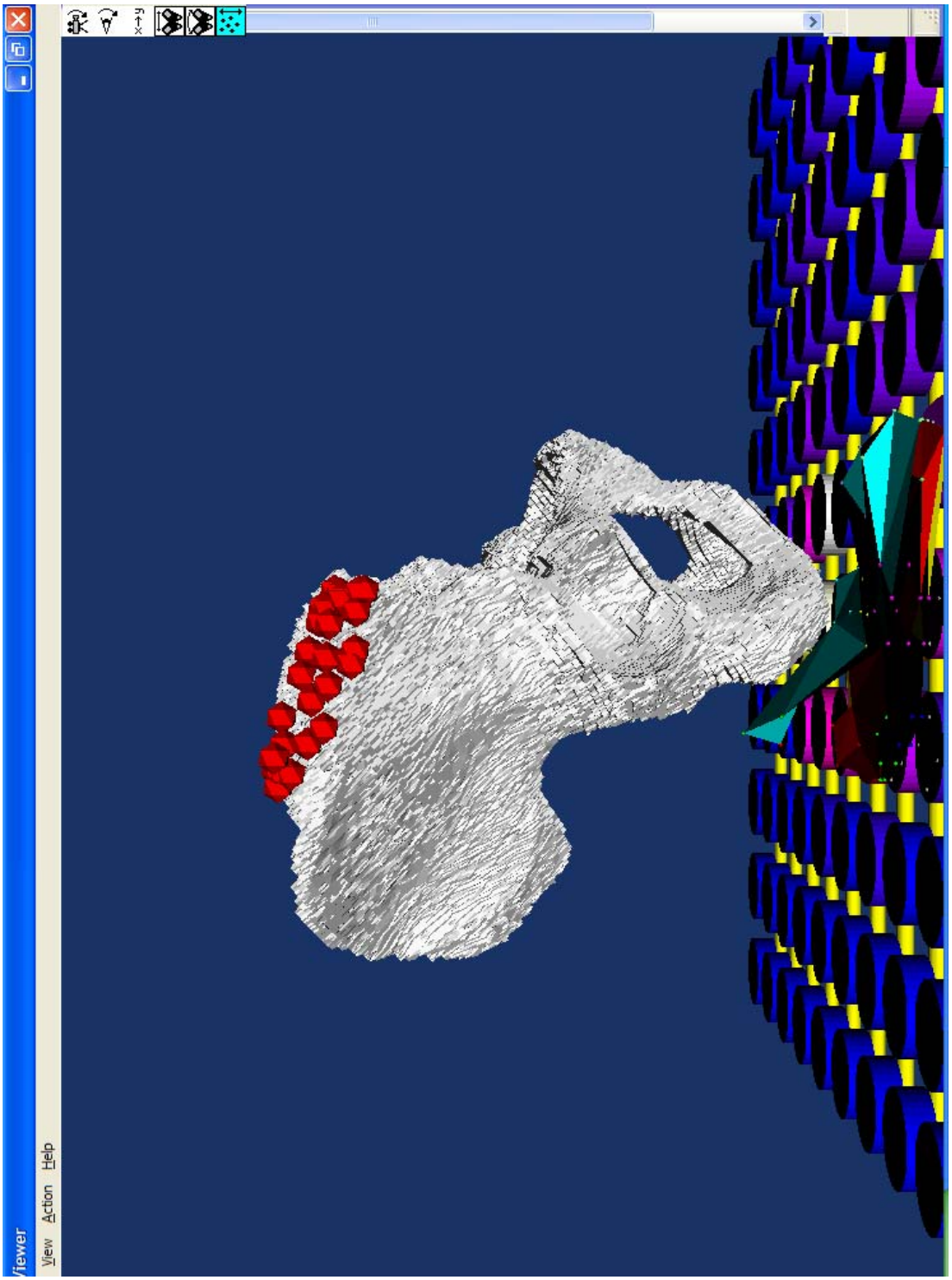

Figure 4.5: Side view of subject #1, flat contour.

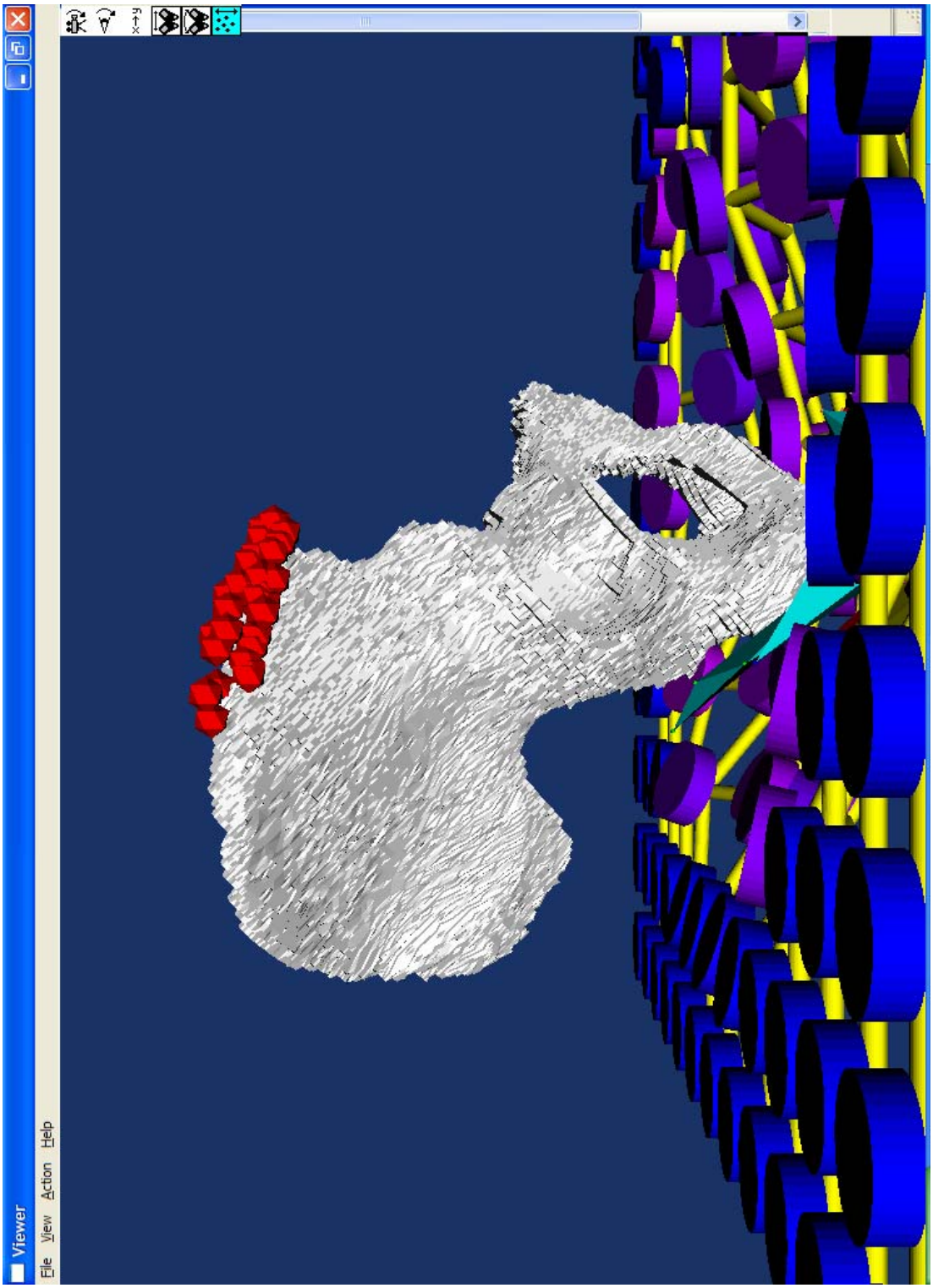

Figure 4.6: Side view of subject # 1, equalized contour.

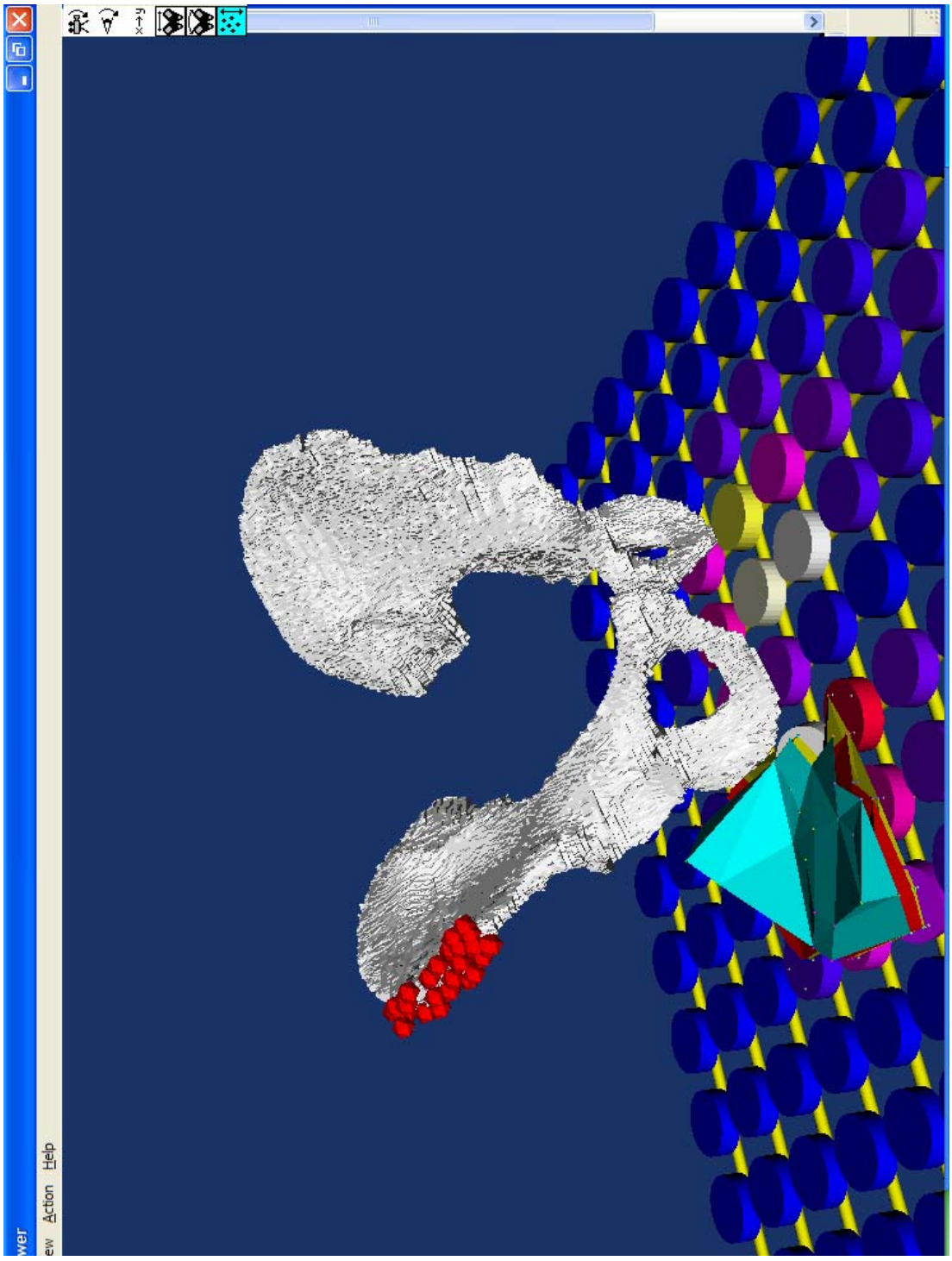

Figure 4.7: View of subject #1, flat contour from the right front corner.

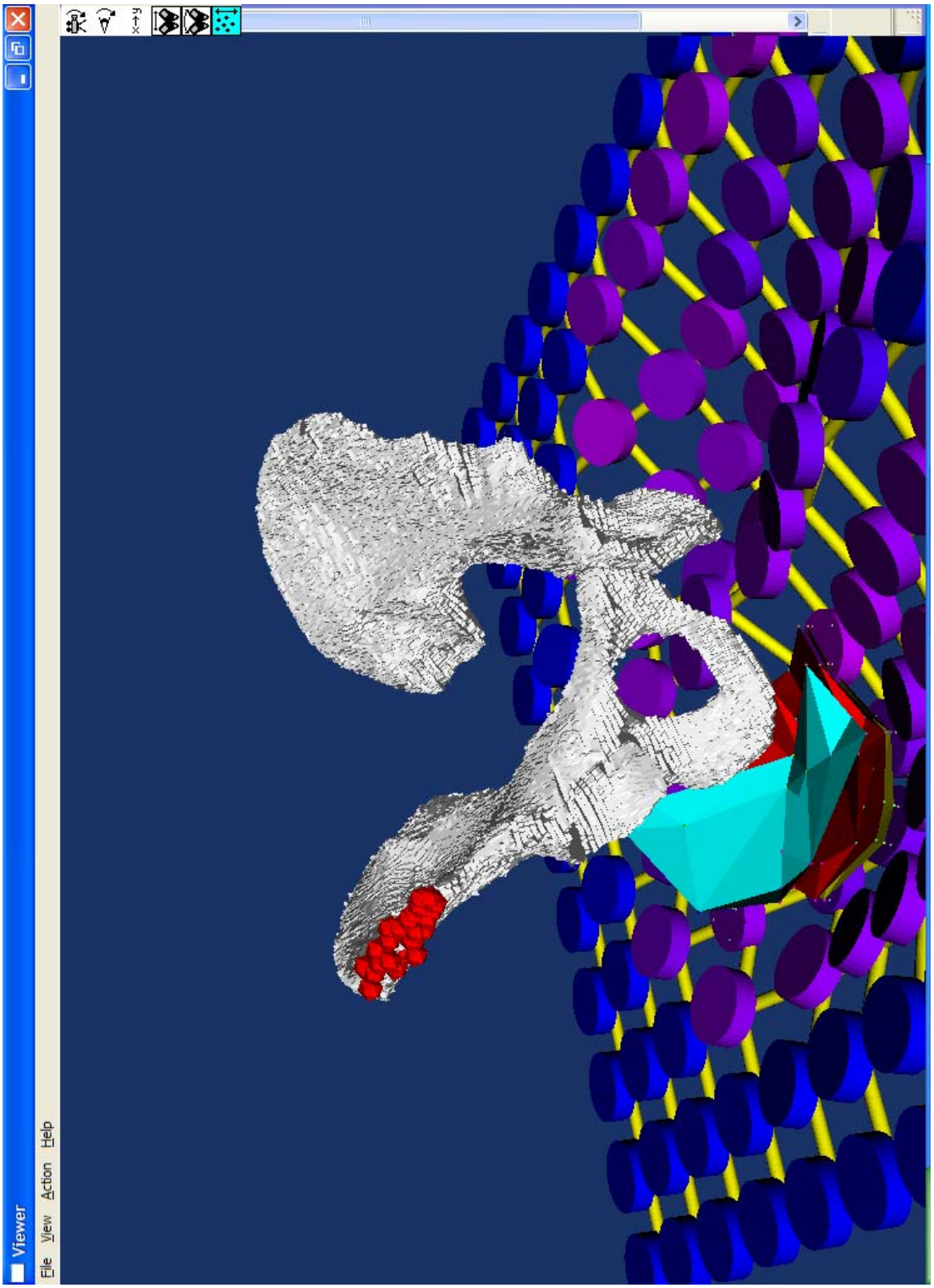

Figure 4.8: View of subject #1, equalized contour from the right front corner..

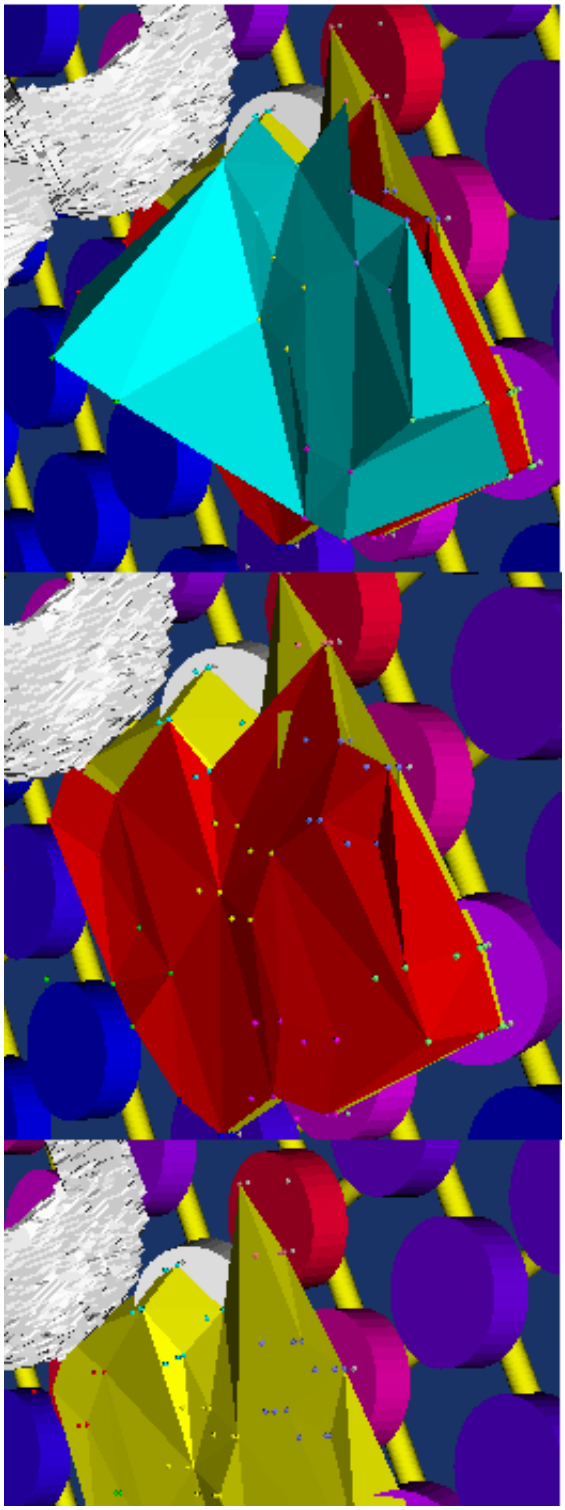

Figure 4.9: Boundaries between tissue layers of subject #1 for the flat contour.

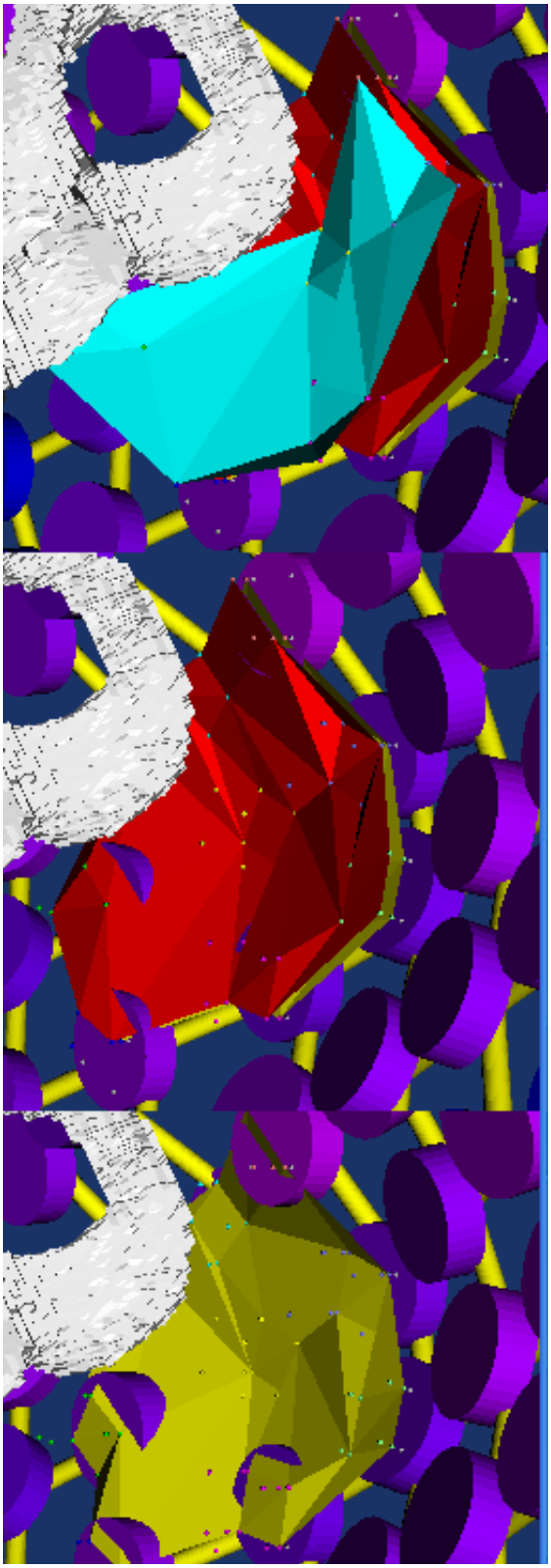

Figure 4.10: Boundaries between tissue layers of subject #1 for the equalized contour.

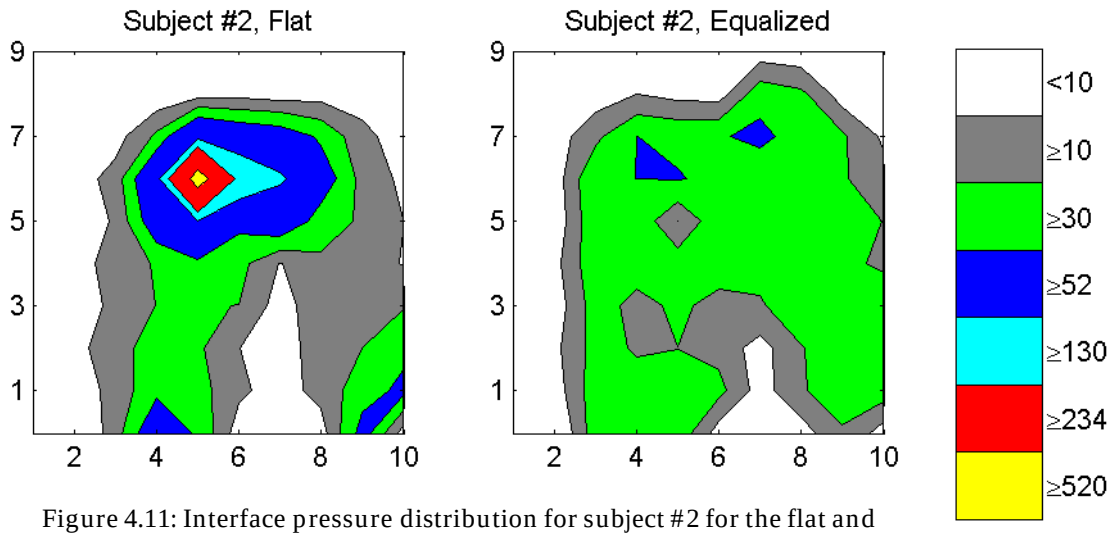

Figure 4.11: Interface pressure distribution for subject #2 for the flat and pressure-equalized contours.

4.3.2 Subject #2

The equalized contour for subject #2 is not quite as deep as the equalized contour for subject #1, as shown by the statistics in table 4.6. The two differ in both mean and maximum depth by about a centimeter. Furthermore, the equalized contour for subject #2 is not symmetric in its left and right halves. The maximum depth on the left side is considerably less than the maximum depth on the right side. In addition, the pressure distribution for the flat contour for subject #2 has only a single peak on the right side (see figure 4.11), whereas the flat contour for subject #1 had separate peaks on the left and right sides.

Table 4.7 illustrates the movement of the pelvis between the flat and equalized contours. If these measurements are accurate, when seated on the flat contour, subject #2's pelvis is pitched forward by more than 13 degrees. Like the roll for subject #1's pelvis, this pitch goes away almost entirely during the equalized contour, while the roll and yaw remain approximately the same. Subject #2's pelvis also moves about half the distance that subject #1's pelvis moved between the flat and equalized contours. Like subject #1, subject #2's movement is mostly downward. However, while subject #1's downward movement of 57.3 mm closely matches the maximum depth of 64.5 mm for his equalized contour, the downward movement of subject #2's pelvis of 27.3 mm is much less than the maximum equalized contour depth of 51 mm. This probably occurs because the depth of the contour on the left side of 34 mm is much less than the maximum depth on the right side of 51 mm and lowering the pelvis and lowering the pelvis all the way down into the right side would require an unnaturally large roll.

Tables 4.9 and 4.8 summarize the thickness and volume of bulk tissue beneath the pelvis for subject #2. A small number of bulk tissue thickness measurements beneath the left ischial tuberosity had to be discarded because they were either negative or too small (less than 3 mm) to be plausible. These errors may have occurred either because we have no orientation sensors beneath the left ischial tuberosity and therefore, we must infer the

seating contour as being completely flat in this region, or because our measurement of the location or orientation of subject #2's pelvis contains errors that place the left side too lower. In the case that subject #2's pelvis has been positioned and oriented accurately, with the left ischial tuberosity positioned above the midpoint between a group of four actuator heads, and so little tissue between the bottom of the ischial tuberosity and surface of the CASS, the actuator heads are probably tilted away from the horizontal. Since all the actuators in this region are at the same height for the flat contour, we would infer the normal to the surface of the actuator heads as pointing straight up beneath the left side of the pelvis, and thus the difference between where the points on the actuator surface actually are and where we believe them to be may be causing the small number of inaccurate bulk tissue thickness measurements. The number of measurements that had to be discarded was sufficiently small that it did not appreciably change the mean bulk tissue thickness and volume in this region.

As with subject #1, the mean and maximum bulk tissue thickness beneath the pelvis decrease between the flat and equalized contour while the minimum increases, albeit not as much for subject #1. These changes and the decreasing standard deviation points to a more even distribution of tissue for the equalized contour than for the flat contour. The volume of bulk tissue decreases only slightly between the two contours. However, the surface area beneath the pelvis increases by 5.5%, a change that is much larger than the corresponding change for the other two subjects, both of which are less than 1%. Provided that the measurement of the orientation of subject #2's pelvis is accurate, this large change in surface area occurs because the large downward pitch of the pelvis when seated on the flat contour exposes less of the pelvis's surface to the CASS than the neutral pitch does for the equalized contour.

Table 4.10 shows the thicknesses of the skin, fat, and first muscle layers. In contrast to subject #1, it was very easy to resolve the boundary between the first and second muscle layers of subject #2's buttocks for both contours. Taken as whole over the right buttock, the layers of skin and fat do not change thickness appreciably between the flat and equalized contour. The first muscle layer increases in thickness from 7.6 to 10.6 mm but this change is not statistically significant. However, while the skin, fat, and first muscle layers may not change that much as a whole between the flat and equalized contours, important changes do occur in the individual regions.

Compared to the other two subjects, the bulk tissue beneath the ischial tuberosities is considerably thinner for the flat contour. Over 26% of the bulk thickness measurements beneath the right ischial tuberosity are less than 10 mm, as are 36% of the bulk thickness measurements beneath the left ischial tuberosity, whereas only a handful of the measurements for subject #1 and none of the measurements for subject #3 beneath the ischial tuberosities are beneath this value. Furthermore, the ultrasound measurements reveal that the fat and first muscle layer are being squashed very thin - to mean thicknesses of 0.66 and 2.42 mm respectively - beneath the right ischial tuberosity. An examination of the lower left corner of figure 4.13 shows that in at least two places, the first muscle layer has been squashed down to approximately 1 mm.

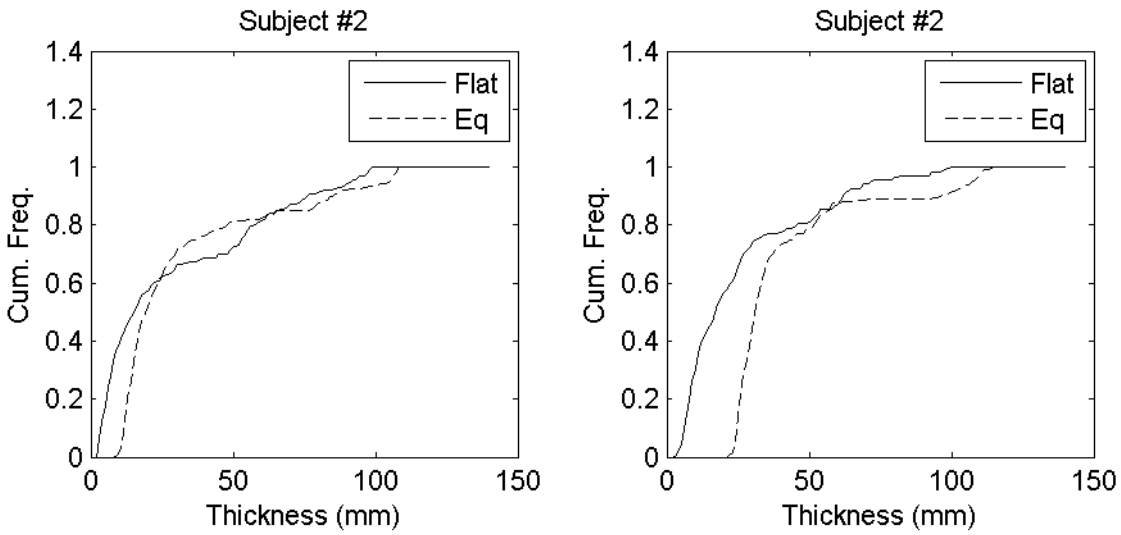

Figure 4.12: Cumulative distribution of soft tissue beneath the left ischial tuberosity (graph on the left) and the right ischial tuberosity (graph on the right) for subject #2.

When seated on the pressure equalized contour, the tissue beneath the right ischial tuberosity thickens considerably from 26.7 mm to 42.1 mm, but the tissue beneath the left ischial tuberosity thickens only slightly from 30.3 mm to 33.4 mm, a difference that is not statistically significant. Bulk tissue volume increases by 63% beneath the right ischial tuberosity and 19% beneath the left. Although the differences in response beneath the left and right ischial tuberosities may occur because of the lower peak pressure on the left side of the flat contour or because the position and orientation of subject #2's pelvis has not been measured accurately, subject #1 had a similar pattern of response in spite of having high peak pressures on both sides. Ultrasonic measurements show that the fat and first muscle layers increase in thickness by 266% and 178% to 2.42 and 7.08 mm respectively beneath the right ischial tuberosity and proportionately more of the load from the ischial tuberosity is being borne by these layers than for the flat contour. In any case, the extreme distortion of that occurs for the fat and muscle layers beneath the right ischial tuberosity when seated on the flat contour cannot be healthy.

Since there are no ultrasound sensors on the left side, we cannot know how the fat and muscle layers change between the two contours. However, as the cumulative frequency plots in figure 4.12 show, the bulk tissue distribution does change beneath the left ischial tuberosity between the flat and equalized contours. The thinnest areas increase in thickness by about 10 mm while thickest areas decrease slightly, showing a redistribution of tissue beneath the left ischial tuberosity. This is much smaller increase in thickness than is observed beneath the right side, where the thinnest areas of tissue increase in thickness by more than 20 mm.

Behind the ischial tuberosities, bulk tissue thickness declines significantly between the flat and equalized contours while bulk tissue volume and surface area above the CASS (which is proportional to the number of measurements) increase significantly. This implies that

more tissue is distributed over a wider area for the equalized contour than for the flat contour. The increase in surface area is due to the decrease in the magnitude of the pitch angle; as the pelvis rotates upwards to neutral pitch, more of the ilium falls behind the ischial tuberosity. Consequently, provided that the position and orientation measurements of the pelvis are accurate, the observed increase in bulk tissue volume behind the ischial tuberosities is more an artefact of the shift in region boundaries relative to the ilium than it is of tissue being moved from one area of the pelvis to another. By adding together the volume of bulk tissue from behind and beside the ishcial tuberosity (the two regions occupied by the ilium of the pelvis), we can see a slight decrease from 921 cm^3 to 880 cm^3 on the right side (a 4.4% decrease) and from 980 cm^3 to 940 cm^3 on the left (a 4.1% decrease). These decreases in volume are consistent with the 4.1% decrease in bulk tissue volume observed for the pelvis as a whole.

The ultrasonic measurements for the regions beside and behind do not show a statistically significant[3] change in thickness for the skin, fat, or first muscle layer beside or behind the right ischial tuberosity. If we consider the thickness measurements for fat and muscle beneath the ischial tuberosity to be representative, then we must conclude that the increase in thickness of these two layers beneath the ischial tuberosity indicates an increase in volume as well. Soft tissue is incompressible at pressures experienced from normal sitting, so this increase in volume must correspond to a decrease elsewhere. But because the thickness of the fat and first muscle layer do not decrease behind or beside the ischial tuberosity, we might conclude that the additional tissue must come from somewhere else in the right buttock. For the fat layer, this is probably correct. Healthy human beings have a cone of fat next to either side of the rectum and fat from this region probably flows beneath the ischial tuberosity as the contour moves from its flat to its equalized state. However, the first muscle layer beneath the ischial tuberosity is almost certainly the gluteus maximus, and the gluteus maximus is found only beneath, behind or beside the ischial tuberosity, leaving us with nowhere to recruit the additional tissue from. Careful observation, however, reveals that if the pitch of the pelvis does in fact decrease in magnitude from -13.28 degrees to 0.26 degrees between the flat and the equalized contours, the right ischial tuberosity should swing forward. This would cause the ultrasonic transducers behind the ischial tuberosity to move farther back relative to the ischial tuberosity, placing them on a part of the gluteus maximus that is naturally thicker than the part they were under for the flat contour. This shift would probably disgusise a decrease in the thickness of the gluteus maximus muscle, a decrease that we would observe in the bulk tissue thickness measurements but not in the individual thickness measurements. Consequently, if the change in pelvic pitch has been measured accurately, the increase in the volume of the gluteus maximus muscle beneath the right ischial tuberosity is most likely the result of a shift of tissue from behind the ischial tuberosity to beneath it.

To sum up, provided that the measurements of pelvic position and orientation are accurate, when seated on the flat contour, subject #2's pelvis has a significant downward pitch that

3. Statistical signifigance was tested using the two-sample t-test.

pushes the ischial tuberosities downwards into the soft tissue, squeezing the layers of soft tissue beneath them such that approximately one third of the bulk tissue has a thickness of less than 1 cm. When seated on the pressure equalized contour, this pitch disappears and the the layers of fat and muscle beneath the right ischial tuberosity thicken considerably, with a larger proportionate increase in the thickness of the fat. Beneath the left ischial tuberosity, the mean thickness of the bulk tissue does not change signficantly, but its distribution does, with the primary change being a large increase in thickness in the portion of the bulk tissue that was formerly less than 1 cm in thickness.

Table 4.6: Contour Depth And Interface Pressure For Subject #2

	Minimum		Mean		Maximum	
	Flat	Eq	Flat	Eq	Flat	Eq
Contour Depth (mm)	0.0	0.0	0.0	7.2	0.0	51.0
Right Side	0.0	0.0	0.0	9.3	0.0	51.0
Left Side	0.0	0.0	0.0	5.0	0.0	34.0
Interface Pressure (mmHg)	10.3	18.7	56.2	37.9	624.4	58.7
Right Side	12.9	22.9	69.0	43.1	624.4	53.6
Left Side	10.3	18.7	41.5	35.3	140.8	58.7

Table 4.7: Position And Orientation Of Pelvis For Subject #2

Contour	Position (mm)			Orientation (degrees)		
	X	Y	Z	Pitch	Roll	Yaw
Flat	266.2	290.6	113.8	-13.28	-4.23	-2.24
Equalized	255.6	289.8	86.5	-0.26	-4.10	-4.12
Change	-10.6	-0.8	-27.3	13.02	0.13	-2.12

Table 4.8: Bulk Tissue Volume For Subject #2

Region		Flat	Equalized	% Change
Whole Pelvis		2294.0	2188.7	-4.6
Beneath Ischial Tuberosity	Right	32.7	53.4	63.1
	Left	37.0	44.0	18.8
Behind Ischial Tuberosity	Right	515.0	726.9	41.1
	Left	537.5	730.9	36.0
Beside Ischial Tuberosity	Right	406.1	153.5	-62.2
	Left	442.5	208.9	-52.8
In Front Of Ischial Tuberosity	Right	59.3	58.3	-1.8
	Left	61.2	27.7	-54.7

Table 4.9: Bulk Tissue Thickness For Subject #2

Side	Contour	N	Min	Mean	StdDev	Max
Whole Pelvis						
N/A	Flat	5042	3.0	113.7	54.2	208.8
	Equalized	5320	9.9	102.9	39.6	170.1
	(% Change)	5.5	230.0	-9.5	-26.9	-18.5
Beneath Ischial Tuberosity						
Right	Flat	306	3.1	26.7	23.1	100.6
	Equalized	317	22.7	42.1	24.6	115.4
	(% Change)	3.6	632.3	57.7	6.5	14.7
Left	Flat	305	3.0	30.3	29.2	99.4
	Equalized	329	9.9	33.4	28.6	109.4
	(% Change)	7.9	230.0	10.2	-2.1	10.1
Behind Ischial Tuberosity						
Right	Flat	841	54.3	153.1	30.0	208.8
	Equalized	1527	50.4	119.0	29.6	170.0
	(% Change)	81.6	-7.2	-22.3	-1.3	-18.6
Left	Flat	897	53.3	149.8	28.2	199.8
	Equalized	1550	50.4	117.9	26.4	161.9
	(% Change)	72.8	-5.4	-21.3	-6.4	-19.0
Left of Left Ischial Tuberosity or Right of Right Ischial Tuberosity						
Right	Flat	738	34.0	137.6	35.3	195.3
	Equalized	315	53.0	121.8	27.4	159.4
	(% Change)	-57.3	55.9	-11.5	-22.4	-18.4
Left	Flat	794	56.3	139.3	33.4	192.2
	Equalized	431	59.3	121.2	26.6	161.0
	(% Change)	-45.7	5.3	-13.0	-20.4	-16.2
In Front Of Ischial Tuberosity						
Right	Flat	183	64.9	81.0	10.8	102.7
	Equalized	137	98.0	106.3	4.9	116.2
	(% Change)	-25.1	51.0	31.2	-54.6	13.1
Left	Flat	193	64.7	79.3	9.5	100.3
	Equalized	80	79.7	86.7	6.9	106.1
	(% Change)	-58.6	23.2	9.3	-27.4	5.8

Table 4.10: Thickness Of Individual Tissue Layers For Subject #2

Tissue Layer	Contour	N	Min	Mean	StdDev	Max
Entire Right Buttock						
Skin	Flat	32	1.79	2.50	0.39	3.30
	Equalized	30	1.89	2.51	0.49	3.70
	(% Change)	-6.25	5.36	0.61	24.15	11.86
Fat	Flat	32	0.00	3.16	1.73	7.77
	Equalized	30	1.51	3.36	1.16	6.53
	(% Change)	-6.25	N/A	6.35	-33.32	-15.87
First Muscle Layer	Flat	30	1.29	7.56	4.73	21.74
	Equalized	27	3.23	10.60	7.98	39.11
	(% Change)	-10.00	150.92	40.13	68.82	79.87
Remaining Muscle	Flat	7	5.58	34.54	29.40	83.55
	Equalized	5	14.47	37.79	30.39	90.26
	(% Change)	-28.57	159.31	9.43	3.34	8.03
Beneath Right Ischial Tuberosity						
Skin	Flat	5	2.00	2.29	0.30	2.72
	Equalized	4	1.89	2.62	0.77	3.70
	(% Change)	-20.00	-5.60	14.18	153.61	35.88
Fat	Flat	5	0.00	0.66	0.88	2.14
	Equalized	4	1.51	2.42	0.77	3.11
	(% Change)	-20.00	-16.89	266.23	-12.23	45.42
First Muscle Layer	Flat	5	1.29	2.54	1.14	3.73
	Equalized	4	5.87	7.08	0.87	7.86
	(% Change)	-20.00	355.83	178.36	-24.10	110.81
Remaining Muscle	Flat	5	5.58	19.98	17.03	42.26
	Equalized	2	30.67	32.32	2.34	33.98
	(% Change)	-60.00	449.52	61.80	-86.27	-19.60
Behind Right Ischial Tuberosity						
Skin	Flat	6	2.18	2.64	0.33	3.00
	Equalized	9	2.00	2.53	0.49	3.30
	(% Change)	50.00	-8.43	-4.08	46.99	10.13
Fat	Flat	6	2.15	2.89	1.05	4.98
	Equalized	9	1.78	3.37	1.11	5.07
	(% Change)	50.00	-16.89	16.61	5.55	1.75

Table 4.10: Thickness Of Individual Tissue Layers For Subject #2

Tissue Layer	Contour	N	Min	Mean	StdDev	Max
First Muscle Layer	Flat	4	9.45	14.90	6.37	21.74
	Equalized	7	6.51	19.01	11.55	39.11
	(% Change)	75.00	-31.10	27.60	81.33	79.87
Remaining Muscle	Flat	0	N/A	N/A	N/A	N/A
	Equalized	2	14.47	17.03	3.62	19.59
	(% Change)	N/A	N/A	N/A	N/A	N/A
To The Right Of The Right Ischial Tuberosity						
Skin	Flat	16	2.00	2.58	0.43	3.30
	Equalized	14	1.89	2.50	0.43	3.50
	(% Change)	-12.50	-5.60	-2.92	0.44	6.05
Fat	Flat	16	2.32	4.10	1.53	7.77
	Equalized	14	2.32	3.68	1.17	6.53
	(% Change)	-12.50	0	-10.22	-23.26	-15.87
First Muscle Layer	Flat	16	3.18	7.69	3.11	14.48
	Equalized	13	3.78	7.81	3.46	13.56
	(% Change)	-18.75	18.61	1.53	11.10	-6.38
Remaining Muscle	Flat	0	N/A	N/A	N/A	N/A
	Equalized	0	N/A	N/A	N/A	N/A
	(% Change)	N/A	N/A	N/A	N/A	N/A
In Front Of The Right Ischial Tuberosity						
Skin	Flat	5	1.79	2.30	0.36	2.70
	Equalized	3	1.98	2.41	0.60	3.10
	(% Change)	-40.00	10.71	4.59	69.49	14.84
Fat	Flat	5	1.60	2.99	0.97	4.29
	Equalized	3	1.51	3.11	1.44	4.29
	(% Change)	-40.00	-5.46	4.10	48.55	0
First Muscle Layer	Flat	5	2.43	6.30	2.54	8.56
	Equalized	3	3.23	7.73	4.34	11.89
	(% Change)	-40.00	32.79	22.68	70.73	38.97
Remaining Muscle	Flat	2	58.32	70.93	17.84	83.55
	Equalized	1	90.26	90.26	0.00	90.26
	(% Change)	-50.00	54.76	27.24	-100.00	8.03

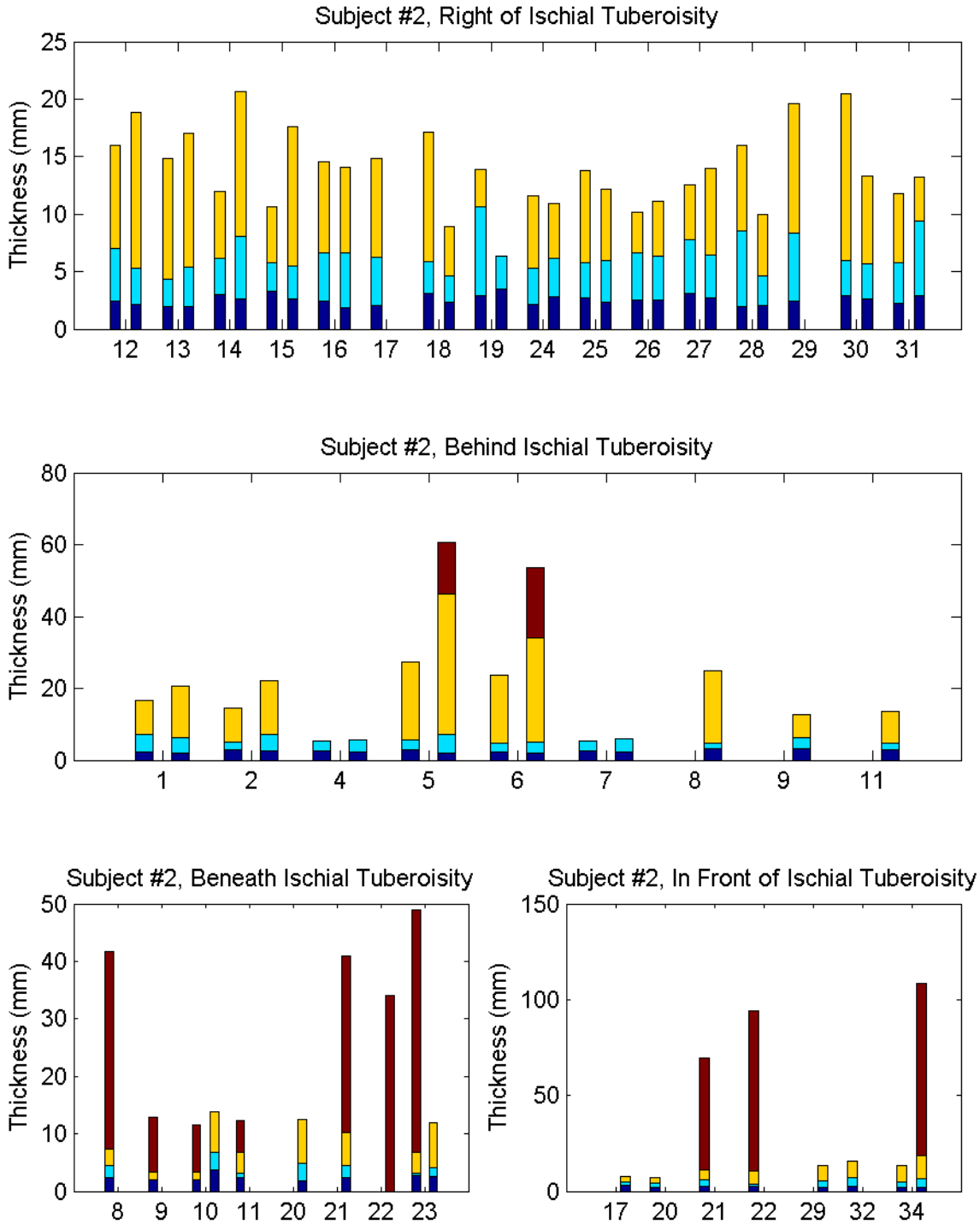

Figure 4.13: Thickness of skin(blue), fat(aqua) and the first muscle layer (yellow) broken down by region for both the flat and equalized contours. Bulk tissue between the last resolved layer and the pelvis is shown by brown bars. Numbers along the x-axis indicate the sensor where the measurements were taken. Each number has two bars associated with it; the bar on the left measures thickness for the flat contour, while the bar on the right measures thickness for the equalized contour. A missing bar indicates that no measurements were available for that combination of sensor and contour.

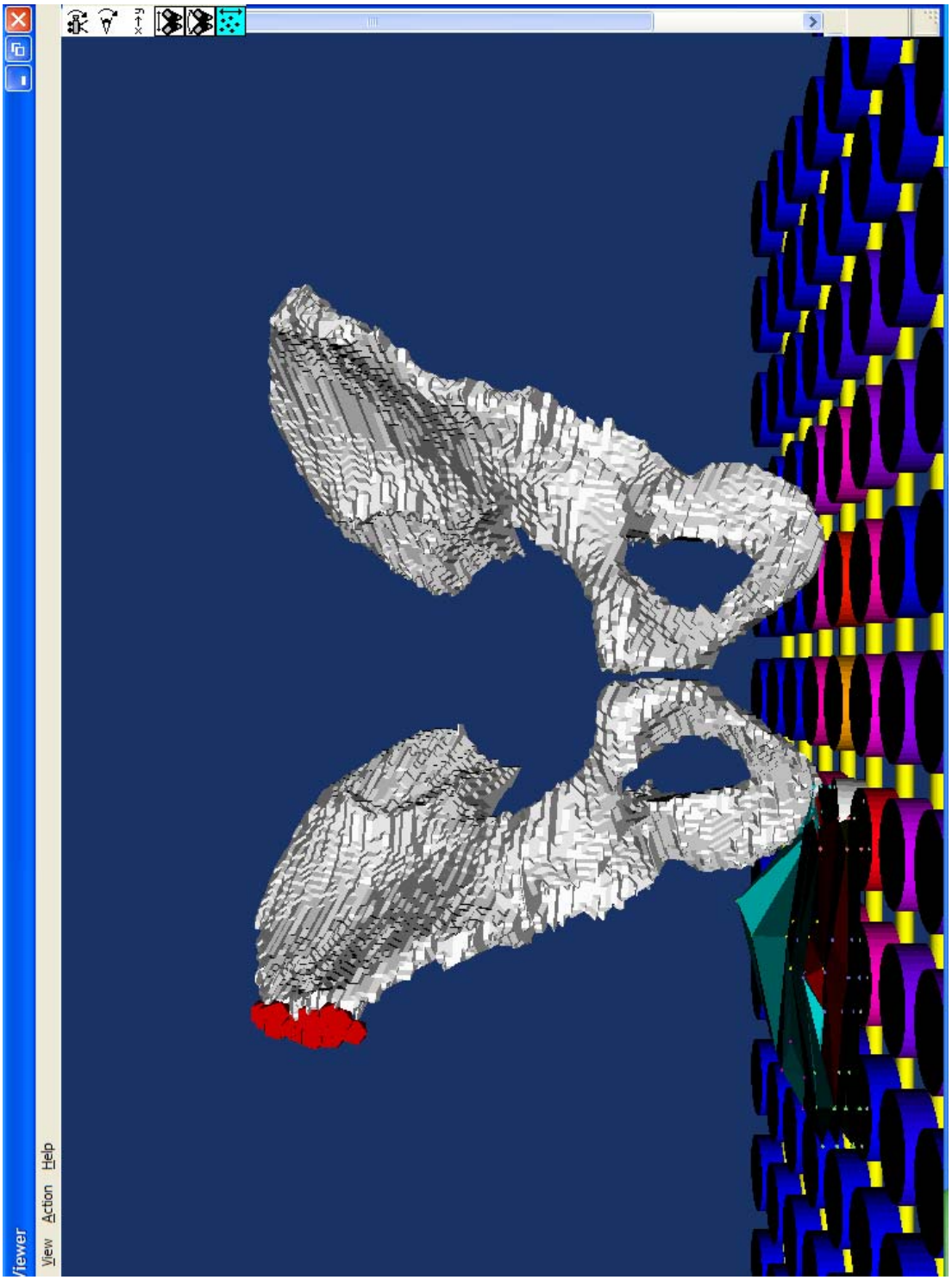

Figure 4.14: Front view of subject #2, flat contour.

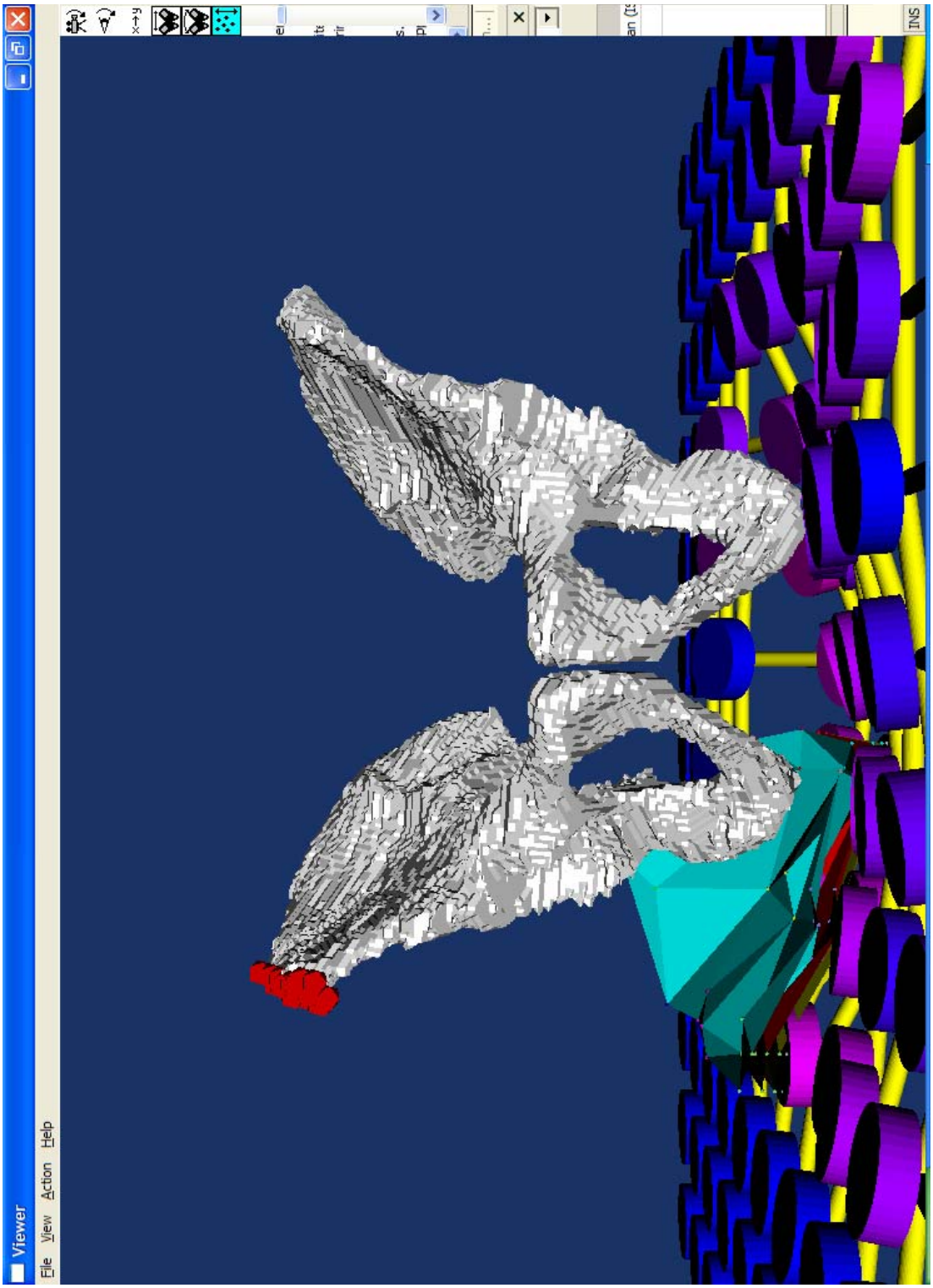

Figure 4.15:: Front view of subject #2, equalized contour.

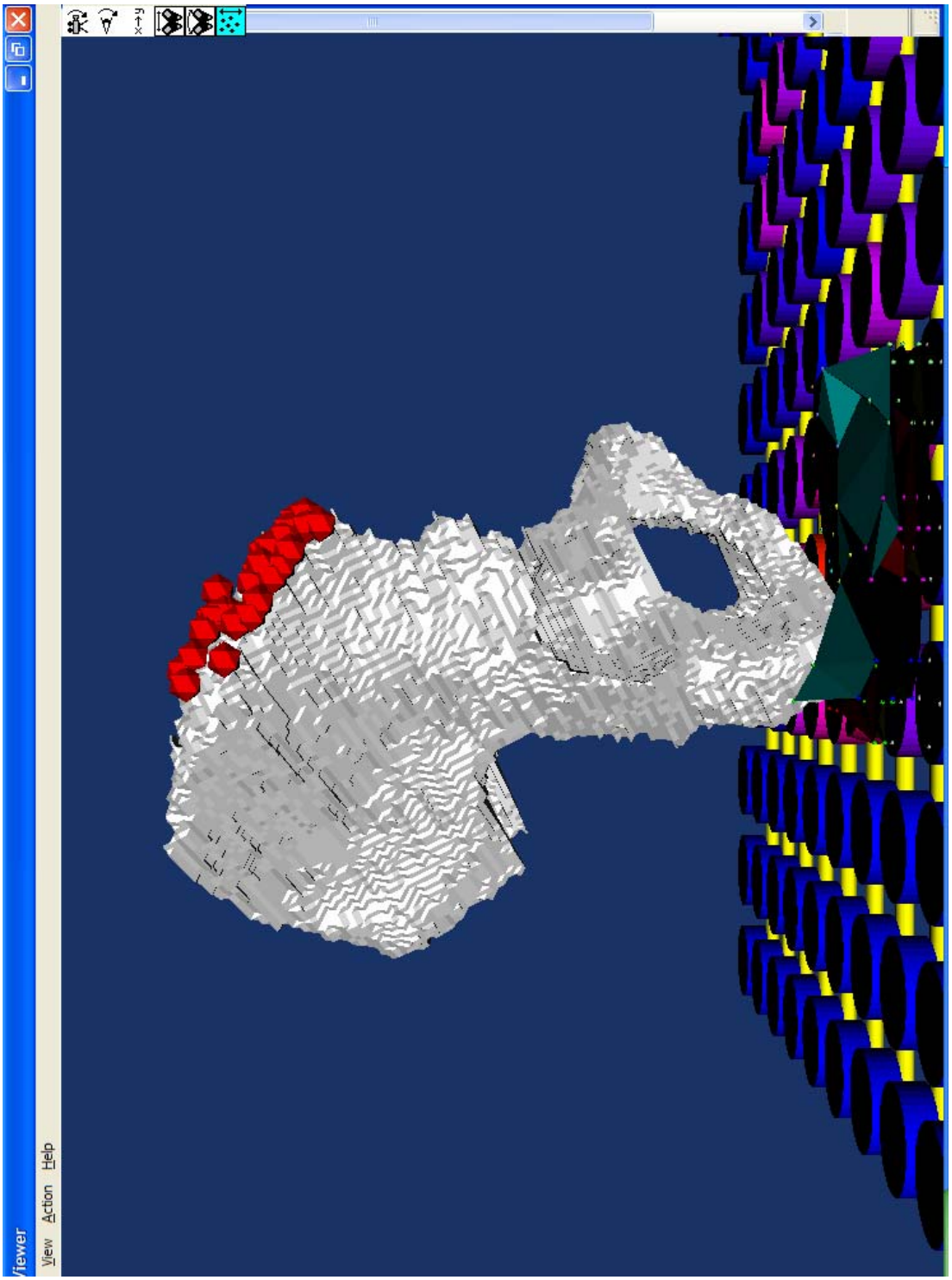

Figure 4.16: Side view of subject #2, flat contour.

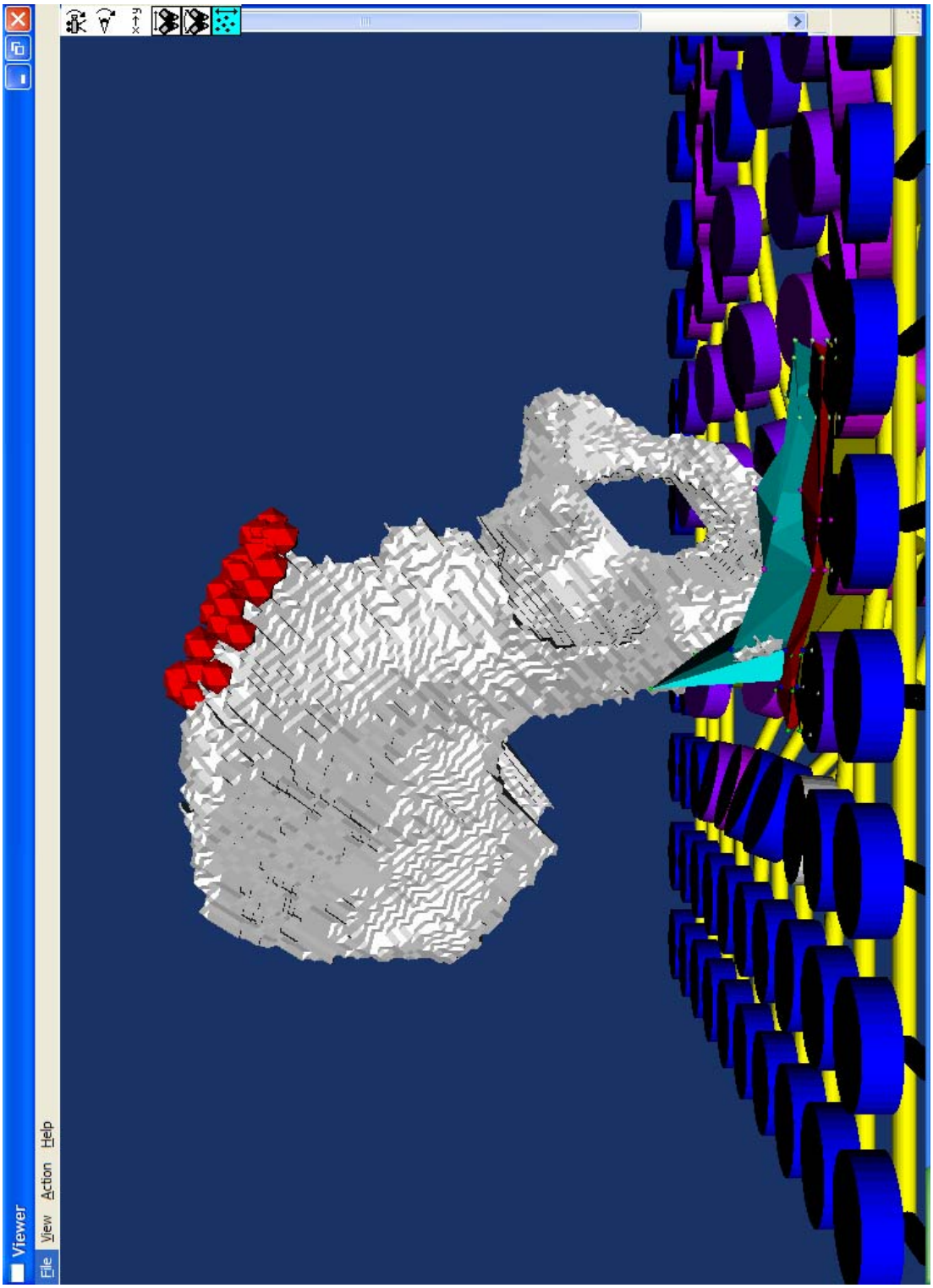

Figure 4.17: Side view of subject #2, equalized contour.

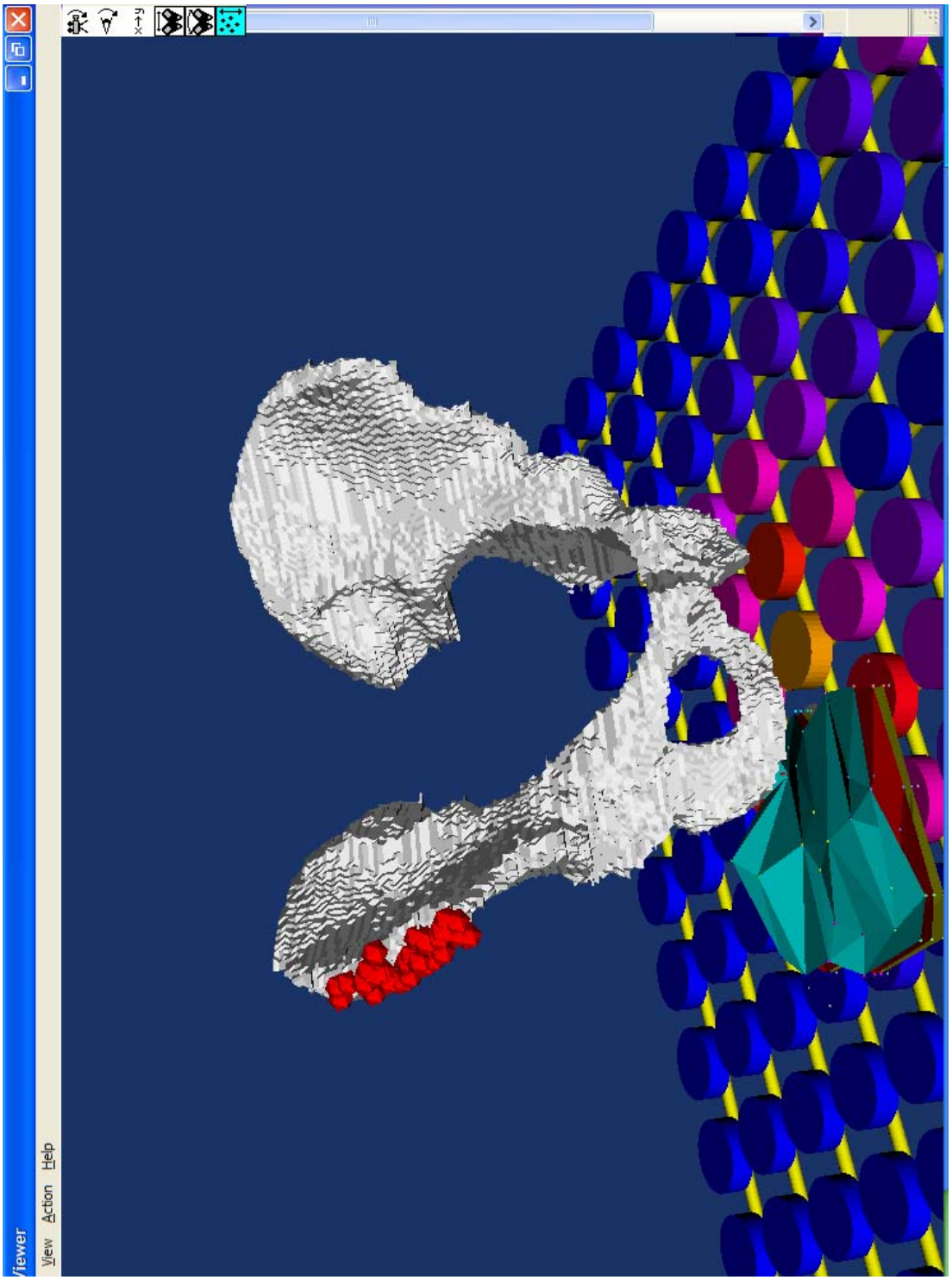

Figure 4.18: View of subject #2, flat contour from the right front corner.

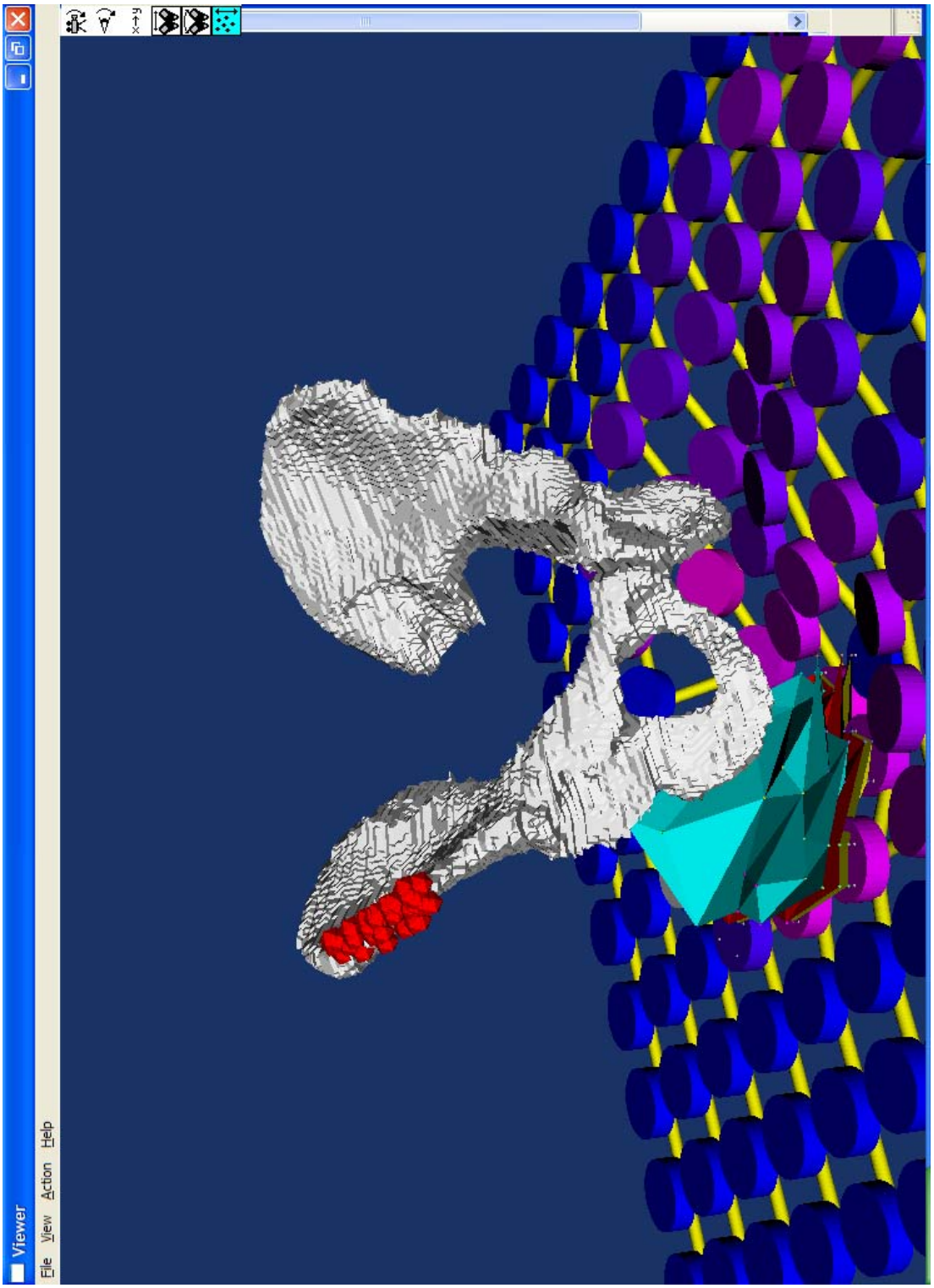

Figure 4.19: View of subject #2, equalized contour from the right front corner..

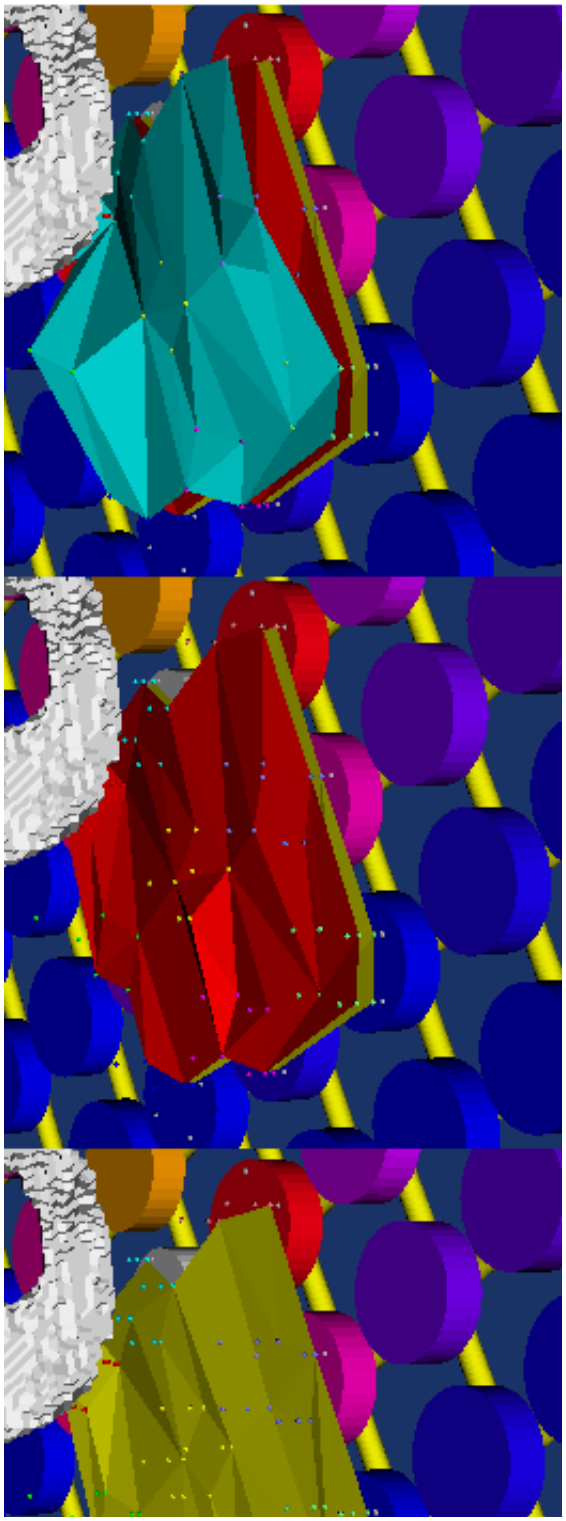

Figure 4.20: Boundaries between tissue layers of subject #2 for the flat contour.

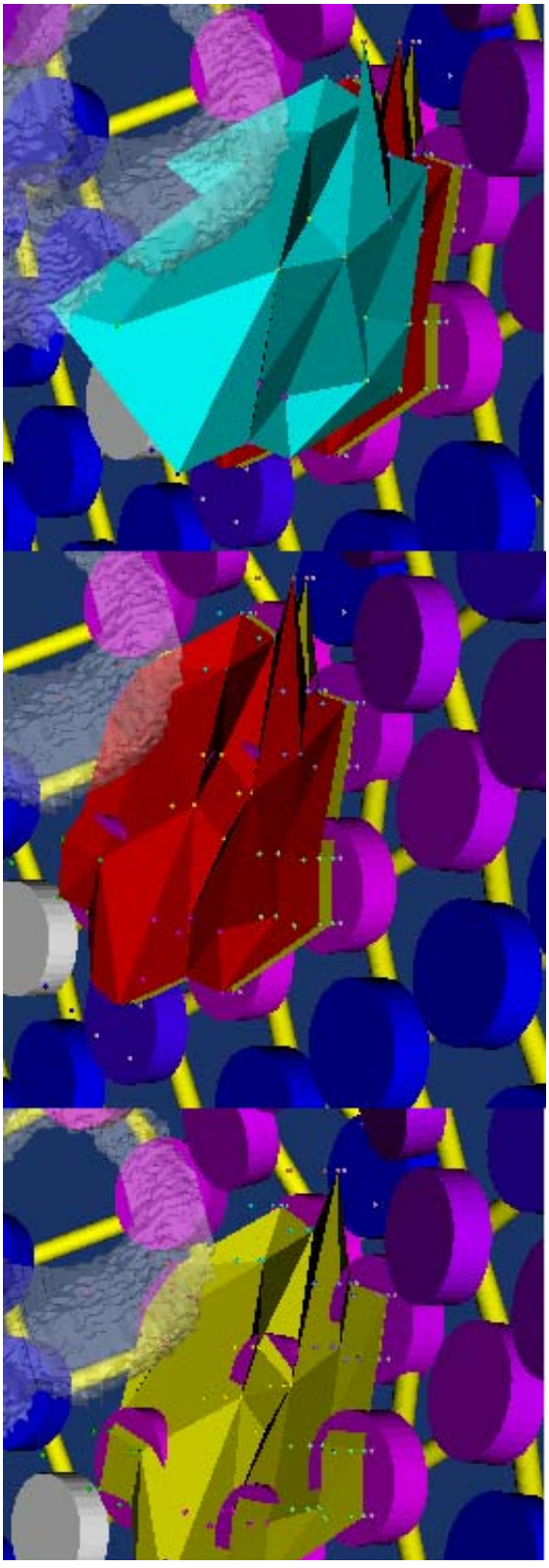

Figure 4.21: Boundaries between tissue layers of subject #2 for the equalized contour.

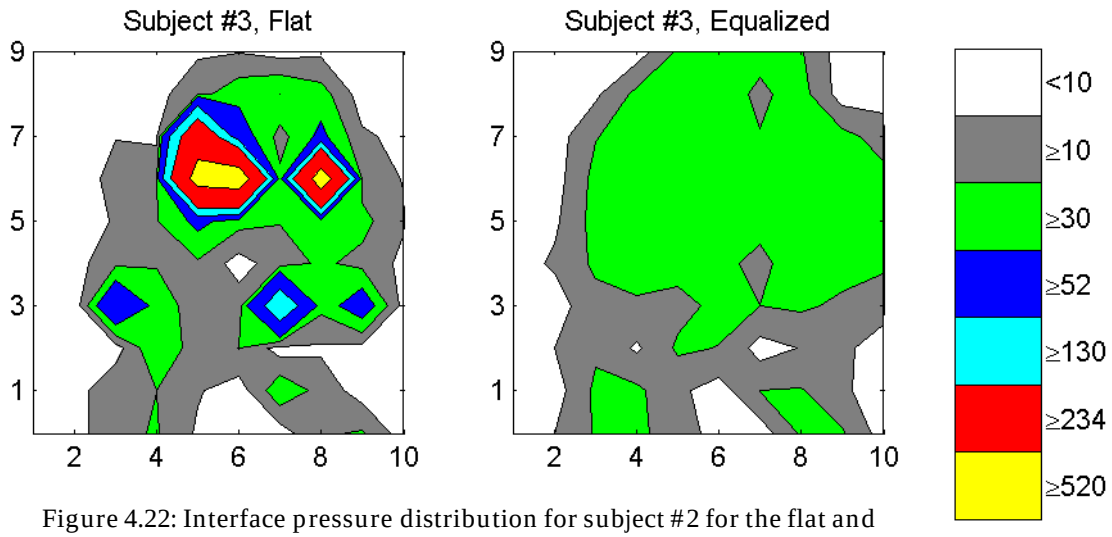

Figure 4.22: Interface pressure distribution for subject #2 for the flat and pressure-equalized contours.

4.3.3 Subject #3

The statistics for the flat and equalized contours for subject #3 are shown in table 4.11. The equalized contour for subject #3 is about as deep as the same contour for subject #2, with a mean depth of 8.7 mm vs. 7.2 mm for subject #2 and a maximum depth of 46 mm vs. 51 mm. Subject #3's equalized contour is also asymmetric between its left and right halves like subject #2's contour, with a maximum depth of 46 mm on the right side vs. 31 mm on the left. However, like subject #1 and unlike subject #2, subject #3 has high peak interface pressures on both sides of the flat contour, as shown in figure 4.22. Both the peak and mean interface pressures for subject #3's flat contour are higher than the correponding values for the other two subjects. However, the peak and mean pressures for the equalized contour are similar to the same values for subject #1.

A bug in the data acquisition software caused a displacement of 31 mm along the -z axis of the wand coordinate system to be introduced into the locations of the registration points for both the flat and equalized contours. This magnitude of this displacement was estimated by using an earlier data set acquired for subject #3 that had the displacement in one set of registration data points but not in the other. The displacement was removed from subject #3's registration points by subtracting it out.

Table 4.12 shows the movement of subject #3's pelvis between the flat and equalized contours. If the measurements of the position and orientation of subject #3's pelvis are accurate, then unlike the other two subjects, subject #3's pelvis does not have a large pitch, roll of yaw when seated on the flat contour. It does have a moderate pitch and yaw of -5.1 and -7.1 degrees registration however. In moving to the equalized contour, the yaw goes away but the pitch and roll do not change appreciably. Subject #3's pelvis moves about the same distance as subject #2 between the flat and equalized contour, with most of it being movement downward. Like subject #2, the downward movement of the pelvis of 26.7 mm matches the maximum depth of the contour on the left side but not the right.

Tables 4.14 and 4.13 show the thickness and volume of the bulk tissue beneath the pelvis for subject #3 for both contours. Like the other subjects, the distribution of tissue beneath the pelvis becomes more uniform as the contour changes from flat to equalized, and the mean thickness and volume decline by about the same percentage as subject #2. However, in terms of absolute volume, subject #3 has more tissue than either of the other two subjects, which is consistent with what is observed on the MRI scans for subject #3. The total surface area beneath the pelvis does not change between the flat and equalized contours, but there is an imbalance between the surface beneath the left and right sides. For the flat contour, the right side of the pelvis has approximately 14 cm^2 more area beneath it than the left. This imbalance increases for the equalized contour to approximately 26 cm^2. An examination of the relationship of subject #3's pelvis to the CASS reveals that this dispairity does not arise from segmentation error, nor from the orientation of the pelvis relative to the CASS surface. At present, there is no satisfactory explaination why this dispairity exists and it may represent a genuine asymmetry in subject #3's pelvis that is not present for either of the other two subjects.

Table 4.15 summarizes the thicknesses of the layers of skin, fat and muscle in subject #3's right buttock. As with subject #2, neither the skin, nor the fat, nor the first muscle layer experiences a significant change between the flat and the equalized contour. Unlike subject #2, we had great difficulty resolving the boundary between the first and second muscle layers, being able to resolve only 11 points on this boundary for the flat contour and 15 points for the equalized contour. Because the number of boundary points is so small and the locations of the points are scattered around the array of ultrasonic transducers, we cannot construct a meaningful triangular mesh to represent the boundary between the first and second muscle layers. Consequently, the mesh for this boundary has been omitted from any of the visualizations for subject #3 shown in figures 4.25 through 4.32. However, we do use the thickness measurements for the first muscle layer obtained from the transducers where the this boundary could be resolved in our analysis below.

Beneath the right ischial tuberosity, the volume and mean thickness of bulk tissue increase significantly by about 20% and 23% respectively as the contour moves from its flat to its equalized shape, provided that the measurements of subject #3's pelvic position and orientation are accurate. The ultrasonic measurements show that in this region, the thickness of the skin remains constant (as expected) while the thickness of the fat increases by 73% from 7.2 mm to 12.4 mm. Unfortunately, no reflections from the boundary between the first and second muscle layers were received by any of the ultrasonic transducers in this region, so it is impossible to measure the thickness of the gluteus maximus beneath the right ischial tuberosity. Instead, we fall back to using the difference between the bulk tissue above the transducers and the sum of the skin and the fat thicknesses as the *total* thickness of muscle above each transducer and use these values in our analysis, keeping in mind that because we are unsure of the accuracy with which the positon and orientation of the pelvis has been measured, these measurements may not be as accurate as the thickness measurements of the skin and fat layers obtained from the ultrasonic echograms. These are the rows labelled "remaining muscle" in table 4.15.

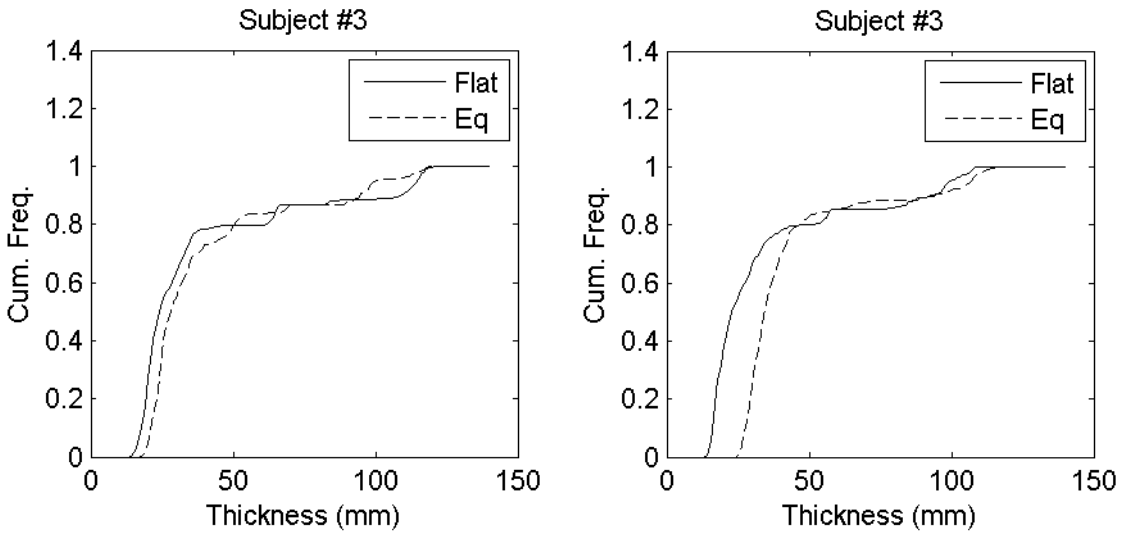

Figure 4.23: Cumulative distribution of soft tissue beneath the left ischial tuberosity (graph on the left) and the right ischial tuberosity (graph on the right) for subject #3.

There are two outliers that we need to correct for in this table. As the chart in the bottom left corner of figure 4.24 shows, one of the transducers did not receive the reflection from the boundary between the fat and first muscle layers. Consequently, the thickness of "remaining muscle" computed for this transducer includes some fat as well. If we subtract the mean thickness of fat for the other three transducers from this thickness, we obtain an adjusted total thickness of muscle of 16.6 mm. Using this thickness of muscle instead of the raw value of 23.8 mm yields a mean muscle thickness of 10.3 mm instead of 12.8 mm and a much smaller standard deviation.

The other outlier occurs for the equalized contour, where we have four transducers beneath the ischial tuberosity instead of three. As the chart in the bottom left corner of figure 4.24 shows, the total thickness of muscle above one of the transducers is quite a bit larger than the other three. This transducer is the one that moved from behind the ischial tuberosity for the flat contour to just barely beneath it for the equalized contour. As a result, the ray eminating from the surface of the transducer along the normal falls on the upper part of the rear of the ischial tuberosity where its surface curves steeply upward, and the bulk thickness measurement above this transducer can be considered an outlier. When we omit this outlier, both the mean thickness of muscle and its standard deviation decrease from 21.9 mm and 13.4 mm respectively to 15.5 mm and 5.1 mm.

The corrected statistics for the overall thickness of muscle beneath the right ischial tuberosity are listed in the rows labelled "adjusted" in table 4.15. A comparison between the thicknesses of fat and muscle for the two contours shows that if the bulk thickness measurements are accurate, subject #3 has about the same relative proportion of fat to muscle for both contours, whereas the other two subjects showed an increase in the proportion of fat to muscle when moving from the flat contour to the equalized contour.

Beneath the left ischial tuberosity, the volume increases by about 24% but the mean thickness remains about the same. The increase in volume is caused by an increase in surface area beneath the left ischial tuberosity of 2 cm^2 that arises from the imperfect placement of the region boundaries on the left side of the pelvis. Although the mean thickness of tissue beneath the left ischial tuberosity remains the same between the two contours, the distrubtion of bulk tissue does change. As figure 4.23 shows, the thinner areas of tissue have thickened by about 5 mm. This contrasts with the distribution of tissue beneath the right ischial tuberosity, where the thinner areas have thickened by more than 10 mm. This pattern is similar to the patterns observed for the other two subjects.

Behind the ischial tuberosities, we see a decrease in both volume and mean thickness of bulk tissue as the contour changes from flat to equalized. Behind the right ischial tuberosity, the thickness of the fat and muscle layers increase slightly but not significantly. Unlike the other two subjects, we cannot resolve the gluteus maximus beneath the right ischial tuberosity, so we cannot tell whether the thickening of muscle in this region occurs because of a change in the thickness of the gluteus maximus, a change in the thickness of the semitendinosus, semimembranosus or biceps femoris muscles, or some combination thereof. While the relative constancy of the thickness of the gluteus maximus behind and beside the ischial tuberosity may suggest that the gluteus maximus is not changing in thickness, we cannot be sure without actual measurements.

Table 4.11: Contour Depth And Interface Pressure For Subject #3

	Minimum		Mean		Maximum	
	Flat	Eq	Flat	Eq	Flat	Eq
Contour Depth (mm)	0.0	0.0	0.0	8.7	0.0	46.0
Right Side	0.0	0.0	0.0	10.1	0.0	46.0
Left Side	0.0	0.0	0.0	7.3	0.0	31.0
Interface Pressure (mmHg)	12.1	11.0	82.6	32.2	678.5	41.7
Right Side	12.1	13.3	77.3	32.2	628.5	40.8
Left Side	12.9	11.0	70.0	31.1	667.8	40.2

Table 4.12: Position And Orientation Of Pelvis For Subject #3

Contour	Position (mm)			Orientation (degrees)		
	X	Y	Z	Pitch	Roll	Yaw
Flat	274.2	276.5	121.7	-5.13	1.26	-7.10
Equalized	277.2	287.7	95.0	-4.34	4.53	0.09
Change	3.0	11.2	-26.7	0.79	3.27	7.01

Table 4.13: Bulk Tissue Volume For Subject #3

Region		Flat	Equalized	% Change
Whole Pelvis		2731.5	2526.8	-7.5
Beneath Ischial Tuberosity	Right	48.2	58.0	20.3
	Left	45.1	55.8	23.7
Behind Ischial Tuberosity	Right	1040.6	925.9	-11.0
	Left	880.4	814.9	-7.4
Beside Ischial Tuberosity	Right	208.7	254.0	21.7
	Left	238.4	186.7	-21.7
In Front Of Ischial Tuberosity	Right	27.0	41.9	55.2
	Left	29.8	18.0	-39.7

Table 4.14: Bulk Tissue Thickness For Subject #3

Side	Contour	N	Min	Mean	StdDev	Max
Whole Pelvis						
N/A	Flat	5921	14.1	115.3	46.2	194.8
	Equalized	5919	18.9	106.7	36.7	171.7
	(% Change)	0.0	34.0	-7.5	-20.6	-11.9
Beneath Ischial Tuberosity						
Right	Flat	334	14.1	36.1	27.0	109.2
	Equalized	327	25.5	44.3	23.4	116.7
	(% Change)	-2.1	80.9	22.7	-13.3	6.9
Left	Flat	289	15.0	39.0	30.5	121.2
	Equalized	340	18.9	41.1	26.6	119.7
	(% Change)	17.6	26.0	5.4	-12.8	-1.2
Behind Ischial Tuberosity						
Right	Flat	1966	41.9	132.3	33.9	184.1
	Equalized	2039	49.9	113.5	22.4	149.8
	(% Change)	3.7	19.1	-14.2	-33.9	-18.6
Left	Flat	1628	44.7	135.2	36.0	194.8
	Equalized	1596	48.7	127.7	28.0	171.7
	(% Change)	-2.0	8.9	-5.5	-22.2	-11.9
Left Of Left Ischial Tuberosity Or Right Of Right Ischial Tuberosity						
Right	Flat	414	56.0	126.0	27.2	164.1
	Equalized	537	54.8	118.2	24.3	152.8
	(% Change)	29.7	-2.1	-6.2	-10.7	-6.9
Left	Flat	443	62.6	134.5	28.9	182.7
	Equalized	374	41.9	124.8	26.8	160.7
	(% Change)	-15.6	-33.1	-7.2	-7.3	-12.0
In Front Of Ischial Tuberosity						
Right	Flat	71	88.2	95.1	3.3	101.8
	Equalized	97	98.1	108.0	3.4	113.7
	(% Change)	36.6	11.2	13.6	3.0	11.7
Left	Flat	76	86.4	98.0	6.6	115.4
	Equalized	43	98.4	104.5	3.5	114.2
	(% Change)	-43.4	13.9	6.6	-47.0	-1.0

Table 4.15: Thickness Of Individual Tissue Layers For Subject #3

Tissue Layer	Contour	N	Min	Mean	StdDev	Max
Entire Right Buttock						
Skin	Flat	32	2.59	3.19	0.36	3.90
	Equalized	31	2.24	3.11	0.49	4.71
	(% Change)	-3.13	-13.58	-2.51	37.62	20.70
Fat	Flat	30	5.57	10.32	2.72	16.84
	Equalized	29	4.59	11.68	2.58	15.52
	(% Change)	-3.33	-17.58	13.12	-5.33	-7.84
First Muscle Layer	Flat	11	6.57	12.15	3.80	19.68
	Equalized	15	4.87	14.34	7.77	38.31
	(% Change)	36.36	-25.75	18.08	104.57	94.66
Remaining Muscle	Flat	7	5.89	47.03	36.95	93.81
	Equalized	9	11.03	44.72	20.72	72.50
	(% Change)	28.57	87.21	-4.91	-43.92	-22.72
Beneath Right Ischial Tuberosity						
Skin	Flat	4	2.65	2.91	0.18	3.00
	Equalized	4	2.34	2.86	0.35	3.10
	(% Change)	0	-11.48	-1.85	98.00	3.20
Fat	Flat	3	6.66	7.15	0.51	7.67
	Equalized	4	11.14	12.37	0.97	13.51
	(% Change)	33.33	67.14	73.02	92.82	76.18
First Muscle Layer	Flat	0	N/A	N/A	N/A	N/A
	Equalized	0	N/A	N/A	N/A	N/A
	(% Change)	N/A	N/A	N/A	N/A	N/A
Remaining Muscle	Flat	3	5.89	12.80	10.05	24.33
	Equalized	4	11.03	21.85	13.42	40.98
	(% Change)	33.33	87.21	70.66	33.50	68.43
(Adjusted)	Flat	3	5.89	10.25	5.67	16.66
	Equalized	3	11.03	15.47	5.10	40.98
	(% Change)	0	87.21	50.93	-10.05	145.98
Behind Right Ischial Tuberosity						
Skin	Flat	10	2.59	3.14	0.45	3.90
	Equalized	9	2.54	2.92	0.31	3.45
	(% Change)	-10.00	-1.85	-6.85	-31.11	-11.68

Table 4.15: Thickness Of Individual Tissue Layers For Subject #3

Tissue Layer	Contour	N	Min	Mean	StdDev	Max
Fat	Flat	10	5.57	10.53	3.42	15.30
	Equalized	9	4.59	11.05	2.97	15.52
	(% Change)	-10.00	-17.58	4.92	-13.03	1.47
First Muscle Layer	Flat	3	15.19	16.75	2.54	19.68
	Equalized	6	8.09	18.05	10.90	38.31
	(% Change)	100.00	-46.75	7.74	329.96	94.66
Remaining Muscle	Flat	3	36.92	65.66	24.96	81.91
	Equalized	5	44.45	55.56	12.17	72.50
	(% Change)	66.67	20.39	-15.39	-51.25	-11.50
To The Right Of The Right Ischial Tuberosity						
Skin	Flat	16	2.90	3.34	0.25	3.70
	Equalized	15	2.70	3.39	0.48	4.71
	(% Change)	-6.25	-6.91	1.63	92.81	27.49
Fat	Flat	16	8.35	10.82	2.23	16.84
	Equalized	14	6.90	11.63	2.78	15.25
	(% Change)	-12.50	-17.45	7.50	24.60	-9.47
First Muscle Layer	Flat	7	6.57	10.97	2.11	12.86
	Equalized	8	4.87	11.25	3.51	15.24
	(% Change)	14.29	-25.75	2.56	65.49	18.49
Remaining Muscle	Flat	0	N/A	N/A	N/A	N/A
	Equalized	0	N/A	N/A	N/A	N/A
	(% Change)	N/A	N/A	N/A	N/A	N/A
In Front Of The Right Ischial Tuberosity						
Skin	Flat	2	2.74	2.74	0.00	2.74
	Equalized	3	2.24	2.54	0.27	2.74
	(% Change)	50.00	-18.37	-7.29	N/A	0
Fat	Flat	1	9.82	9.82	0.00	9.82
	Equalized	2	13.06	13.43	0.53	13.81
	(% Change)	100.00	33.01	36.85	N/A	40.69
First Muscle Layer	Flat	1	6.57	6.57	0.00	6.57
	Equalized	1	16.84	16.84	0.00	16.84
	(% Change)	0	156.44	156.44	N/A	156.44
Remaining Muscle	Flat	1	93.81	93.81	0.00	93.81
	Equalized	0	N/A	N/A	N/A	N/A
	(% Change)	-100.00	N/A	N/A	N/A	N/A

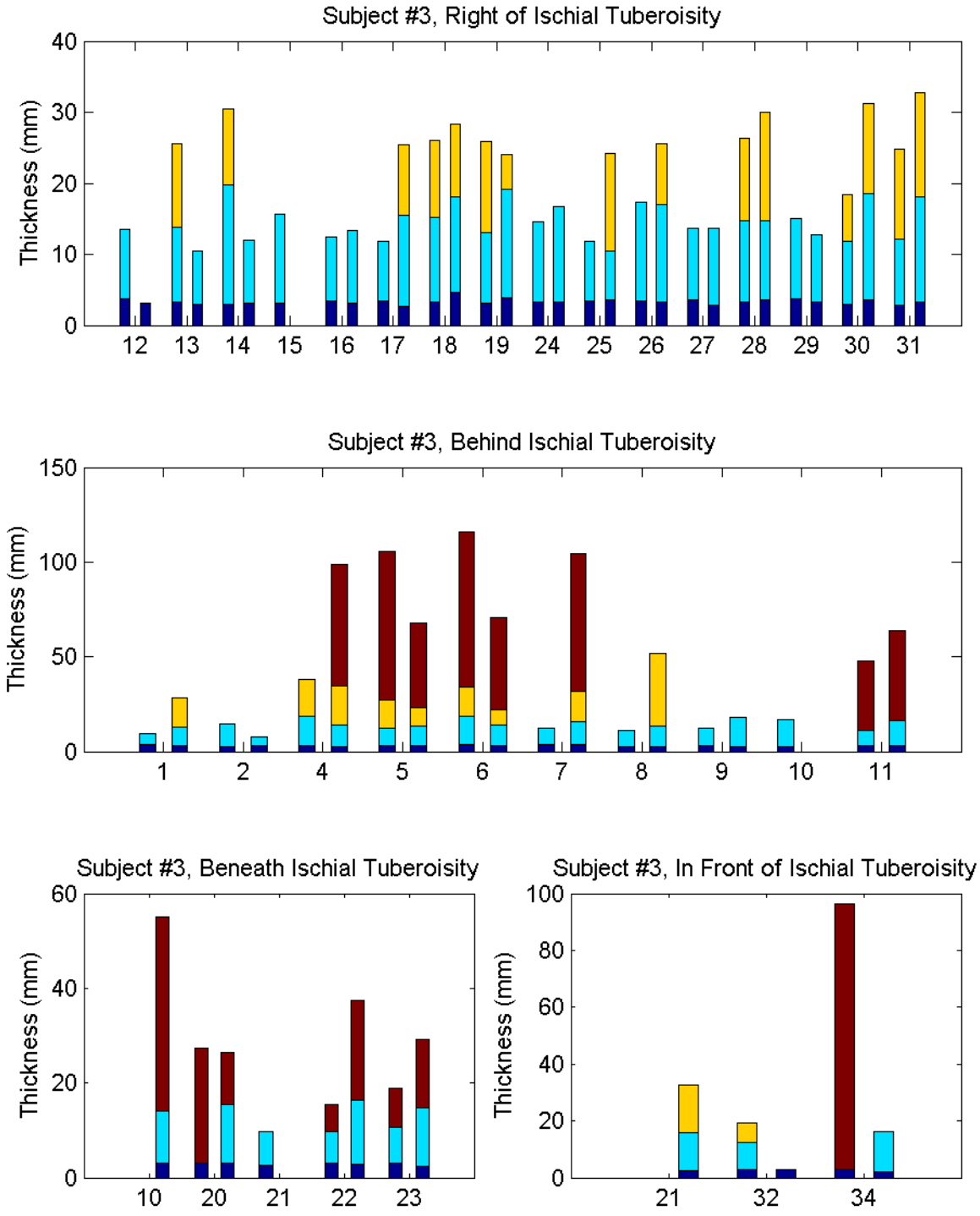

Figure 4.24: Thickness of skin(blue), fat(aqua) and the first muscle layer (yellow) broken down by region for both the flat and equalized contours. Bulk tissue between the last resolved layer and the pelvis is shown by brown bars. Numbers along the x-axis indicate the sensor where the measurements were taken. Each number has two bars associated with it; the bar on the left measures thickness for the flat contour, while the bar on the right measures thickness for the equalized contour. A missing bar indicates that no measurements were available for that combination of sensor and contour.

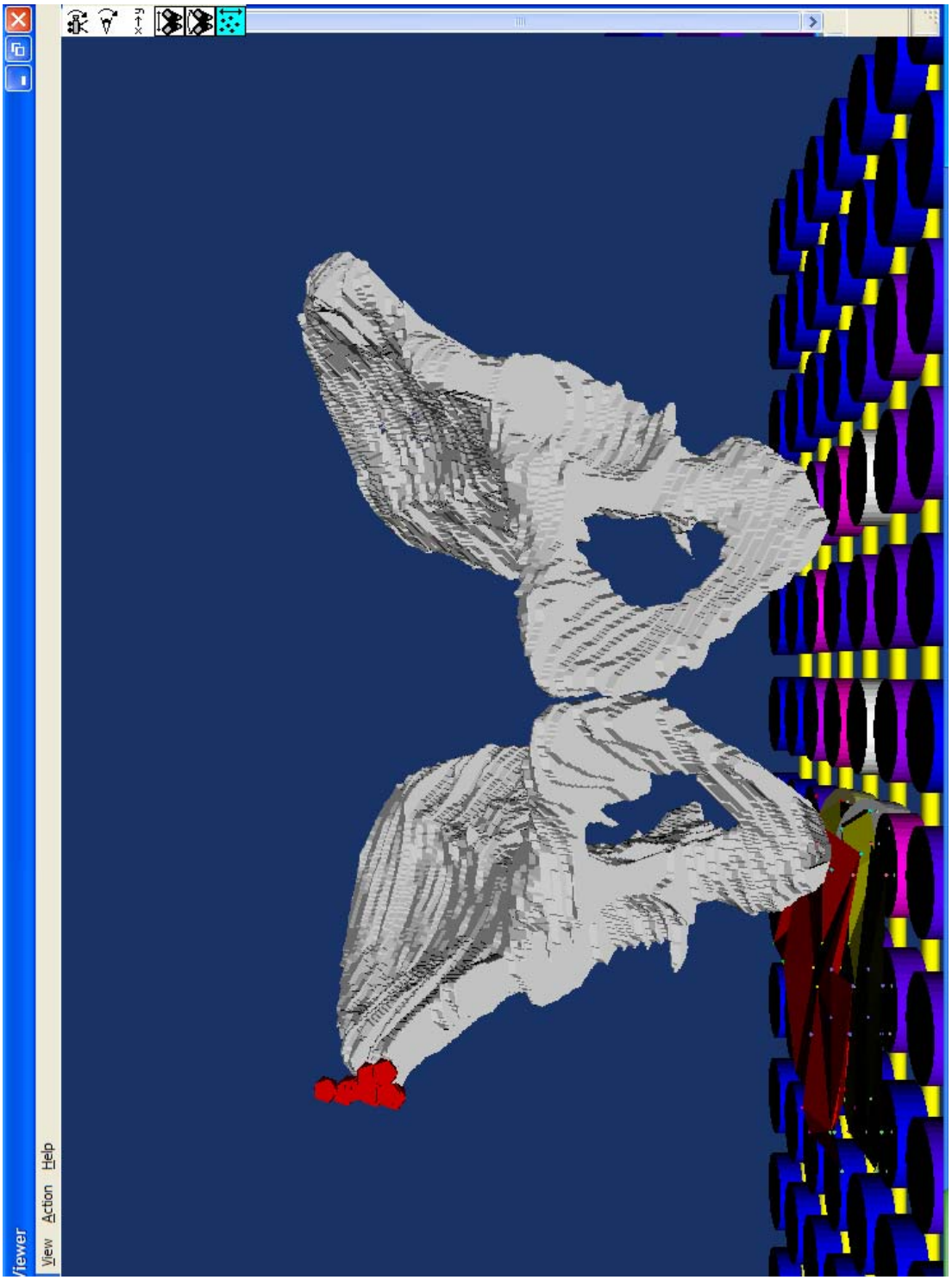

Figure 4.25: Front view of subject #3, flat contour.

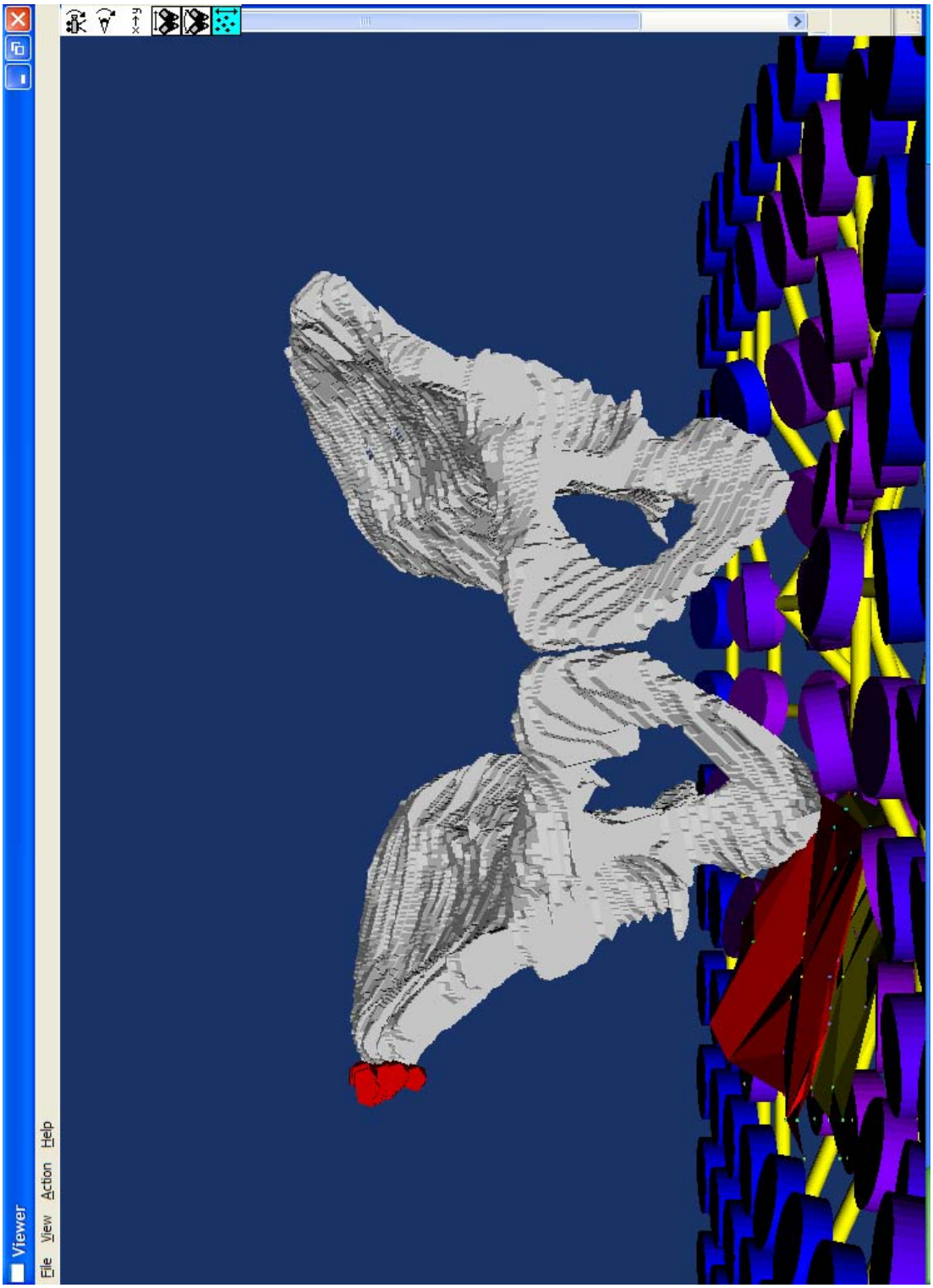

Figure 4.26: Front view of subject #3, equalized contour.

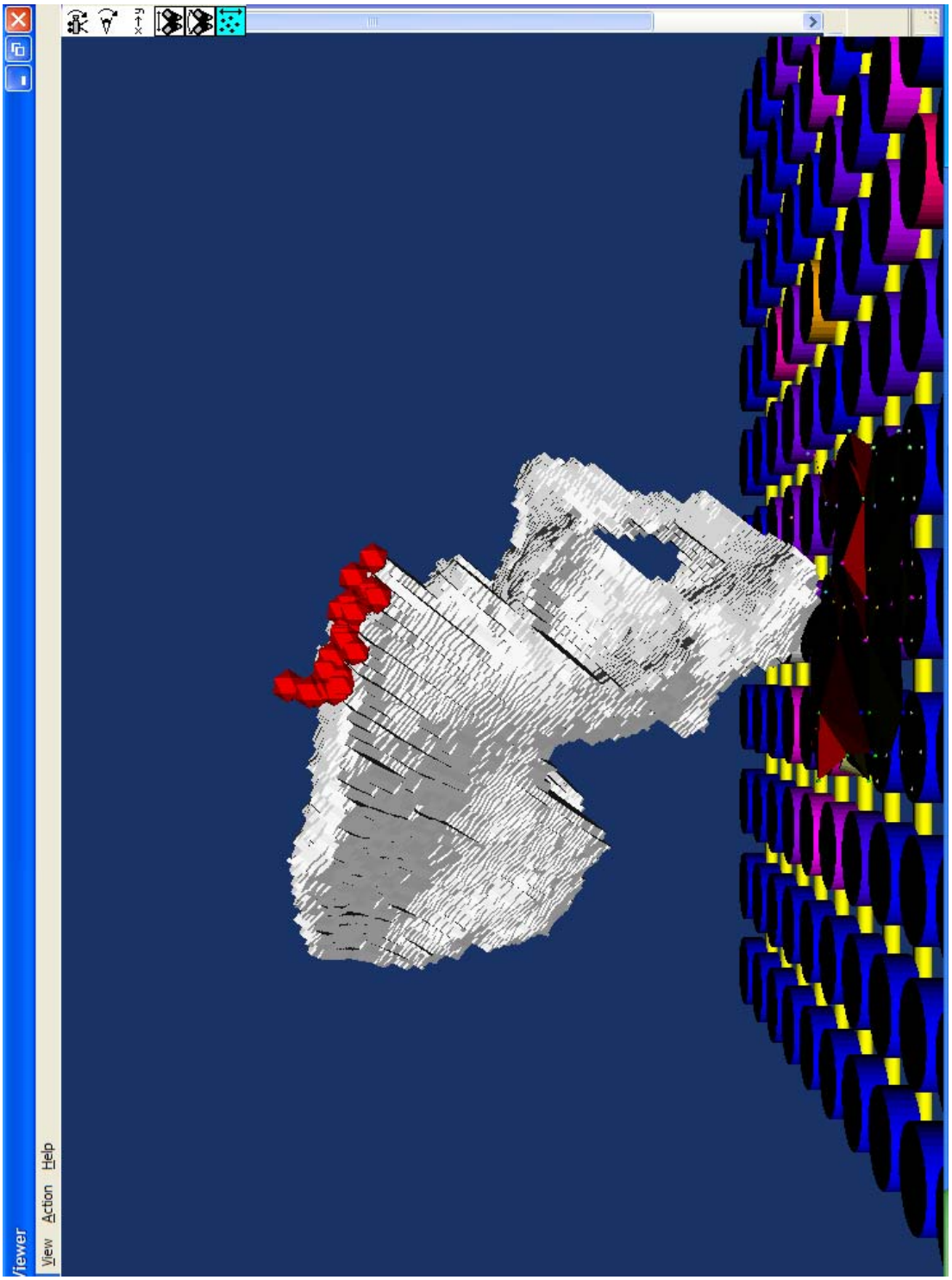

Figure 4.27: Side view of subject #3, flat contour.

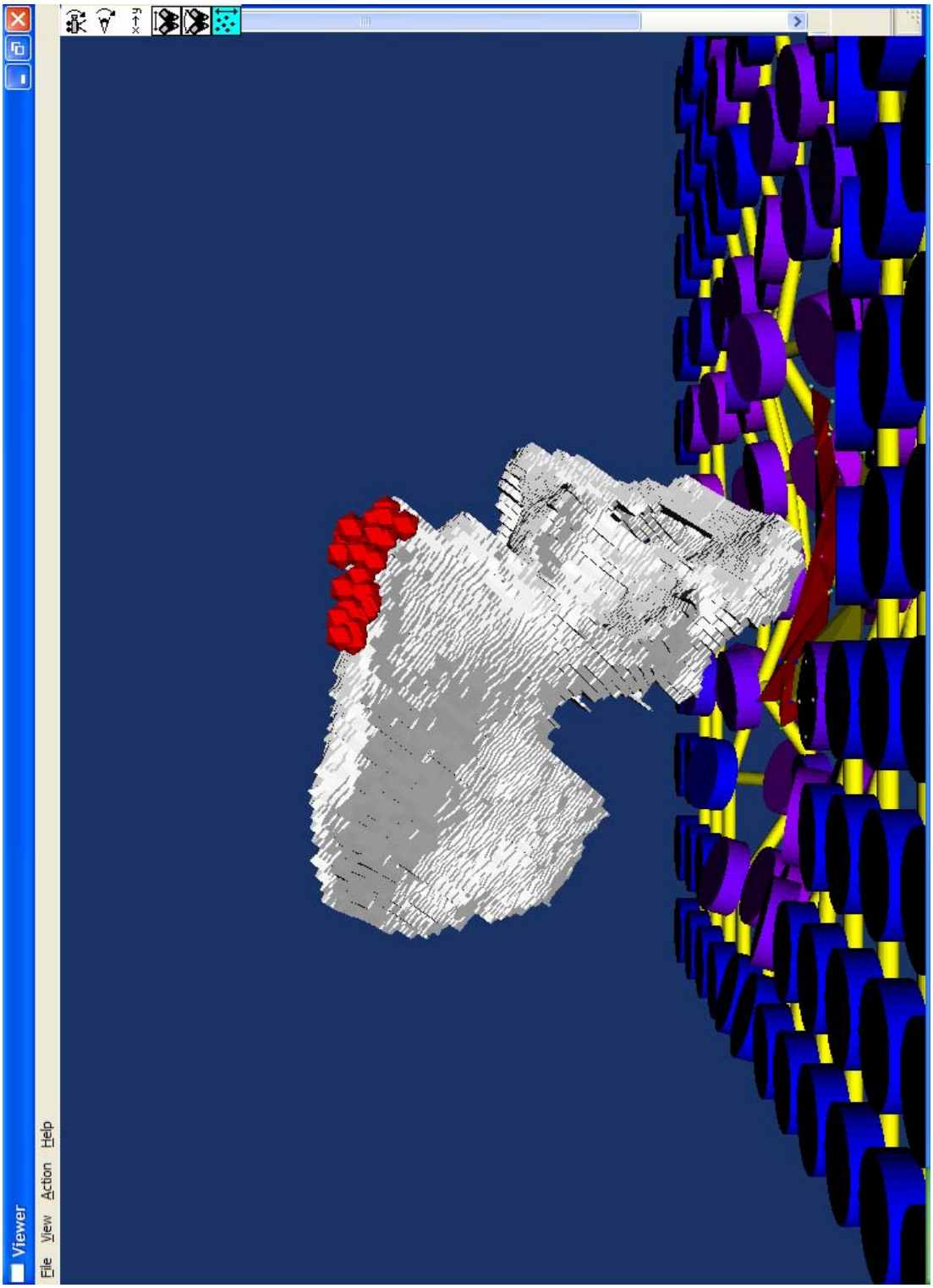

Figure 4.28: Side view of subject #3, equalized contour.

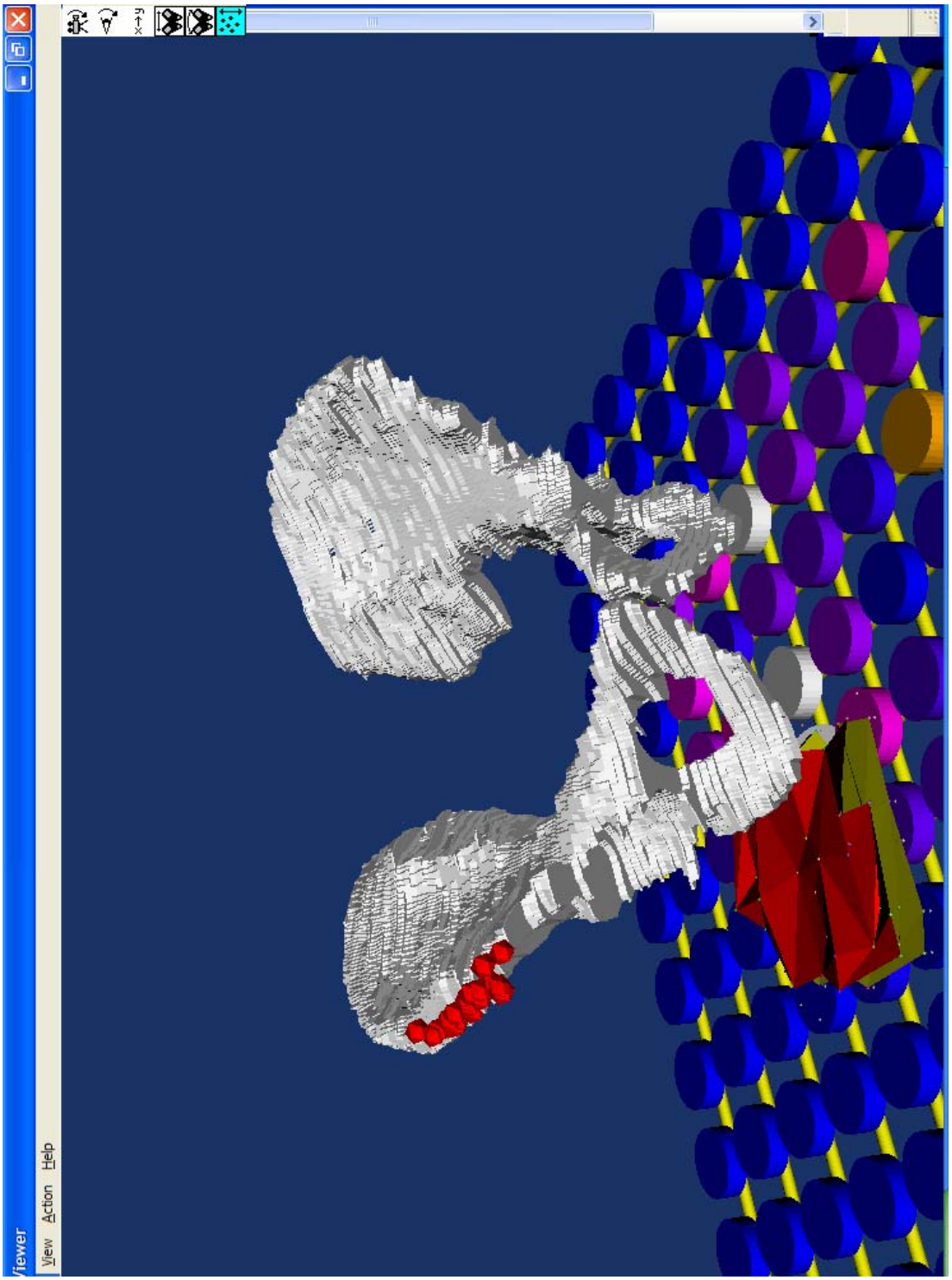

Figure 4.29: View of subject #3, flat contour from the right front corner.

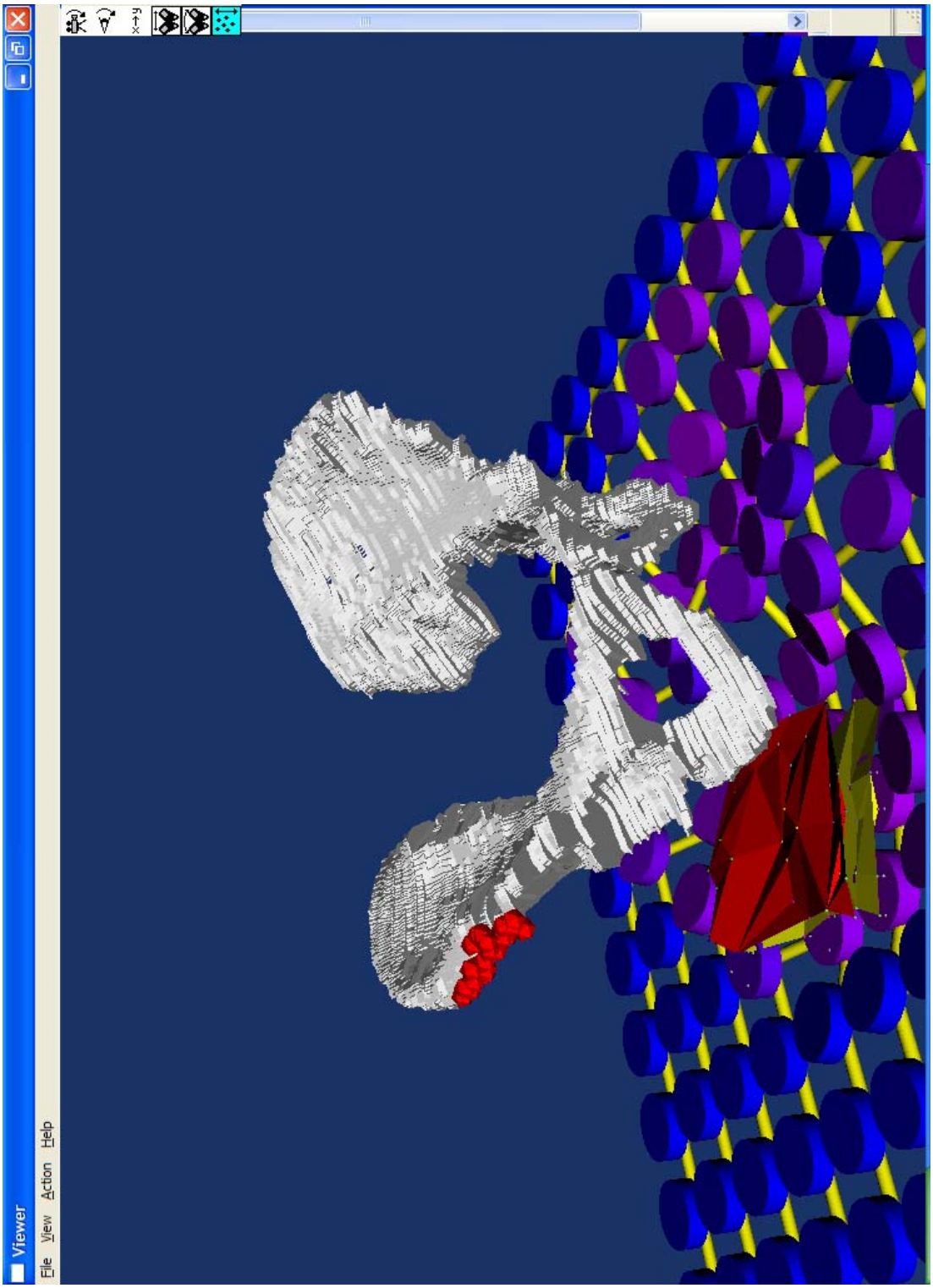

Figure 4.30: View of subject #3, equalized contour from the right front corner..

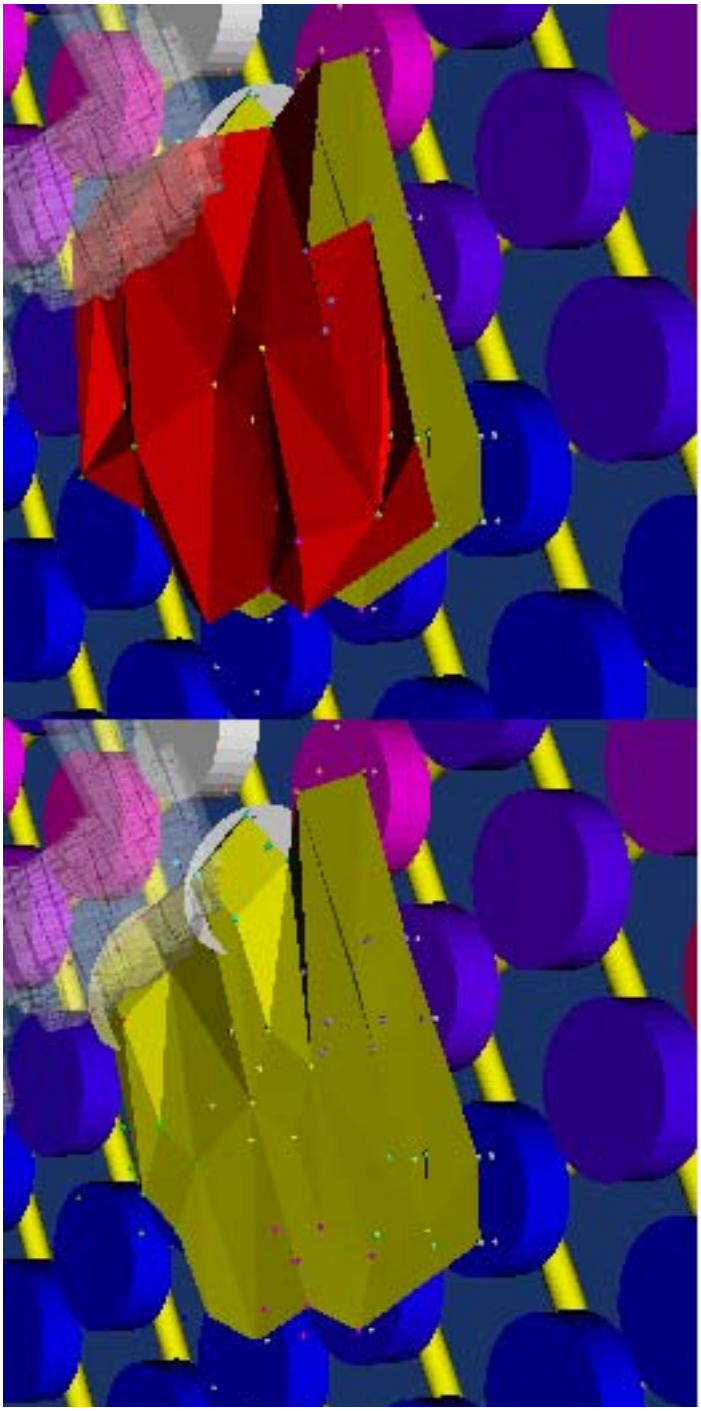

Figure 4.31: Boundaries between tissue layers of subject #3 for the flat contour.

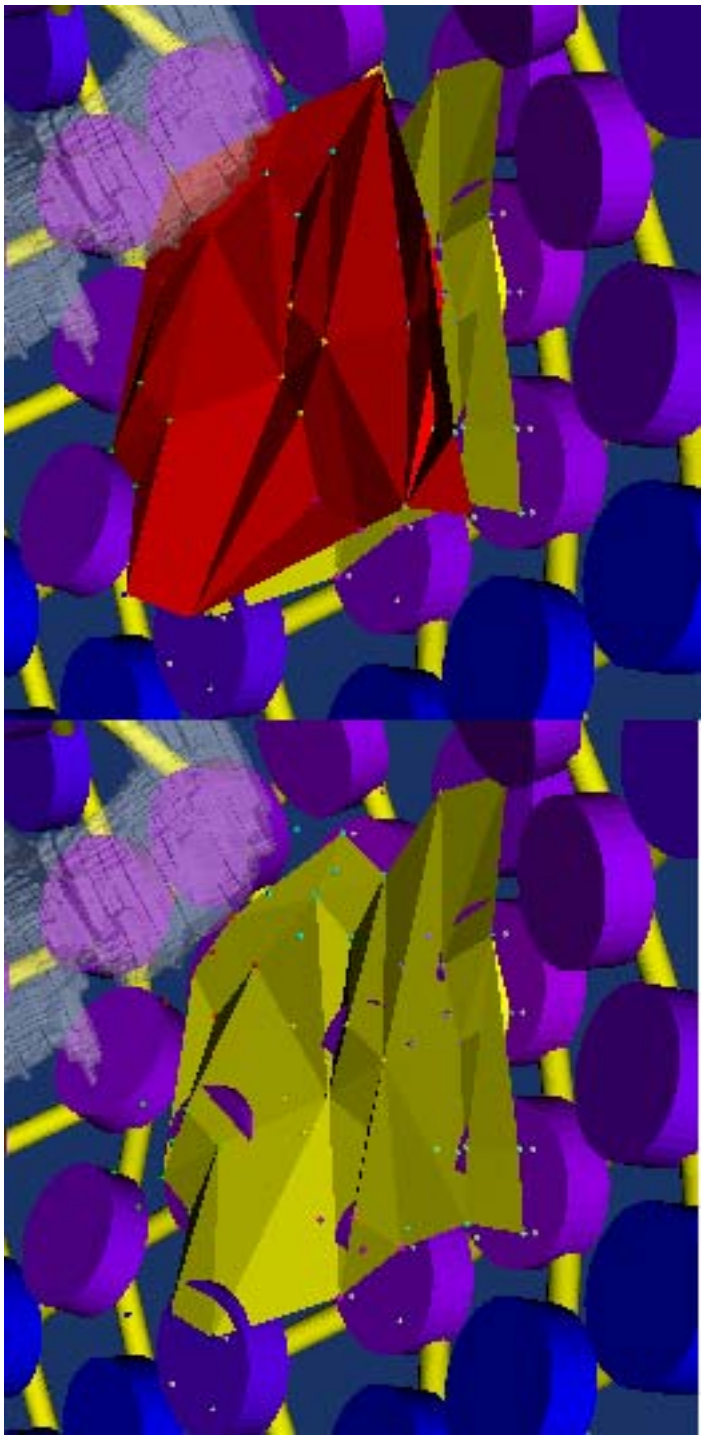

Figure 4.32: Boundaries between tissue layers of subject #3 for the equalized contour.

4.4 Discussion

4.4.1 Comparison Across Subjects

In this section, we compare the changes in the position and orientation of the pelvis and the changes that occur in the soft tissue layers of the buttocks for all three subjects with one another and draw conclusions about their similarities and differences. Because of the small number of subjects and becuase of the potentially large errors in the manual registration method, these conclusions are preliminary and serve primarily to suggest interesting research directions for a larger study. We begin by comparing the contours and interface pressure distributions, then examine the movement of the pelvis relative to the CASS surface, and finish with an examination of the changes to the soft tissues of the buttocks.

We observed two basic shapes for the equalized contours, one that was symmetric between its left and right halves and had the same maximum depth on either side and one that was asymmetric and had a much shallower left side than its right. These two shapes are the same as two of the four basic shapes obtained by Yue Li *et al*[66] from a cluster analysis of the contours obtained from 30 elderly subjects sitting on a surface that yields to match the shape of the buttocks, so it is unlikely that these patterns are just an artefact of the small population size of the study. However, there was no correlation between either injury status and the shape of the pressure-equalized contour. One of the healthy subjects and the subject with spinal cord injury had asymmetric contours while the remaining healthy subject had a symmetric contour. It is not clear at this time what factors influence which basic shape the pressure-equalized contour will assume for a given subject.

We also observed two types of interface pressure distribution: one that had peaks of equal magnitude on both the left and right sides and one that had only one peak on the right side. It is not clear at present why one subject had a peak only on one side while the other two had peaks on both sides. The interface pressure distribution type did not match the seating contour shape or the injury status of the subjects. Likewise, the one subject that had a significant roll to his pelvis had almost equal peak pressures on both sides, while the subject that had a single peak on the right side had no significant roll. This may be attributed to errors in the measurement of the position and orientation of the pelvises for all three subjects. That is, the subject who displayed a pressure distribution with one peak may have a large roll to the right in his pelvis that was hidden by the measurement error and would explain the pressure distribution. Likewise, the large roll in the pelvis for the subject with peaks on both the left and right side for his pressure distribution may not be present at all. However, if the positions and orientations of the pelvis for these subjects has been measured accurately, then center of gravity of the torso, which we did not measure, may play a role. If the center of gravity is positioned over the center of the buttocks, then we would expect both sides to be pushed down evenly on both sides. Likewise, if the pelvis is tilted to the right, but the center of gravity of the torso is shifted to the left, we would also expect to see an interface pressure distribution with peaks on both sides. However, if the pelvis is not tilted significantly to the left or the right and the center of gravity of the torso is shifted to one side or the other, then we would expect to see the pressure on one side be much higher than the other. However, it may also be that the

Table 4.16: Distance From Midpoint For All Three Subjects

Subject	Flat Contour				Equalized Contour			
	X	Y	Z	Total	X	Y	Z	Total
#1	-0.87	-4.73	5.77	7.51	-11.31	-0.04	-14.43	18.33
#2	-3.58	9.40	-6.83	12.16	-5.15	1.10	2.94	6.03
#3	4.45	-4.67	1.06	6.54	16.46	-1.06	11.49	20.10

location of the center of gravity of the torso has little influence over the interface pressure distribution, and the differences in the interface pressure distribution on the left and right sides arise from an asymmetry in the ability of the body to distribute the load on the soft tissues, e.g. the tissues on one side of the body do a better job of redistributing pressure than the tissues on the other side. This asymmetry may manifest in some subjects but not in others. Finally, the low peak pressure on the left side for subject #2 may simply be a difference in the way that subject is positioned on the CASS. Future studies will need to take into account the position of the center of gravity of the upper body, either by measuring it or by controlling for it, to resolve this question. They will also need to more carefully control how subjects are positioned, so as to rule out that factor as a cause of the difference in distributions of interface pressure.

One of the main findings of this pilot study is that if the measurements of the position and orientation of the pelvis are accurate, seating subjects on a flat contour can result in a large amount of tilt in the pelvis either from front to back or to one side or the other. For the equalized contour, however, the pelvises of all three subjects were more closely aligned with the seating surface. This may not be a coincidence. A large pitch or roll will by necessity push at least one of the ischial tuberosities downward into the soft tissues, squashing the tissue and producing a high amount of pressure beneath the ishcial tuberosity. In order for pressure to be equalized over the seating contour, the pelvis must be aligned with the seating surface so this does not happen.

During the equalization process, subject #1’s pelvis moved twice as far as subject #2 and #3. An interesting question is whether the pelvises of the three subjects are convering towards the same point on the CASS just as they converged to the same orientation. Table 4.16 shows the distance between the location of the center of the pelvis for each subject relative to the CASS and the midpoint for all three subjects for the same seating contour. If the pelvises are converging towards the same point, this distance should decrease. As the table shows, the distance between each subjects pelvis and the midpoint increases as the contour changes from flat to its equalized shape. However, in moving from flat to equalized, all three subjects converge to the same y-coordinate. This places both ischial tuberosities directly over the seventh row of actuators instead of between rows. The pelvis also moves from left to right such that the ischial tuberosities wind up over the top of an actuator head rather than in between them. For all three subjects, the equalization algorithm positioned the right ischial tuberosity somewhere over the <5,6> actuator and the left ischial tuberosity over the <7,6> or <8,6> actuator, depending on the width of the

pelvis. Not coincidentally, these are the deepest points on the seating contour. This positioning makes sense, since having the ischial tuberosities over the empty space between actuators would allow the ischial tuberosity to push the soft tissues of the body through the hole, generating a lot of pressure. Because the pelvises of the three subjects differ in width, each would wind up at a different x-coordinate to make this happen.

If the bulk thickness measurements are accurate, all three subjects show a decrease in bulk tissue volume and mean bulk tissue thickness over the entire pelvis when the contour changes from flat to its equalized shape. The relative change in volume is largest for subject #1 and possibly represents the redistribution of tissue towards the thighs. A similar redistribution probably occurs for subjects #2 and #3 but is harder to detect because the change in volume is much smaller. In terms of changes to the individual layers of skin, fat and muscle in the right buttock, the skin thickness does differ appreciably between the flat and equalized contours for all three subjects. Subjects #1 and #3 showed a small, but significant, increase in the mean thickness of the fat layer, while the mean thickness of the fat layer for subject #2 remained constant. All three subjects showed an increase in the thickness of the first muscle layer of between 2 and 5 mm, but only the increase for subject #2 was statistically significant. The lack of statistical significance for the changes to the first muscle layer of subject's #1 and #3 probably occurs because of the difficulty in resolving the far side of this layer for those subjects for the equalized contour. Only about half of the ultrasonic transducers for the equalized contours of subjects #1 and #3 received echoes from the boundary between the first and second muscle layers, compared to 84% of the sensors for subject #2.

Assuming that the measurements for subjects #1 and #3 represent a real thickening of the first muscle layer rather than a statistical artefact, since most of the transducers fall beneath the pelvis rather than outside of it, this increase in thickness represents an increase in volume of the first muscle layer, most of which is the gluteus maximus. Consequently, if the total tissue volume beneath the pelvis does in fact *decrease* between the flat and equalized contours, any shift in tissue volume towards the thighs and upper leg must occur in the deeper muscle layers, such as the semitendinosus, semimembranosus or the long head of the biceps femoris. For the most part, the gluteus maximus muscle covers the back of the buttocks and rises to attach to the upper third of the back of the femur towards the outside of the body. By the time one reaches the upper part of the thighs and the leg, the most superficial muscles are the semitendinosus and semimembranosus muscles. Consequently, any shift in muscle mass towards the thighs and upper leg would need to come from these muscles. However, because we cannot resolve the these muscles, we cannot say for certain that this is happening. Improvements need to be made to the ultrasonic transducers of the CASS that will allow us to resolve these muscles in the upper part of the leg.

More interesting patterns occur beneath the ischial tuberosities of all three subjects. One very important observation is that while the mean thickness of soft tissue beneath the right ischial tuberosity for the three subjects is very different for the flat contour - having values of 37.9, 26.7 and 36.1 mm - the mean thicknesses of soft tissue beneath the right ischial tuberosity for the equalized contour are very similar - having values of 45.6, 42.1 and 44.3

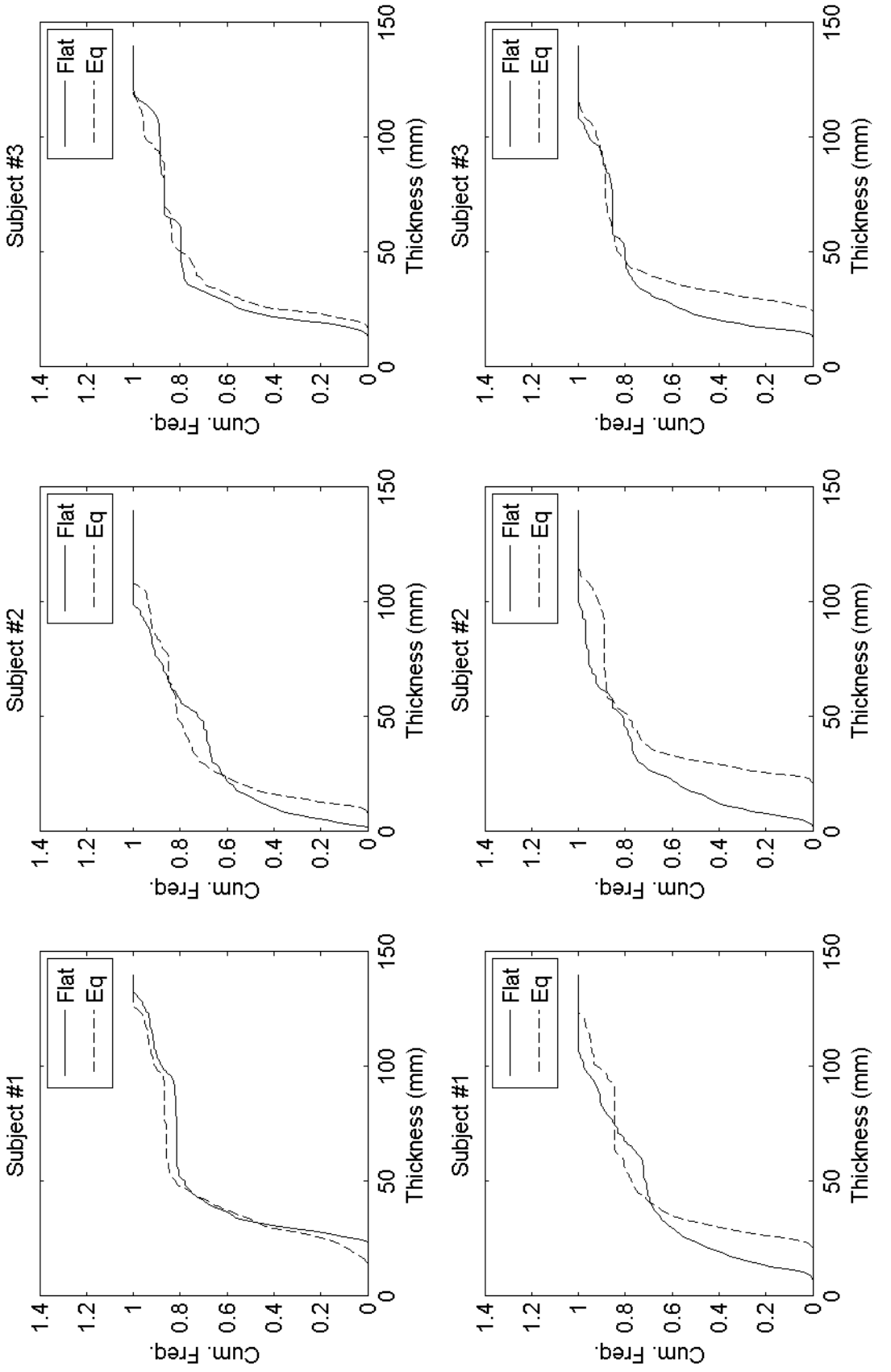

Figure 4.33: Cumulative thickness of bulk tissue beneath the left (top) and right (bottom) ischial tuberosities for all three subjects.

mm. This equality is surprising, since subject #3 is heavier and has a very different body composition from subjects #1 and #2. While this equality may simply be the result of inaccurate bulk thickness measurements, it may also reflect a real similarity in the response of the tissues of all three subjects to movement from a flat to a pressure-equalized contour. If the bulk tissue thickness measurements are accurate, it would mean that since subject #3 has a much thicker layer of fat, he is bearing more of the weight of the pelvis on the fat than subjects #1 and #2. This finding is significant because fat is stiffer than muscle and more resistant to fluid loss[112] and can tolerate larger pressures than muscle[40]. If this finding holds up for a larger subject pool, then it implies that subjects with more fat beneath the ischial tuberosity will show a greater resistance to developing pressure ulcers than subjects with more muscle.

Another interesting pattern can be observed beneath the left ischial tuberosity. Here we see that the mean thickness of tissue beneath the left ischial tuberosity does not change significantly between the flat and the equalized contour for all three subjects, although the distribution of bulk tissue does change, with a thickening of the tissue in the thinnest areas for subjects #2 and #3. For subject #1, we see a slight thinning of some of the tissue as the roll to the right disappears. That the mean thickness of tissue remains constant for all three subjects between the flat and equalized contours is very surprising because the interface pressures beneath the left ischial tuberosities for subjects #1 and #3 for the flat contour are nearly as high as the interface pressures beneath the right, where for all three subjects, we see a substantial increase in the mean thickness of soft tissue.

The simplest explaination for the difference in the reaction of the soft tissue beneath the left and right ischial to loading is that the measurements of the position and orientation of the pelvises for the three subjects are inaccurate and that the changes on the left side are similar to those on the right. If this is not the case, and the position and orientation measurements are accurate, then the simplest explanation becomes that the mechanical properties of the soft tissues on the left are very different from those on the right. Under this interpretation, the soft tissues on the right side for all three subjects are much more compressible than the soft tissues on the left. Thus, when loaded, the left side distorts less than the right side, and as the load from the pelvis is redistributed as the contour moves towards its equalized shape, the tissue on the left side does thicken as much in response to the reduced load as the tissue on the right side. If this hypothesis is true, then we would expect to see that the tissue beneath the left ischial tuberosity is substantially thicker than the tissue beneath the right when seated on the flat contour.

Figure 4.33 shows the cumulative fraction of bulk thickness measurements beneath the left and right ischial tuberosities for each subject. While subject #1 exhibits the expected pattern, subjects #2 and #3 do not. Consequently, differences in mechanical properties alone cannot explain the different response of the tissue beneath the left and right ischial tuberosities.

Another posibility is that factors outside the relationship to the pelvis to the seating surface and the biomechanical properties of the soft tissue play an important role in determining the relationship between interface pressure and the distortion of the soft

tissues under load from the pelvis. Much of the load placed by the pelvis on the soft tissues of the buttocks comes not from the weight of the pelvis itself, but from the upper half of the body which is positioned above the pelvis. As described previously, as the center of mass for the upper torso shifts to one side or the other, that side of the pelvis will press harder downward into the soft tissues. However, as the pelvis changes location and orientation during the pressure equalization process, its movement is going to affect the location of the center of gravity of the torso through its connection with the spine. Consequently, it may be that one of the principal effects of sitting on the equalized contour is to center the torso above the pelvis so that the load from the pelvis is evenly distributed on either side. Another possibility is that the body favors distributing the load of the pelvis to one side or the other. In this case, sitting on the pressure equalized contour may shift the torso to the favored side, where the distribution of tissue is altered to better handle the increased load. Because the load from the torso is shifted to the favored side, the distribution of tissue on the other side may not need to change as much to distribute the load from the pelvis and reduce the interface pressure beneath that side. However, without measuring the center of gravity of the torso with respect to the pelvis, we cannot confirm or deny this hypothesis.

Regardless of the cause for the asymmetry in the response to loading between the left and right sides of the buttocks, it is clear that if the position and orientation of the pelvises for all three subjects have been measured accurately, interface pressure cannot be used as a surrogate for soft tissue thickness measurements. Indeed, for all three subjects, there was no correlation between interface pressure and bulk tissue thickness for either contour, nor did the interface pressure on the flat contour predict the change in bulk tissue thickness between the flat and equalized contours or the depth of the equalized contour at the pressure sensor.

The final observation we will make in this section is that the behavior of the pelvis and the soft tissues of the spinal cord injured subject observed in this study are remarkably similar to the behaviors of the healthy subjects. There was no simple, immediately obvious difference between the way his body responded to sitting on the flat contour or in how his tissues distributed the load for the equalized contour. This similarity may have occured because the spinal cord injured subject is an outlier and the similarities are the result of coincidence. In this case, a study using a larger subject population is all that is needed to reveal the differences in the way the pelvis and soft tissues of people with spinal cord injury and those that are healthy react to sitting on different-shaped seating surfaces. It may also be the case that large measurement errors in the position and orientation of the pelvises of all three subjects may be hiding differences between the response of the subject with spinal cord injury and the healthy subjects. In this case, the improvements to the registration algorithm described in section 3.4.1.4 will reveal the differences in the way the pelvis and soft tissues of healthy subjects and those with spinal cord injury respond to sitting on different-shaped seating surfaces. However, if neither the small study size nor the potential errors in measuring the position and orientation of the pelvises of the three subjects can account for the differences in response, it may be the case that there are no clear differences in the way the soft tissues distort for subjects with and without spinal cord injury, and differences in succeptibility to pressure ulcers can be attributed to

differences in the ability of the soft tissues to tolerate distortion for prolonged periods rather than differences in the amount of distortion.

4.4.2 Comparison With Previous Work

4.4.2.1 Related Work On Measuring Pelvic Orientation

Since posture affects the distribution of pressure at the interface between the buttocks and the seating surface, Lalonde *et al*[60] measured how different seated positions affected the posture of twelve subjects with spinal cord injury. They defined posture in terms of three angles: the angle between the trunk of the body and the seating surface (the *trunk angle*), the angle between the pelvis and the seating surface (the *pelvis angle*), and the angle between the pelvis and the femur (the *hip angle*). The way they defined the pelvis and hip angles makes them similar to the pitch and roll angles used in this thesis, but they had no corresponding measurement to the yaw angle. The trunk, hip, and pelvis angles were computed by measuring the locations of markers on the surface of the body above eight anatomical landmarks using a system of video cameras and computing the angles from the relative orientations of lines drawn between the markers. They found that over a combination of eight different seating positions, they found that tilting the chair as a whole changed the orientation of the pelvis but not the trunk with respect to the seating surface. They also found that altering angle between the seat and the back changed both the orientation of the trunk and the pelvis and affected the former more than the latter. While superficially similar to the work in this thesis in measuring the orientation of the pelvis, Lalonde et al did not vary the seating contour but instead varied the orientation of the seating apparatus with respect to the floor and the angle between the back of the seat and the bottom. In addition, they only reported the changes in pelvic orientation relative to the initial seating position, so their work cannot be directly compared to ours. Finally, they used markers on the skin surface to measure the orientation of the pelvis, and because the skin is not rigidly attached to the pelvis, these markers may slip relative to the anatomical landmarks they were placed above. In constrast, the points we measured for registration were matched directly to a surface model to compute orientation, treating the skin as noise and so we did not suffer from this problem.

4.4.2.2 Related Work On Seating Contour Shape

Yue Li and her coworkers investigated the natural seating contours for 30 elderly subjects[66]. The natural seating contours were measured by the electronic shape sensor (ESS), a device developed at the Seating and Soft Tissue Biomechanics Laboratory by David Brienza and his group[13]. The ESS is a chair whose surface is an 12x11 array of actuators. However, unlike the CASS, the actuators are not driven by motors but are instead connected to springs in such a way that the deflection of each actuator can be measured and recorded by a computer system. When a subject sits on the ESS, his or her buttocks create a seating contour that is an approximation of the unloaded shape of the buttocks.

In her work, Yue Li applied Ward's hierarchical method for cluster analysis [137] to the contours measured by the ESS for 30 elderly subjects. She found that there were four basic seating contours:

(1) A contour in which the left lobe was deeper than the right lobe.
(2) A contour in which the right lobe was deeper than the left lobe.
(3) A contour in which both lobes were the same depth.
(4) A contour in which both lobes were the same depth, but the width between their peaks was significantly larger than the width between the peaks of shape (3).

Yue Li and her collaborators did not measure interface pressure or other variables, so no attempt was made to relate contour shape to other factors. In the pilot study, the pressure-equalized contours for two subjects displayed contour (2), while the pressure-equalized contour for one subject displayed contour (3). As discussed above, the contour shapes did not correlate with interface pressure distribution for the flat contour, injury status, or the orientation of the pelvis for the flat or the equalized contour. However, given the small number of subjects in the pilot study, it cannot be stated definitively that no relationship exists between these variables.

4.4.2.3 Related Work On Biomechanical Properties Of Soft Tissue

In her PhD thesis work, Jue Wang developed the ultrasonic instrumentation for the CASS[131,132,135] and computed the parameters of Fung's quasilinear viscoelastic (QLV) model[133,136] for soft tissue for six healthy men and three men with spinal cord injury. These parameters are of interest because differences in the biomechanical properties of the soft tissues of the buttocks may give some clue why some individuals are more succeptible than others to developing pressure ulcers. She computed the QLV model parameters by using one of the ultrasonic transducers to track the change in the thickness of the soft tissue layers during an indentation test conducted beneath the femur approximately 4 cm distal from the right ischial tuberosity. The indentation test was performed by using the ultrasound sensor to measure the thickness of the bulk tissue above the transducer and then moving the actuator containing the sensor up until either a maximum indentation depth of 20% of the initial bulk thickness or a maximum indentation load of 16 N was reached. Once the actuator had reached its final height, it was held there for five minutes, then returned to its rest height. Throught the entire process, the thickness of the fat and muscle layers, the interface pressure, force, and sensor orientation were tracked. By fitting the changes in soft tissue thickness over the hold interval to the QLV model, Ms. Wang was able to measure the parameters of the reduced relaxation function and the elastic response of the soft tissues. The results of her work[133,134,136] showed that the soft tissues of the subjects with spinal cord injury had significantly different mechanical properties than the soft tissues of the healthy subjects. The subjects with spinal cord injury tended to have a decreased amplitude of stress compared to the healthy subjects, and the former exhibited much less relaxation over time than the latter. Furthermore, the relaxation function for the subjects with spinal cord injury tended to be linear, while the relaxation function for the healthy subjects showed a clear reduced relaxation and a fast viscous response. Mechanical parameters were measured for the bulk tissue rather than for fat and muscle separately, but similar work by Zeltwanger *et al*[143,144] using essentially the same method measured the effective Young's Modulus of the fat layer for six able-bodied male subjects and found it to lie within 14 to 76 kPa.

The primary implication of Ms. Wang's results for this thesis is that the elastic response of

the soft tissues of the buttocks to the indentation of the pelvis should be weaker for the spinal cord injured subject than for the two able-bodied subjects. Consequently, the soft tissues for the subject with SCI should distort more between the flat and the pressure-equalized contours and the change in thickness for the soft tissues beneath the ischial tuberosity should be larger for subject #3 than for the other two subjects. However, this is not what we observe. Instead, the change in thickness beneath the ischial tuberosities for subject #3 has about the same magnitude as the change in thickness for subject #1. If this behavior cannot be attributed to errors in measuring the position and orientation of the pelvises of the three subjects, this may indicate that subject #3 is an outlier and the mechanical properties of his soft tissues did not vary significantly from those of able bodied subjects.

4.4.2.4 Related Work On Measuring Soft Tissue Thickness

Although both Wang[133,136] and Zeltwanger[143] measured the thickness of the fat and muscle layers beneath the femur as part of their experimental protocols, they did not report these values[4]. Other researchers have endeavored to measure the distortion of the soft tissues of the buttocks *in vivo* using a variety of methods. Reger *et al* [107] measured the changes in soft tissue thickness between the skin and the ischium of the pelvis for supine subjects using MRI imaging, but because they could not make these measurements for seated subjects, their work is not directly comparable to ours. Clark *et al* [19] measured the thickness of bulk tissue between the skin and the sacrum for seated subjects with a B-mode ultrasound device and concluded that soft tissue thickness alone could not predict the development of pressure ulcers beneath the sacrum. They also found that women had more soft tissue beneath the sacrum than men, with the thickness of soft tissue ranging between 5.0 and 37.6 mm (mean 14.8 mm) for women but only between 4.0 and 16.7 (mean 8.7 mm) for men. Because measurements were taken by seating subjects on a soft cushion with a hole cut out for the ultrasound device, and such an arrangement would necessarily prevent any attempts at simultaneously measuring interface pressure at the location of the ultrasound transducer, the techniques used by Clark *et al* were not suitable for this thesis.

Indirect Measurements Of Soft Tissue Shape Through Stiffness Measurements

The work in the literature that has the most bearing on this thesis is the work done by Brienza *et al* [11][13] using the first generation of the CASS. Because they could not measure soft tissue thickness directly, Brienza *et al* used stiffness measurements as a proxy for thickness measurements, working under the assumption that thinner tissue has a higher stiffness than thicker tissue under an identical load. Based on this assumption, they reasoned that minimizing the stiffness of the soft tissues across the buttocks would minimize the distortion of the soft tissues from their unloaded shape. Their method was very similar to ours. A pilot study was performed on ten able-bodied subjects [12]. Subjects were first seated on the electronic shape sensor (ESS) described in section 4.4.2.2

4. In her PhD thesis, Jue Wang did report some values for the thickness of the fat and layers of muscle in the vicinity of the test site for her subjects. However, these values were obtained were obtained from a B-mode ultrasound examination with the subjects lying down and are not directly comparable to our thickness measurements, which are for seated subjects.

above to measure an initial approximation to the unloaded shape of their buttocks. Subjects were then transferred to the CASS and seated on a flat contour, where an initial set of interface pressure and soft tissue stiffness measurements were taken. Stiffness was computed by moving each actuator down by 0.4 mm and measuring the change in pressure. Since the area over which the change in pressure was measured remains constant, the soft tissue stiffness could be computed as:

$$k_i = \frac{P_i - P_{i-1}}{0.4} \tag{4.1}$$

where P_{i-1} and P_i are the interface pressure before and after the move and 0.4 is the distance moved in mm.

After the pressure and stiffness measurements were made for the flat contour, the actuators of the CASS were moved downward to create the contour measured by the ESS and another set of pressure and stiffness measurements were obtained for this initial contour. Then an iterative algorithm [11] was applied to minimize the soft tissue stiffness. This algorithm would compute an optimal shape based on the current pressure and stiffness distribution, move the actuators of the CASS to match that shape, and then measure the resulting pressure and stiffness distribution. If these values were close enough to the optimal values, the algorithm would terminate. Otherwise, a new optimal shape was computed and the process repeated. During the operation of the algorithm, stiffness measurements were smoothed by averaging them with the previous measurement using the formula:

$$k_i = 0.75k_{i-1} + 0.25\frac{P_i - P_{i-1}}{0.4} \tag{4.2}$$

Once the algorithm converged, pressure and stiffness would be recorded for the final contour, and the shapes of the initial and final contours for each subject were carved into high-grade polyurtheane foam cushions. Subjects were then seated on these cushions and the pressure at the interface between the buttocks and the cushion was measured using a thin mat of pressure sensors to see if minimizing soft tissue stiffness would create a more even pressure distribution for subjects seated on actual seat cushions instead of just the CASS. The results of the pilot study and a study performed on 30 elderly subjects who used wheelchairs for their daily locomotion showed that contours computed by the stiffness minimization algorithm resulted in lower peak pressures and a more even distribution of pressure than either the flat contour or the contour measured by the ESS, regardless of whether the subject was seated on the CASS or a foam cushion. The results of these studies also showed that the contour generated by the stiffness minimization algorithm shifted higher pressures towards areas of low stiffness. Under the assumption that higher stiffness meant thinner tissue, these results meant that areas of higher load were being redistributed towards areas of thicker tissue.

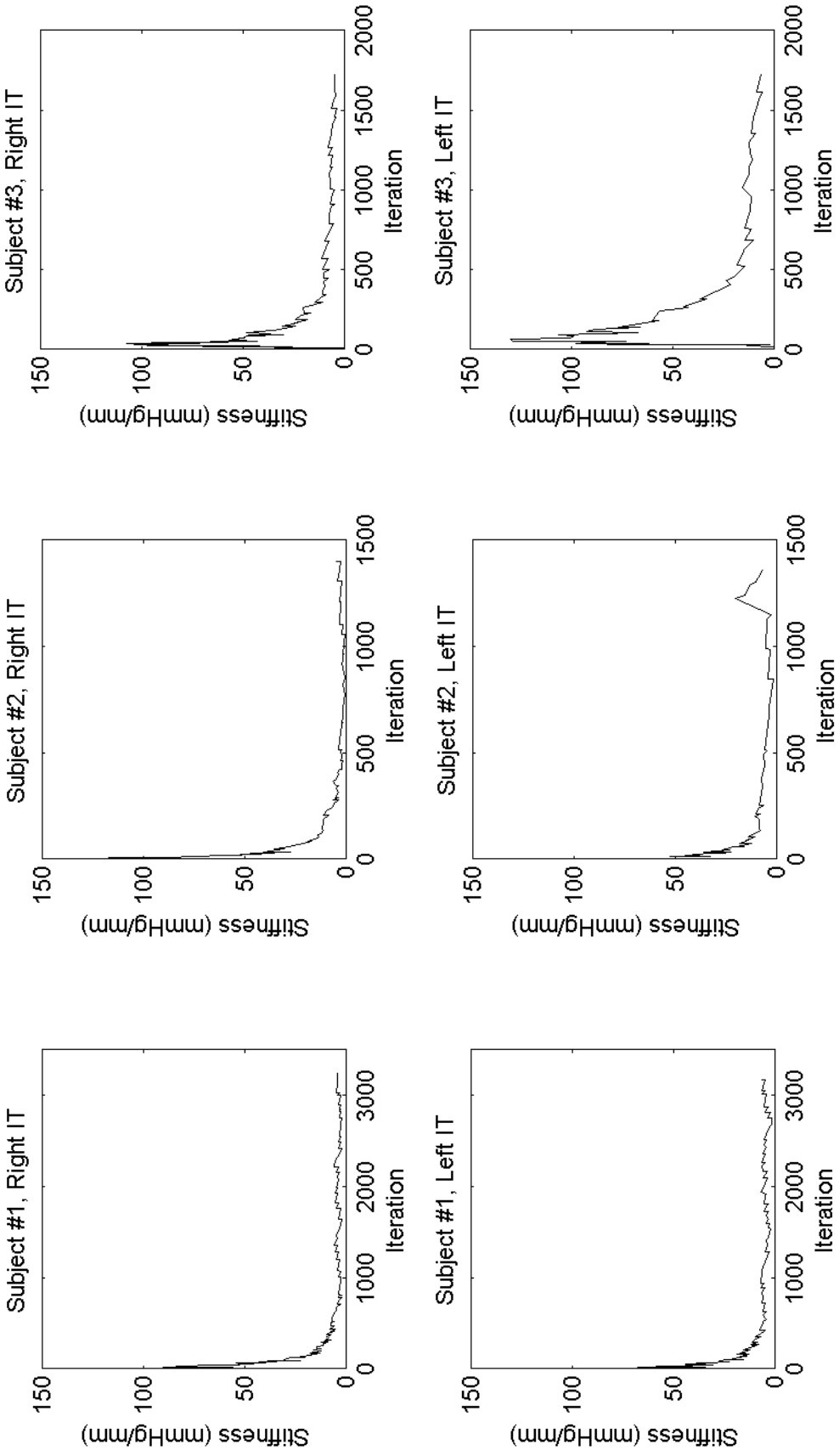

Figure 4.34: Development of soft tissue stiffness beneath the left (top) and right (bottom) ischial tuberosities over the course of the equalization algorithm for all three subjects.

Differences Between Our Measurements Of Soft Tissue Shape And Previous Work

However, if the position and orientation of the pelvises of the three subjects used in our pilot study have been measured accurately, the results of this pilot study call this assumption into question. Although we did not measure soft tissue stiffness across the entire contour as Brienza *et al* did, we did record the interface pressure across the entire contour at each step of the equalization algorithm. These measurements allow us to compute the soft tissue stiffness at the actuator that moved during each iteration using equation (4.2). Figure 4.34 shows how the soft tissue stiffness beneath the ischial tuberosities changes between the flat and equalized contours. The stiffness beneath the ischial tuberosities for the flat and equalized contours in our study is comparable to the mean stiffness observed by Brienza *et al* [13] for their flat and stiffness-minimized contours. We note that there is no clear difference in the way stiffness declines between the subject with spinal cord injury (subject #3) and the healthy subjects, which is consistent with the lack of difference in the change of soft tissue thickness beneath the ischial tuberosities. We also note that the decreases in soft tissue stiffness are similar between the left and right ischial tuberosities for all three subjects, *even though the changes in soft tissue thickness are not*. Indeed, if the small change in soft tissue thickness beneath the left ischial tuberosity has been accurately measured, then these observations indicate that large changes in stiffness do not necessarily correspond to large changes in soft tissue shape, and therefore stiffness measurements cannot be used as a proxy for thickness measurements. Furthermore, if accurate, the results of our pilot study show that there is no correlation between pressure and soft tissue thickness for either contour, and so we cannot say that the load on the pelvis has been redistributed from areas of thinner tissue to areas of thicker tissue.

Reasons For The Differences

At this point, we can clearly see that the results of this pilot study differ significantly from what we would expect based on previously published work. There are several possible explainations for these differences. One explanation is that the three subjects in the pilot study are not representative of the population as a whole and the differences in behavior of their soft tissues between what was expected and what was observed is simply due to random chance. In this case, a larger study will correct this problem. Another explanation is that changes in soft tissue thickness beneath the left ischial tuberosity are obscured by our inability to measure the true orientations of the actuator heads on that side. In this case, the actual changes in soft tissue thickness on the left side are similar to those on the right, but the poor approximation to the true orientation of the actuator heads we compute from the heights of their neighbors results in a set of thickness measurements results in a set of thickness measurements that hide this fact. If this is the problem, we need only install orientation sensors on the left side of the CASS to correct it. Likewise, inaccurate measurement of the position and orientation of the pelvises of the three subjects caused by the limited ability of the CASS system to measure registration points only on the right superior anterior iliac spine may be disguising the true changes in soft tissue thickness beneath both ischial tuberosities. In this is the problem, then adding a second position wand and reconfiguring the CASS to allow measurement of registration points on both superior anterior iliac spines and both superior posterior iliac spines will fix the problem by allowing accurate measurement of the position and orientation of the pelvis.

However, neither an unrepresentative subject pool, inaccurate measurement of the position and orientation of the pelvis, or the lack of orientation sensors beneath the left buttock may explain the differences between the results of our study and those published in the literature. In this case, our study shows a genuine discrepancy between the actual behavior of the soft tissues of a seated subject and what we would expect based on current models. If the results of our pilot study hold up for a larger subject pool, with an accurate registration method, and with orientation sensors positioned under both buttocks, then the current models for soft tissue behavior in a seated subject will have to be revised. We describe what some of these revisions might look like in the following paragraphs.

Suggested Revisions To Chow And Odell's Model

The belief that soft tissue distortion in the buttocks should be greater for subjects seated on a flat contour than for a pressure equalized contour stems from the work done by Chow and Odell[18], who used a finite element model to simulate the change in the shape of the soft tissues of the buttocks for a seated subject. In their work, Chow and Odell modelled behavior in only one buttock, assuming that the other buttock would be similar. They modelled the ischial tuberosity as a rigid cylinder with a spherical cap bearing half the weight of the torso, and they modelled the soft tissues as a homogeneous incompressible elastic solid. They found that when seated on a flat contour, the tissue beneath the ischial tuberosity at equalibrium would be squeezed very thin by the weight of the ischial tuberosity and that the interface pressure between the buttocks and the seating surface would be greatest at this point and would fall off rapdily the farther one moved from the ischial tuberosity. However, for someone seated on a contour that matched the unloaded shape of the buttocks, distortion would be minimized and pressure would be distributed much more evenly across the interface of the buttock and the seating surface.

As currently formulated, Chow and Odell's model cannot explain some of the results of this pilot study. Given that there are no significant differences in the mechanical properties of the left and right sides of the buttocks, Chow and Odell's model would predict that the changes in soft tissue thickness on the left and right sides of the buttocks between the flat and equalized contours would likewise be symmetric. However, we observed that the change in soft tissue shape on the left and right sides of the buttocks were not symmetric. Furthermore, since Jue Wang's work strongly suggests that the soft tissue in the buttocks of people with spinal-cord injury should have a lower elastic modulus than those that are uninjured, Chow and Odell's model would predict a larger change in the thickness of the soft tissues of the buttocks of the subject with spinal-cord injury, especially beneath the ischial tuberosities, than would be observed for the healthy subjects. However, this study showed no clear difference in the way the soft tissues of the subject with spinal-cord injury changed shape between the flat and equalized contours and the way the soft tissues of the buttocks of the healthy subjects changed shape between those two contours. Finally, Chow and Odell's model would suggest that unipolar pressure distributions, as observed for subject #2, would be impossible without the pelvis having a significant roll to one side or another.

Since the results of our pilot study differ from what Chow and Odell's model would predict, and if a larger study whose registration method has been sufficiently validated

confirms the results of our pilot study, then Chow and Odell's model will need to be revised to take into account the results of these studies. The main revision we would suggest to Chow and Odell's model would be to remove the assumption that the responses of the left and right halves are the buttocks are similar and to account for the attachment of the pelvis to the spine and to the femurs. Chow and Odell's model assumes that the movement of the pelvis is constrained in its vertical movement only by the behavior of the soft tissues, neglecting its interaction with the spine or the femurs. However, interaction with the spine may force a roll into the orientation of the pelvis, which would prevent one side from sinking into the soft tissues as much as it would if it were unconstrained. Likewise, the position of the torso relative to the pelvis may result in more weight on one side than on the other. Furthermore, the interaction between the pelvis and the femurs may not be the same between the flat and the pressure-equalized contour, and it may be the case that more of the weight of the pelvis comes to rest on the femurs in the latter case than the former. Since the femurs would be a primary mechanism for transmitting the load of the pelvis into the soft tissues of the thighs, this change would result in the load of the body being distributed over a much larger area for the equalized contour than for the flat contour. Finally, we need to consider that the movement of the soft tissue within the body is not completely unconstrained. While the layer of fat is very mobile, the muscles of the body are attached to the bones by tendons and wrapped by sheaths of fascia. Conseqeuntly, the layers of muscle can only distort so much when exposed to the forces incurred in normal sitting. The limits on this distortion are not currently known, but if significant, they may limit the amount the tissue can thin beneath the ischial tuberosities.

4.4.3 Strengths And Weaknesses Of Our Approach

Compared to other approaches, the primary strength of the system developed in this thesis is its ability to measure the thickness and shape of the soft tissues of the buttocks for a seated subject directly. Other approaches have been limited to prone subjects [107], have been restricted to a very small area of the buttocks and have not been able to measure interface pressure simultaneously[19], or have used only indirect measurements of soft tissue thickness [11,13]. Because it can measure pelvic position, pelvic orienation and soft tissue thickness directly, our system represents a significant improvement over previous work in this area. However, there are several areas where our system can be improved, which we discuss below. Ways to overcome these weaknesses are described in the section on future work.

As discussed previously in section 3.4.1, the values of the position and orientation of the pelvis of a subject may have large errors because the position wand of the CASS is limited to measuring registration points on the right anterior superior iliac spine. If a second position wand were added, and the CASS reconfigured so that the position wands could measure points on the posterior iliac spines as well as the anterior iliac spines, then large errors in the measurement of the position and orientation of the pelvis could be ruled out.

When the ultrasound system of the CASS was designed, it was assumed that the response of the right and left buttocks would be similar, and so ultrasound and orienation sensors were deployed only beneath the right buttock. However, our pilot study indicates that in the most likely case, the response is not symmetric, so sensors need to be deployed

beneath both buttocks. Even if ultrasound is not deployed beneath the left buttock, orientation sensors are needed because the approximation to the orienation of the actuator heads in this region we compute from the heights of the neighboring actuators is not very accurate. It is, however, better than any other approximation we can make.

Our present system only measures the position and orientation of the pelvis and can only measure changes in the soft tissues that fall beneath it. However, the results of the pilot study have lead us to conjecture that both the center of gravity of the torso and the femurs play an important role in how the body redistributes the load on the pelvis between the flat and the equalized contours. While measuring the location of the center of gravity of the torso is difficult, measuring the position and orientation of the femurs can be done by including them in the MRI scan and using the position wand to measure points on the patellar surface. By registering these points to the surface model of the femur and taking into account the location of the acetabular cup on the pelvis, the position and orientation of both femurs can be accurately measured. These measurements will, in turn, allow us to examine how the relationship between the pelvis and the femurs changes between flat and pressure equalized contours.

Finally, almost every step in the data analysis process decribed in Chapter 3, from the segmentation of the MRI images and ultrasound echograms to the regirstration of the wand points to the pelvis is done manually. Automation of all the steps of the data analysis phase in our system is important not only for conducting large studies, where manual analysis will become tedious, but also for reducing the bias and inconsistency inherent in the judgements made by human beings at different steps in the data analysis process. Places where such bias and inconsistency may occur include the judgements of which echoes in an ultrasonic echogram correspond to tissue layer boundaries or whether the chosen alignment of the pelvic model with the registration points is the best possible one. Automating these procedures would reduce inconsistency in judgements made at different times and for different subjects and would exchange the controlled bias of an automatic procedure for the uncontrolled bias of a human judge. In addition, automating the data analysis procedure may allow the visualization the changes in pelvic position, pelvic orientation, and soft tissue shape to take place in real time. Manual operation is necessary because sufficiently accurate automated techniques either do not exist or we do not have sufficient data to implement them. No fully automated technique exists to segment the pelvis from the MRI scans, although semiautomated techniques that produce an initial segmentation that can be improved by a human operator do exist. As shown in section 3.4.1, given sufficient data, the iterative closest point algorithm can produce accurate registrations between the wand points and the pelvis. Automated techniques for segmenting the ultrasound into different tissue layers do exist (see Appendix C), we needed to develop a technique for segmenting the ultrasound manually that we have confidence in. Without a sufficiently strong estimate of the true segmentation of the layers, we would have no way to know how accurate the automated techiques were.

4.5 Conclusions

In this chapter, we conducted a small pilot study to test the usefulness of the technique we

created in Chapter 3 for measuring the position and orientation of the pelvis and the thickness and shape of the soft tissues of a seated subject. This study was conducted on two able bodied males and one male with spinal cord injury. We used the procedure to measure the pelvic position, pelvic orientation, bulk soft tissue thickness beneath the pelvis and thickness of the individual layers of skin fat and muscle beneath the right buttock while seated on a flat contour and a pressure-equalized contour that was customized for each subject by an iterative algorithm. By comparing results between contours and subjects, we observed the following:

(1) When seated on a flat contour, the pelvis can exhibit a relatively large pitch or roll with respect to the seating surface. However, the pelvis tends to align with the plane of the seating surface when seated on the equalized contour.
(2) For all three subjects, the pelvis moves so that the ischial tuberosities are positioned above an actuator rather than between actuators.
(3) For the flat contour, there were two different pressure distributions, one that had peaks on both the left and right sides and one that had a peak only on the right side. For the equalized contour, the load from the upper body was distributed over a much wider area than for the flat contour.
(4) Mean bulk tissue thickness and volume beneath the pelvis decreases when going from the flat to the equalized contour, possibly representing a redistribution of soft tissue towards the legs. The mean thickness of the skin layer in the right buttock remains the same between the two contours. The mean thickness of the fat layer increased for one of the healthy subjects and for the subject with spinal cord injury, but did not increase significantly for the other healthy subject. The mean thickness of the gluteus maximus increased by 2 to 5 mm for all subjects. Because of the thickness of the fat layer for the subject with spinal cord injury, it was very difficult to resolve the far boundary of his gluteus maximus.
(5) The distribution of soft tissue beneath the left and right ischial tuberosities was not symmetric, and the two sides did respond in the same manner as the contour moved from its flat to its pressure-equalized shape. For all thres subjects, the right ischial tuberosity showed a considerable increase in soft tissue thickness in the thinnest areas, while the left side remained almost the same.
(6) There was no obvious difference between the healthy subjects and the subject with spinal cord injury in the way the pelvis moved or the soft tissues changed shape between the flat and pressure-equalized contour, other than that the subject with spinal cord injury had a higher proportion of fat to muscle and bore more of the load of the pelvis on the fat layer for both contours. However, this difference may be due to that subject's body composition, since he had much more fat over his entire body than the two healty subjects, rather than due to his injury.

Points (5) and (6) are at odds with what would be expected based on current models and previously-published work. Based on previous work, we would expect the soft tissue beneath the ischial tuberosities to thicken considerably on both sides, not just the right, as the contour moves from its flat to its equalized shape and the load from the pelvis is redistributed. We would also expect the soft tissues of the subject with spinal cord injury to display a lower elastic modulus and therefore, to see a larger difference between the thickness of soft tissue beneath the ischial tuberosities between the flat and equalized

contours than we observe for the healthy subjects. Even if our measurements of absolute tissue thickness have been subject to systematic errors (due to uncertainties in the speed of sound, for example), the changes in relative thickness still indicate a significant departure from what we would expect from previous work on soft tissue distortion in seated subjects. If future studies show that the differences between what we observed in the pilot study and what would be predicted based on previous studies cannot be attributed to the peculiarities of the small subject population, to the presence of potentially large errors in the measurement of the position and orientation of the pelvises of the three subjects, or to the lack of orientation sensors on the left side of the CASS, then they will require a revision to our current models of how the pelvis and the soft tissues behave in a seated subject.

The technique we have developed for measuring the position and orientation of the pelvis and the thickness of the soft tissue layers of the buttocks for a seated subject and the pilot study we used to validate this techique constitute the primary contribution of this thesis to the literature. Until now, it has not been possible to measure the thickness of the layers of soft tissue in the buttocks of a seated subject, and researchers have had to use indirect measurements of soft tissue shape or work with finite element models that were assumed to be correct. The technique developed in this thesis opens a new line of research into the relationships between the seating surface, the pressure measured at the interface between the seating surface and the buttocks, the pelvis and the soft tissues of the body. The pilot study suggests that if its measurements are accurate, the current models for the interaction between the soft tissues of the buttocks and the pelvis may be too simple and may need to be revised.

In developing the technique, we build a ray model of the propagation of an ultrasonic pulse through the soft tissues and investigated how assumptions about the speed of sound in soft tissue and the local orientations of the soft tissue boundaries affected the accuracy of measurements of the thickness of the soft tissue layers and the locations of the reflections from those boundaries. In anticipation of automating the segmentation of the ultrasonic echograms, we have conducted a survey of current techniques in automated ultrasonic tissue characterization.

4.6 Future Work

4.6.1 Improvements To The Experimental Procedure To Increase Its Accuracy

Given the intriguing and potentially groundbreaking results of the pilot study, the natural next step is to conduct a larger study with sufficient statistical power to generate definitive results. Future studies using the technique developed in this thesis will need to control for body composition, so that the effects of injury status and the effects of having a substansive amout of body fat can be differentiated. Ideally, such studies would draw from all four possible combinations of injury status (healthy vs. spinal-cord-injured) and body composition (low percentage of body fat vs. high percentage of body fat). Future studies should also not assume that the response of the left and right buttocks are the same but should place ultrasound and orientation sensors beneath both buttocks. The position wand should be mounted further back on the CASS and a second position wand should be

mounted on the left side so that registration points can be obtained from the posterior and anterior iliac spines on both sides of the pelvis. This will greatly improve the accuracy of the registration algorithm and rule out large errors in the measurement of the position and orientation of the pelvis as the cause of any of the behaviors of the pelvis or soft tissues observed in this study. The actuator heads should be locked down to prevent them from rotating. Although measurements of the sensor locations before and after running the experimental protocol on each subject shows that the heads do not rotate very much during the procedure, locking them down would nevertheless improve the accuracy of the ultrasonic measurements.

The interpretation of the ultrasonic echograms can be strengthened by conducting a B-mode ultrasonic examination of the subject's buttocks while the subject is lying down. By using internal landmarks on the pelvis or external registration marks, the B-mode images can be aligned with the digitized echoes from the ultrasonic transducers on the CASS. These images can assist in the interpretation of those echoes by providing measurements of the initial thicknesses of the layers of fat and muscle, which in turn can be used to compute the sizes of the fat and muscle zones used to identify the echoes from the fat and muscle layers. The B-mode images can also be used to ascertain how echogenic each layer is, which can also help segment the digitized ultrasonic echograms.

4.6.2 Improvements To The Experimental Procedure That Will Increase Our Understanding Of Seating Biophysics

Future work with the technique developed in this thesis should endeavor to measure the thickness of not only the most superficial muscle layer, but the deeper muscle layers as well. Such measurements will allow researchers to explore how the load from the pelvis is distributed among the different layers of muscle. Furthermore, most of the difference in thickness between the flat and equalized contours in the muscle layers beneath the femur occurs in the deeper layers. Imaging the deeper layers can be improved by using a lower frequency transducer with a larger diameter. The lower frequency pulse will attenuate less as it travels through the body, while the larger diameter will allow the transducer to receive reflections from larger angles of incidence. The cost of using such a transducer is lower axial and lateral resolution, but neither of those quantities was a limiting factor in this study.

Future studies should endeavor to measure not only the position and orientation of the pelvis, but the position and orientation of the femurs as well. This can be accomplished by including the femurs in the MRI scan, acquiring registration points on the patellar surface, and registering these points to surface model of the femurs, using the locations of the acetabular cups of the pelvis as an additional constraint. Not only will placing the femurs in the scene assist in the interpretation of the ultrasound in this region, but the interaction between the pelvis and the femurs may provide an important constraint on the movement of the pelvis between the flat and the equalized contours.

Likewise, future studies should measure where the center of gravity of the torso is located relative to the pelvis. By measuring the center of gravity, future studies can ascertain what effect, if any, the relationship between the torso's center of gravity and the pelvis has on

the orientation of the pelvis, the distribution of pressure at the interface between the seat and the buttocks, and the way that the soft tissue change shape as the contour changes from its flat to its equalized shape. However, measuring the torso's center of gravity is not an easy task. Its location depends upon the size and the composition of the subject, and crude approximations may not produce useful results. The best way to measure the torso's center of gravity remains an open question.

Finally, the technique developed in this thesis for measuring the thickness and shape of the soft tissues of the buttocks should be combined with the indentation technique developed by Jue Wang for measuring the mechanical properties of those soft tissues. This would allow the relationship between the mechanical properties of the soft tissues and their distortion under seated conditions. Indentation testing would be performed at several locations throughout the buttocks after the echoes from the full array of ultrasonic transducers have been digitized. The primary difficulty is that strong echoes from the pelvis or the femur are needed for Wang's technique. However, it may be possible to modify her technique to work with measurement of the thicknesses of the individual muscle layers rather than the bulk thickness of muscle between the fat and the bone. This would allow the measurement of the mechanical properties of each muscle layer and would remove the need to obtain an echo from the pelvis or femur, except when the mechanical properties of the deepest muscle layer must be measured.

Data gathered from these studies can be used to construct new models of the interaction between the seating surface, the skeleton, and the soft tissues of the body. Current models treat the pelvis as a rigid indentor pulled into the soft tissues by gravity and may allow the pelvis to sink too far into the soft tissues. If larger studies confirm the results of the pilot study conducted in this thesis, these models will need to be revised to take into account the interaction of the upper torso with the pelvis through the spine, and the interaction of the pelvis with the femurs. Once validated on data acquired through the measurement technique developed in this thesis, researchers can use these models to predict what kinds of seating contours will minimize soft tissue distortion for the elderly and those with spinal cord injuries.

4.6.3 Improvements To Techniques For Pressure Ulcer Prevention

The ultimate goal of all pressure ulcer research is to reduce or eliminate the incidence of pressure ulcers in at-risk populations. Consequently, future studies will need to explore the relationship between pelvic orientation, and soft tissue thickness and succeptibility to the development of pressure ulcers. In the pilot study, we noted an asymmetry in the way the left and right sides of the buttocks responded as pressure was relieved. This asymmetry may correspond to a tendency to develop pressure ulcers on one side of the buttocks more than the other. Variation in the response of a subject's soft tissues over time to the same seating environment over time may also be important in understanding and preventing pressure ulcer development. Changes in the pattern of response of the soft tissues of the buttocks to the same seating environment may foreshadow the development of a pressure ulcer or an increase or decrease in the subject's vulnerability to developing pressure ulcers. Long-term studies using the techniques developed in this thesis will also be able to definitely confirm or deny the hypothesis that reducing soft tissue distortion reduces

succeptibility to pressure ulcers.

Although the measurement techique developed in this thesis is not likely to be used itself in a clinical setting, portions of it may be. For example, if alignment of the pelvis with the plane of the seating surface is a critical factor in designing effective seat cushions, clinicians may employ the same registration procedure used in this thesis to measure the relationship between the subject's pelvis and his or her seating cushion and make adjustments to the seating contour to properly align the pelvis. Likewise, improvements to the existing models of the response of the soft tissues of the buttocks to different seating conditions may improve them to the point where clinicans can use them to design seating contours that will do a better job of preventing pressure ulcers.

Appendix A
Structure and Mechanical Properties of Soft Tissue

This appendix describes the anatomy of the skin, fat, muscle and pelvis that is needed to understand the work detailed in the main body of the thesis. It begins with a description of the different planes used by medical professionals to describe different cross-sections of the body. This section is followed by a detailed description of the structure of the skin, which is necessary to understand some of the proposed mechanisms for pressure ulcer formation described in chapter 2. Following the anatomy of the skin is a brief description of the anatomy of the pelvis, including the muscles that attach the pelvis to the femur. An understanding of which muscles occupy the region of the pelvis and upper thigh and where they connect is important for segmenting the ultrasonic echograms and interpreting the results of our small pilot study described in chapter 4. This appendix also provides a brief description of the biomechanical properties of the soft tissues of the body.

A.1 The Planes Of The Body

The study of human anatomy requires visualization of the different structures of the human body and their relationship to one another. Very often, cross-sections of the human body are used to visualize and discuss its anatomy. These cross-sections are obtained by computing the intersection of a plane with the three-dimensional human body, and medical professionals have developed a vocabulary to describe the common planes used to create cross-sections. These planes are illustrated in figure A.1 and described below:

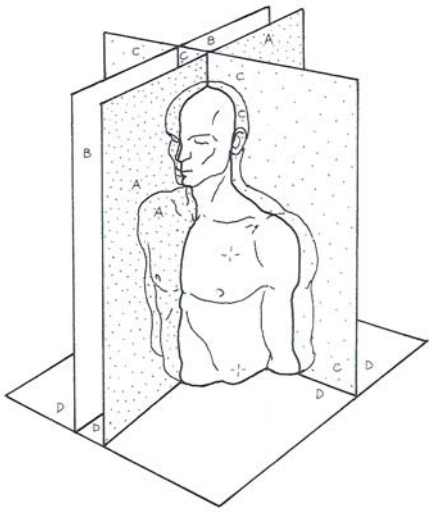

Figure A.1: The planes of the body.

The **medial plane** (plane “A” in figure A.1) lies in the center of the body and divides it into equal left and right halves.

A **sagittal plane** (plane “B” in figure A.1) divides the body into unequal left and right sides. A sagittal plane is always parallel to the medial plane, and the medial plane can be considered the middle saggital plane.

A **frontal plane** (plane “C” in figure A.1) divides the body into equal or unequal front and back sides. Radiologists and technicans who work with CT and MRI imaging typically call frontal planes **coronal planes**. The two terms are equivalent.

A **transverse plane** (plane "D" in figure A.1) divides the body into equal or unequal upper and lower portions. Radiologists and technicans who work with CT and MRI imaging may call these planes **axial** or **transaxial planes** of the body.

The sagittal, frontal and transverse planes of the body are all perpendicular to one another.

A.2 Anatomy

A.2.1 Anatomy of the Skin

The skin is illustrated in Figure A.2 (taken from [111]). The epidermis is the outermost layer of the skin, with a thickness of 0.07 mm to 0.12 mm (except on the palms and soles, where it varies from 0.8 mm to 1.4 mm)[27]. The epidermis consists of **keratinized** dead cells. It serves to protect against physical injury, damage from chemicals or ultraviolet rays, and microbial infection. Intercellular attachments via **demosomes** and fine filaments increase the mechanical strength of the epidermis.

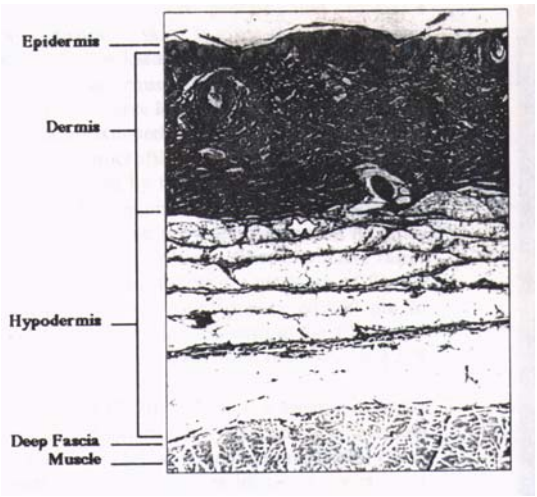

Figure A.2: The structure of the skin

Beneath the epidermis lies the dermis. The two layers are connected by the dermal-epidermal junction, which is composed of a wavy **basement membrane** with finger-like projections that extend into the dermis. Collagen filaments anchor the dermal side of the basement membrane to the upper layer of the dermis, while the epidermis is connected to the basement membrane by the same bonds that connect epidermal cells to one another.

The dermis lies beneath the epidermis and varies in thickness between 1 and 3 mm. Its primary function is to provide structural strength, and its principal components are elastin, collagen, **glycosaminoglycans**, water, and cells. Elastin and collagen give skin its load bearing capabilities. Elastin forms a meshlike network in the dermis and is responsible for its mechanical integrity under low mechanical loads. Collagen also forms a meshlike network within the body, and, because of the larger diameters of its fibers (2-15 μm vs. 1-3 μm for elastin) and cross-links between individual collagen molecules, is responsible for the mechanical integrity of the skin at high load levels. The density and structure of the collagen network is not constant but undergoes remodeling when subjected to mechanical stress, disease, or wound healing. This is accomplished through shifting equilibrium of competing **catabolic** and **synthetic processes**; mechanical stress inhibits collagen synthesis, allowing collagen catabolisis to dominate and dissolve the existing collagen network. The presence of catabolized collagen by-products increases the level of **collagenase inhibitors**, which decrease the rate of the catabolic process to the point where the synthetic process is able to build a new network, whose density and structure is more

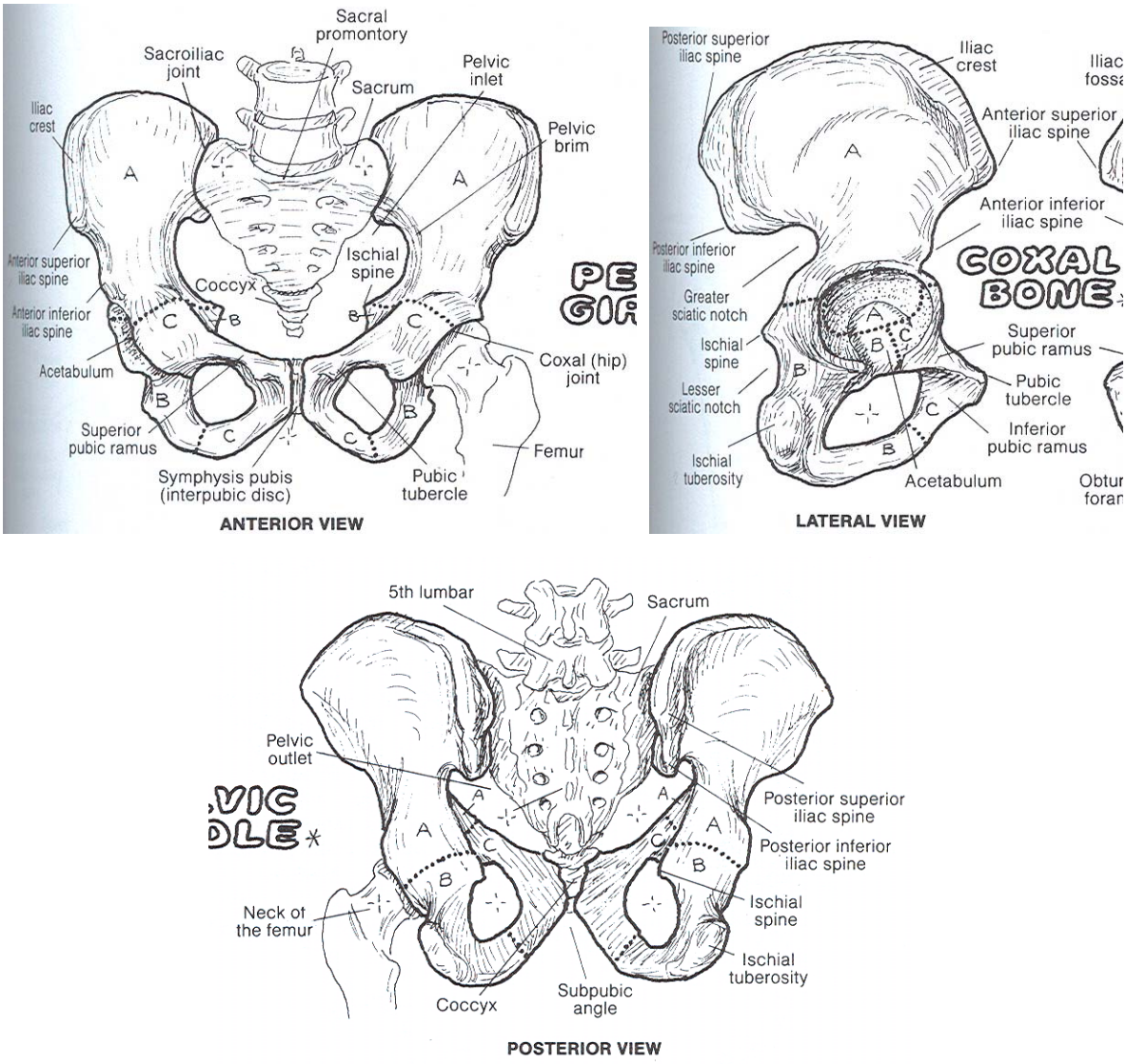

Figure A.3: The front (anterior), side (lateral) and rear (posterior) views of the pelvis with important anatomical landmarks indicated.

suited to the current load.

The spaces between the network of collagen and elastin fibers are filled with cells, **vasculature**, and interstitial fluid and ground substances (IFGS). Cells found in the dermis include fibroblasts, **macrophages**, **mast cells**, and leukocytes. Fibroblasts are the most important of these for our purposes, as they regulate the remodeling of the collagen network. The vasculature of the dermis can be divided into two distinct parts: the capillaries, which carry nutrients to and waste products away from the cells of the dermis, and the thermoregulatory blood vessels, which are larger, deeper arteries and veins that run parallel to the skin surface and help regulate the body's internal temperature via heat transfer to and from the skin. Interstitial fluid and ground substances compose approximately 10-20% of the skin by volume. It flows between the cells and vasculature of the dermis. The flow of the interstitial fluid is responsible for several important physiological functions, including nutrient and waste transport between the cells and capillaries of the dermis and the electromechanical behavior of the dermis.

A.2.2 Anatomy of the Pelvis

Anterior (front), posterior (back), and lateral (side) views of the pelvis are shown in figure A.3. Like most of the skeleton, the pelvis exhibits a large degree of bilateral symmetry and so some the lateral illustration shows only the right side. From point of view of this thesis, the important regions of the pelvis are:

The **pubic tubercle**, which is shown in the anterior and lateral views of figure A.3, is the farthest point forward on the pelvis and can be thought of as its "nose." It is the origin of the pubic ramii and several muscles of the anterior thigh attach here. It is important to us because we define the y-axis of the pelvic coordinate system as extending from the public tubercle along the public crest to the ischial spine (see the lateral view of figure A.3).

The **superior pubic ramus** and the **inferior public ramus** extend upwards and downwards from the pubic tubericle to form the remainder of the *os pubis* or pubic bone, as illustrated in the lateral view of figure A.3. Many important muscles of the posterior thigh, including the aductor magnus attach to the inferior public ramus.

The **anterior superior illiac spine** is found at the front of the ilium, the wide broad section that forms the "wings" of the pelvis. It is shown in the lateral and anterior views in figure A.3. In this region, the skin lies directly on top of the bone, even in obese persons. This region and the front part of the illiac crest are where we measure points to register the pelvic coordinate system to the CASS coordinate system.

The **illiac crest** extends along the top edge of the ilium from the anterior superior illiac spine to the posterior superior illiac spine. It is shown in the lateral view of figure A.3. Like the anterior superior illiac spine, the skin lies directly atop the bone in the front part of the iliac crest, so we obtain registration data in this region as well.

The **posterior superior illiac spine** is the farthest point back on the pelvis and forms the other endpoint of the iliac crest. It is shown in the posterior and lateral views of figure A.3. The gluteus maximus muscle attaches to the pelvis at this point. Like the

anterior illiac spine, the body tends not to accumulate fat here. Registration points could be collected from this region if the position wand were a little longer.

The **ischial tuberosity** extends from the end of the inferior pubic ramus to the spine of the ischium and comprises the very bottom of the pelvis. It is shown in the posterior and lateral views of figure A.3. During normal sitting, the ischial tuberousity is pulled by gravity into the soft tissues of the body, squeezing them between the bottom of the ischial tuberosity and the seating surface. It is thus no suprise that a large fraction of pressure ulcers typically occur in this region[58].

The **acetabulum** is the cup that holds the head of the femur, which is its primary importance to this thesis. It is shown in the lateral view of figure A.3. Because we do not locate the femur explicitly, we use the position and orientation of the acetabulum to infer its approximate location.

The **sacrum** is the large, triangular bone at the end of the spine. It is visible in all three views shown in figure A.3. The sacrum is wedged between the two halves of the pelvis. Several muscles and ligaments of the posterior thigh attach to it, including the gluteus maximus. Pressure ulcers commonly occur beneath the sacrum.

These regions of the pelvis are important because they serve as landmarks for locating other structures on the pelvis, are places where important muscles attach to the pelvis (and are therefore constraints on the locations of those muscles), or are places where pressure ulcers tend to occur. The important muscles attached to the pelvis are:

The **gluteus maximus** is the most superficial muscle in the gluteal region. It is very thick and broad and has a quadrilateral shape. It attaches on one end to the posterior superior iliac spine, a portion of the iliac crest above the iliac spine, and almost the entire length of the sacrum. From there, it extends downwards and around the entire region of the buttocks where it attaches to the upper third of the femur on the outside of the thigh. The gluteus maximus is also attached to the ischial tuberousity by means of the sacrotuberous ligament. Because of its attachments, the gluteus maximus covers almost the entire surface of the buttocks when one sits.

The **semitendinosus** muscle arises from the rear of the ischial tuberosity where it stretches downward and inward until it terminates in a long, round tendon just after the middle of the thigh. This tendon continues downward and inward until it attaches to the upper part of the anterior tibia. Beneath the ischial tuberosity, the semitendinosus muscle, along with the biceps femoris are wrapped by the gluteus maximus, but it soon emerges from beneath the gluteus maximus to become one of the superficial muscles of the posterior thigh.

The **biceps femoris** muscle also originates from the rear of the ischial tuberosity and stretches downward until it inserts into the outside of the fibia. Hence, while the semitendinosus covers the inner portion of the posterior thigh, the biceps femoris covers the outer portion. As its name implies, the biceps femoris muscle has two heads: one that attaches to the rear of the ischial tuberosity at about the same place as the semitendinosus, and the other that attaches to the femur just beneath the gluteus maximus.

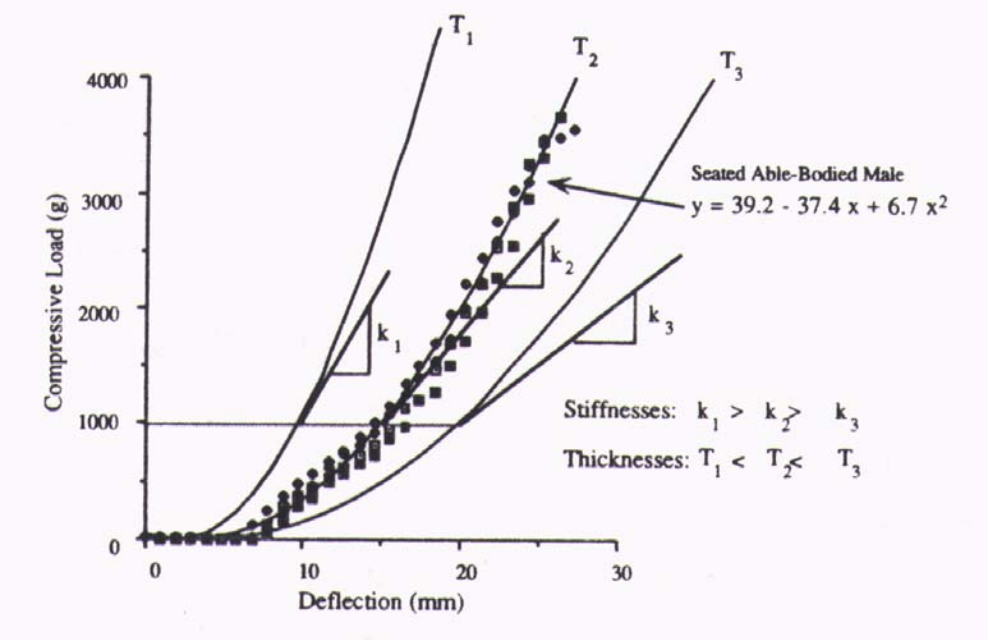

Figure A.4: Typical force / deformation relationship for the buttocks of a seated able-bodied male (from [15]). The compressive load is measured in grams.

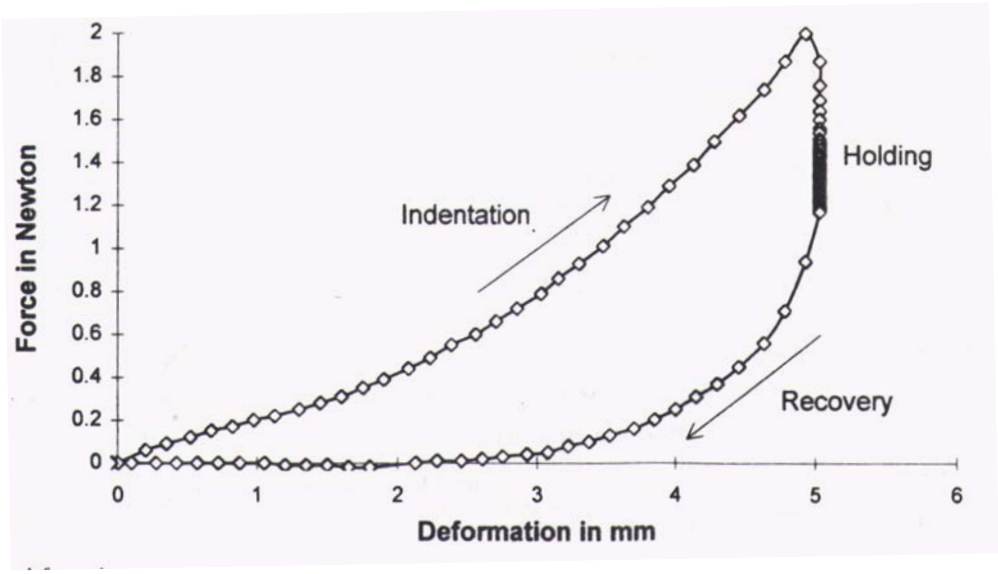

Figure A.5: Example of the non-linear force / deformation relationship and hysteresis of porcine tissue (from [145]). Indentation took 5 seconds, the holding interval was 10 seconds, and recovery took 5 seconds. Human tissue has a similar response.

The **semimembranous** muscle attaches to the back part of the ischial tuberosity above the region where the semitendinosus and the biceps femoris attach. It streches downwards along the femur and attaches to the upper posterior part of the tibia. The semimembranous muscle remains above the biceps femoris and semitendinosus muscles until about halfway down the thigh, where it emerges from beneath them on the inside of the posterior thigh.

The **aductor magnus** is a large triangular muscle that originates from the front of the descending ramus of the pelvis and attaches almost along the entire inside of the femur. Like the biceps femoris and semitendinosus muscles, the aductor magnus emerges from beneath the gluteus maximus at the top of the thigh, and it is visible in a posterior view for about the first half of the thigh, where it disappears beneath the semimembranous muscle.

A.3 Mechanical Properties of Soft Tissue

Human soft tissue is best modeled as a quasi-linear viscoelastic solid[30]. It exhibits a non-linear stress/strain relationship, hysteresis and preconditioning. Figures A.4 and A.5 show two example force/indentation curves, one for a seated able-bodied male, and one for porcine tissue, whose histology and mechanical properties are very similar to human tissue. The creep times for many different types of human soft tissue, including skeletal muscle, the walls of arteries and veins, and skin, are known to be on the order of hours[30]. Although these response times are for uniaxial tension, similar creep times have been shown to hold for indentation as well. For example, Reddy[104] reported a continual increase in indentation depth even after six hours in response to a constant force applied by an indenter.

One of the most commonly used models for soft tissue is Fung's quasi-linear viscoelastic model[30], which relates the tensile stress $P(t)$ at time t to its instantaneous stress response $P_e(u(t))$ and its reduced relaxation function $G(t)$:

$$P(t) = P_e(u(t)) + \int_0^t P_e(u(t-\zeta))\frac{\partial G(\zeta)}{\partial \zeta}\partial\zeta \qquad \text{(A.1)}$$

where $u(t)$ is the relative strain with time. For indentation into soft tissue, the reduced relaxation function $G(t)$ is usually assumed to have the form:

$$G(t) = 1 + \alpha - \alpha e^{-t/\tau} \qquad \text{(A.2)}$$

where α and τ are characteristic parameters of the soft tissue, while the instantaneous elastic response is:

$$P_e(t) = \frac{2ah}{1-\nu^2}u(t)k(h, u(t))E_e(u(t)) \qquad \text{(A.3)}$$

where a is the radius of the indentor, h is the original thickness of soft tissue, v is Poisson's ratio (assumed to be 0.45 for soft tissue), $k(h, u(t))$ is a scaling factor that depends on v, a, h and $u(t)$, and $E_e(u(t))$ is the unrelaxed elastic modulus. The unrelaxed elastic modulus is usually assumed to be a linear function of indentation depth[146]:

$$E(u(t)) = E_0 + E_1 u(t) \tag{A.4}$$

Several attempts have been made to measure values for a, t, E_0 and E_1 for different types of soft tissues. Examples such attempts include the work done by Zheng[146], Wang[133] and Zeltwanger[143].

Appendix B
Ultrasonic Measurement

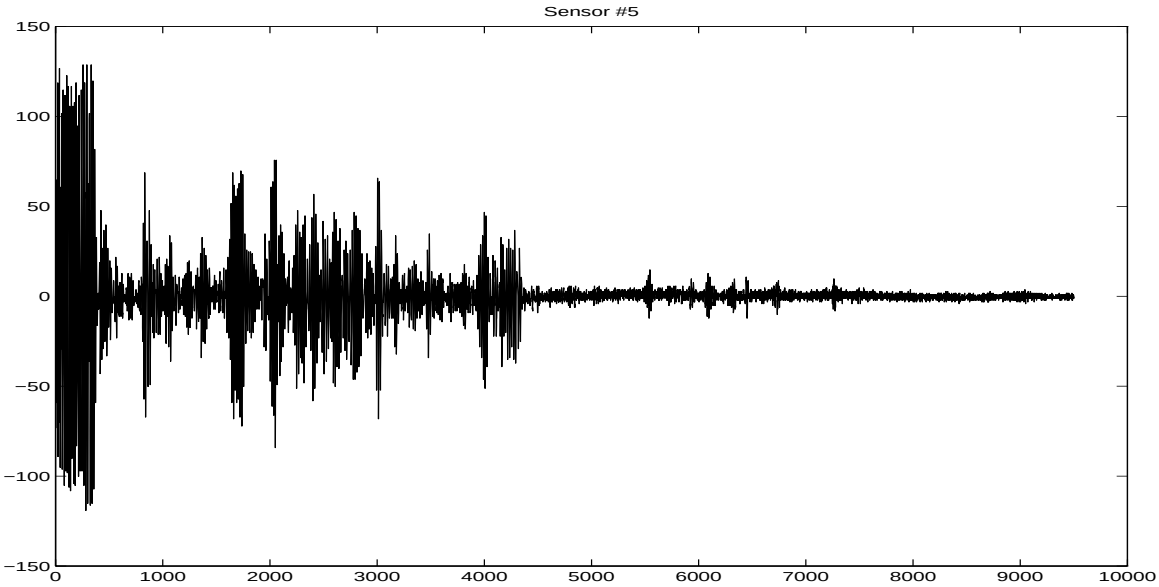

Figure B.1: A typical echogram of the return echoes for a 7.5 MHz ultrasonic pulse emitted into the buttocks of a 29 year-old healthy human male. The x-axis measures time in ADC samples collected at a rate of one sample every 10^{-8} seconds. The y-axis measures voltage differential across the transducer in ADC bits, where one bit equals 390.625 μV.

B.1 Introduction

Figure B.1 illustrates the echoes received by one of the transducers used by our experimental apparatus from an ultrasonic pulse as it travels through the upper thigh of a human male. The experimental procedure described in chapter 3 requires that we obtain from these echoes the thickness of each layer of soft tissue the ultrasonic pulse passed through as well as the locations in 3-space of the places where the pulse intersected the boundaries of those layers. These points are combined with other points measured along the same boundaries by different transducers to produce a mesh that describes the shape of the soft tissues in the buttocks. To accomplish this task, we must develop an imaging model that explains the important features of the echogram in terms of the relevant properties of the ultrasonic pulse, the relevant properties of the transducer, and the relevant properties, geometries and arrangement of the soft tissue layers. In this appendix, we develop such an imaging model and use it to create a process to compute the

thicknesses of the soft tissue boundaries and the locations of their boundaries from the information contained in the echoes such as those illustrated in figure B.1 received by the transducer. We analyze this process to investigate how the assumptions it makes and the uncertainties in its inputs affect the accuracy of the tissue thicknesses and boundary point locations it computes. The accuracy of this process reflects the quality of the system we have built and the strength of the conclusions we can draw from its use.

B.2 The Imaging Model

We begin our development of the imaging model by identifying the relevant properties of the ultrasonic pulse and the media it travels through (e.g. the soft tissues of the buttocks), followed by a model of the pulse as it propagates through a single tissue layer. Then we combine multiple instances of the single layer model into the multi-layer model that constitutes our imaging model.

B.2.1 Properties of the Pulse and the Medium

An ultrasonic pulse is a three-dimensional disturbance localized in time that travels intact in space and time through a solid, liquid or gas medium and obeys the three-dimensional wave equation:

$$c^2\left(\frac{\partial^2\psi}{\partial x^2}+\frac{\partial^2\psi}{\partial y^2}+\frac{\partial^2\psi}{\partial z^2}\right) = \frac{\partial^2\psi}{\partial t^2} \qquad \text{(B.1)}$$

where $\Psi(x, y, z, t)$ is a possibly complex function whose real part $u(x, y, z, t)$ represents the magnitude of the disturbance at the point (x,y,z) at time t. Usually, the function u represents deviation in local pressure at (x,y,z) from its undisturbed value, but sometimes, it represents the change along the local direction of pulse travel in position of a small volume or particle of the medium at (x,y,z) from its rest position.

For all but the simplest of initial conditions, writing an analytical solution of (B.1) is not feasible. Nevertheless, we can gain tremendous insight into the behavior of an ultrasonic pulse inside the body from (B.1). In particular, since our transducers are circular in cross-section, we make use of the well-known result that the beam from such a transducer can be separated into two regions: the near field (or Frensel zone) and far field (or Fraunhoffer zone). In the near field, the beam has planar wavefronts that are axially-symmetric transverse to the direction of propagation; its intensity profile is generally a decreasing function of the distance from the axis of propagation. In the far field, the transducer appears to be a point source and hence the wavefronts have a spherical shape whose intensity falls off as the square of the distance from the source.

If the transducer is axially-symmetric (i.e. the spatial distribution of its electrical and acoustic properties depends only on the distance from the axis along which the pulse it generates propagates), then the ultrasonic field it generates will also be axially-symmetric. In this case, we can simplify the three-dimensional problem to a two-dimensional problem by applying the following transformation: call the axis along which the pulse is emitted

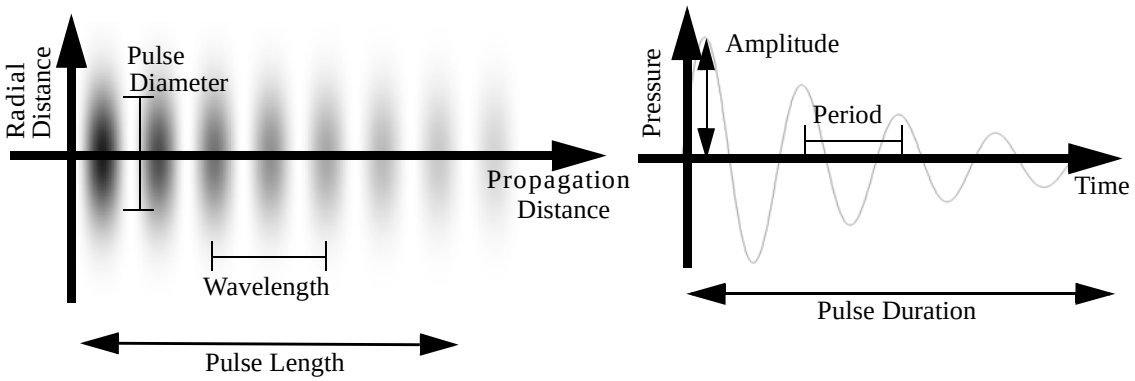

Figure B.2: Illustration of our model of an ultrasonic pulse. In the left diagram, the intensity of the ultrasonic pulse (equal to the square of the amplitude) at any point is space is represented by the grey level. Maximum intesity is black; minimum is white. The pulse diameter is measured at -3 dB from the maximum intensity of the pulse.

the z-axis and let the xz-plane be the plane we want to perform our computations; map all points (x, y, z) not in the xz-plane (e.g. $y \neq 0$) to their corresponding point (a, 0, z) in the xz-plane by equation (B.2) below:

$$\begin{aligned} a &= \operatorname{sgn}(x)\sqrt{x^2 + y^2} \qquad && x \neq 0 \\ a &= y && x = 0 \end{aligned} \tag{B.2}$$

Since the field is axially-symmetric, the values of the field amplitude at all the points in 3-space that map to the same point in 2-space by equation (B.2) will be the same and no information is lost. In our analyses of ultrasonic imaging in this appendix and ultrasonic tissue characterization in Appendix C, we will model the ultrasonic pulse as a traveling cylindrical, axially-symmetric disturbance. This transformation allows us to build our models in 2-space, where the computations will be much simpler, and have the results apply equally to 3-space.

Using this simplification, we can describe the pulse completely in terms of seven scalar quantities - *length, diameter, duration, center frequency, bandwidth, amplitude,* and *wavelength* and one vector quantity - *velocity,* which are illustrated graphically in figure B.2 and described in more detail below:

- The most important characteristic of an ultrasonic pulse are its *center frequency* (f_0) and *bandwidth* (Δ_f). Although the frequency spectrum of the pulse depends strongly on the characteristics of the transducer and its coupling to the medium, for our purposes, it is sufficient to model this spectrum as a gaussian distribution of mean f_0 and standard deviation $\Delta f/2$.
- The *duration* of a pulse (T_p) is its extent in time and is defined as the duration between the arrival of the front end of the pulse at a fixed point in space and the departure of its back end from the same point. The smaller the bandwidth of the pulse, the longer its duration will be.

- The *velocity* ($\bar{c}$) of a pulse is a vector that gives both the speed and direction the pulse travels. Since the speed of sound of a harmonic wave is a function both of its frequency and the mechanical properties of the medium in which it travels, an ultrasonic pulse technically has a different speed for each component of its frequency spectrum. However, for the frequency spectrum produced by the transducers we use in our apparatus and for the time intervals we are interested in measuring echoes, the difference in the speed of sound over the spectrum of the ultrasonic pulse is not significant. In other words, we ignore dispersion effects. We refer to the magnitude of a pulse's velocity vector as its speed (c).
- The *length* (L) of a pulse is its extent in space along the direction of propagation. It is equal to the duration of the pulse times its speed.
- The *diameter* (D) of a pulse is its extent in space in the plane perpendicular to the velocity vector. It is defined as the full width of the pulse at half of its maximum amplitude along the direction of propagation.
- The *amplitude* (A) of a pulse is the maximum over- or underpressure generated by the pulse as it propagates. Because the pulse is a mechanical disturbance in an imperfectly elastic medium, it loses energy as it propagates and thus its amplitude decreases over time, a phenomenon known as *attenuation*.
- The *wavelength* (λ) of a pulse is equal to twice the distance between consecutive zero crossings. It is equal to the center frequency divided by the magnitude of the velocity vector.

The frequency and duration of the pulse depend upon the characteristics of the transducer, the magnitude of its velocity depends upon the medium through which the pulse travels, and the remaining parameters - length, diameter, amplitude, and wavelength - depend upon the characteristics of both the medium and the transducer. Furthermore, because the ultrasonic pulse is a mechanical disturbance in an imperfectly elastic medium, it will lose energy, and therefore amplitude, as it travels. The rate of this energy loss depends upon both the frequency of the pulse and the mechanical characteristics of the medium in which it travels. Finally, when the pulse encounters discontinuities in the medium, such as the boundary between two different tissue layers, some of the pulse's energy will be reflected back towards the direction of propagation while the rest will continue on. The fraction of the energy reflected depends upon the mechanical properties of the media on both sides of the discontinuity as well as the angle of incidence of the pulse upon the boundary. For these reasons, we need to model the medium the pulse travels through as well as the pulse itself, using five scalar parameters:

- The *density* (ρ) of the medium is its mass per unit volume.
- The *bulk modulus* (B) of the medium is a measure of how compressible it is. It is defined as the ratio of stress applied along the normal to the surface of the medium to the resulting change in volume.
- The *speed of sound* (c) is the rate at which sound propagates through the medium. As discussed above, this value is a function of the frequency of that wave, but is effectively constant over the frequencies and durations we wish to measure.

- The *coefficient of attenuation* (α) describes how rapidly the medium attenuates any pulse that passes through it. Like the speed of sound, the coefficient of attenuation is a function of frequency, but we treat it as a constant for our discussions in this appendix.
- The acoustic impedance (r) of the medium describes how "stiff" the medium appears to a sound wave travelling through it. It is equal to the density of the medium times the speed of sound travelling through it.

B.2.2 Model of Propagation in a Single Layer

Within a single, homogeneous tissue layer, the propagation of the ultrasonic pulse is governed by the following equations:

$$p(t) = p_0 + \bar{c}(t - t_0) \tag{B.3}$$

$$A(t) = A_0 e^{-\alpha c(t - t_0)} \tag{B.4}$$

where p_0 is the origin of the pulse in the layer, t_0 is the time it originated, and A_0 is its amplitude at the origin. When it reaches the far boundary of the layer, where the acoustic properties of the layer change abruptly, some of the energy of the pulse will be reflected away from the discontinuity while the rest will propagate into the adjacent medium, possibly along a different path, a phenomenon called refraction. The reflected and refracted pulses will have both diffuse and specular components. The specular components obey the following equations:

$$\theta_r = \theta_i \tag{B.5}$$

$$A_r = A_i \frac{r_0 \cos\theta_i - r_1 \cos\theta_t}{r_0 \cos\theta_i + r_1 \cos\theta_t} \tag{B.6}$$

$$\frac{\sin\theta_i}{c_0} = \frac{\sin\theta_t}{c_1} \tag{B.7}$$

$$A_t = A_i \frac{2 r_1 \cos\theta_t}{r_0 \cos\theta_i + r_1 \cos\theta_t} \tag{B.8}$$

where θ_i, θ_r, and θ_t are the angles of the incident, reflected, and transmitted pulses respectively and r_0 and r_1 are the acoustic impedences on either side of the boundary; these angles are measured relative to the local normal of the discontinuity at the point of incidence. Likewise, A_i, A_r, A_t are the amplitudes of the incident, transmitted and reflected pulses, respectively. The parameters c_0 and r_0 are the velocity and acoustic impedance of the medium in which the incident and reflected pulses travel; c_1 and r_1 are the velocity and acoustic impedance of the medium in which the transmitted pulse travels. The behavior of the diffuse components are difficult to predict, but for our purposes, we assume they obey the Lambertian model, with equal energy scattered per unit solid angle in the forward and reverse directions.

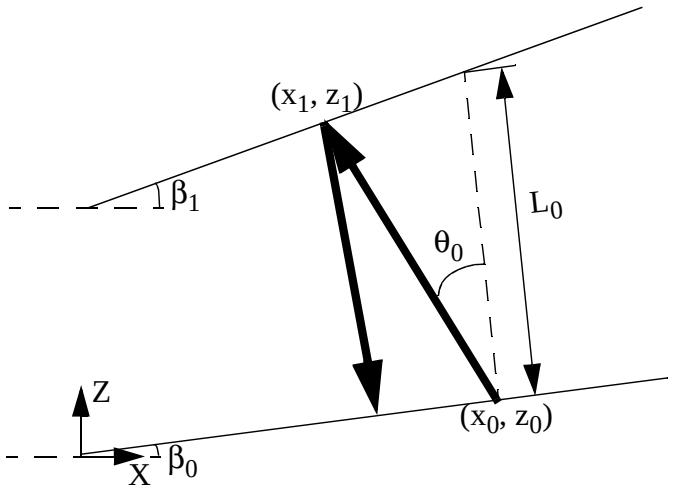

Figure B.3: Imaging model for a single tissue layer whose boundaries are inclined at angles β_0 and β_1 to the x-axis respectively. The pulse enters the tissue layer at (x_0, z_0) at an angle of θ_0 to the normal and reflects from the far side of the layer at (x_1, z_1). The thickness of the layer, L_0, is defined to be the distance from the near side to the far side along the normal to the near side at (x_0, z_0)

Reflection and refraction occur only when the transverse extent of a discontinuity is much larger than the wavelength of the pulse. Even nominally homogenous tissues of the body, such as skin, fat or muscle, will have many small structures within them whose size is on the order of or smaller than the wavelength of the pulse. These discontinuities will not cause the pulse to divert its course but will scatter energy away from the pulse as it travels through the tissue layer instead. The amount of energy scattered depends upon the density, size and arrangement of these scatters. Some of it will reach the transducer, where it can produce quite a lot of “chatter” in between the reflections from the near and far boundaries of the tissue layer. This is illustrated in figure B.1 inbetween the echoes at 900, 1700, 3000 and 4100; in this case, there are two layers of muscle between the transducer and the femur, and the muscle fibers scatter quite a lot of energy. Because the size, density, and arrangement of these scattering structures are characteristic of the type of tissue, analysis of this backscattered energy can be used to automatically identify the tissues the pulse has passed through, a subject discussed in more detail in Appendix C. These scatterers also contribute to the attenuation of the pulse as it travels through the medium.

Since the diffuse components of a reflected pulse are much weaker than the specular components, it is much harder to identify reflections from tissue interfaces for which the incident pulse is not normal or nearly normal, as the diffuse component of the reflection will typically be obscured by the coherent backscatter from small structures within the tissue layer. Consequently, when a single transducer is used as both transmitter and receiver, we must rely almost entirely on the specular component to locate boundaries between soft tissue layers in the signal received by the transducer.

By measuring the time between the arrival at the transducer of the reflections of the pulse from the near and far boundaries of the tissue layer (Δt_0) and with knowledge of the speed

of sound in the that layer (c_0), the relative orientations of the tissue layer boundaries (β_0,β_1), the point (x_0, z_0) at which the pulse entered the layer, and angle (θ_0) at which it entered, we can calculate the thickness (L_0) of the tissue layer and the location the pulse reflected from the far boundary (x_1, y_1) by:

$$L_0 = c_0 \Delta t_0 \frac{\cos\vartheta_0}{\cos\vartheta_0 + \cos\theta_0}(\cos\theta_0 + \sin\theta_0 \tan(\beta_1 - \beta_0)) \tag{B.9}$$

$$\begin{bmatrix} x_1 \\ z_1 \end{bmatrix} = \begin{bmatrix} x_0 \\ z_0 \end{bmatrix} + c_0 \Delta t_0 \frac{\cos\vartheta_0}{\cos\vartheta_0 + \cos\theta_0} \begin{bmatrix} -\sin(\theta_0 + \beta_0) \\ \cos(\theta_0 + \beta_0) \end{bmatrix} \tag{B.10}$$

$$\vartheta_0 = 2(\beta_1 - \beta_0) - \theta_0 \tag{B.11}$$

This is illustrated in figure B.3. If the pulse strikes the far boundary along its normal or close to it, so that the pulse travels back along the same path that it travelled through the layer, equations (B.9) through (B.11) can be approximated by:

$$L_0 = c_0 \frac{\Delta t_0}{2}(\cos\theta_0 + \sin\theta_0 \tan(\beta_1 - \beta_0)) \tag{B.12}$$

$$\begin{bmatrix} x_1 \\ z_1 \end{bmatrix} = \begin{bmatrix} x_0 \\ z_0 \end{bmatrix} + c_0 \frac{\Delta t_0}{2} \begin{bmatrix} -\sin(\theta_0 + \beta_0) \\ \cos(\theta_0 + \beta_0) \end{bmatrix} \tag{B.13}$$

Furthermore, if the boundaries of the layer are parallel, equation (B.12) reduces to:

$$L_0 = c_0 \frac{\Delta t_0}{2} \cos\theta_0 \qquad (14) \tag{B.14}$$

B.2.2.1 Curved Pulse Paths

In the previous discussion, we modelled the path of the pulse as a straight line, but this is not necessarily the case in reality. One interesting implication of equations (B.7) and (B.8) is that if a soft tissue layer has a smoothly-varying gradient in its speed of sound, the path of the pulse through that gradient will be curved. In other words an infinitesimal change in the speed of sound over an infinitesimal distance produces refraction but not reflection. In particular, if the gradient is linear and represented by the equation $c = c_0 + \Delta c_0 z$, where Δc_0 represents the change in sound speed with depth, these curved paths will be arcs of circles with radius: $R = \frac{c_0}{\Delta c_0 \sin\theta_0}$ [115]. Both thermal[1] and stress[2] gradients can create

1. While homeostasis insures that the temperature of the inner tissues of the body remains relatively constant at 37 C, there is a definite temperature gradient (and hence velocity gradient) between the surface of the skin and the inside of this skin.

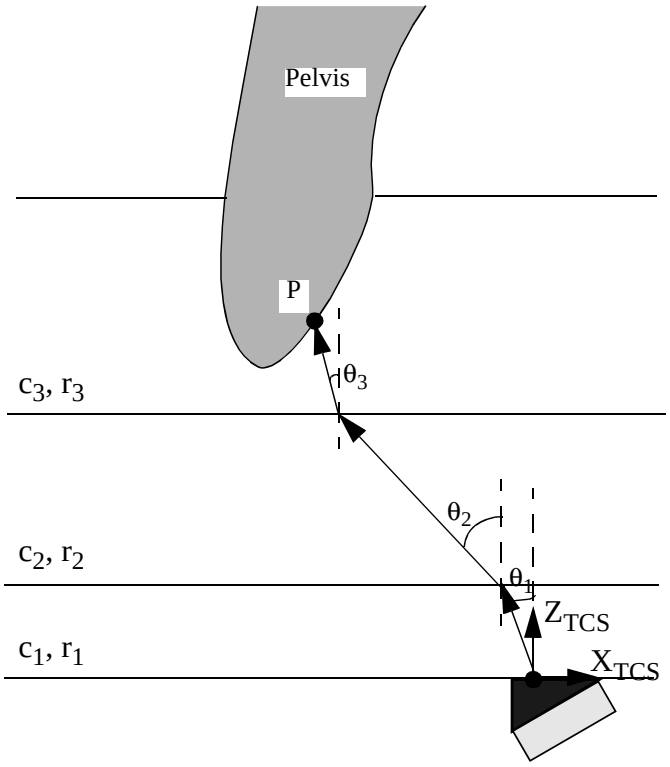

Figure B.4: Model of pulse-echo imaging for multiple tissue layers- in this case, multiple tissue layers between the transducer and the pelvis- shown with all layers parallel for clarity. The pulse enters the body through a coupling wedge which serves two purposes: (1) its shape gives the angle of entry (θ_1) of the ultrasonic pulse and (2) it matches the acoustic impedance of the skin to the acoustic impedance of the transducer, so that no reflections arise from the skin / transducer interface. The pulse reflects from the pelvis at point P.

sound velocity gradients in the body. However, the exact effect of thermal and stress gradients (e.g. appropriate values for Δc_0) on the gradient of sound within human soft tissue has not yet been characterized, and therefore, whether their effect is comparable to other sources of uncertainty in the parameters of equations (9)-(14) is not known. For this reason, we ignore the potential effect of sound velocity gradients and only consider straight paths in our imaging model.

B.2.3 Multiple Tissue Layers

Our model for multiple tissue layer is a straightforward extension of the single-layer one. We place a transducer at (Q_x, Q_y, Q_z) and stack the single layer models, one for each tissue layer, on top of each other, as illustrated in figure B.4. The axes of the coordinate system the pulse travels in are aligned so that the pulse propagates in the *xz*-plane towards $+z$. If there are N such layers, numbered 1 through N, then we can compute the thickness and the location where the pulse intersected the far boundary of each layer by a repeated application of equations (B.9) and (B.10):

2. In general, soft tissues have non-linear mechanical properties, and hence the bulk-modulus is not constant, but a function of the strain. Hence, external stress which produces a change in tissue shape produces a change in bulk modulus and a change in velocity.

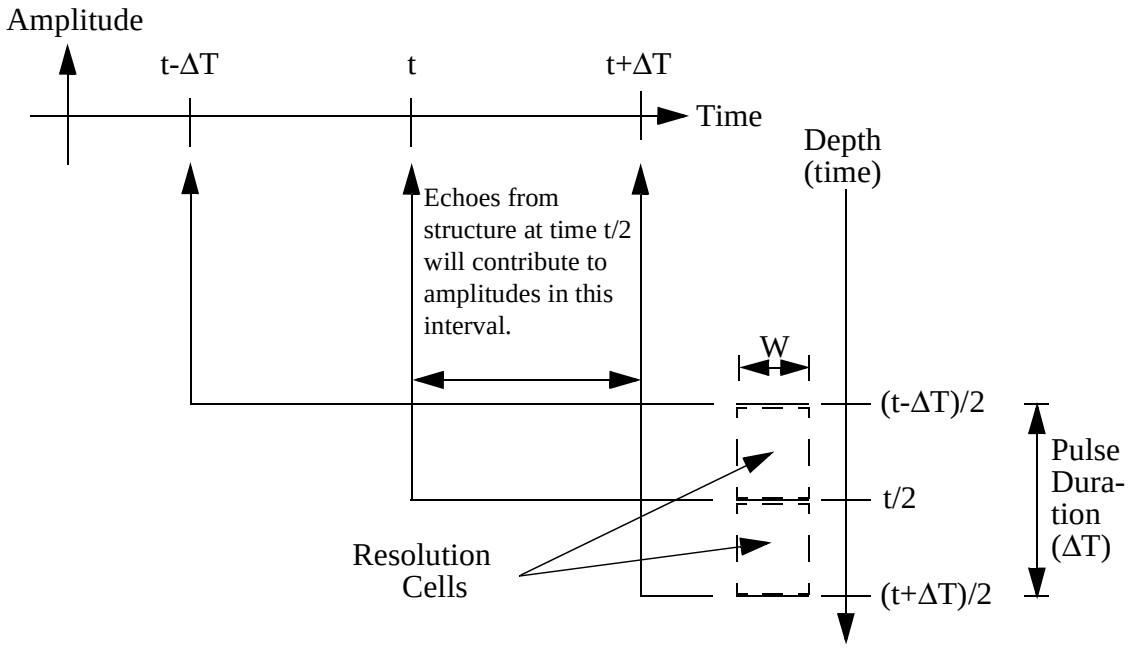

Figure B.5: The resolution cell concept illustrated in two dimensions. As the pulse propagates through the soft tissue it encounters many discontinuities. A discontinuity encountered at time t/2 will continue to reflect energy until time t/2+ΔT, where ΔT is the duration of the pulse, provided that the acoustic response of the discontinuity ceases quickly after insonation. Since it takes time t/2 for the scattered energy to return to the transducer, this discontinuity will contribute to the amplitude of the received signal over the interval [t, t+ΔT].

$$L_i = c_i \Delta t_i \frac{\cos\vartheta_i}{\cos\vartheta_i + \cos\theta_i} (\cos\theta_i + \sin\theta_i \tan(\beta_{i+1} - \beta_i)) \tag{B.15}$$

$$\begin{bmatrix} P_{x,i} \\ P_{y,i} \\ P_{z,i} \end{bmatrix} = \begin{bmatrix} Q_x \\ Q_y \\ Q_z \end{bmatrix} + \sum_{i=1}^{n} c_i \Delta t_i \frac{\cos\vartheta_i}{\cos\vartheta_i + \cos\theta_i} \begin{bmatrix} -\sin(\theta_i + \beta_i) \\ 0 \\ \cos(\theta_i + \beta_i) \end{bmatrix} \tag{B.16}$$

$$\vartheta_i = 2(\beta_{i+1} - \beta_i) - \theta_i \tag{B.17}$$

The angle θ_i can be calculated recursively from θ_1 by:

$$\theta_{i+1} = \sin^{-1}\left(\frac{c_{i+1}}{c_i}\sin(\theta_i - \beta_{i+1} + \beta_i)\right) \qquad -\frac{\pi}{2} \le \theta_i, \theta_{i+1} \le \frac{\pi}{2} \tag{B.18}$$

Note that the same simplifications we applied to equations (B.9) and (B.10) when the angle of reflection is small or the boundaries of the two layers are parallel for the single layer model can be applied to equations (B.16) and (B.17) of the multi-layer model. In addition, because the surface of the first layer conforms to the surface of the transducer or coupling wedge (if one is present), β_1=0 by definition.

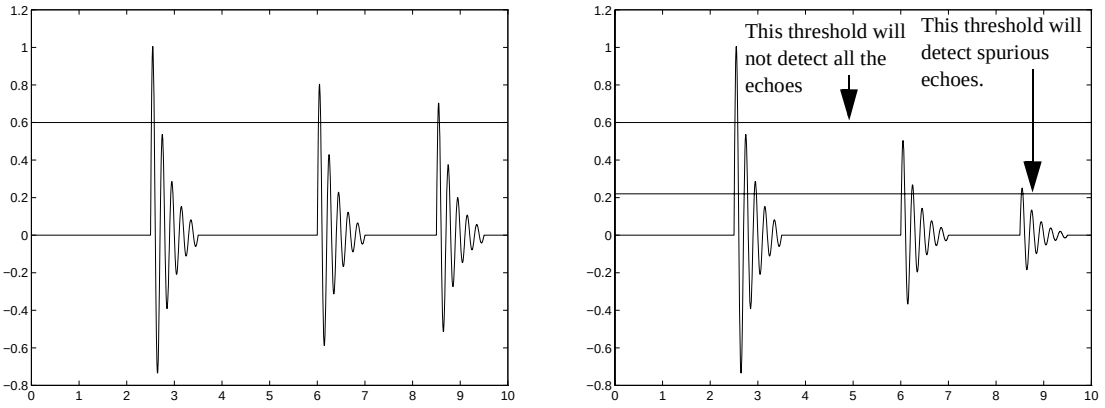

Figure B.6: Amplitude thresholding for echo detection. All echoes above a certain threshold are considered to be echoes from tissue interfaces. The basic technique is illustrated in the figure to the left, and some of the problems with amplitude thresholding are illustrated in the figure to the right.

B.2.4 The Resolution Cell

Although we have built our imaging model by treating the pulse essentially as a large cylindrical particle that splits in two when it intersects a tissue boundary, we must now consider the effects of the finite wavelength of the ultrasonic pulse on our ability to resolve separate structures within the body. Under the assumption that the wavefronts of the pulse can be approximated as plane waves and that the structures within the body stop radiating quickly after the pulse passes, the smallest distance that two objects can be separated axially and still be resolved as separate objects is $c\frac{\Delta T}{2}$ (see figure B.5) and the smallest distance they can be separated laterally is twice the diameter of the pulse. These quantities are called the *axial* and *lateral resolution* of the pulse and the volume they define is called the *resolution cell*. Any two structures within the body can be resolved as separate entities if and only if they occupy different resolution cells. Naturally, the dimensions of the resolution cell are quite dependent upon the characteristics of the transducer, but for a broadband focussed Gaussian pulse with a center frequency of 7 MHz with a duration of 1μs delivered from a circular transducer 3mm in diameter, the dimensions of its resolution cell in the focal zone will measure approximately 6 mm laterally and 0.77 mm axially.

B.3 Echo Detection

To compute the thicknesses and boundary point locations from our imaging model, we must measure the value of Δt_i in equations (B.15) through (B.17) from the echogram of return echoes for all tissue layers. The basic method for such echo detection is **amplitude thresholding**, in which all amplitudes above a certain threshold are considered to be soft tissue interfaces (see figure B.6). Amplitude thresholding has the advantage of simplicity and will be effective if the signal-to-noise ratio is large so that the threshold can be set above the expected amplitude of the noise but not above the expected amplitude of the echoes. The level of the threshold imposes a trade-off between false-alarms (noise mistaken for an echo) and missed echoes from tissue boundaries; lower thresholds result

in fewer misses but more false positives than higher ones. The specificity and sensitivity of the amplitude thresholding approach to echo detection can be improved by suppressing false-alarms through dead-time delays, Schmidt triggers, and excluding echoes detected in regions where it is known a boundary cannot occur.

The signal-to-noise ratio of a well-designed ultrasound system for targets close to the transducer will be quite large. However, because the pulse attenuates as it travels through the tissue layers, the signal-to-noise ratio will decrease as the target range increases. The receiving system usually compensates for this attenuation by passing the received echoes through a voltage-controlled variable-gain amplifier whose gain increases exponentially with time, a process called *time-gain compensation* in the ultrasonic literature. Although time-gain compensation compensates for the loss of amplitude in the received signal and removes the need to vary the threshold with time, it amplifies the noise as well, so it does not improve the signal-to-noise ratio. If the signal-to-noise ratio vs. time profile is insufficient for a particular application, autocorrelation filters can be used to improve it, provided that a clean echo of the pulse can be obtained to serve as the template.

B.4 Error Analysis

In an ideal world, we would know or be able to measure the values of the independent variables in equations (B.15) through (B.18) with sufficient precision and accuracy so that the tissue layer thicknesses and locations of the boundary points could be calculated with values that were arbitrarily close to their actual values. However, our equipment and experimental conditions limit the accuracy with which we can measure the location of the transducer ($[Q_x\ Q_y\ Q_z]$) and the time-of-flight (Δt_i) in each tissue layer and, although they allow us to be reasonably certain that angle of entry into the first layer (θ_1) is zero, they provide us with no knowledge of the speed of sound *in vivo* within the layers (c_i) and the relative orientations of their boundaries (β_i). Consequently, we make the standard assumption for ultrasonic imaging that all tissue layers are perpendicular or nearly perpendicular to the path of the pulse (e.g. $\beta_i = 0$ for all i), so that refraction can be neglected, and we assume that the speed of sound within each tissue layer is equal to its textbook value of 1600 m/s for skin, 1450 m/s for fat, and 1580 m/s for muscle[77]. When we cannot identify a tissue layer, we use the “average” value of 1540 m/s typically used in ultrasonic imaging for generic soft tissue. This allows us to compute the estimated thickness of each layer and the location of each boundary points as:

$$\begin{bmatrix} P'_{x,i} \\ P'_{y,i} \\ P'_{z,i} \end{bmatrix} = \begin{bmatrix} Q'_x \\ Q'_y \\ Q'_z \end{bmatrix} + \sum_{k=1}^{i} c'_k \frac{\Delta t'_k}{2} \begin{bmatrix} 0 \\ 0 \\ 1 \end{bmatrix} \tag{B.19}$$

$$L'_i = c'_i \frac{\Delta t'_i}{2} \tag{B.20}$$

where the prime mark (’) indicates that the variables in question are estimated or assumed

quantities as opposed to their actual values.

Obviously, the values calculated by equations (B.19) and (B.20) will be different from the actual values calculated by equations (B.15) and (B.16) when the layer boundaries are not parallel, the speeds of sound in each layer differ from their textbook values, or when the angle of entry for the ultrasonic pulse in the first tissue layer is not zero. In the remainder of this section, we quantify these differences and explore how the assumptions we make about the physical properties of the tissue layers and the shapes of their boundaries affect the accuracy of our measurements.

B.4.1 Uncertainty in Location of the Transducer

From equations (B.15) and (B.16), we see that uncertainty in the location of the transducer produces uncertainty in the locations of the boundary points ($\vec{P}_i$) but not in the thickness of the individual tissue layers. If the uncertainty in $[Q_x\ Q_y\ Q_z]$ is $[\Delta Q_x\ \Delta Q_y\ \Delta Q_z]$, then the uncertainty in $\vec{P}_i$ will also be $[\Delta Q_x\ \Delta Q_y\ \Delta Q_z]$.

B.4.2 Uncertainty in Time-of-Flight

The time-of-flight for a tissue layer is the difference between the arrival times of the echoes from its near and far boundaries, and thus the maximum uncertainty in Δt_i is equal to twice the maximum uncertainty in measuring the locations of these echoes. Measuring the location of the echoes is simply a matter of observing the positive and negative crossings of a threshold and averaging them to find the location of the first detected peak in the returned pulse. Subtracting 1/4 of the pulse's period gives the location of the start of the echo. In the absence of noise, this procedure has an accuracy equal to the sampling time of the digitizer. In the presence of the incoherent and coherent noise common to ultrasonic imaging systems, the analysis becomes much more complicated, but the uncertainty in locating the pulse is no larger than 1/4 of the period, and therefore the uncertainty in measuring Δt_i will be no larger than 1/2 of the period. For a 5 Mhz pulse of monotonically decreasing amplitude, this corresponds to an uncertainty of 0.08 mm in skin, 0.07 mm in fat, and 0.08 mm in muscle in the location of the boundary point along the direction of travel of the ultrasonic pulse. These contributions to the overall uncertainty in the boundary point location are much smaller than the contributions from other sources and can be neglected. The same holds true for the uncertainties in the thickness measurements for each layer, which are equal to the values for the boundary points times $\cos(\theta_i) + \sin(\theta_i)\tan(\beta_{i+1} - \beta_i)$. Although this factor can grow quite large for extreme values of its variables, it also applies to other sources of uncertainty in the thickness measurements whose base values are much larger than 0.08 mm. Consequently, the relative contribution from uncertainty in the time of flight will still be negligible even if θ_i and $\beta_{i+1} - \beta_i$ are large.

B.4.3 Uncertainty in the Speed of Sound, Angle of Entry and Tissue Boundary Orientations

Having analyzed the effects of uncertainty in the transducer location and time of flight measurements, we can now turn our attention to the remaining independent variables: the

speed of sound in each of the soft tissue layers, the orientations of their boundaries, and the angle of entry of the ultrasonic pulse into the body. The effects of these variables on the uncertainty in the tissue thicknesses and boundary point locations are coupled, and so a simple analysis will not do. Instead, we will consider how the difference between the actual value of these variables and their assumed values affects the difference between the actual thickness of the tissue layer and the value we would compute for it using equation (B.20) and the actual locations of the boundary points and the locations we would compute for them using equation (B.19). Furthermore, because the thickness of each tissue layer will vary from subject to subject, we will compute these two differences between actual and calculated values per unit thickness of the tissue layer they belong to. The differences between the actual and calculated values of $\overline{P}_i$ and L_i per unit thickness of tissue layer *i* are:

$$\frac{\overline{P}'_i - \overline{P}_i}{L_i} = \frac{\Delta P_i}{L_i} = \frac{\begin{bmatrix} \sin(\theta_i + \beta_i) - \chi_i \sin(\theta'_i + \beta'_i) \\ 0 \\ \chi_i \cos(\theta'_i + \beta'_i) - \cos(\theta_i + \beta_i) \end{bmatrix}}{\cos\theta_i + \sin\theta_i \tan(\beta_{i+1} - \beta_i)} \tag{B.21}$$

$$\frac{L'_i - L_i}{L_i} = \frac{\Delta L_i}{L_i} = \chi_i \frac{\cos\theta'_i + \sin\theta'_i \tan(\beta'_{i+1} - \beta'_i)}{\cos\theta_i + \sin\theta_i \tan(\beta_{i+1} - \beta_i)} - 1 \tag{B.22}$$

$$\chi_i = \left(\frac{c'_i}{c_i}\right)\left(\frac{\cos\vartheta'_i}{\cos\vartheta_i}\right)\left(\frac{\cos\vartheta_i + \cos\theta_i}{\cos\vartheta'_i + \cos\theta'_i}\right) \tag{B.23}$$

where θ'_i, β'_i and c'_i are the estimated (or measured) angle of entry, orientation of the near boundary, and speed of sound in layer *i*; θ_i, β_i, and c_i are the actual values of those variables; and $\vartheta_i = 2(\beta_i+1 - \beta_i) - \theta_i$ and $\vartheta'_i = 2(\beta'_{i+1} - \beta'_i) - \theta'_i$. In our case, θ'_1 and β'_i for all layers are zero. The uncertainty per unit thickness in $\overline{P}'_i$ and L'_i arising from uncertainty in θ'_1, β'_i and c'_i is simply the minimum and maximum values of $\Delta P_i/L_i$ and $\Delta L_i/L_i$ over the range of possible values for θ_1, β_i, and c_i allowed by the uncertainty in θ'_1, β'_i and c'_i.

To simplify our analysis, we will assume that we have four soft tissue layers in the following order: skin, fat, muscle, and bone. This is the order that these layers normally appear in the body, although there may be multiple layers of muscle separated by thin layers of fascia. We will furthermore assume that the ultrasonic pulse does not penetrate into the bone but reflects completely from its surface. In spite of these assumptions, the general conclusions from our analysis will apply to other arrangements of soft tissue within the body.

B.4.3.1 Effects on Thickness Measurements

Figures B.7 through B.14 illustrate the uncertainty in the measured thickness of skin, fat

and muscle caused by the uncertainty in the independent variables of equations (B.21), (B.22) and (B.23), while figures B.15 through B.24 show the effect on the uncertainty in the locations of the points where the ultrasonic pulse intersected the far boundaries of those layers. Figures B.7, B.8, and B.9 graph uncertainty in the thickness of skin, fat and muscle vs. uncertainty in the speed of sound in those layers (Δc_i), uncertainty in the speed of sound in skin (Δc_1) and uncertainty in the angle of entry of the ultrasonic pulse in skin ($\Delta\theta_1$) under the assumption that the layer boundaries are parallel ($\beta_i = 0$). Figures B.15, B.16 and B.17 graph the uncertainty in the locations of the boundary points vs. the same variables. Figures B.10 through B.14 graph uncertainty in the thickness of skin, fat and muscle vs. uncertainty in the near and far boundaries of each layer ($\Delta\beta i$, $\Delta\beta_{i+1}$) and the speed of sound in each layer (Δc_i) and the previous one (Δc_{i-1}) under the assumption that the angle of entry in skin and the orientation of the boundaries of the other layers is zero. Figures B.18 through B.24 graph the uncertainty in the boundary point locations for the same variables. The assumptions made in the first two and last two sets of figures allow us to isolate the effects of varying different collections of variables from one another. We use Δc_1 instead of Δc_{i-1}, the speed of sound in the previous layer, in the first two sets of figures because when the boundaries are all parallel, the speeds of sound in the intervening layers cancel in the repeated applications of equation (B.18), leaving θ_i a function of c_i, c_1 and θ_1 alone. This is not true when β_i is not identically zero.

Examining figures B.7, B.8 and B.9, one can see that the uncertainty in the speed of sound and angle of entry in skin have little effect on the uncertainty of the thickness of any of the tissue layers. Most of the uncertainty comes from uncertainty in the speed of sound in the layer itself and the orientations of the layer boundaries. The baseline error from the former quantity can be as large as 15% of the thickness of the layer for large uncertainties of +/- 200 m/s.

One also notices from figure B.7 that the actual orientations of the near and far boundaries of the skin layer have no effect on the uncertainty in the thickness of that layer. This is a by-product of the way we defined the orientation of the layers and our assumption that $\theta_1 = 0$ for this figure. The orientation of the near boundary of a layer is its inclination from the x-axis at the point where the pulse enters the layer and the orientation of the far boundary is its inclination from the x-axis where it leaves. With an angle of entry of zero, the pulse travels along the normal to the near boundary of skin, and since thickness is measured along this normal, changing the orientation of the far boundary will not change the thickness nor where the pulse intersects it. Changing the near boundary will change the thickness and point of intersection, but will not increase the uncertainty in either quantity per unit thickness of skin.

In contrast to their effects in skin, the orientations of the boundaries of the fat and muscle layers have a very large impact on the uncertainty in measuring the thickness of those layers, producing uncertainties per unit thickness of up to 27% - 50% in fat and 31-51% in muscle, depending on the uncertainty in the speed of sound in those layers. When the boundaries are not parallel, uncertainty in the speed of sound for the previous layer (e.g. skin for the fat layer, and fat for the muscle layer) has a slight impact on the thickness

measurements for the fat and muscle layers of about +/- 2.5% per unit thickness over and above the contribution from uncertainty in the orientation of the layer boundaries (figures B.11 and B.13).

B.4.3.2 Effects on Measurement of Boundary Points

Whereas the uncertainty in the thickness of a tissue layer is sensitive to three variables - the orientation of the near and far boundaries and the speed of sound within the layer itself - the location of the boundary points is sensitive to five. As shown in figures B.15, B.16 and B.17, even small uncertainty in the angle of entry of the pulse into the skin can have a huge effect on the uncertainty in the location of the boundaries between the skin, fat, muscle and bone layers, resulting in uncertainties of up to +/-20% when even the uncertainties in all of the other variables are neglidible. Fortunately, it is difficult to accidentally generate a nonzero angle of entry into the body. However, for those rare occasions when an application needs a nonzero angle of entry, care must be taken in the construction of the coupling wedge or focussing lens to insure that the beam is sent out at the proper angle to ensure accurate results.

An examination of figures B.18, B.20 and B.23 shows that the uncertainty in the speed of sound within the layer itself has a large impact on the uncertainty in the location of the far boundary for that layer, and the value of this uncertainty determines the potential impact that uncertainty in the boundary orientations or angle of entry may have. The same also holds true for the uncertainty in the speed of sound in the previous layer when the layer boundaries are not parallel. The uncertainty of the location of the fat/skin boundary point is insensitive the orientation of the boundaries of the skin layer for the same reasons that the thickness of that layer is.

A careful examination of figures B.20 and B.23 reveals an interesting anomaly. As expected, the distance per unit thickness between the actual and calculated locations of the fat/muscle and muscle/bone boundary points increases as the absolute difference between the actual and assumed speeds of sound within the fat and muscle layers increases. However, while for some curves the distance per unit thickness between the actual and calculated points increases as the boundaries tilt away from their assumed orientation of zero, for others, this distance actually *decreases* with increasing $|\beta_i|$. Furthermore, the condition under which this decrease occurs are different in fat and muscle. For fat, this phenomenon occurs as the actual speed of sound increases from its textbook value of 1540 m/s, while for muscle, it occurs as the actual speed of sound decreases.

We can explain this behavior in terms of the effect the orientations of the tissue layer boundaries have on the thickness of the layer and the ratio of the actual speed of sound in the layer itself to the actual speed of sound in the previous layer. Since we have defined thickness to be the distance between the near and far boundaries along the normal to the former, rotating the far boundary away from the near boundary will increase the thickness of the layer without changing the locations of the actual and calculated boundary points, resulting in a decrease in the distance per unit thickness even though the absolute distance remains the same. Rotating the near boundary away from the far boundary will have the same effect on the thickness of the layer, but will change the locations of the actual and

calculated boundary points as well. We can understand the how these points move in response to a change in the near boundary orientation by decomposing the distance between them into two components: one along the z-axis and one along the far boundary. Note that in general, these components are not orthogonal. The component along the z-axis is entirely a function of the difference between the actual and assumed speeds of sound in the layer itself. The component along the far boundary is a function of the deflection of the actual path of the pulse from its assumed path, which is in turn a function of the near boundary orientation and the absolute difference between the ratio of the speed of sound in the current layer to the speed of sound in the previous layer and one. The larger the difference between this ratio and one, the more effect a change in the orientation of the near boundary will have on the second component. Hence, when the ratio is small, the distance between the actual and calculated boundary points is insensitive to the change in the orientation of the near boundary, and the change in tissue layer thickness will dominate the overall value of the uncertainty-per-unit-thickness, causing it to decrease as the near boundary tilts away from the far boundary. However, when the ratio is large, there will be a region in which the calculated and actual boundary points separate faster than the thickness of the layer grows as the near boundary tilts away from the far boundary, and thus the uncertainty per unit thickness between the points will increase. For the fat layer, the previous layer is skin, in which the textbook value for the speed of sound of 1600 m/s is higher than the speed of sound in fat of 1450 m/s. Therefore, increasing the speed of sound from its textbook value will cause the ratio between the speeds of sound in fat and skin to move towards one, resulting in curves where the uncertainty per unit thickness decreases as the near boundary tilts away from the far layer. For the muscle layer, the textbook speed of sound is 1580 m/s, which is higher than the value for the previous layer of fat. Hence, decreasing the speed of sound from this textbook value brings their ratio closer to one and produces the curves of decreasing uncertainty.

B.4.4 Discussion

Summarizing what has been learned so far about the effects of uncertainty in the speeds of sound in the individual tissue layers, the orientations of the soft tissue boundaries, and the angle of entry on measurement of the soft tissue layer thicknesses and boundary point locations, which uncertainty has the most impact depends upon the quantity being measured. When measuring the tissue thickness, uncertainty in the orientations of the boundary layers will have the most impact on the uncertainty in the thickness measurements. Uncertainty in the speed of sound in each of the tissue layers also has a large impact, but uncertainty in the angle of entry of the pulse into the body has little impact. When measuring boundary points on the other hand, it is very important to minimize the uncertainty in the angle of entry, since even small deviations from its assumed value can lead to large differences between the actual and calculated locations of the boundary points. Large uncertainties in the speed of sound in each tissue layer can also have a large impact, although not quite as large as uncertainties in the angle of entry. Uncertainties in the angle of entry can have a large or a small impact, depending on the uncertainty in the speeds of sound in each layer. Finally, large uncertainties in some quantities do not necessarily lead to large uncertainties in the final result. For example, we can tolerate large uncertainties in the tissue layer orientations provided that the angle of entry and speeds of sound are close to their assumed values.

So far, we have considered the effects of the effects of uncertainty in selected groups of three variables by setting the uncertainty in the other variables to zero. While this gives a good feel for how changes in these variables affect the final uncertainties in the calculated tissue thicknesses and boundary point locations, the individual uncertainties obtained from these results do not combine linearly to compute the total uncertainty resulting from the individual uncertainties in all seven variables (speeds of sound in skin, fat and muscle; orientations of the skin/fat, fat/muscle and muscle bone boundaries; and the angle of entry in skin). However, they do give us a sense that large uncertainties in all seven variables potentially produce very large uncertainties in the final results. Indeed, the maximum uncertainties we have used in our results so far - +/-200 m/s for each speed of sound, +/-30 degrees for each tissue boundary, and +/-10 degrees for the angle of entry - result in a huge uncertainty per unit thickness in the thickness measurements of 14% for skin, 24% for fat, and 76% for muscle! Likewise, the uncertainties per unit thickness in the boundary point locations under these same conditions are 14%, 23% and 69% for the skin/fat, fat/muscle and muscle/bone boundaries respectively.

Fortunately, for the single-element pulse-echo system we use in our experiments, it is almost impossible to generate an angle of entry that is significantly different from zero. Furthermore, the farther away from the transducer a tissue layer boundary is, the closer its orientation must be to perpendicular to the pulse's direction of travel in order for the reflection to reach the transducer. For a pulse 3 mm in diameter, even a deflection of as little as ten degrees from the perpendicular will cause most of the energy from the reflected pulse to miss the transducer if it is farther than 6 mm from the transducer, and a distance of 8 mm will cause it to miss almost entirely. Consequently, we need only worry about large boundary orientations for layers that are close to the transducer, such as the skin/fat boundary. Finally, extreme variations of 200 m/s in the speed of sound in the tissue layers would require extreme changes in the mechanical properties of those layers. Although no one has yet completely characterized how the speed of sound varies with mechanical stress, disease or injury, such large variations are unlikely for moderately healthy tissue. For a more realistic scenario with no uncertainty in the angle of entry and uncertainties of +/-100 m/s in the speed of sound and +/-10 degrees for each tissue boundary, the uncertainty per unit thickness in the thickness measurements becomes 6.7% in skin, 8.7% in fat and 14% in muscle. The uncertainties per unit thickness in the skin/fat, fat/muscle and muscle/bone boundaries are 6.7%, 8.4% and 14.1% respectively. Considering all sources of uncertainty - transducer location and echo location as well as the speed of sounds, tissue boundary orientations, and the angle of entry - and assuming an uncertainty of 0.3 mm in the location of the transducer (equal to the accuracy of the position wand we use to locate the transducers prior to running our experiments), the total uncertainty in our thickness measurements will be $(0.3 + 0.067L_1)$ mm in skin, $(0.3 + 0.084L_2)$ mm in fat and $(0.3 + 0.14L_3)$ mm in muscle, where L_1, L_2 and L_3 are the thicknesses of the respective tissue layers in mm. The uncertainties in the boundary point locations will be almost the same: $(0.3 + 0.067L_1)$, $(0.3 + 0.081L_2)$ and $(0.3 + 0.14L_3)$ mm for the skin/fat, fat/muscle, and muscle/bone boundaries respectively.

It is common practice in ultrasonic imaging to ignore the effects of refraction (which is

equivalent to assuming that the boundaries of the tissue layers are parallel) and to use estimated “textbook” values for the speed of sound in soft tissue[77]. Perhaps the most important point of this analysis is to show that these simplifying assumptions still produce reasonably accurate measurements. However, to measure very thin layers or to make very accurate measurements, better estimates of the speed of sound in the individual tissue layers, the orientations of their boundaries, or both will be needed. The implications of this analysis for imaging arrangements in which one transducer emits the pulse but multiple transducers at different spatial locations are used to listen for its echoes are quite different than those that arise when a single transducer is used by itself. Although not used currently, such arrangements would be useful for automatic tissue characterization, as they would allow one to estimate the density of scatterers along directions other than the path the pulse propagates along. However, such arrays can easily receive reflections from boundaries whose orientations are not perpendicular to the pulse’s direction of travel or close to perpendicular. As our analysis in this section has shown, neglecting the effects of refraction in such an arrangement will produce a very large error in the result, rendering it practically useless. Consequently, when using multiple arrays of receivers, it is important to incorporate a mechanism for accurately estimating the orientation of the tissue layer boundary the pulse reflected from. Sophisticated techniques for dealing with multiple receivers, non-normal paths, multiple reflections and so on have developed particularly in geophysics, where acoustic methods similar to those used for ultrasonic measurement of soft tissue thickness are used to search for petroleum deposits.

B.5 Conclusions

In this appendix, we developed a model of the propagation of the ultrasonic pulse through the body that takes into account the nature of the ultrasonic pulse, the mechanical characteristics of the soft tissue layers themselves, and the orientations of the boundaries between the soft tissue layers. Because of the limits of our knowledge and experimental conditions, we are unable to measure several important quantities of this model, such as the speed of sound in the tissue layers and the orientations of their boundaries, and therefore, we must make assumptions about their values. We then analyzed the effects of these assumptions on the accuracy of our ability to measure the thickness of each tissue layer and the locations where the ultrasonic pulse intersected their boundaries. Under a realistic set of assumptions about the variability of the speeds of sound in skin, fat and muscle and the orientations of the skin/fat, fat/muscle, and muscle/bone boundaries, we found that the accuracies of the thickness measurements are ($0.3 + 0.067L_1$) mm for skin, ($0.3 + 0.084L_2$) mm for fat and ($0.3 + 0.14L_3$) mm for muscle, where L_1, L_2 and L_3 are the thicknesses of those respective tissue layers in mm. The accuracy in measuring the skin/fat, fat/muscle and muscle/bone boundaries are ($0.3 + 0.067L_1$), ($0.3 + 0.081L_2$) and ($0.3 + 0.14L_3$) mm respectively. This analysis shows that the common practice in ultrasonic imaging of neglecting refraction and assuming a textbook value for the speed of sound in skin, fat and muscle is reasonable so long as one is not measuring extraordinarily thin layers and can tolerate 10% errors in nearby layers and 15% errors in deeper ones. For more accurate measurements, one must take into account the orientation of the tissue layer boundaries, the actual speed of sound in the tissue layers, or both. Finally, for arrangements in which one is using a different transducer to receive the echoes than the

one that transmitted the pulse, the effects of refraction cannot be neglected at all if accurate measurements are to be obtained. However, in such cases, it is possible to exploit the fact that the transmitter and receiver can be moved relative to one another to measure the actual speed of sound in the various layers.

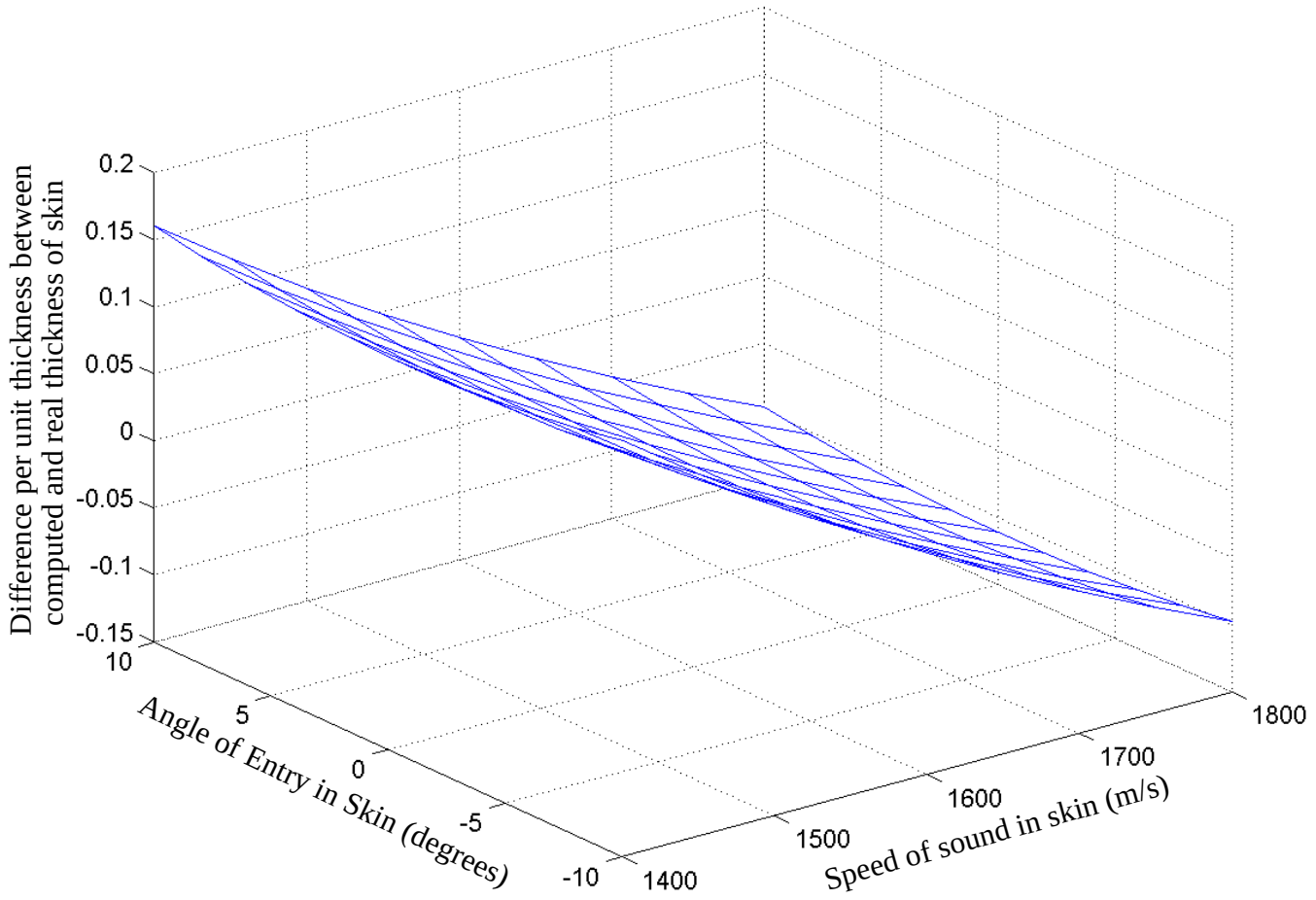

Figure B.7: Difference per unit thickness between the calculated thickness of skin and its actual value as a function of the actual speed of sound and angle of entry in skin. The thickness of the layer was calculated assuming c_1=1600 m/s and θ_1=0.

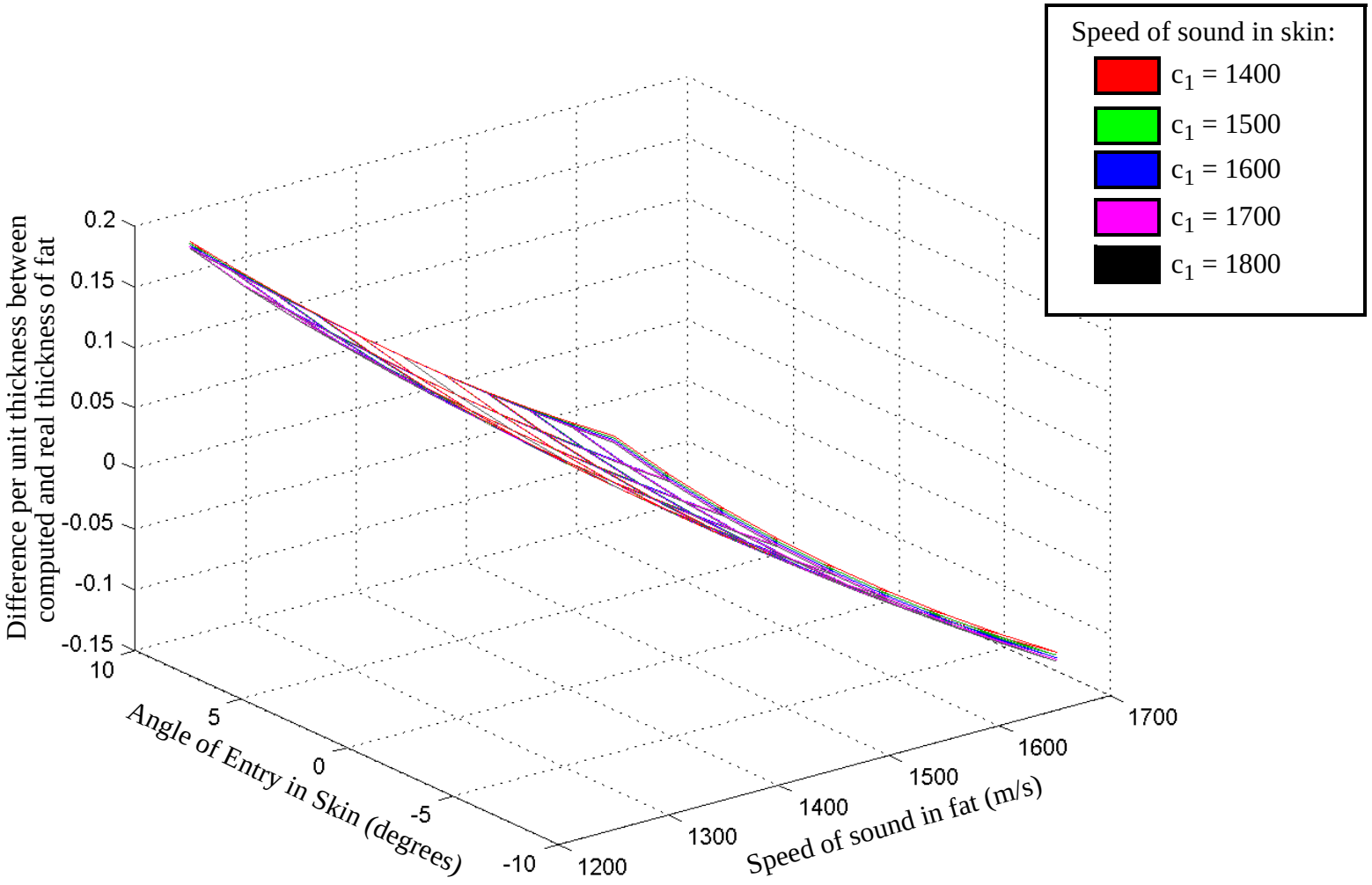

Figure B.8: Difference per unit thickness between the calculated thickness of the layer of fat and its actual value as a function of the actual speeds of sound in skin and fat and the actual angle of entry in skin with all layer boundaries parallel. The calculated thickness of the fat layer was obtained by assuming c_1=1600 m/s, c_2=1450 m/s and θ_1=0.

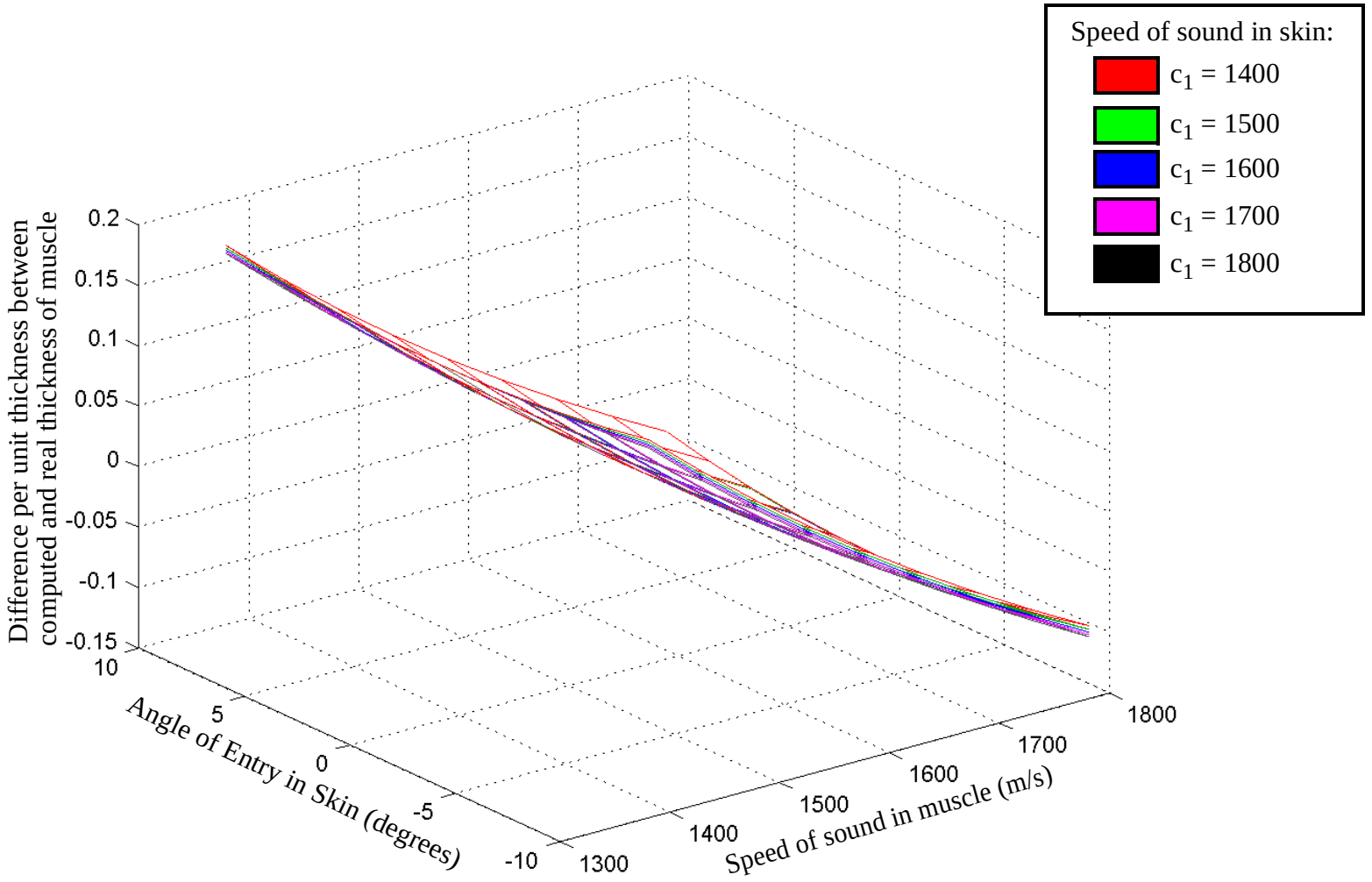

Figure B.9: Difference per unit thickness between the calculated thickness of the layer of muscle and its actual value as a function of the actual speeds of sound in skin and muscle and the actual angle of entry in skin with all layer boundaries parallel. The calculated thickness of the muscle layer was obtained by assuming c_1=1600 m/s, c_3=1580 m/s and θ_1=0.

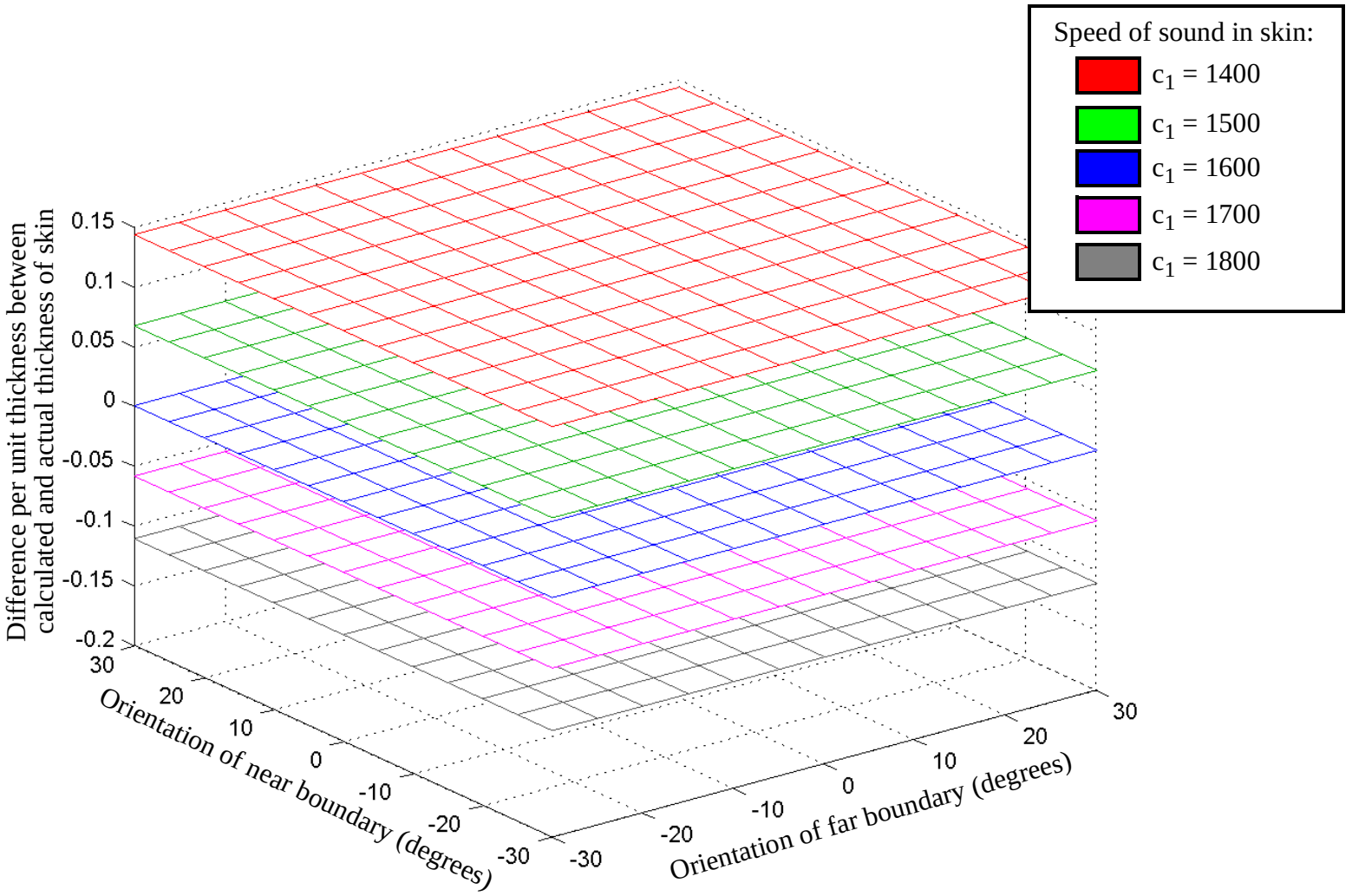

Figure B.10: Difference per unit thickness between the calculated thickness of the skin layer and its actual value as a function of the actual speeds of sound in skin (c_1) and the orientations of the near and far boundaries of the layer (β_1, β_2) with the angle of entry (θ_1) held constant at zero. The calculated thickness of skin was obtained by assuming c_1=1600 m / s and β_1=β_2=0.

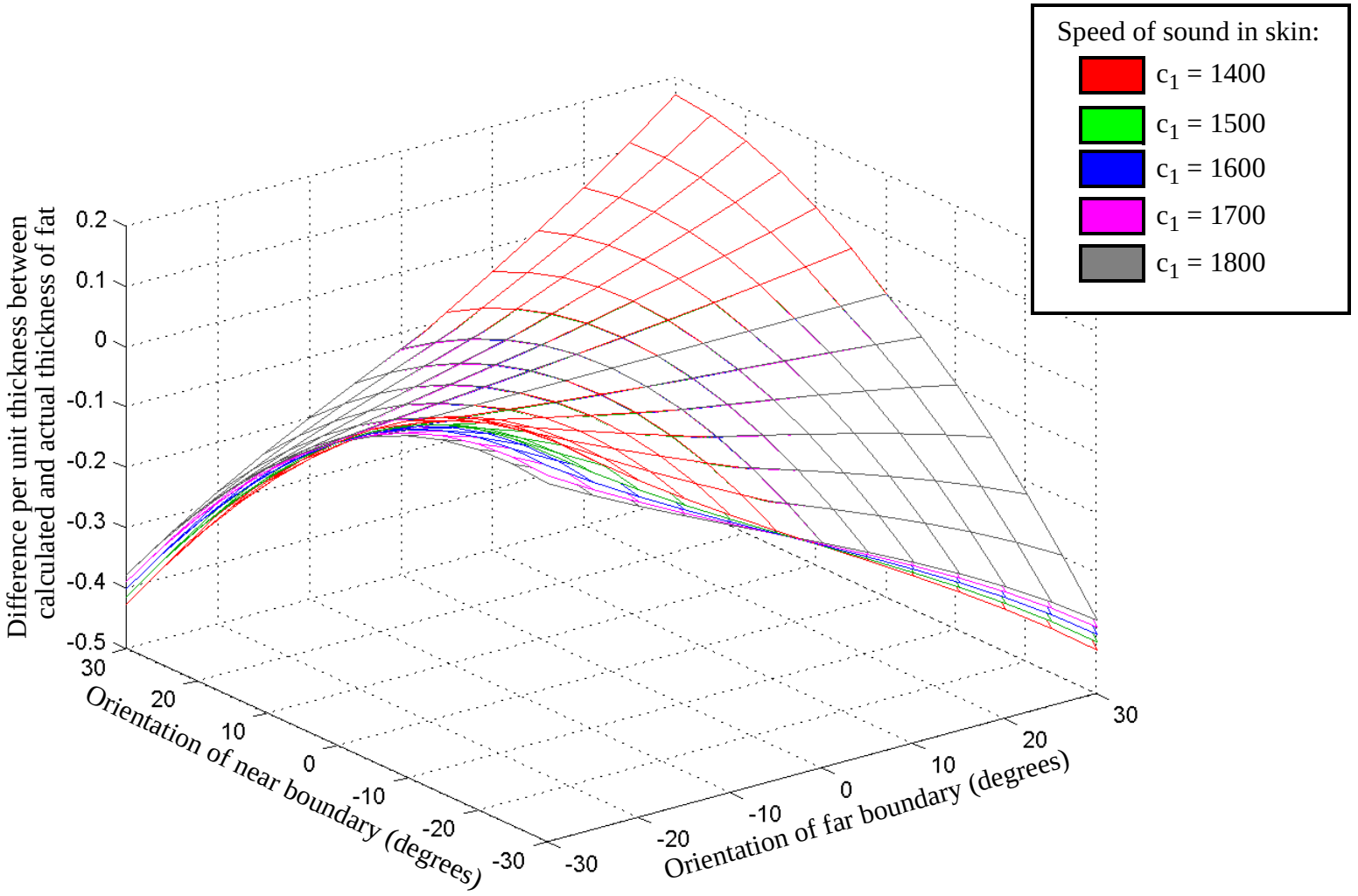

Figure B.11: Difference per unit thickness between the calculated thickness of the fat layer and its actual value as a function of the actual speed of sound in skin (c_1) and the orientations of the near and far boundaries of the fat layer (β_2, β_3) with the angle of entry (θ_1) held constant at zero. The calculated thickness of the fat layer was obtained by assuming c_1=1600 m/s, c_2=1450 m/s and β_2=β_3=0.

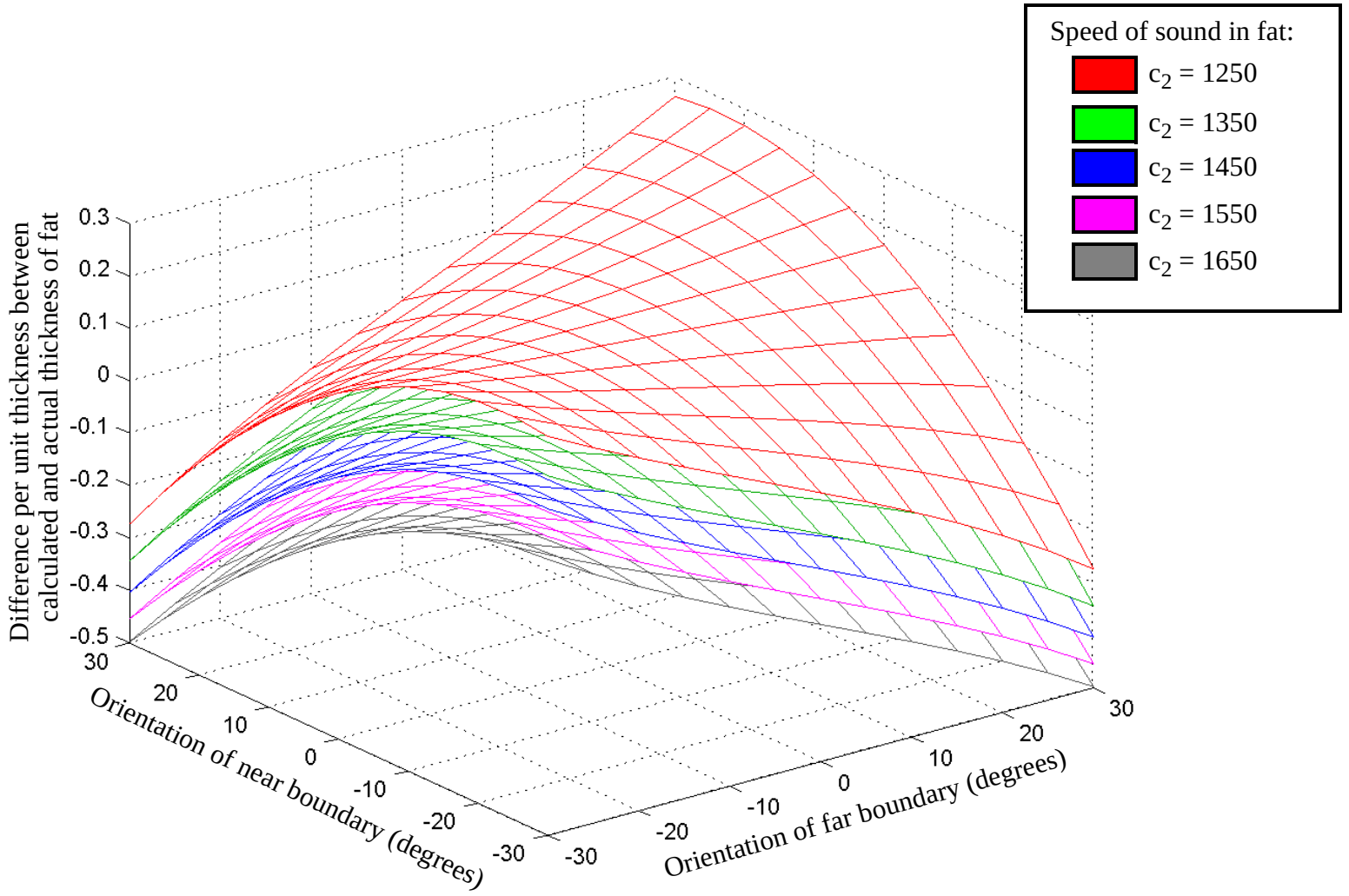

Figure B.12: Difference per unit thickness between the calculated thickness of the fat layer and its actual value as a function of the actual speed of sound (c_2) and the orientations of the near and far boundaries (β_2, β_3) of the fat layer itself with the angle of entry (θ_1) held constant at zero. The calculated thickness of the fat layer was obtained by assuming c_1=1600 m / s, c_2=1450 m / s and β_2=β_3=0.

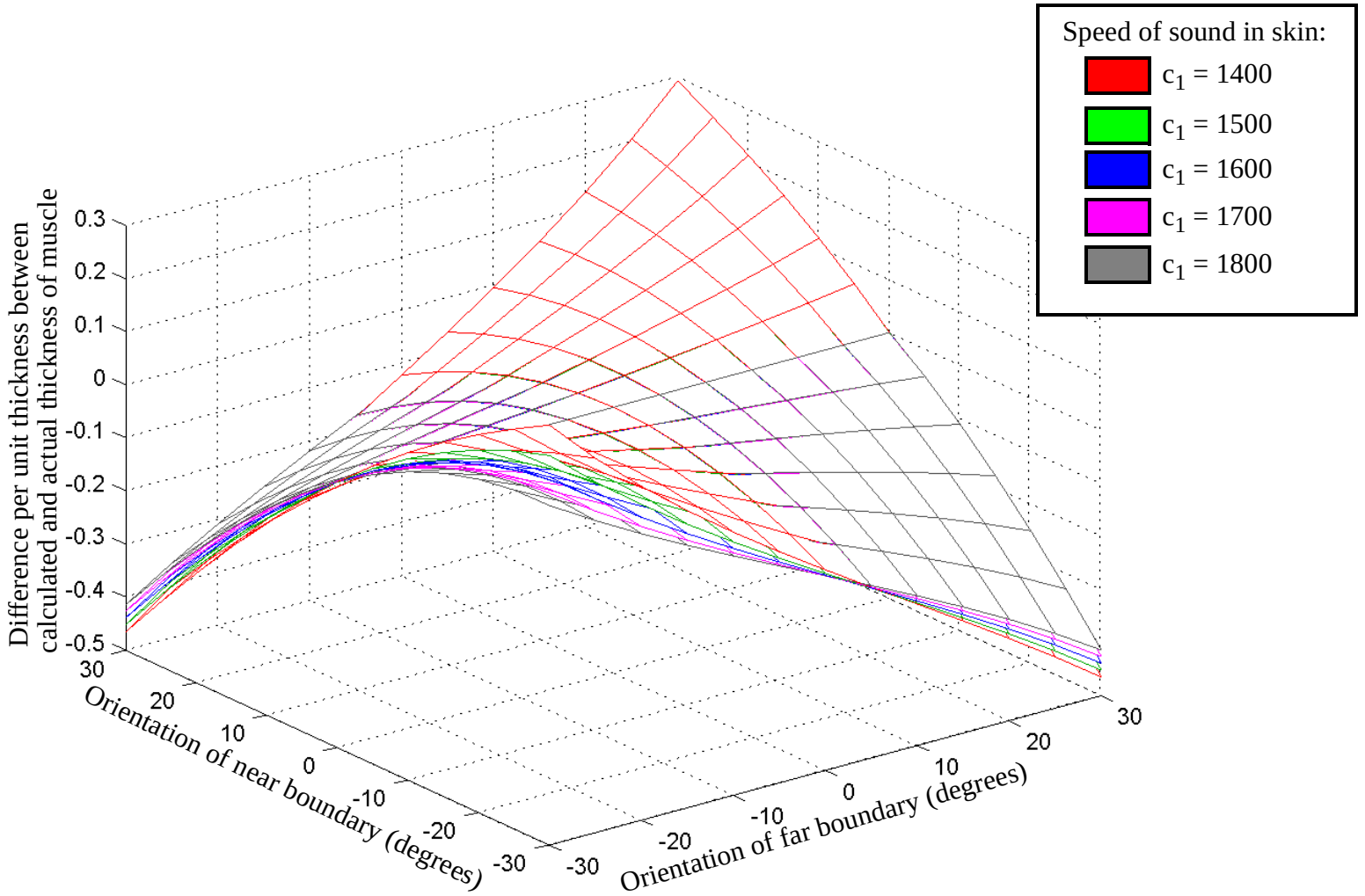

Figure B.13: Difference per unit thickness between the calculated thickness of the muscle layer and its actual value as a function of the actual speed of sound in skin (c_1) and the orientations of the near and far boundaries (β_3, β_4) of the muscle layer itself with the angle of entry (θ_1) held constant at zero. The calculated thickness of the fat layer was obtained by assuming c_1=1600 m / s, c_3=1580 m / s and β_3=β_4=0.

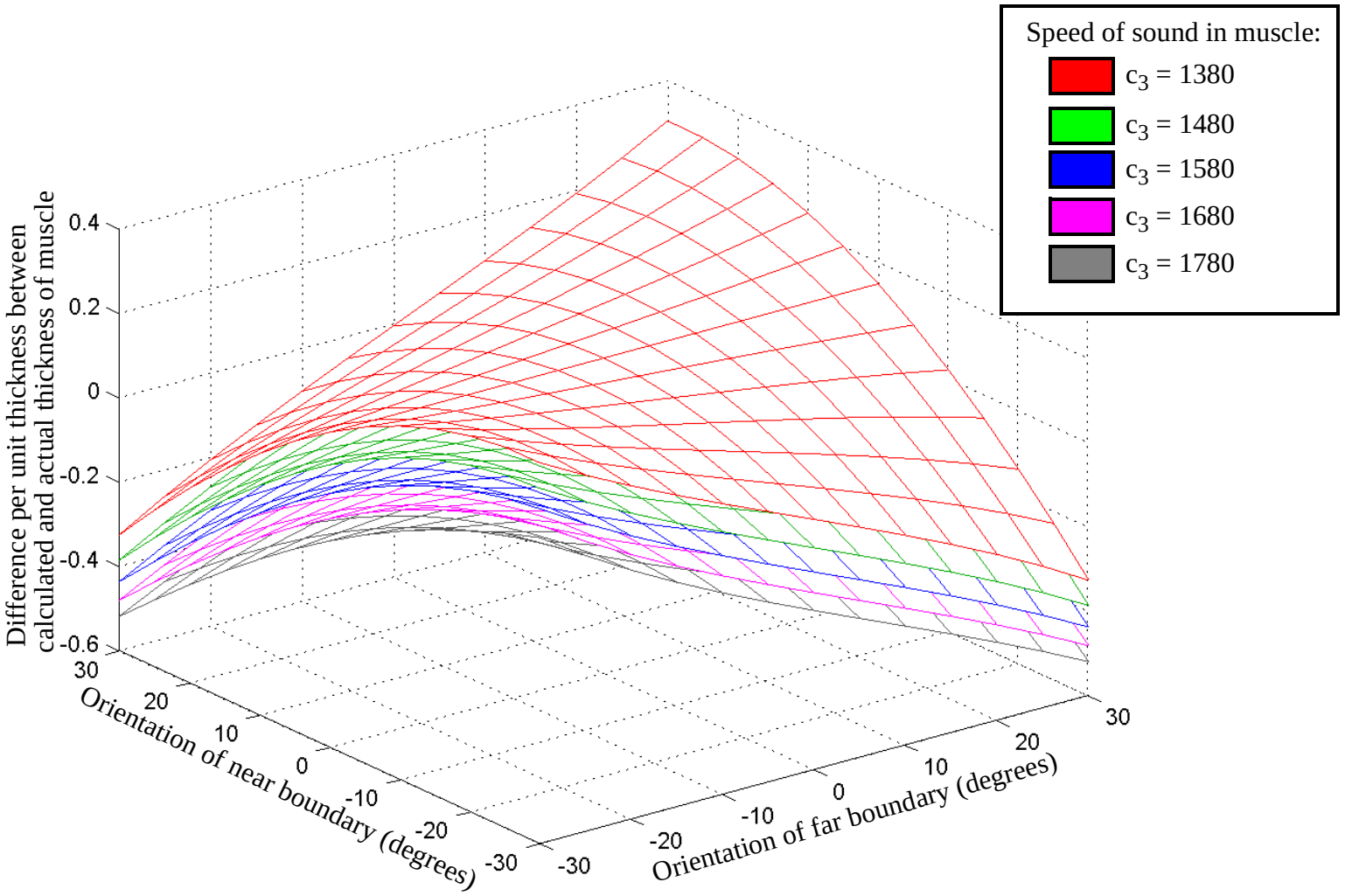

Figure B.14: Difference per unit thickness between the calculated thickness of the muscle layer and its actual value as a function of the actual speed of sound (c_2) and the orientations of the near and far boundaries (β_3, β_4) of the muscle layer itself with the angle of entry (θ_1) held constant at zero. The calculated thickness of the fat layer was obtained by assuming c_1=1600 m / s, c_2=1450 m / s and β_3=β_4=0.

Figure B.15: Difference between the calculated location where the ultrasonic pulse intersected the skin / fat boundary its actual value as a function of the actual speed of sound (c_1) and angle of entry (θ_1) in skin with the boundaries of the layer kept parallel. The thickness of the layer was calculated assuming c_1=1600 m / s and θ_1=0.

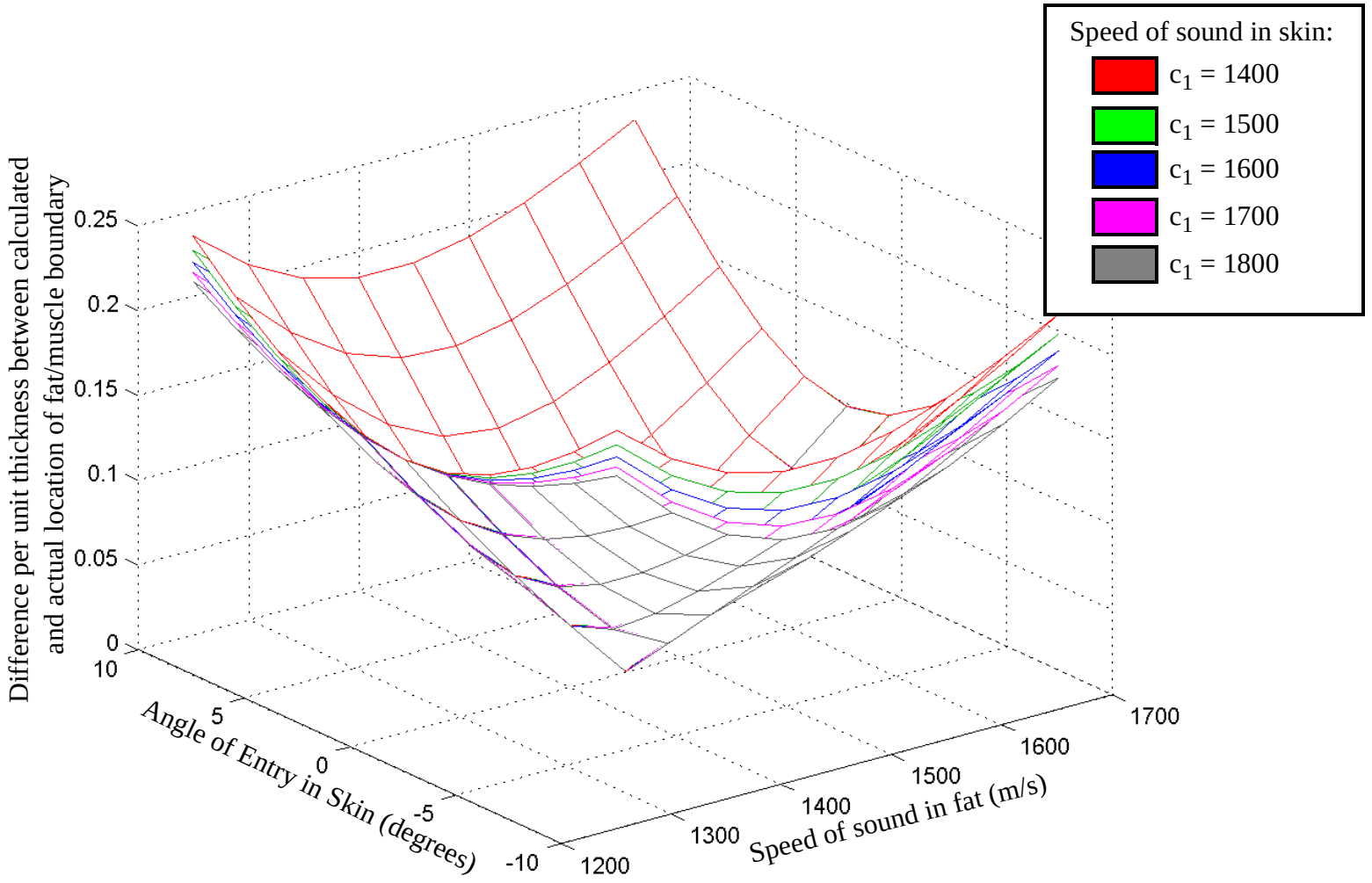

Figure B.16: Difference between the calculated location where the ultrasonic pulse intersected the fat / muscle boundary and its actual value as a function of the actual speed of sound in fat (c_2) and skin (c_1) and the actual angle of entry (θ_1) in skin with the boundaries of the layer kept parallel. The location of the boundary point was calculated assuming c_1=1600 m / s, c_2=1450 m / s and θ_1=0.

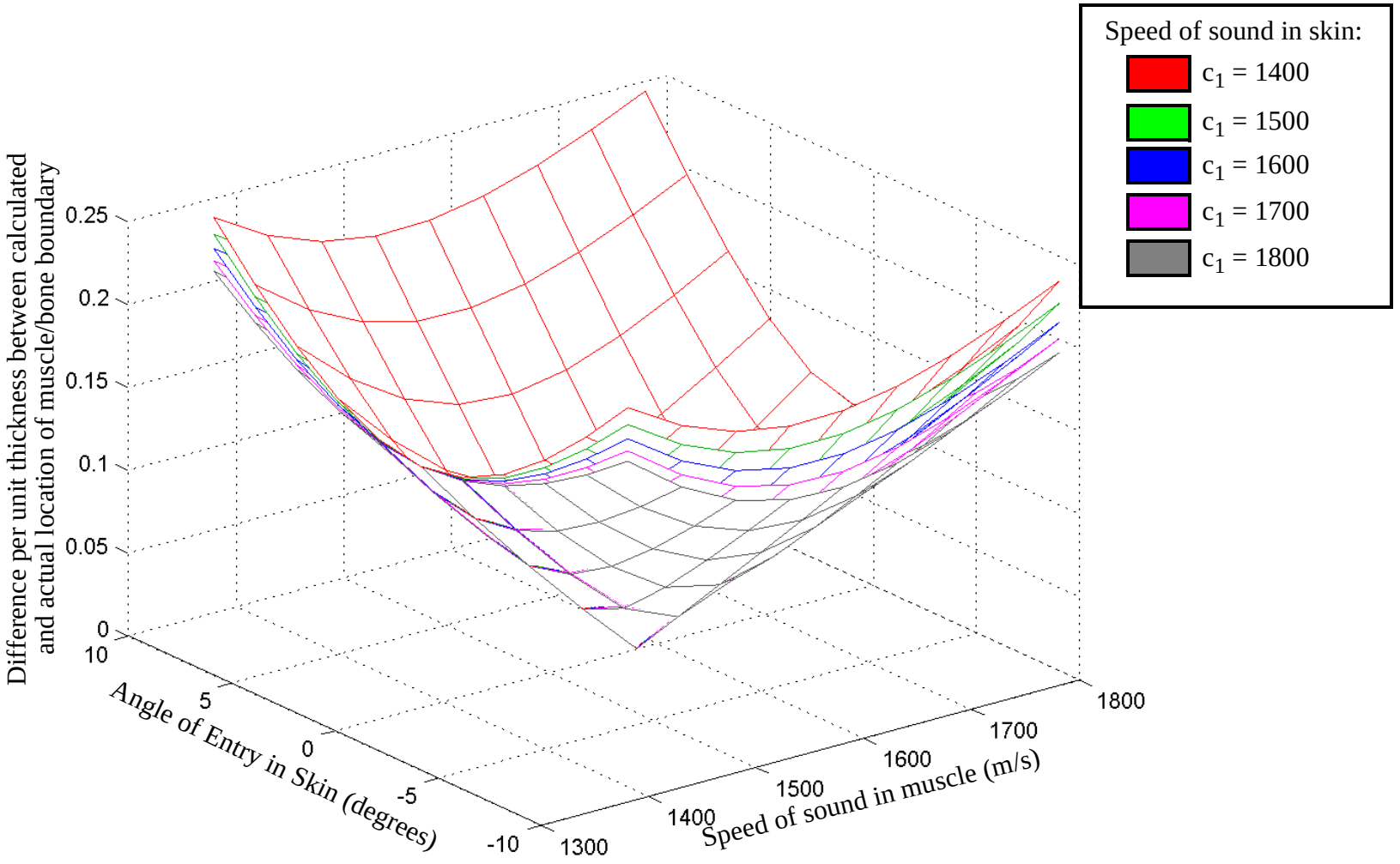

Figure B.17: Difference between the calculated location where the ultrasonic pulse intersected the muscle / bone boundary and its actual value as a function of the actual speed of sound in muscle (c_3) and skin (c_1) and the actual angle of entry (θ_1) in skin with the boundaries of the layer kept parallel. The location of the boundary point was calculated assuming c_1=1600 m / s, c_3=1580 m / s and θ_1=0.

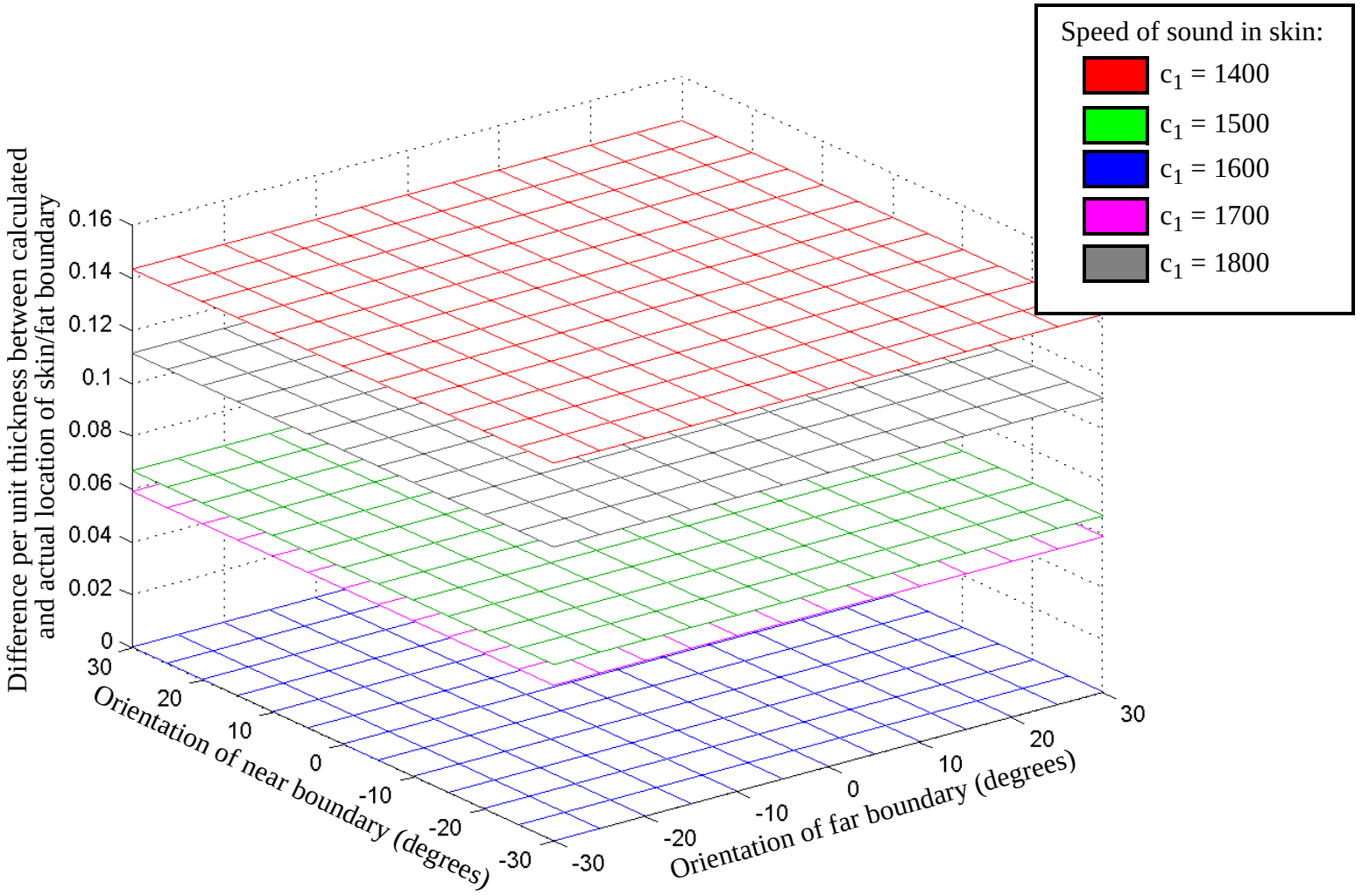

Figure B.18: Difference per unit thickness between the calculated location where the ultrasonic pulse intersects the skin / fat boundary and its actual value as a function of the actual speed of sound in skin (c_1) and the orientations of the near and far boundaries (β_1, β_2) of the skin layer with the angle of entry (θ_1) held constant at zero. The calculated location of the boundary point was obtained assuming c_1=1600 m / s and β_1=β_2=0.

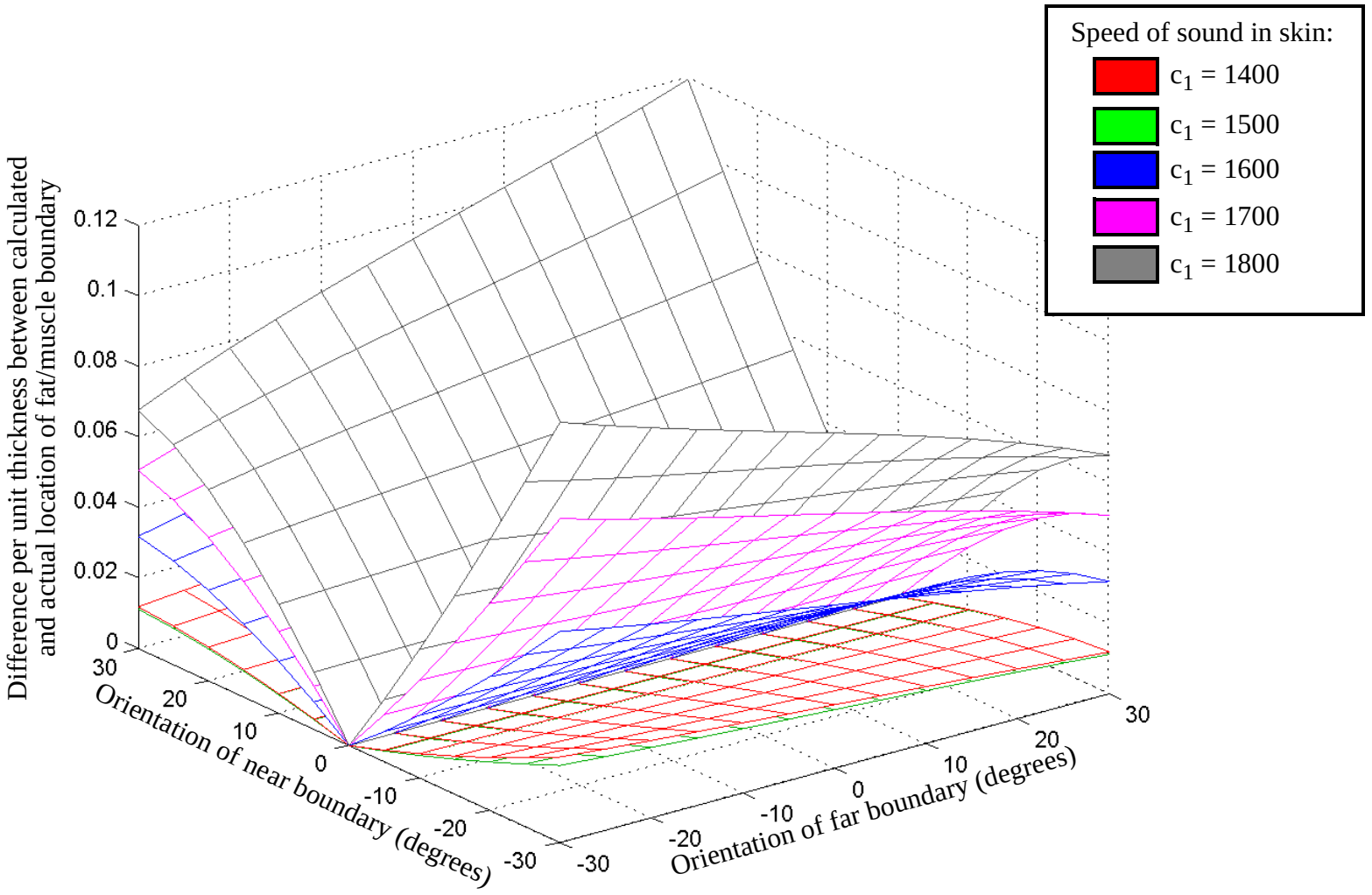

Figure B.19: Difference per unit thickness between the calculated location where the ultrasonic pulse intersects the fat / muscle boundary and its actual value as a function of the actual speed of sound in skin (c_1) and the orientations of the near and far boundaries (β_2, β_3) of the fat layer with the angle of entry (θ_1) held constant at zero. The calculated location of the boundary point was obtained assuming c_1=1600 m / s, c_2=1450 m / s and β_2=β_3=0.

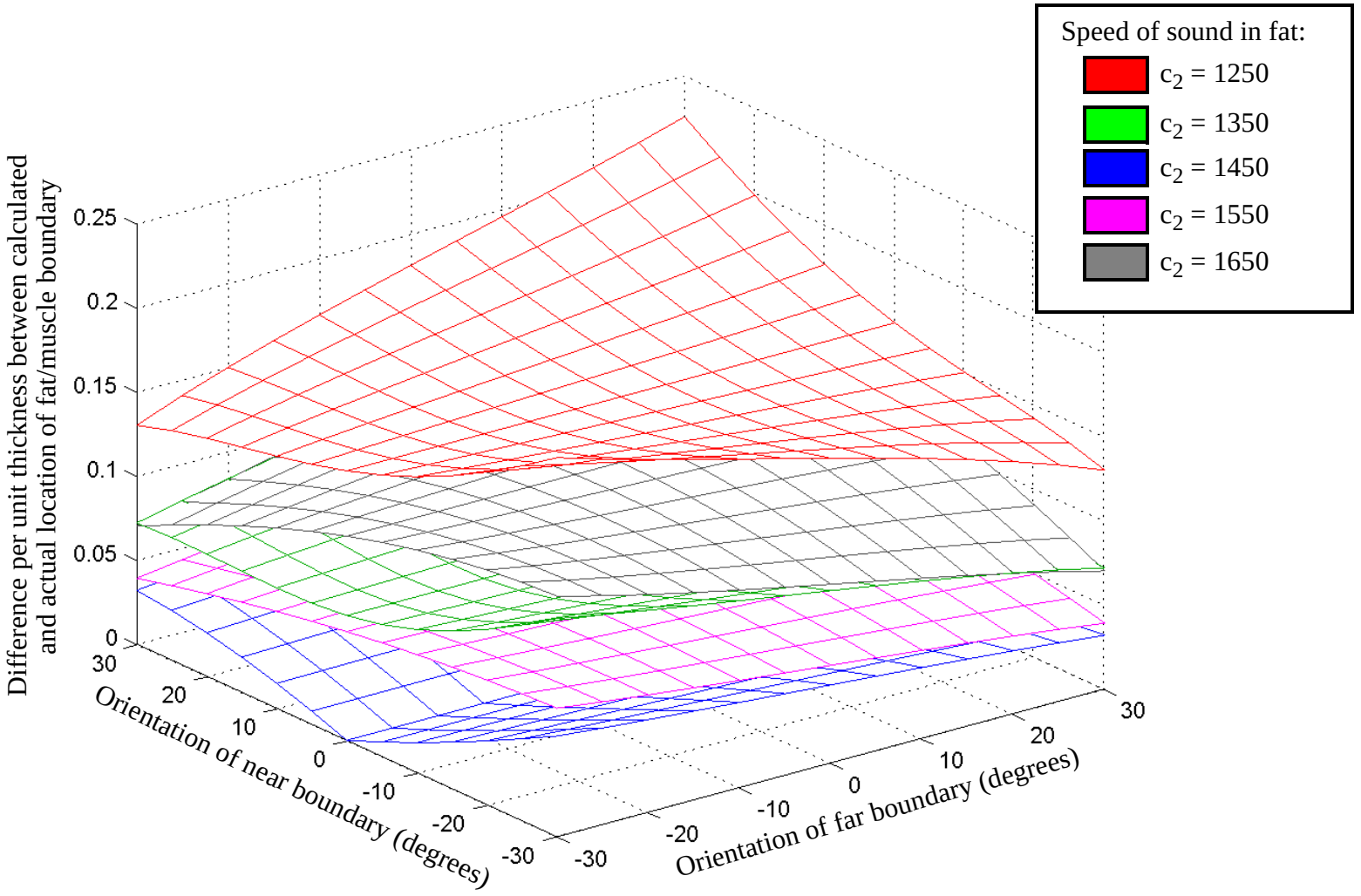

Figure B.20: Difference per unit thickness between the calculated location where the ultrasonic pulse intersects the fat/muscle boundary and its actual value as a function of the actual speed of sound (c_2) and orientations of the near and far boundaries (β_2, β_3) of the fat layer itself with the angle of entry (θ_1) held constant at zero. The calculated location of the boundary point was obtained assuming c_1=1600 m/s, c_2=1450 m/s and β_2=β_3=0.

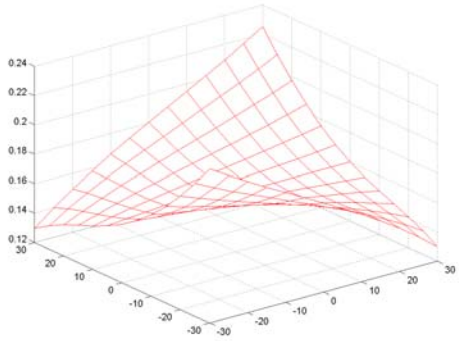

Speed of sound in fat = 1250 m/s

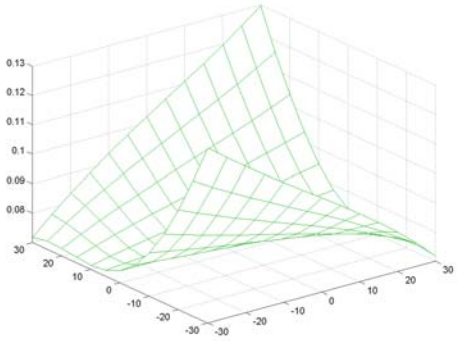

Speed of sound in fat = 1350 m/s

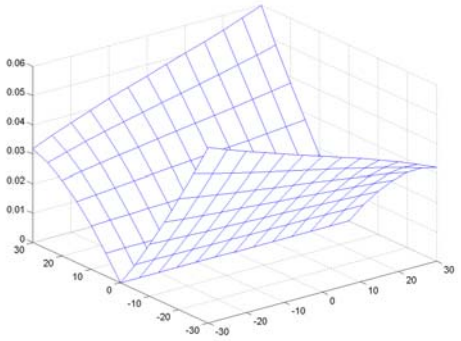

Speed of sound in fat = 1450 m/s

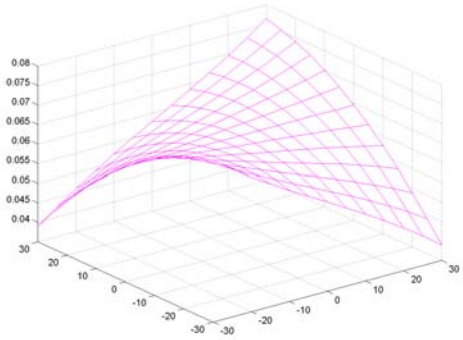

Speed of sound in fat = 1550 m/s

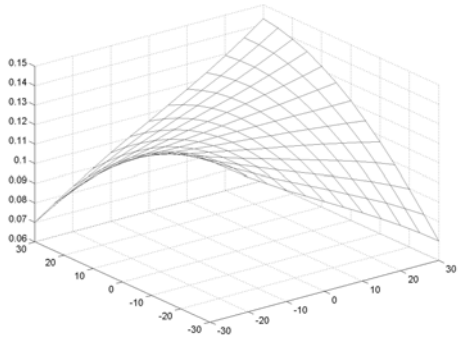

Speed of sound in fat = 1650 m/s

Figure B.21: The individual contours that make up figure B.20 displayed separately for comparison.

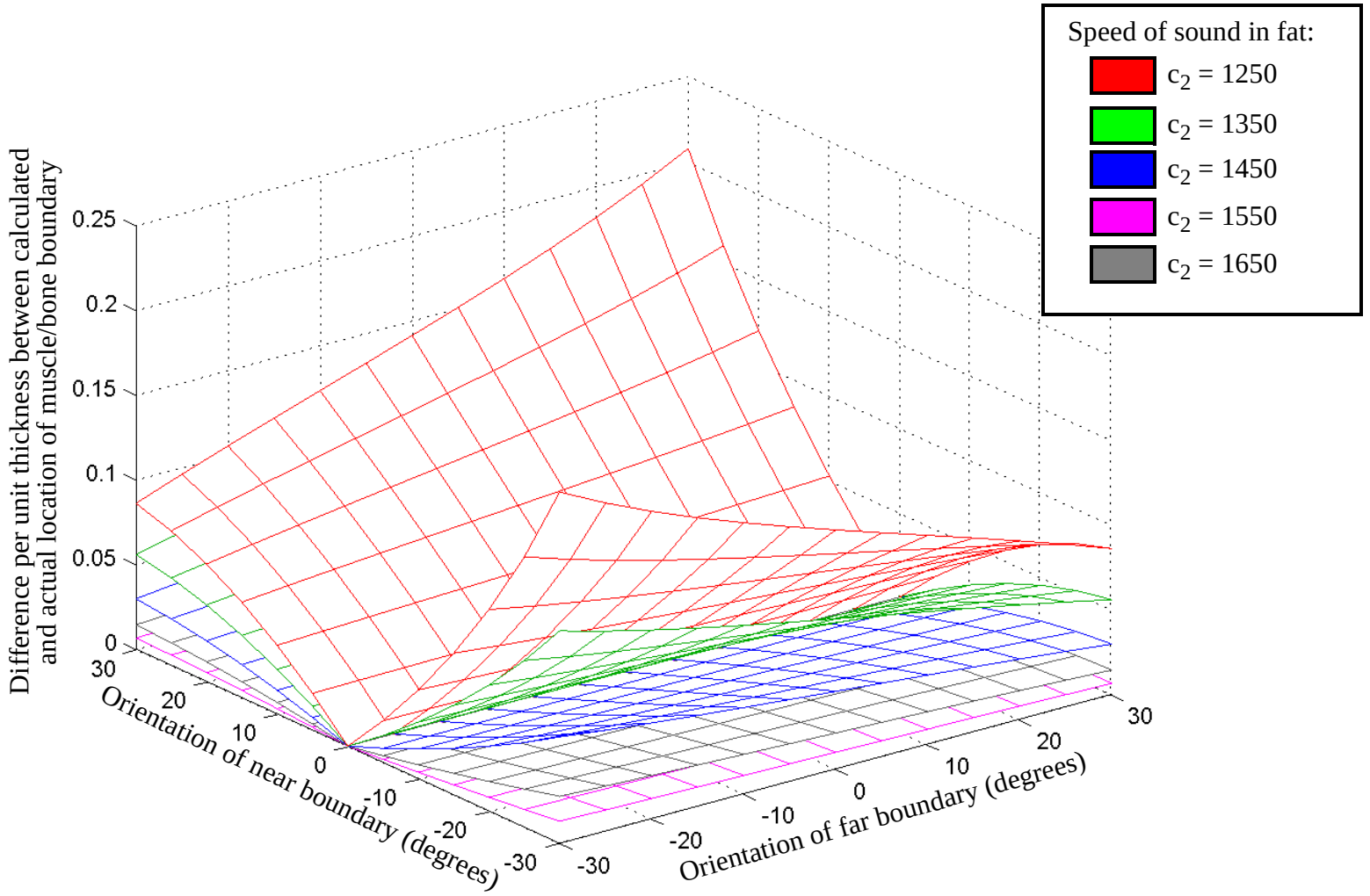

Figure B.22: Difference per unit thickness between the calculated location where the ultrasonic pulse intersects the muscle / bone boundary and its actual value as a function of the actual speed of sound in fat (c_2) and the orientations of the near and far boundaries (β_3, β_4) of the muscle layer with the angle of entry (θ_1) held constant at zero. The calculated location of the boundary point was obtained assuming c_2=1450 m / s, c_3=1580 m / s and β_3=β_4=0.

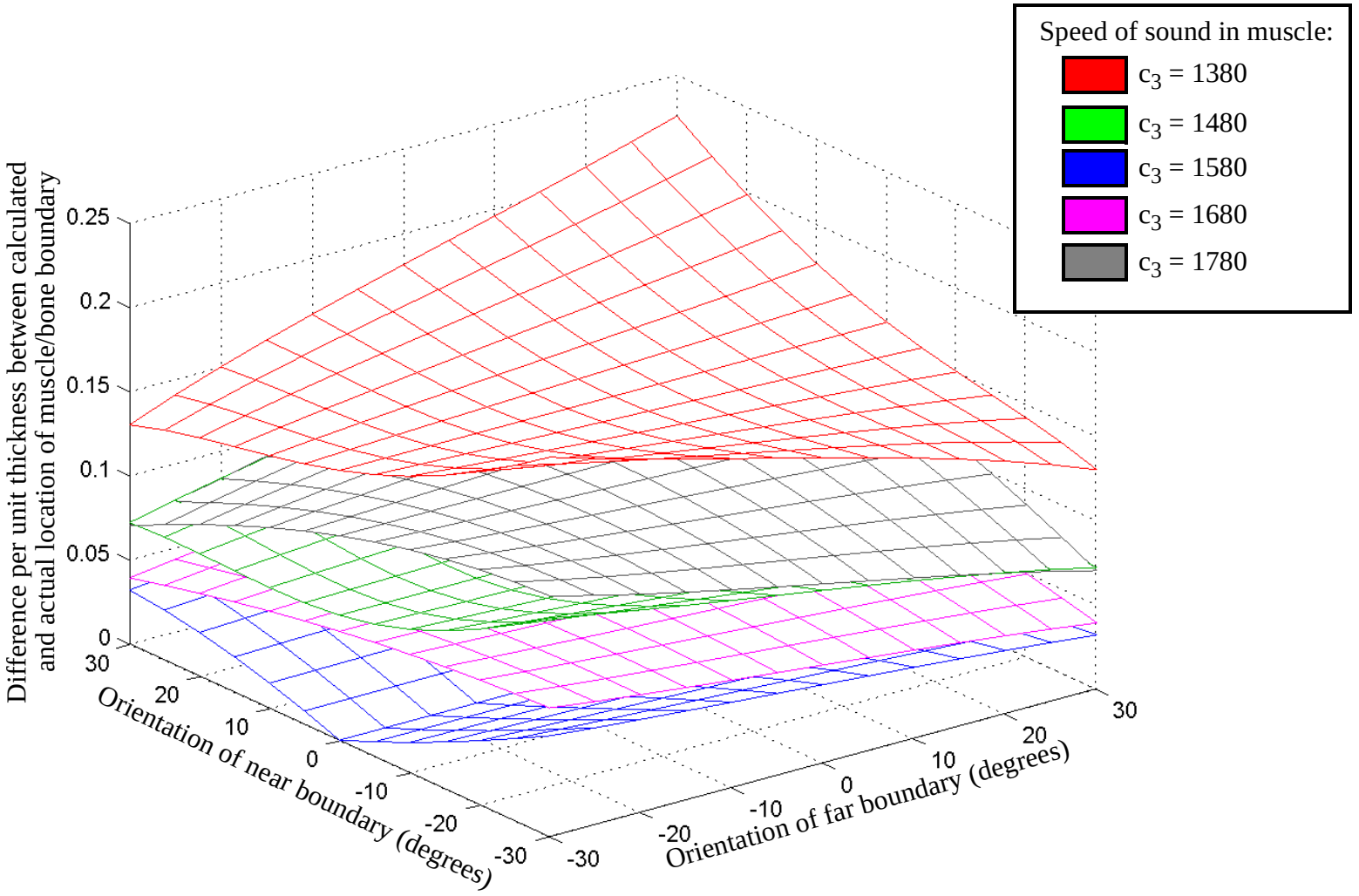

Figure B.23: Difference per unit thickness between the calculated location where the ultrasonic pulse intersects the muscle / bone boundary and its actual value as a function of the actual speed of sound (c_3) and orientations of the near and far boundaries (β_3, β_4) of the muscle layer itself with the angle of entry (θ_1) held constant at zero. The calculated location of the boundary point was obtained assuming c_2=1450 m / s, c_3=1580 m / s and β_3=β_4=0.

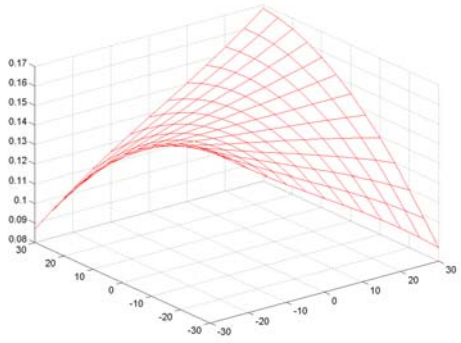

Speed of sound in muscle = 1380 m/s

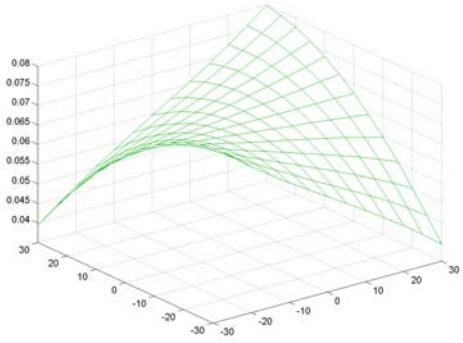

Speed of sound in muscle = 1480 m/s

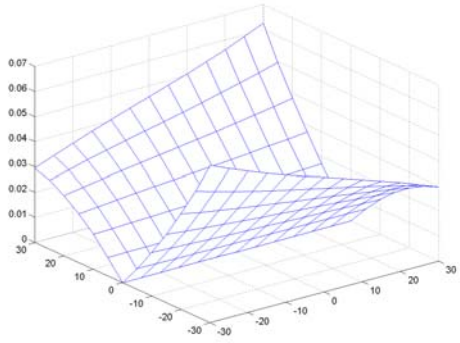

Speed of sound in muscle = 1580 m/s

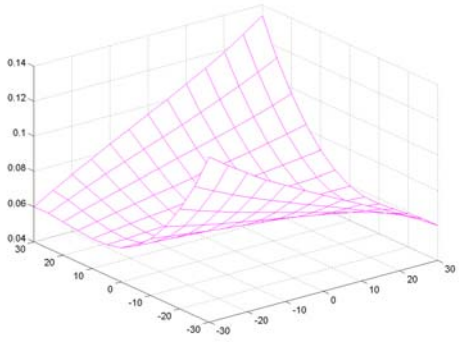

Speed of sound in muscle = 1680 m/s

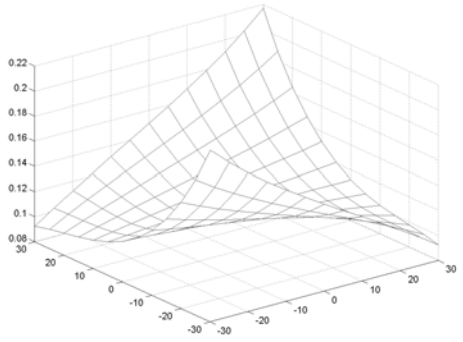

Speed of sound in muscle = 1780 m/s

Figure B.24: The individual contours that make up figure B.23 displayed separately for comparison.

Appendix C
Ultrasonic Tissue Characterization

C.1 Introduction

Ultrasonic tissue characterization methods are algorithms that automatically distinguish between different types of soft tissue in an ultrasonic A-mode echogram or a B-mode image. The input to an ultrasonic tissue characterization algorithm is either a continguous segment of an A-mode echogram or a region of a B-mode image that is believed to belong to a single tissue type. The output of the tissue characterization algorithm is one or more real-valued parameters that can be used to distinguish between different types of tissue. At present, the values of these parameters are intended to be interpreted by a human being, who assigns a tissue type to the segment of the A-mode echogram or B-mode image. However, the assginment process can be automated by using one or more fixed thresholds calibrated from a large data set of echograms or images whose tissue type assignments are known.

Fundamentally, ultrasonic tissue characterization is a classification task, and so we will occasionally speak of *classifying* a region of an A-mode echogram or B-mode image or of *identifying* the type of tissue that region belongs to or *characterizing* the tissue type. These terms are equivalent and we will use them interchangably. We will also follow the conventions of the tissue characterization literature and speak of the backscattered signal rather than the A-mode echogram in the remainder of this appendix. The change in terminology follows a shift in perspective. In conventional ultrasonic imaging, the focus is primarily on identifying echoes reflected from structures that are much larger than the wavelength of the ultrasonic pulse. These echoes usually represent boundaries between different structures in the body, and when the primary task is to locate these boundaries in space relative to the transducer, focusing on these echoes in appropriate. However, in ultrasonic tissue characterization, we are interested in identifying the region that lies between the boundaries between different types of tissue. The information we use to identify the region comes from small structures whose size is typically much smaller than the wavelength of the pulse. These structures are too small to be individually resolved by the ultrasonic imaging system, and they scatter, rather than reflect, the energy of the pulse. Some of this scattered energy travels back to the transducer. Although the signal produced at the transducer by this scattered energy may appear to be random, it actually has a structure that depends upon the density, size, shape and arrangement in space of the small scatterers. The scatterers in different kinds of tissue will have different characteristics, so analyzing this scattered energy will allow us to distinguish between different tissue types. Because the primary interest is in the part of the A-mode signal that is scattered from these

small structures in the body rather than the part of the A-mode signal that is reflected from the boundaries between large structures, the tissue characterization literature refers to the A-mode signal as the backscattered signal (or occasionally the backscattered echogram) rather than the A-mode echogram.

Tissue characterization methods assume that the region of the backscattered signal or B-mode image that they are applied to belongs to a single tissue type. Since different kinds of tissue will have different scattering properties, applying a tissue characterization method to a region that spans different tissue types may produce unpredictable results. However, being able to classify different regions in a backscattered signal or B-mode image implies the ability to segment that signal or image into different regions, so the segmentation task and the ultrasonic tissue characterization task are almost equivalent.

Although tissue characterization methods described in this appendix can be used to distinguish betwen different layers of tissue in the body, such as skin, fat, muscle, kidney, liver, and so on, the most typical use of ultrasonic tissue characterization is to distinguish between healthy and diseased tissue of the same nominal type (e.g. healthy and diseased liver tissue). Current ultrasonic tissue characterization work is seen primarily as a diagnostic aid for radiologists to increase their ability to identify pathological conditions in ultrasonic B-mode images. Consequently, the perspective is one of providing additional information that the radiologist can use to interpret the image.

In the remainder of this appendix, we survey the ultrasonic tissue characterization literature and describe and compare the major methods in use. We begin by explaining the basic theory behind ultrasonic tissue characterization and how the properties of the individual scatterers within a layer of soft tissue give rise to the backscattered signal seen by the transducer. Then we describe the major tissue characterization methods and the applications of each. Finally, we summarize the work done on comparing these methods and make some recommendations on their use.

C.2 Theory

C.2.1 Imaging Model

Ultrasonic tissue characterization uses the standard linear image-formation model common to computer vision[48] and other imaging fields:

$$y(\ ) = f(\ ) * h(\ ) \tag{C.1}$$

In our case, y(t) is the output of the imaging system (e.g. the A-mode RF signal or B-mode image). The function f(t) models the characteristics of the imaging system, include the transducer characteristics, the waveform of the transmitted ultrasonic pulse, and any post-processing done by the imaging system (e.g. logarithmic compression, envelope detection, etc.). Where it is needed by the various tissue characterization methods, f(t) will be derived from a theoretical model or measured from the reflection from a highly-specular surface or a strong point scatterer.

The function h(t) models the time-varying response of the tissue in contact with the transducer to insonuation with an impulse (e.g. the echoes appearing at the transducer face from the ultrasonic pulse as it propagates through the body). The function h(t) is indicative of the structure of the soft tissue, not just at the transducer/tissue interface but everywhere the pulse propagates to. Hence, if we know or can measure the properties of the imaging system, we can compute h(t) by deconvolution and deduce the structure of the underlying tissue from it. For any realistic situation, h(t) will be a very complicated function, modeling the effects of reflection, refraction, diffraction, attenuation, scattering, and any other properties of the tissue that may affect the ultrasonic echoes generated by the transmitted pulse as it travels through the body. Since we are concerned here with tissue characterization from backscattered radiation, we will simplify h(t) to represent a uniform isotropic medium with discrete scatterers which are possibly non-homogeneous in shape, structure or spatial distribution. This means that we will only be considering the attenuative and scattering properties of the medium.

As discussed in Appendix B, the three-dimensional structure of an ultrasonic pulse can be reduced to two dimensions if the pulse is axisymmetric. Hence, to simplify our illustrations, we will consider only the two dimensional case without loss of generality. The basic concepts derived in this section will also apply to pulses or transducers that are not axisymmetric, but a more sophisticated three-dimensional analysis will be needed to work out the details. Following the conventions of Appendix B, we will use (x,z) coordinates, where the z-axis is aligned with the direction of pulse propagation and the x-axis points to the right along the transducer face as one looks at the front of the transducer. The origin of the coordinate system is placed in the center of the transducer so that the transducer of width W occupies the coordinates from (-W/2, 0) to (W/2).

C.2.1.1 Response of a Single Scatterer

The amplitude response of a single scatterer located at (x_i, z_i)[1] in a medium with speed of sound c_0 to insonuation with a pure harmonic of angular frequency ω_0 is:

$$s_i(x, z, t) = \frac{a_i}{\sqrt{(x - x_i)^2 + (z - z_i)^2}} e^{j\left(\frac{\omega_0}{c_0}\sqrt{(x - x_i)^2 + (z - z_i)^2} - \omega_0 t\right)} \tag{C.2}$$

where a_i is the complex amplitude, and j is the square-root of -1. The constant a_i, called the *form factor*, depends on the shape of the scatterer, its material properties and the insonuation frequency ω_0, For example, if a scatterer can be approximated by a small sphere of diameter r_i, where $r_i << c_0/\omega_0$, and mean compressibility $\bar{\gamma}$, then a_i will be

1. Although the wave from the scatterer propagates in three dimensions, we consider only two, since we are concerned only one-dimensional (A-mode) and two-dimensional (B-mode) imaging modes. Following the conventions of Appendix B, we take the z-axis normal to the face of the transducer and the x-axis pointing to the right as one looks at the face of the transducer, such that the beam propagates in the xz-plane.

proportional to $\bar{\gamma} r_i^3/\omega_0^2$[130]. As the dimensions of the scatterer become larger and $r_i \sim c_0/\omega_0$, the relationship governing a_i becomes more complex, but still obeys equation (C.2). However, when $r_i >> c_0/\omega_0$, equation (C.2) no longer applies and the behavior of the scatterer is governed by the rules of geometrical optics. Scatterers of this size will be completely resolved in ultrasonic images and may be removed by a matched filter prior to ultrasonic tissue categorization.

Exactly which structures in the body are responsible for the scattering of an ultrasound pulse are not entirely known. The speeds of sound in human soft tissues range from 1460-1600 m/s, so for the frequencies used in diagnostic ultrasound (2-10 MHz), c_0/ω_0 ranges from 146 to 800 μm, so such structures should be around 0.5 mm in diameter or less. Structures which have been suggested as scatterers in human tissue include collagen fibers, capillaries and venules, muscle fibers, red blood cells, hepatic portal triads in the liver, cell nuclei, and individual cells.

Equation (2) is for a simple harmonic wave. The response to a broadband signal, x(t), is obtained by integrating equation (2) over the frequency spectrum of x(t):

$$s_i(x, z, t) = \int_{-\infty}^{\infty} X(\omega) \frac{a_i(\omega)}{\sqrt{(x - x_i)^2 + (z - z_i)^2}} e^{j\left(\frac{\omega}{c_0}\sqrt{(x - x_i)^2 + (z - z_i)^2} - \omega t\right)} d\omega \qquad \text{(C.3)}$$

where $X(\omega)$ is the Fourier transform of x(t), and the frequency-dependence of a_i has been made explicit.

The response of an ideal piezoelectric transducer (one whose voltage varies linearly with strain) to $s_i(x,z,t)$ can be found by integrating $s_i(x,z,t)$ over the face of the transducer. For our two-dimensional model, the response of the ideal transducer of width W whose face is aligned with the x-axis with its center is located at (0,0) to an isolated scatterer located at (x_0, z_0) insonuated by a pure harmonic of frequency ω is:

$$z_i(t) = V \int_{-\frac{W}{2}}^{\frac{W}{2}} \frac{a_i(\omega)}{\sqrt{(x - x_i)^2 + z_i^2}} e^{j\left(\frac{\omega}{c_0}\sqrt{(x - x_i)^2 + z_i^2} - \omega t\right)} dx \qquad \text{(C.4)}$$

where V is the constant relating voltage and strain in the transducer. If we factor $e^{-j\omega t}$ out of the integral and assume that the scatterer remains in a fixed location relative to the transducer during insonuation, then the definite integral of equation (C.4) will be equal to some complex number, which may be written $A_i(\omega)e^{j\phi_i(\omega)}$. If we include the constant V in $A_i(w)$ also, then equation (C.4) reduces to:

$$z_i(t) = A_i(\omega)e^{-j(\omega t - \phi_i(\omega))} \quad \text{(C.5)}$$

where A_i (w) incorporates the transducer aperture (W), transformation between displacement and voltage (V), the form factor of the scatterer (a_i), and the distance between the transducer and the scatterer ($\sqrt{(x - x_i)^2 + z_i^2}$, and ϕ_i(w) gives the effective phase of the scatterer relative to the transducer. Following equation (C.3), z_i(t) for a broadband pulse with frequency spectrum X(ω):

$$z_i(t) = \int_{-\infty}^{\infty} A_i(\omega)X(\omega)e^{-j(\omega t - \phi_i(\omega))}d\omega \quad \text{(C.6)}$$

Since tissue characterization algorithms usually assume static conditions, we will be using the approximations given by equations (C.5) and (C.6) in our discussions below.

C.2.1.2 Resolution Cells

Ultrasonic tissue characterization typically uses pulses of finite duration, and so the amplitude of the backscattered signal at any time t will be the superposition of the waves scattered from a finite volume called the *resolution cell*, which is the smallest area that can be resolved completely by the ultrasonic pulse. The shape and dimensions of the resolution cell depend upon the shape and dimensions of the pulse and the acoustic properties of the medium, but if the scattering structures within the cell stop radiating acoustic energy quickly after the pulse passes and the pulse's wavefronts can be approximated as plane waves (e.g. we are in the focal zone of the transducer), the dimensions of the resolution cell will equal to FWHMxcΔT/2 (FWHM= full-width at half-maximum of pulse amplitude, c= speed of sound, ΔT= duration of pulse). These dimensions are the smallest distances by which structures can be separated and still be distinguished from one another in the received signal. Structure within the resolution cell is not resolvable into separate components.

If there are N scatterers in the resolution cell corresponding to time t, then the amplitude of the backscattered signal from a broadband ultrasonic pulse at that time will be:

$$z(t) = \sum_{i=1}^{N} z_i(t) = \sum_{i=1}^{N} \int_{-\infty}^{\infty} A_i(\omega)X(\omega)e^{-j(\omega t - \phi_i(\omega))}d\omega \quad \text{(C.7)}$$

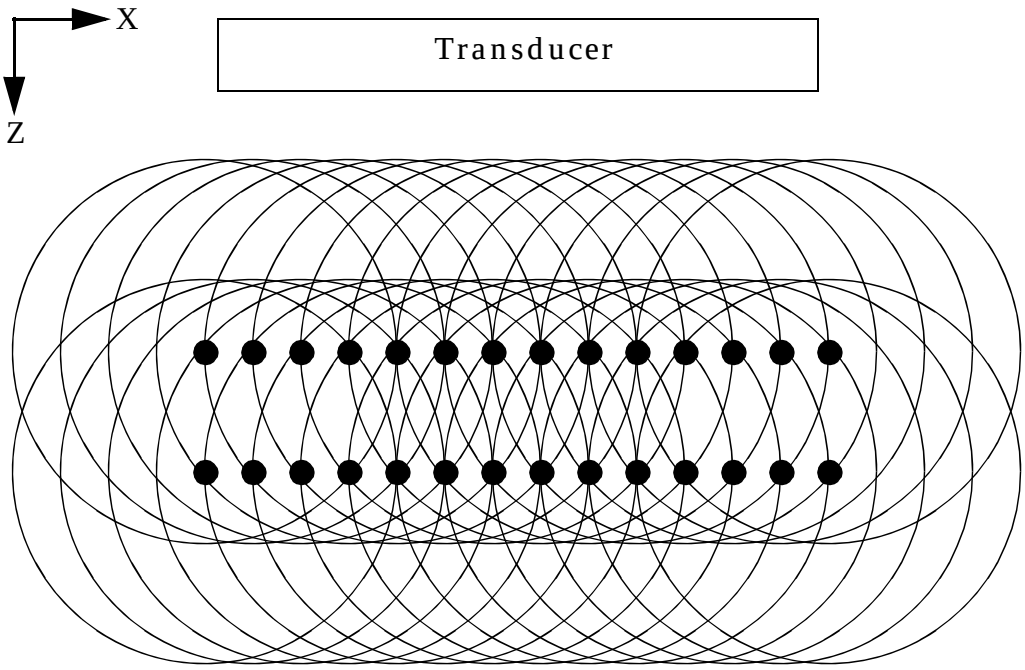

Figure C.1: Scattering of an ultrasonic pulse from a rectangular crystal array of circular objects that are much smaller than the wavelength of the pulse.

After swapping the integral and the summation and grouping terms, equation (C.7) becomes:

$$z(t) = \int_{-\infty}^{\infty} \left(\sum_{i=1}^{N} A_i(\omega) e^{j\phi_i(\omega)} \right) X(w) e^{-j\omega t} d\omega \qquad \text{(C.8)}$$

The value of N depends upon the size of the resolution cell and the distribution of the scatterers in the soft tissue. The size of the resolution cell in turn depends upon the frequency, bandwidth, and duration of the ultrasonic pulse as well as the speed of sound in the medium in which the pulse travels and any focussing applied to the transducer. For a broadband Gaussian 5 MHz ultrasonic pulse with a duration of 1 ms in a medium whose speed of sound is 1540 m/s, the depth of a resolution cell will be approximately 0.77 mm in the focal zone. The width of the resolution cell for this transducer will depend the extent of the focussing present, but it is reasonable to assume a pulse diameter in the focal zone of no less than half the diameter of the transducer. For a 1 mm diameter transducer emitting the pulse described above, the resolution cell will measure at least 0.5 mm by 0.77 mm, and hence, N is possibly quite large. However, a large N does not imply a large amplitude for z(t); the spatial distribution of the scatterers within the resolution cell is equally important. We explore the effects of this distribution on the amplitude of z(t) below, beginning first with a regularly-spaced scatterer distribution followed by random and pseudo-random distributions.

C.2.1.3 Response of Homogeneous Regularly-Spaced Scatterers

Figure C.1 illustrates the scattering from a perfect rectangular crystal of homogeneous elements with a separation of Δx between adjacent elements along the x-axis and Δz along the z-axis. The ultrasonic pulse is assumed to propagate along the z-axis. Although perfect crystals, or structures approximating perfect crystals, do not exist in human tissue, we can gain considerable insight into the effect of the spatial distribution of scatterers on the backscattered signal by considering such structures. Suppose the crystal lies within the focal zone of the transducer with its face parallel to the wavefront. Then the relative phase between scatterers in neighboring layers will be $4\pi\Delta z/\lambda$, where λ is the wavelength of the ultrasonic pulse. If Δz is a multiple of $\lambda/2$, then the scattered waves will be in-phase with one another and the amplitude of the measured signal will be very large. On the other hand, if Δz is an odd multiple of $\lambda/4$, then scatterers in successive layers will be π radians out-of-phase with one another, and the amplitude of the measured signal will be very small (it will not be completely zero, because the amplitudes of the scattered waves will not be equal, and the waves from scatterers at even multiples of $\lambda/4$ will interfere constructively). Thus, if we insonuate the crystal with a broadband pulse, we will see peaks in the frequency spectrum ($Z(\omega)$) of the backscattered signal at frequencies which are positive integer multiples of $\pi c/\Delta z$. A robust way of identifying the fundamental frequency, and thus the value of Δz, of the peaks is through cepstrum analysis. The cepstrum of a signal is the Fourier transform of the logarithm of its power spectral density[97][140]. Periodicy in $Z(\omega)$ will produce a peak in the cepstrum corresponding to the fundamental frequency of the periodicity.

The smallest value of Δz that can be measured in this manner depends upon the noise in the system, the depth of the crystal (the amplitude of the spectral peaks at resonance is roughly proportional to the number of layers in the z-direction), and the bandwidth of the pulse. Except for exceptionally noisy conditions or short pulse durations, Δz will be smaller than the depth of the resolution cell and will usually be much smaller (for example a Gaussian pulse with a 5 MHz center frequency and 3 MHz bandwidth will have a resolution cell depth of approximately 1.2 mm, but the smallest Δz measurable by the center frequency alone is approximately 0.1 mm). Thus, while the individual scatterers themselves are not resolvable, their structure along the direction of pulse propagation may be.

Measurements of Δz will also be complicated by frequency-dependent attenuation. Such attenuation will result in a reduction of spectral magnitude that is proportional to frequency, biasing measurements of Δz towards larger values.

The separation Δx will also produce an interference pattern, but the different interference patterns for different frequencies will tend to cancel out when insonuated with a broadband pulse. Furthermore, for a crystal distant (>5W, where W is the width of the transducer) from the transducer, the variation in signal phase across the transducer will be negligible. In this case, changes in Δx will produce changes only in the amplitude of the backscattered signal, not its shape. However, relatively large changes in scatterer separation only produce slight changes in amplitude and separating such changes from other effects in the system (e.g. attenuation). Hence, it is not feasible to measure

separation between scatterers in the x-direction as it is for separation in the z-direction.

The dimensions of the resolution cell need not be an integer multiple of the interscatterer spacing. If the resolution cell dimensions and interscatterer spacing do not match, then N, the number of scatterers per resolution cell, will vary as the pulse propagates through the crystal, and the total energy scattered from the cell, which is proportional to N, with it. This adds an additional time-varying component to z(t), but the location of the peaks in $Z(\omega)$ remains unchanged.

Rectangular crystals are not the only arrangement of scatterers that produce spectral peaks. Any regular distribution of sufficient depth will produce spectral peaks corresponding to the interscatterer separation in the direction of pulse propagation. Such crystals may in fact have several different fundamental frequencies. Random variation in the location of the scatterers will also produce produce peaks in the Fourier spectrum that correspond to the mean separation between scatterers along the path of the pulse (which the z-axis in figure C.1). The peaks will not be as sharp as the peaks for a completely regular distribution of scatterers. As the magnitude of random variation increases, the height of the peaks decreases. A completely random distribution of scatterers will have no peaks in the Fourier spectrum at all.

C.2.1.4 Response of Homogeneous or Heterogeneous Randomly-Spaced Scatterers

Perfectly regular arrangements of scatterers do not occur in human soft tissue, even in bone. When random variation in the position, size, shape, or acoustic properties of the scatterers is present, the number of scatterers in a resolution cell becomes a random variable and z(t) - the signal scattered by those scatterers and received at the transducer - becomes a random process. The spectrum $Z(\omega)$ will still have peaks corresponding to the mean interscatterer spacing, but these peaks will be less sharp as the variance in the distribution increases.

Since z(t) is a random process, we can characterize it by its probability density function. For a large number of randomly distributed scatterers of uniform effective cross-section (e.g. uniform $A_i(\omega)$), the sum of equation (8) becomes a random walk in the complex plane starting at the origin, and the amplitude z(t) is Rayleigh-distributed modulated by a sinusoid of frequency equal to center frequency of the transducer[130]. As the scatterer distribution becomes more regular, the distribution of z(t) becomes Rician, again modulated by a sinusoid of frequency equal to the center frequency of the transducer. A large number of diffuse scatterers with a small number of isolated, strong point scatterers will also produce a Rician distribution[130]. If the number of scatterers is small or their effective cross-section is non-uniform, the demodulated amplitude will obey a K- or Nakagami-m distribution[88][20].

In 1993, Clifford, Fitzgerald and James evaluated five distributions (the four given about, plus the lognormal distribution) on computer-simulated and real backscattered signals using the Anderson-Darling test for goodness-of-fit[20]. The simulations used a Poisson distribution to simulate both sparse and dense distributions of scatterers.Results from the simulations were as expected, with the Nakagami-m distribution being the best fit for

extremely sparse distributions of scatterers, the K-distribution being best for moderately dense distributions, and the Rayleigh being best for extremely dense distributions. The authors also compared the distributions on real A-mode backscattered data from canine myocardia and found that in almost all cases, the K-distribution produced the best fit, followed by the Nakagami-m distribution, the Rayleigh distribution, the Rician distribution, and the lognormal distribution in that order. In a few cases, the Nakagami-m distribution outranked the K-distribution, but only in one case did the Rayleigh distribution outrank either the K- or Nakagami-m distributions. This is in contrast to earlier papers, which assumed a Rayleigh model for ultrasonic scattering[130,148]. Since the density, distribution and strength of the scatterers are characteristic of a tissue type, measurements of the distribution of amplitudes of a demodulated ultrasonic signal can be used for ultrasonic tissue characterization. These methods are known as *envelope-based* tissue characterization methods and are described in greater detail below.

C.3 Methods For Tissue Characterization

There are two basic types of ultrasonic tissue characterization methods: those that analyze the A-mode backscattered signal from the transducer and those that analyze the texture of the B-mode image. The primary advantage of the A-mode algorithms is that they can take advantage of the frequency information contained within the backscattered A-mode signal. However, they do require access to the echoes received at the transducer before they have undergone significant processing. The primary advantage of the B-mode algorithms is that they can be used with conventional imaging equipment without modification. Within each type there are several different algorithms, which are described in detail below.

C.3.1 Signal-Based Methods

Signal-based methods are those that process the echoes received at the ultrasonic transducer before they have processed and rendered as a set of grey-level values upon the screen of an imaging device. As such, they focus on the characterization of tissue along the path of a single pulse rather than over an entire region, as the image-based methods do. There are several different signal-based methods for ultrasonic tissue characterization:

Coefficient Of Attenuation: The information contained in the A-mode signal can be used to compute the coefficient of attenuation for the soft tissue the signal has passed through. Since different tissue types have different ranges for the coefficient of attenuation, measurement of this value can be used to distinguish between tissue types.

Coefficient Of Integrated Backscatter: The coefficient of integrated backscatter measures the average power scattered by a region of soft tissue. The average backscattered power is a function of the number, density and arrangement of the scatterers within that region, which is in turn characteristic of the tissue type.

Slope And Intercept: The slope and intercept of a straight line fit to the normalized logarithmic power spectrum of a backscattered signal from a region of soft tissue are related to the density and structure of the scatterers within that tissue.

Consequently, these values can be used to identify the tissue type and status.

Envelope-Based Methods: Since the scattering of the ultrasonic pulse from the soft tissues can be modelled as a random process, the amplitude of the received signal can be treated as a random variable. By fitting the received complex amplitude to a probability distribution function, the properties of the distribution can be used to deduce the properties of the scatterers.

Other Methods: Some techniques, such as the autoregressive moving average, do not fit into one of the categories above.

All of the signal-based methods considered in this appendix make use the Fourier spectrum of the backscattered signal in one way or another. Consequently, they are subject to the trade-off between the spatial resolution, spectral resolution, and leakage[2] imposed by the duration and shape of the time domain window used to select the part of the signal to be processed. The details of this trade-off can be found in any digital signal processing textbook (such as [97]), but will be summarized here. Tissue characterization algorithms typically assume that the region of soft tissue they are applied to is homogeneous. This region is selected by multiplying the backscattered signal in the time domain with a window function that is zero everywhere outside of the region of interest. The shorter this window is, the more likely the tissue is to be homogeneous and the better the spatial resolution of the method will be. However, the shorter the window used to select the portion of the signal for processing, the worse the resolution in the frequency domain will be, and computations that depend implictly or explictly on the Fourier spectrum will suffer.

The shape of the window function within the region of interest also has an effect on the resolution in the time and frequency domains and on the amout of leakage in the frequency domain. Rectangular windows give both the greatest spectral resolution and the most leakage, while gradually tapered windows (such as the Kasier window with a large value of β) have less spectral resolution and leakage. In general, tissue characterization methods use rectangular windows of the shortest duration that is practical, both to increase the likelihood that the region being characterized belongs to a single tissue type and to maximize the spectral resolution.

In the following sections, we describe the different kinds of signal-based tissue characterization methods and how they have been applied to different problems. We discuss the similarities and differences between the methods at the end of the appendix, after we have described the image-based methods.

C.3.1.1 Coefficient of Attenuation

The coefficient of attenuation can be estimated from the power spectrum of the

2. Leakage is said to occur when a spectral component affects other spectral components in the vicinity due to smearing imposed by the time-domain window. The extent of the leakage imposed by a time-domain window is a function of the amplitude of the side-lobes of its Fourier transform relative to the amplitude of the main lobe.

backscattered signal. All of them require that the power spectrum be computed over several progressively deeper small regions in the tissue layer. As with all such mechanisms, the shape and duration of the window in the time domain limits the spectral resolution in the frequency domain; the shorter the window, the coarser the resolution in the frequency domain. However, long windows require thicker layers of tissue, since several successive estimates of the power spectrum at different depths are needed to compute the coefficient of attenuation. The power spectrum should be normalized with respect to a reference spectrum to correct for the characteristics of the imaging system. This reference spectrum can be collected from normal reflection of the ultrasonic pulse from a glass plate [71].

Once power spectra at several different depths within a homogeneous tissue layer have been acquired, linear regression is used to fit a line to the high frequency components, where attenuation effects will be dominant. The change of the slope of this line with depth is then used to compute the coefficient of attention[71,72]. A variant of this algorithm uses the change in center frequency with depth instead of the slope of the line to compute the coefficient of attenuation. Because the coefficient of attenuation is strongly related to the mechanical properties of the soft tissue, the value of the coefficient of attenuation can be used to identify the tissue type. Likewise, because pathological conditions such as disease or injury can also change the mechanical properties, the relative value of the coefficient of attenuation can be used to diagnose these conditions.

The coefficient of attenuation is not used by itself to identify tissue types in modern ultrasonic tissue characterization. Instead, it is used by other methods to correct for the effects of attenuation. Furthermore, Thijssen *et al*[123] have demonstrated that the slope of the coefficient of attenuation computed in this manner can be used in combination with other tissue characterization methods to more reliably identify diffuse liver disease than any single method alone.

C.3.1.2 Coefficient of Integrated Backscatter

The coefficient of integrated backscatter (CIB) is computed by averaging the power spectrum of the backscattered signal over some pre-defined bandwidth and is a measure of the average power scattered from the tissue in the region of interest, which is in turn characteristic of the number, density and cross-section of the scatterers within that region. The coefficient of integrated backscatter can be computed in both the frequency and time domains, with the two being theoretically equivalent. A discussion of several techniques for computing the coefficient of integrated backscatter and a cross-comparison of them on canine myocardium can be found in [109].

The value of the CIB is strongly influenced by the effects of attenuation, transducer center frequency, transducer bandwidth, and the intensity of the transmitted pulse[98]. Variation with transducer center frequency and bandwidth is to be expected, since the backscattered energy is a function of the number of resonant frequencies overlapped by the envelope of the transmitted pulse in the frequency domain. For example, more energy will be scattered, and the CIB will be higher, if the center frequency is equal to one of the resonant frequencies of the tissue insonuated than the center frequency is not equal to any of them.

The relationship between transmitted intensity, attenuation, and the CIB has been shown to be non-linear in normal myocardium both *in vivo* and *in vitro*[98]. This non-linear relationship may be due in part to the dependence of attenuation on frequency, and if so, would mean that it would hold for other tissues as well. In any case, it is important to keep the effect of these properties in mind when comparing CIB values across studies.

Computation of the coefficient of integrated backscatter is a very popular method for diagnosing pathological conditions in a variety of tissues. In the heart, the CIB has been shown to vary with the cardiac cycle, reaching a maximum at relaxation and a minimum at contraction[28]. The magnitude of this variation has been shown to decrease with ischemia, cardiomyopathy, hypertrophy, and acute rejection of a transplanted heart. In addition to diagnosing heart disease, the CIB can also be used to evaluate treatments. Davidson *et al* have used the CIB to evaluate the effectiveness of captopril in treating cardiomyopathy in Syrian hamsters[23]. They found an overall decrease in the CIB from the excised hearts of hamsters which had been treated with captopril compared to those who had not; this decrease was correlated with decreased calcification of the scar tissue, demonstrating the usefulness of the CIB in evaluating changes in mechanical properties of soft tissue.

One of the complications in using the CIB for myocardial evaluation is its susceptibility to the anisotropy of cardiac muscle. Both Davidson *et al*[98] and Reccia *et al*[103] have documented the dependence of the magnitude of the both the mean value and cyclic variation of the CIB on the alignment of the ultrasonic pulse with the cardiac muscle fibers. Cyclic variation in CIB is greater when the pulse is parallel to the fibers than when it is perpendicular, even though the mean value of the CIB is greater in the latter case than the former. Compensation for the anisotropy of cardiac muscle is necessary if results between studies are to be compared.

The CIB has also been used to characterize tissues other than the myocardium. Hete and Shung have used the CIB to evaluate the mechanical properties of normal and dystrophic skeletal muscle[37]. Based upon the differences in CIB between normal and dystrophic skeletal muscle of chickens and the results of a previous study[36], they concluded that the increased stiffness of dystrophic muscle was due to the inability of the collagen structures and capillary networks to reorient themselves with the stretching of the muscle. They also showed that like cardiac muscle, the CIB from skeletal muscle is anisotropic[36], but whereas the anisotropy of the CIB from cardiac muscle is attributed to changes in the orientation of the muscle fibers, Hete and Shung attributed the anisotropy in skeletal muscle to the orientation of the collagen networks and microvasculature.

Forsberg *et al*[29] applied the CIB method to distinguishing between ruptured and intact breast implants on the hypothesis that the mixture of breast tissue and silicon would have different acoustic properties than silicon alone. They examined 26 intact implants and 19 ruptured ones and compared the effectiveness of using the speed of sound the CIB in distinguishing between them. They found significant differences in the mean values for both the speed of sound and the CIB between the intact and ruptured implants, but also found that the variance for both measures was so large that individual diagnosis would be

difficult.

Wear *et al*[139] used the CIB to measure relative bone density in the *os calcis* bone of the foot in an attempt to develop an non-invasion method for diagnosing osteoporosis that did not require ionizing radiation. Data taken from ten healthy subjects showed a strong correlation between the CIB and bone density after attenuation was corrected for.

Bridal *et al*[10] developed a real-time imaging system for examining artherosclerotic plaque *in vivo*. Their system displayed the CIB from the arterial wall as a grey-scale image. Because of the high frequency and tight focussing of their ultrasonic transducer, they had to correct for diffraction effects as well as the characteristics of the imaging system. In vitro tests on segments of arterial wall whose plaque composition was known showed that their system could usefully identify fibrous lesions but not distinguish between healthy aortic tissue and other forms of arterial plaque.

Pan *et al*[99] explored the connection between mechanical stress and the CIB for human and rabbit skin. Samples of skin taken from rabbits immediately after sacrifice and humans immediately after breast reduction surgery were subjected to mechanical stress in vitro while their ultrasonic properties were measured. They found that both the attenuation coefficient decreases linearly with increasing relative strain while the CIB increased linearly by a small amount.

C.3.1.3 Slope And Intercept

The slope and intercept method of ultrasonic tissue characterization was developed F. Lizzi and his colleagues[70,71]. In this method, a straight line is fit to the logarithm of the power spectrum (in dB vs. MHz) of the backscattered signal from a homogeneous region of soft tissue. Theoretically, the slope is related to the effective sizes of the scatterers within the region, while the intercept is related to the effective sizes, density and acoustic impedance of the scatters within the region, and thus, these values can be used to identify different kinds of soft tissue or to distinguish between healthy and diseased tissue. Furthermore, while the value of the slope of the line is affected by the soft tissue attenuation, the intercept is not[3][71]. Work by Lizzi *et al* has shown good agreement between the predictions of the theory and data acquired from human subjects in vivo[72,73]. Sometimes the total or peak power in the backscattered signal is used in addition to the slope to characterize tissue. Theoretically, if the scatterers within the soft tissue are small compared to the wavelength of the ultrasonic pulse and are distributed randomly, the total backscattered power will be strongly correlated to the slope and intercept values. However, as will be discussed below, this relationship does not necessarily hold in practice.

The slope and intercept method of tissue characterization is almost as popular as the

3. Technically, the intercept is unaffected by that component of attenuation that is linearly dependent on frequency. Higher-order relationships between attenuation and frequency will affect the value of the intercept. However, to a first-order approximation, the value of the intercept is independent of the coefficient of attenuation.

coefficient of integrated backscatter. One common use of the slope and intercept method is to identify pathological changes to arterial walls. Noritomi *et al*[94] used the slope, intercept and total backscattered power (integrated over the useful bandwidth of the transducer) to distinguish between the fibrous, lipid pool and thrombus components of arterial plaque in 20 carotid endarterectomy specimens *in vitro*. They found that slope, intercept and total power could be used individually to successfully identify fibrous tissue in the plaque, but only the intercept and total power could distinguish lipid pools and thrombus tissue on their own. Taken together, slope and intercept alone could correctly identify 92.5% of the fibrous components, 57.6% of the lipid pools, and 72.4% of the thrombus components of the arterial plaque and using all three measures improved the accuracy in identifying fibrous tissue, lipid pools and thrombus tissue to 93%, 69.7% and 72.4% respectively. Since, theoretically, total power strongly correlates with the slope and intercept if the scatterers are small or randomly distributed, Noritomi *et al* concluded that because the addition of total power to the slope and the intercept improved classification accuracy, the scatterers within the arterial plaque may not be small or randomly distributed.

Spencer *et al*[118] conducted a post-mortem examination of sections of arterial wall from four subjects post-mortem. They investigated whether the slope, intercept and maximum backscattered power could distinguish between the loose fibrotic tissue, dense fibrotic tissue and calcium deposits in artherosclerotic plaque taken from 33 regions within the four samples. All three measures were able to distinguish on their own between loose and dense fibrotic tissue and between loose fibrotic tissue and calcium deposits, but the intercept had the most predictive power. None of the statistics were able to distinguish between dense fibrotic tissue and calcium deposits. Combinations of statistics were not considered. Because Spencer *et al* examined different components of arterial plaque than Noritomi *et al*, their results are not directly comparable.

Parsons *et al*[101] studied the ability of the slope and intercept method of ultrasonic tissue characterization to identify different damaging effects in thrombi that had deliberately induced in the jugulars of normal pigs. Examination with a light microscope was used as the gold standard to evaluate the performance of the tissue characterization algorithm. They reported that the slope and intercept method could successfully distinguish between intimal hyperplasia and luminal thrombosis and between recent and older intimal hyperplasia.

The slope-and-intercept method has been applied to tasks other than characterizing pathological changes to arterial walls. Silverman *et al*[116] used a variation of the slope-and-intercept method to distinguish between ocular tumors that high a high potential to metastasize. Their hypothesis was that the dense vascular structure of the high-risk tumors would produce scattering characteristics that were detectably different from the less-dense vascular structure of the low-risk tumors. They used the values of the slope and intercept to compute the mean scatter size and “acoustic concentration” (equal to the number of scatterers per unit volume times the square of their mean acoustic impedence relative to the surrounding medium) and used these values to classify the tumors from 40 subjects in vivo, 14 with low-risk tumors and 26 high-risk tumors. They computed the mean scatterer

size and acoustic concentration in two different manners. One method computed a mean power spectrum across the entire spectrum and fitting the slope and intercept to the mean spectrum. The other method computed the scatterer size and acoustic concentration at regularly-spaced points within the tumor and then averaged these values to compute the mean scatterer size and acoustic concentration. Using these metrics, they were able to correctly classify 31 (77.5%) tumors, seven of the 14 low-risk tumors and 24 of the 26 high-risk tumors. Despite the relatively high false-positive rate, Silverman *et al* concluded that the slope-and-intercept method could be used to distinguish high-risk ocular tumors from low-risk ones.

Kimitsuki *et al*[48] examined the livers of ten pigs both pre- and post-mortem to investigate the effects of perfusion status on the measurement of the slope and intercept measurements. They compared the slope and intercept measured under four different conditions:

- Liver tissue, pre-mortem, *in vivo* with normal perfusion
- Liver tissue, pre-mortem, *in vivo*, with the hepatic artery clamped to induce ischemia
- Liver tissue, immediately post-mortem, *in situ*
- Excised liver tissue, immediately post-mortem

Their examinations revealed that normal liver tissue had a higher mean slope and lower mean intercept than the excised liver tissue, but there was no significant difference between the slopes and intercepts of ischemic liver tissue and liver tissue examined *in situ* immediately post-mortem. They concluded that care was needed when studies characterizing liver tissue *in vivo* to studies characterizing liver tissue *in vitro*, since changes to the tissue post-mortem could change the scattering properties.

C.3.1.4 Envelope-Based Methods

As discussed in section C.2.1.4, when random variation exists in the position, size, shape or acoustic characteristics of the scatters, the complex amplitude of the backscattered signal received at the transducer becomes a random process. Acoustic scattering theory allows us to predict the parameters of this random process from the random variation in the characteristics of the scatterers[70]. For example, if the number of scatterers is large, their size is small compared to the wavelength of the ultrasonic pulse, they have uniform cross-section in the plane perpendicular to the direction of travel of the pulse, and they are randomly distributed, then the envelope of the backscattered signal will follow a Rayleigh distribution.

The reverse process is also possible: the distribution of the amplitudes of the envelope of the backscattered signal received from a region of interest in soft tissue can be used to identify the characteristics of the scatterers within that region. These characteristics can in turn be used to identify the tissue type or to distinguish the presence of abnormal regions, such as tumors. Such an observation forms the basis for the *envelope-based methods* of soft tissue characterization. In these methods, the envelope of the backscattered signal is computed by demodulation with a sinusoid of frequency equal to the center frequency of the transducer. Then an estimate of the probability density function is computed from the

histogram of the amplitudes of the signal envelope in the region of interest. The histogram is used to estimate the parameters of a distribution function, such as the Rayleigh distribution or K-distribution, which has been selected based on *a-priori* assumptions about the properties of the scatterers within the region of interest. These parameters are then used to classify the region of interest.

The choice of which distribution to fit the histogram to is very important. A poor choice for the distribution will produce poor fits to the histogram of the signal envelope, resulting in low confidence in the estimation of the distribution's parameters. Much work has been done to identify an appropriate distribution function for soft tissue, with the K-distribution being the clear winner. Clifford *et al*[20] fit five different distributions - the K-,Rayleigh, Rician, Nakagami-m, and lognormal distributions - to the backscattered signal from canine myocardia and found that the K-distribution had the best fit. Computer simulations and experiments on tissue-mimicking phantoms by Narayanan *et al*[88] also demonstrated that the K-distribution fit the envelope of the backscattered signal than the Rayleigh distribution. Finally, Mothen *et al*[85] examined the breast tissue of 35 women (10 healthy and 25 with various pathologies of the breast) and the liver tissue of 37 men and women (19 healthy and 18 with various pathologies of the liver). Their experiments also showed that the K-distribution was a superior fit to the Rayleigh distribution for both types of tissue. Comparisons with the Rayleigh distributions are common, becuase under the assumption that the scatterers are small, have uniform acoustic properties and cross-sections in the plane perpendicular to the pulse, and are randomly distributed, the Rayleigh distribution is theoretically correct. That the Rayleigh distribution has been shown consistently to be a poor fit to the envelope of the backscattered signal from human tissue *in vivo* indicates that at least some of these assumptions about the characteristics of the scatterers within human tissue are not correct.

So far, much of the work on envelope-based methods has focussed on choosing an appropriate distribution and these methods have seen little application to actually classifying tissue *in vivo*. Shankar *et al*[114] computed the characteristic parameter M of the K-distribution from the first and second moments of the histogram of the envelope of the backscattered signal from regions of healthy and diseased tissue within the breasts of 19 patients that had been clinically diagnosed as suffering from different abnormalities of the breast. Their experiments demonstrated that the value of M could be used to distinguish healthy breast tissue from pathological tissue within a single patient. However, variation in the value of M between patients for both healthy and pathological breast tissue was too large to allow successful classification of breast tissue across all of the patients. That is, the threshold on the value of M needed to distinguish healthy and pathological breast tissue varied too much from one patient to the next for any threshold that was not calibrated to the patient to be effective.

Shankar *et al* also examined using the phase information from the backscattered signal to classify healthy and pathological breast tissue. Their hypothesis was that since a random distribution of uniform scatterers would generate a backscattered signal whose phase was uniformly distributed, measuring the deviation of the distribution of the phase component of the backscattered signal from a uniform distribution would allow them to estimate the

degree of regularity in the spatial distribution of the scatteers and their non-uniformity. Presumably this degree of deviation from a uniform phase distribution would be different in different tissue types and could therefore be used to classify them. Using the chi square statistic to measure how far the phase distribution of the backscattered signal received from regions of healthy and diseased tissue within the breasts of their 19 subjects deviated from a uniform distribution, they concluded that the chi square measure of non-uniformity of the phase distribution could be used to distinguish healthy and pathological breast tissue on a qualitative basis.

Following up on the work of Shankar et al, Mothen *et al*[83] used the chi-square measure of non-uniformity in the phase distribution to characterize the tissue in 44 B-mode scans of 18 patients who had been clinically diagnoses with different liver diseases. The unprocessed A-mode data was obtained in addition to the B-mode data, and this A-mode data was used to compute the phase distribution. Each of the 44 scans contained both healthy and diseased tissue. They found that the chi-square measure of deviation from uniform phase could correctly distinguish between healthy and pathological tissue in 28 of the 44 scans.

C.3.1.5 Other Signal-Based Methods

Stetson *et al*[120] used the mean frequency of the backscattered signal to distinguish between healthy and chirrotic liver tissue in 23 subjects and between benign and malignant liver tumors in 24 subjects. The mean frequency of the backscattered signal was computed as the weighted average of the Fourier spectrum over the usable bandwidth of the transducer. Because the mean frequency of the backscattered signal depends upon the bandwidth of the transducer used to generate the ultrasonic pulse, Stetson *et al* compared the mean frequency in the bakcscattered signal generated by a 3.5 MHz broadband transducer to that generated a 5 MHz broadband transducer. They found that the mean frequency of the backscattered signal generated by the 3.5 MHz pulse could effectively distinguish between healthy and chirrotic liver tissue and between benign and malignant liver tumors, but the mean frequency in the backscattered signal generated by the 5 MHz transducer could not.

Wear *et al*[140] invented the autoregressive moving average technique for computing the mean spacing between scatterers in the direction parallel to the velocity vector of the ultrasonic pulse. As discussed in section C.2.1.3, regular or semi-regular arrangements of scatterers in soft tissue in the direction parallel to the pulse's velocity vector give rise to regularly-spaced peaks in the Fourier spectrum at positive integer multiples of a fundamental frequency whose value is a function of the speed of sound in the tissue layer and the mean spacing between scatterers along the velocity vector of the ultrasonic pulse. The fundamental frequency corresponding to these regularly-spaced peaks can be detected using the cepstrum[97]. However, the trade-off between resolution in the spatial and Fourier domains discussed at the end of section C.3.1 limits the cepstrum to window sizes of 10 mm or greater[140] when the Fast Fourier Transform is used to compute the spectrum of the backscattered signal from soft tissue *in vivo*. Shorter windows produce unacceptable distortions in the spectrum that limit the ability of the ceptrsum to measure interscatterer spacing effectively.

Wear *et al* proposed the autoregressive moving average as an alternative to the Fast Fourier Transform for estimating the power spectral density of the backscattered signal. The autoregressive moving average is a linear combination of the autocorrelation of the backscattered signal with the moving average of a white noise process with zero mean and a variance that is a function of the autocorellation of the backscattered signal (details can be found in Wear *et al*'s paper[140]). The locations of peaks in the Fourier spectrum can be computed directly from the coefficients of the autoregressive moving average without ever leaving the time domain. Although the autoregressive moving average is still subject to the trade off between the size of the window used to compute its value and the resolution with which the locations of the peaks in the Fourier can be located, this trade-off is less stringent than the trade-off imposed by using the Fast Fourier Transform and the cepstrum to compute the same values. That is, for a given window length, the autoregressive moving average will have a higher resolution in the Fourier domain than the ceptrum computed using the Fast Fourier Transform.

Wear *et al* compared the values of interscatterer spacing along the velocity vector of the ultrasonic pulse measured by the autoregressive moving average to the values measured by the cepstrum on tissue mimicking phantoms whose interscatter spacing was known. As predicted, both methods made accurate measurements of the interscatter spacing for longer window sizes, but the autoregressive moving average gave better estimates than the ceptrum when the window size was less than 5 mm. They also showed that the estimate of interscatter spacing for human liver in vivo made by the autoregressive moving average did not vary as much with window size as the estimate made by the cepstrum.

C.3.2 Image-Based Methods

In contrast to signal-based methods, which process the A-mode backscattered signal, image-based methods process the B-mode image generated by ultrasound imaging systems in common clinical use. Image-based methods work by computing the statistical properties of the grey levels within a nominally homogeneous region of the B-mode image called the *region of interest*. Since the grey levels in the image are ultimately derrived from the amplitude of the backscattered A-mode signal from the soft tissues of the body, some of the same information present in the backscattered A-mode signal that distinguishes one type of soft tissue from another will be present. However, because they work with the B-mode image, they are isolated from the spectral characteristics of the backscattered signal, which contain a lot of information about the size, shape, density and arrangement of the scatterers in the path of the ultrasonic pulse, the image-based methods may not be as accurate as the signal-based methods. Image-based techniques have access to this information only inasmuch as it impacts the distribution of grey levels within the region of interest. This inability to directly access the information contained in the spectrum of the backscattered signal is the primary disadvantage of image-based methods when compared to signal-based methods.

However, image-based methods do have several advantages over signal-based methods. First of all, they can be used with conventional ultrasonic imaging systems without modification, whereas signal-based methods need access to the A-mode signal from the transducer before it has undergone significant processing. In addition, unlike the

computation of the coefficient of attenuation, coefficient of integrated backscatter or slope and intercept of the logarithmic power spectrum, image-based methods do not need to correct for the imaging characteristics of the transducer using a reference spectrum. Furthermore, because image-based methods do not make direct use of the characteristics of the Fourier spectrum, they are not subject to the same trade-off between spatial and spectral resolution that the signal-based methods are. Finally, because they collect statistics over a two-dimensional region in the image, image-based methods can use information from a broader area than signal-based methods, which are limited to the information contained along a single line that follows the path of the ultrasonic pulse.

Despite their advantages, image-based methods are not as popular as signal-based methods. So far, only a few groups have developed image-based methods of tissue characterization. These techniques are described below.

Some of the earliest work done on image-based tissue characterization methods was done by Insana *et al*[41], although they made use of the power-spectrum from the A-mode backscattered signals from the region of interest as well as the characteristics of its grey-levels. They computed a histogram of the grey levels within the region of interest and computed its first and second moments. From the square of the first moment of the histogram, the second moment, and the integral of the average power spectrum after subtracting Rician noise to compute the mean intensity of the diffuse scattering component (the portion of the backscattered signal that comes from a large number of randomly-distributed scatterers that are much smaller than the wavelength of the ultrasonic pulse), the mean intensity of the specular scattering component (the portion of the backscattered signal that comes from strong, isolated point scatterers), and the mean distance between scatterers along the path of the ultrasonic pulse. Results on seven healthy subjects showed that the mean intensity of diffuse scattering and the mean intensity of specular scattering could be used to distinguish between kidney, spleen and liver tissue. They also found that the mean distance between scatterers along the path of the pulse could be used to distinguish between healthy and diseased liver tissue, but not between different types of liver disease.

Zimmer and his colleagues developed two different techniques for segmenting B-mode images based on the local entropy at each pixel in the image. One technique[149] was derrived from Li and Lee's minimum cross-entropy technique[64] for segmenting regions within ariel photographs. When applied to ultrasonic imaging, the minimum cross-entropy technique as originally developed by Li and Lee computes the threshold on the grey level within the region of interest that minimizes the cross-entropy between the pixels with grey levels at or above the thresholds and the pixels with grey levels below the threshold. Zimmer *et al*[149] extended Li and Lee's cross-entropy method to apply to multivariate distributions of parameters. In their particular case, they extended the method to segment B-mode images based on both on the grey level and the local entropy at each pixel within the region of interest. Instead of selecting the single threshold that minimized the cross-entropy between the pixels above or at the threshold and those below it, Zimmer *et al*'s extension of the minimum cross-entropy method selected the best line or the best circle in the two-dimensional parameter space that minimized the cross-entropy between the pixels

in the image whose grey level and local entropy placed them on one side of the partition made by the line or circle in parameter space and those pixels whose grey level and local entropy placed them on the other side of the partition. They tested their multivariate minimum cross entropy method on images of ovarian cysts acquired in vivo and found that their multivariate minimum cross-entropy method qualitatively produced better segmentations than Li and Lee's original univariate version.

The other image segmentation technique developed by Zimmer and his colleagures segmented ultrasonic images based on the histogram of local entropy in the vicinity of each pixel in the image[150]. They constructed a model the scattering properties of soft tissue that treated the properties of each pixel in the image as arising from local variations in the global distribution of scatterers throughout the entire image. Regions of the image with similar local distribution functions were considered to be of the same tissue type. Based on this model, they concluded that the histogram of local entropy in the image would exhibit peaks in the vicinity of the boundary between two different types of tissue, and thus by applying a threshold to the local entropy histogram at each pixel in the image, they could segment different regions within the image. They applied this segmenting method to ultrasonic images of ovarian cysts in vivo and reported that it performed well when applied to images where the contrast between the cyst and the surrounding tissue was high, but did not perform well when it was low.

The main disadvantage of the segmentation techniques developed by Zimmer and his colleagues is that they can only identify boundaries between different regions in the image, but do not provide a theoretical basis for deciding which tissue type should be assigned to each region in the image. However, once the region has been segmented by one of Zimmer's methods, other techniques can be used to identify the tissue in each region.

Valckx and Thijssen[127] used computer simulations to explore how statistics derrived from the co-occurence of grey levels within a region of the B-mode image could be used to classify the tissue within that region. The co-occurence matrix measure how often pairs of grey levels at pixels separated by a distance of d pixels within the region being classified occur. The value of d is an argument to the method. The co-occurence matrix is used to compute several parameters, including the entropy, contrast, correlation, angular second moment and Parkinnen's kappa[100]. The entropy measures the amount of "disorder" in the co-occurence matrix, while contrast measures the variation in intesity, correlation the strength of the correlation between grey levels in the matrix, the angular second moment the degree of homogeneity, and Parkinnen's kappa the periodicity of the image texture. Simulations were used to evaluate how changes in the density of the scatterers within a layer of tissue, their arrangement within that layer (e.g. randomly distributed or having some structure), the value of d, and the size of the region being characterized affected the values of entropy, contrast, correlation, angular second moment and Parkinnen's kappa. Their simulations showed that:

- The values of entropy, angular second moment, contrast, correlation and Parkinnen's kappa will depend strongly on the depth at which the image is acquired in the body.

- If only diffuse scattering is present (e.g. the scatterers are small compared to the wavelength of the pulse and their spatial distribution is random), then the angular second moment is the best parameter to distinguish between different tissue types.
- If the scatterers have a regular or semi-regular arrangement in space, then contrast or correlation are the best parameters to use to distinguish between different tissue types.
- The optimal value of *d* is one.
- When *d* is small, the values of entropy and angular second moment will be highly correlated, as will the values of contrast and correlation. Only one of each of these pairs should be used for classification.

However, Valckx and Thijssen did not evaluate their co-occurence matrix method on soft tissue either *in vitro* or *in vivo.*

C.3.3 Discussion

Given the wide variety of tissue characterization methods available, it is natural to ask which method is the best at classifying different types of soft tissue. While evaluations of the individual methods have been published, variations in the experimental conditions and methods makes a meaningful direct comparison of these results impossible. Unfortunately, evaluations of different tissue characterization methods under the same experimental conditions are very rare and only one is known to us at this time. Huisman *et al*[38] compared the ability of the coefficient of attenuation, the slope and intercept of the logarithm of the spectrum of the backscattered signal, and the signal-to-noise ratio of the local image texture (ratio of mean to standard deviation of the local grey level in the region of the B-mode image to be classified) to distinguish between liver metastates and healthy tissue. Their test set consisted of 100 instances of liver metastates and 43 examples of healthy tissue acquired from ultrasonic examinations of human subjects *in vivo*. Although they did not present a quantitative comparison of the accuracy of each method, they did present scatter plots showing the overlap between the values of each metric for healthy and metastatic tissue. Neither the coefficient of attenuation nor the signal-to-noise ratio of the local image text could clearly distinguish healthy tissue from metastatic tissue, but the slope of the logarithm of the spectrum of the backscattered signal was able to clearly distinguish between healthy and metastatic tissue.

Another natural question to ask is whether some of parameters computed by the different tissue characterization methods (e.g the coefficient of integrated backscatter, the slope and intercept of the logarithmic power spectrum, the entropy of the co-occurence matrix) are strongly correlated with one another, and if so, which ones. Understanding the answer to this question is important if more than one method is used to classify a region of soft tissue, since using strongly correlated methods together will do no better than using the individual methods alone.

Thijssen *et al*[123] computed the values of eighteen different parameters computed by seven different methods on the backscattered signals acquired *in vivo* from the livers of

126 healthy subjects. The parameters they examined included:

- The coefficient of attenuation, computed by each of the three different methods described in section C.3.1.1.
- The angular second moment, contrast, correlation, entropy and Parkinnen's kappa of the co-occurence matrix, using the method developed by Valckx & Thijssen[127].
- The slope and intercept of the logarithm of the Fourier spectrum of the backscattered signal, using the method developed by Lizzi *et al*[70,71].
- The ratio of the mean intensity of the diffuse scattering component to the mean intensity of the specular scattering component, using the method developed by Insana *et al*[41].
- The mean grey level of the B-mode image in the region being classified.
- The mean spacing between scatterers along the path of the ultrasonic pulse computed from the mean spacing between peaks in the Fourier spectrum.
- The signal-to-noise ratio of the grey levels of the B-mode image in the region being classified (used by Huisman *et al*[38] in their comparative evaluation of three different tissue characterization methods described above).

as well as several other parameters drawn from some minor tissue characterization methods not described in this study. Only nine of the eighteen parameters did not correlate strongly with each other. Of the parameters described in this survey, the slope of the attenuation coefficient computed by linear regression through zero, the slope of the attenuation coefficient computed by linear regression without going through zero, the slope of the logarithm of the backscattered power spectrum, the mean grey level in the region being classified, the signal-to-noise ratio of the grey levels in the region being classified, and the mean spacing between scatterers along the path of the pulse did not correlate strongly with one another.

Building on the work done by Thijssen *et al*, Oostervald *et al*[96] used linear discriminant analysis to identify which of the 18 parameters used by Thijssen *et al* would be the most important in distinguishing diffuse liver disease from healthy tissue in 129 healthy subjects and 98 subjects suffering from diffuse liver diseases of one sort or another, where the "importance" of a parameter measured the relative contribution it made towards distinguishing between healthy and diseased liver tissue with respect to the other parameters. They found that the mean grey level in the region being classified, the signal-to-noise ratio of the grey level in the region being classified, slope of the attenuation coefficient computed by linear regression through zero, and the slope and intercept of the logarithm of the Fourier spectrum were the most important parameters at classifying diffuse liver disease. The texture-based parameters derrived from the co-occurence matrix and the ratio of the mean intensity from the diffuse scattering component to the mean intensity of the specular scattering component were not very informative compared to the other parameters considered in Oostervald *et al*'s study.

Which tissue characterization method should be applied to a particular problem depends primarily upon the information available. If the A-mode signal is available, then on the basis of the work done by Huisman *et al* and Oostervald *et al* described above, signal-based methods should be prefered preferred over image-based methods. Even though the mean values and signal-to-noise ratio of the grey levels in the region being classified have been shown by Oostervald *et al* to be informative compared to the other image-based parameters, neither of them is as effective on their own as the parameters computed by the signal-based methods in classifying soft tissue. However, if only the B-mode image is available, then the mean grey level and signal-to-noise ratio should be used in conjunction with the parameters computed other image-based methods from section C.3.2.

Which signal-based method one should choose depends upon what properties of the tissue layers being classified are believed to be most distinctive. If the spacing between scattering centers along the path of the ultrasonic pulse is believed to be the most distinctive, then the autoregressive moving average method is probably a good choice. If the density, size and shape of the scatterers is believed to be as important as their spacing, then either the coefficient of integrated backscatter or the slope and intercept of the logarithm of the Fourier spectrum of the backscattered signal would be the better choice. Since there are strong theoretical reasons to believe that these two methods are strongly correlated, there is no preference for one over the other. Although the attenuation coefficient does not do well at classifying tissue type on its own, Oostervald *et al* have shown that it can be used to augment the effectiveness of the coefficient of integrated backscatter or the slope and intercept method. Since both of these methods benefit from correction for attenuation, and the coefficient of attenuation can be computed from the same data used to compute the parameters of both methods, the coefficient of attenuation almost comes “for free” and there is little reason not to use it.

Missing from current tissue characterization work is any sort of comparative evaluation of the different methods on a standard data set. Such evaluations are common in other classification domains, such as the extensive comparative evaluations done by Yang[141] or Li and Yang[65] in the categorization of text documents. Although the work done by Huisman *et al*[38] is a step in the right direction, it only compares three methods and only uses qualitative measures of performance. A benchmark comparative evaluation for tissue characterization in which a wide variety of methods are evaluated on a standard data set under realistic conditions using quantitative measurements of performance is still needed. The data set used for such an evaluation should be released to the public, so that developers of new tissue characterization methods can evaluate these new methods in such a way that their performance can be compared to the current state-of-the-art in tissue characterization.

C.4 Conclusions

Ultrasonic tissue characterization is the process of classifying or identifying the type of soft tissue that a region in the backscattered A-mode signal or B-mode image belongs to. Although tissue characterization may be used to distinguish between different kinds of tissue in body such as skin, fat, muscle, and so on, it is primarily used to distinguish

between healthy and diseased tissue of the same nominal type, such as distinguishing between healthy and metastatic liver tissue.

Many methods have been developed for ultrasonic tissue characterization, and they may be divided into two broad classes: those that use the information contained in the backscattered A-mode signal before it has undergone significant processing and those that use the information contained in the B-mode image. Which method or methods should be used to classify a image depends upon the needs of the application, the information available and prior beliefs about what characteristics of the structures of the tissues being classified will be most distinguishing. Although little work has been done on comparing the different tissue characterization methods has been done, the work that has been done so far indicates that methods based on analyzing the A-mode signal are preferable to methods based on analyzing the B-mode image. Among the methods based on analyzing the A-mode signal, the two most popular methods are strongly correlated with one another, so choosing between them is largely a matter of preference. More work is needed in comparing the different tissue characterization methods available under the same experimental conditions *in vivo* so that the relative performance characteristics of the different methods can be better understood and a benchmark can be established against which the performance of new tissue characterization methods can be measured.

Appendix D
The Coordinate System Rotation Distance Metric

In order to evaluate the performance of the Iterative Closest Point (ICP) registration algorithm in chapter 3, the distance between two transformations, one that represents the true pose of the object and one that represents the pose estimated by the ICP algorithm, must be computed. The smaller this distance, the better the performance of the algorithm. Each transformation corresponds to a set of coordinate axes in 3-space that is described by a rotation and a translation. The translation defines the location of the origin of the transformation's coordinate axes with respect to some arbitrary coordinate system, which will be called the "world coordinate system," while the rotation defines the orientation of the transformation's *x*-, *y*- and *z*-axes with respect to the corresponding axes of the world coordinate system. The distance between two transformations has two components: the distance between their translations and the distance between their rotations. These two components can be reported separately, or combined into a single value using a weighted average, depending on the needs of the application. In this thesis, the distance between translations and the distance between rotations are reported separately, so that errors in the translation between the registration points and the surface model computed by the ICP algorithm can be distinguished from errors in the rotation computed by that algorithm.

The distance between the translations of two transformations is simply the Euclidean distance between the origins of their coordinate systems. How to measure the distance between the rotations of two transformations is not as straightforward. Intuitively, two rotations are close together if the coordinate (x,y,z) in the coordinate system represented by one rotation is close to the same coordinate (x,y,z) in the coordinate system represented by the other rotation when the origins of those two coordinate systems are coincident. Kuffner[54] describes two different metrics for measuring the distance between two rotations: one based on the Euler angle representation of those rotations and one based on the unit quaternion representation of those rotations. The distance between two rotations represented using Euler angles $(\alpha_0, \beta_0, \gamma_0)$ and $(\alpha_1, \beta_1, \gamma_1)$ (using any Euler angle convention) is:

$$\sqrt{(\alpha_1 - \alpha_0)^2 + (\beta_1 - \beta_0)^2 + (\gamma_1 - \gamma_0)^2} \qquad \text{(D.1)}$$

However, as Kuffner notes, this metric is problematic because there are multiple Euler angle representations of any rotation, and the values of the Euler angles for these multiple representations may not be close together at all. Consequently, (E.1) may take on large values even when the distance between the rotations is quite small in the intuitive sense

described above.

There are actually several options for measuring the distance between two rotations using unit quaternions. One is to use the absolute value logarithm of the dot product of the unit quaternions:

$$\left|\log(Q_0^T Q_1)\right| \tag{D.2}$$

where Q_0 and Q_1 are the unit quaternions that represent the two rotations. Another is simply to use the the dot product of the quaternions subtracted from one:

$$1 - (Q_0 \cdot Q_1) \tag{D.3}$$

or the angle between the quaternions:

$$\theta = \operatorname{acos}(Q_0 \cdot Q_1) \tag{D.4}$$

These metrics have the disadvantage that they are defined in terms of quaternions, so if the application is not using quaternions to represent its rotations, then it must convert them. In addition, for any rotation, there are exactly two quaternions that represent them, so care must be taken to normalize the quaternions Q_1 and Q_2 before using them to compute the distance between the rotations they represent. Finally, it is difficult to assign physical meaning to any of the values computed by equations (E.2), (E.3) or (E.4). While small values of these equations indicate that the rotations are close together, it is difficult to tell how close together they are. In terms of the intuitive notion of "closeness" of rotations described earlier, it is difficult to tell from equations (E.2), (E.3) or (E.4) how close the coordinate *(x,y,z)* in the coordinate system represented by rotation Q_0 is to the same coordinate in the coordinate system represented by rotation Q_1.

In this thesis, we use a different metric to measure the distance between two rotations, one that has an intuitive physical meaning and is independent of the means used to represent those rotations. Because this metric is defined in terms of the axes of the coordinate systems used to represent the two rotations, we call it the *coordinate system rotation distance metric* and designate it by the letter *r*. One of the nice properties of *r* is that the distance between the coordinate *(x,y,z)* in the coordinate system represented by one rotation and the same coordinate *(x,y,z)* in the coordinate system represented by the other rotation is no more than:

$$r\sqrt{x^2 + y^2 + z^2} \tag{D.5}$$

Thus, if one rotation represents the true orientation of a rigid body and the other rotation represents the orientation computed the ICP algorithm, then *r* gives a bound on the error in computing the location of any point on that body that arises from the error in computing

its rotation.

In the remainder of this appendix, we define the coordinate system rotation distance metric and prove the property described by equation (E.5) above.

D.1 Definition of the Metric

Given two rotations R_0 and R_1, let the axes of the coordinate system represented by R_0 be $(\hat{u}_0, \hat{v}_0, \hat{n}_0)$ and the axes of the coordinate system represented by R_1 be $(\hat{u}_1, \hat{v}_1, \hat{n}_1)$. Then the coordinate system rotation distance metric is defined to be:

$$r = \sqrt{\|\Delta\hat{u}\|^2 + \|\Delta\hat{v}\|^2 + \|\Delta\hat{n}\|^2} \tag{D.6}$$

where $\|\Delta\hat{u}\|$ is the difference between the u-axes of R_1 and R_0 (e.g $\hat{u}_1 - \hat{u}_0$), $\|\Delta\hat{v}\|$ is the difference between the v-axes, $\|\Delta\hat{n}\|$ is the difference between the n-axes, and $\|\hat{a}\|$ is the magnitude of vector $\hat{a}$. Although the coordinate system rotation distance metric requires the computation of the coordinate axes of R_0 and R_1, these axes must normally be computed anyway to do any useful work with the rotations. This property gives the coordinate system rotation distance metric some independence from the mechanism used to represent R_0 and R_1. However, the most useful property of r is that its value is an upper bound on the distance between any coordinate *(x,y,z)* on the unit sphere in the coordinate system represented by R_0 and the same coordinate in the coordinate system represented by R_1, a property we prove in section E.2. For coordinates not on the unit sphere, the distance between *(x,y,z)* in R_0 and *(x,y,z)* in R_1 is bounded by $r\sqrt{x^2 + y^2 + z^2}$. Since the distance between *(x,y,z)* in R_0 and R_1 is:

$$d = \|x\Delta\hat{u} + y\Delta\hat{v} + z\Delta\hat{n}\| \tag{D.7}$$

the value of r will be small when R_0 and R_1 are close in the intuitive sense. Finally, it is possible to visualize how close or far apart R_0 and R_1 by computing the average angle between their axes, e.g. the average angle between $\hat{u}_0$ and $\hat{u}_1$, $\hat{v}_0$ and $\hat{v}_1$, $\hat{n}_0$ and $\hat{n}_1$. This average angle ϕ is equal to:

$$\phi = \operatorname{acos}\left(1 - \frac{r^2}{6}\right) \tag{D.8}$$

The primary disadvantage of the coordinate system rotation distance metric is that it requires more effort to compute than metrics based on the distance between the Euler angles or quaternions.

D.2 Proof of Bounds on Distance Between Corresponding Points

In this section, we prove that the value of *r* calculated by equation (D.6) is an upper bound on the distance between the coordinate *(x,y,z)* on the unit sphere in the coordinate system represented by rotation R_0 and the same coordinate *(x,y,z)* in the coordinate system represented by rotation R_1. That is, we need to prove:

$$d \leq \sqrt{\|\Delta\hat{u}\|^2 + \|\Delta\hat{v}\|^2 + \|\Delta\hat{n}\|^2} \tag{D.9}$$

where *d* is the distance between he coordinate *(x,y,z)* in the coordinate system represented by rotation R_0 and the same coordinate *(x,y,z)* in the coordinate system represented by rotation R_1 and *(x,y,z)* is constrained to lie on the unit sphere. The value of *d* may be calculated by equation (D.7).

We begin by using the law of cosines to expand equation (D.7) to:

$$\begin{aligned} d^2 \;=\; & x^2\|\Delta\hat{u}\|^2 + y^2\|\Delta\hat{v}\|^2 + z^2\|\Delta\hat{n}\|^2 + \\ & 2xy(\Delta\hat{u}\cdot\Delta\hat{v}) + 2xz(\Delta\hat{u}\cdot\Delta\hat{n}) + 2yz(\Delta\hat{v}\cdot\Delta\hat{n}) \end{aligned} \tag{D.10}$$

Now consider a function *f(x,y,z)* such that:

$$\begin{aligned} f^2(x,y,z) \;=\; & x^2\|\Delta\hat{u}\|^2 + y^2\|\Delta\hat{v}\|^2 + z^2\|\Delta\hat{n}\|^2 + \\ & 2|xy|\|\Delta\hat{u}\|\|\Delta\hat{v}\| + 2|xz|\|\Delta\hat{u}\|\|\Delta\hat{n}\| + 2|yz|\|\Delta\hat{v}\|\|\Delta\hat{n}\| \end{aligned} \tag{D.11}$$

where $|ab|$ is equal to the absolute value of the product of *a* and *b*. By definition, we will constrain the value of *f* itself to be greater than or equal to zero. Since

$$\begin{aligned} -|xy|\|\Delta\hat{u}\|\|\Delta\hat{v}\| \leq xy(\Delta\hat{u}\cdot\Delta\hat{v}) \leq |xy|\|\Delta\hat{u}\|\|\Delta\hat{v}\| \\ -|xz|\|\Delta\hat{u}\|\|\Delta\hat{n}\| \leq xz(\Delta\hat{u}\cdot\Delta\hat{v}) \leq |xz|\|\Delta\hat{u}\|\|\Delta\hat{n}\| \\ -|yz|\|\Delta\hat{v}\|\|\Delta\hat{n}\| \leq yz(\Delta\hat{u}\cdot\Delta\hat{v}) \leq |yz|\|\Delta\hat{v}\|\|\Delta\hat{n}\| \end{aligned} \tag{D.12}$$

the constraint:

$$0 \leq d^2 \leq f^2 \tag{D.13}$$

must hold. The function f(x,y,z) can be simplified to:

$$f^2(x,y,z) \;=\; \left(|x|\|\Delta\hat{u}\| + |y|\|\Delta\hat{v}\| + |z|\|\Delta\hat{n}\|\right)^2 \tag{D.14}$$

Using Lagrange multipliers, it can be shown that the maximum value of f^2 on the unit sphere occurs at:

$$x = \pm\frac{\|\Delta\hat{u}\|}{s} \qquad y = \pm\frac{\|\Delta\hat{v}\|}{s} \qquad z = \pm\frac{\|\Delta\hat{n}\|}{s}$$
$$s = \sqrt{\|\Delta\hat{u}\|^2 + \|\Delta\hat{v}\|^2 + \|\Delta\hat{n}\|^2} \tag{D.15}$$

Substituting these values for x, y, and z into equation (D.14) yields a maximum value for f^2 on the unit sphere of:

$$max\ f^2(x, y, z) = \|\Delta\hat{u}\|^2 + \|\Delta\hat{v}\|^2 + \|\Delta\hat{n}\|^2 \tag{D.16}$$

Since d measures a distance between two points, its value must be greater than or equal to zero. Likewise, the definition of f constrains its value to be greater than or equal to zero. So $d^2 \le f^2$ implies that $d \le f$ and therefore:

$$d \le \sqrt{\|\Delta\hat{u}\|^2 + \|\Delta\hat{v}\|^2 + \|\Delta\hat{n}\|^2} \tag{D.17}$$

which is what we set out to prove.

Glossary

basement membrane
A thin extracellular supporting layer that separates the epidermis from the dermis.

carcinoma
A malignant tumor of an epithelial origin. In the context of this thesis, carcinomas refer to tumors of the skin.

catabolic process
A destructive metabolic process that consumes complex materials by breaking them down into simpler components.

collagen
An insoluble fibrous protein that forms long fibers in the connective tissues of the body. Collagen is the chief constituent of connective tissue and yields gelatin and glue upon prolonged heating with water.

collagenase inhibitors
Enzymes that inhibit the production of collagenase - a substance that breaks down collagen.

demosomes
A junctional complex that connects cells of the epidermis together.

dermal papillae
A vascular protuberance of the dermis that extends into the epidermis. Dermal papillae frequently contain bundles of nerves that act as tactile sensors for the body.

elastin
A protein similar to collagen and is the chief constituent of elastic fibers.

eosinophilia, diffuse or focal
An abnormal increase in the number of eosinophils (a kind of white blood cell) in the blood, usually because of an allergic reaction or parasitic infection. Diffuse eosinophilia is an increase in the number of eosinophils throughout the body, while focal eosinophilia limits the increase to a specific region of the body.

erythema
An abnormal redness of the skin due to capillary congestion. A non-blanchable erythema is one that does not turn white when it is rubbed.

eschar
A scab, especially one formed after a burn.

fascia
A sheet of connective tissue covers or binds body structures. Superficial fascia bind the underside of the dermis to the deeper structures of the body, while deep fascia cover the muscles of the body.

fibroblast
A cell that secretes collagen and other proteins used to build connective tissue.

glycosaminoglycans
A component of different proteins found in the body. Among other things, glycosaminoglycans are used to manufacture collagen.

ground substances
See “interstitial fluid.”

hemorrhagic crust
A crust of dried blood left behind after a hemorrhage (a copious discharge of blood).

in vivo
Literally “in life.” Refers to measurements or experiments carried out on cells or living organisms in their natural state, as opposed to measurements or experiments conducted *in vitro*, which designates that the measurements or experiments were carried out in an artificial environment, such as a test tube or a petri dish.

in vitro
See “in vivo.”

interstitial fluid (and ground substances)
The fluid that surrounds the cells of the organs of the body. Interstitial fluid keeps the cells from bumping against each other and acts as the transport mechanism for oxygen and nutrients between the cells and the blood vessels of the body. The phrase “ground substances” refers to any one of a wide variety of substances that can be found within the interstitial fluid.

ischemia
A deficient supply of blood to a body part due to the obstruction of the inflow of blood in an artery or capillary.

.

keratinized cells
Dead cells that have been coated in keratin, a fibrous protein that makes up the hair and nails of the body.

leukocyte
A type of white blood cell that helps the body fight off infection.

macrophage
A type of cell that seeks out and consumes foreign matter, such as bacteria and viruses.

mast cells
A type of cell in the connective tissues of the body that mediates allergic reactions.

necrosis
The death of living tissue.

osteomyelitis
An infection that results in the inflammation of bone. Osteomyelitis is usually very painful.

sepsis
A systemic response by the body to a serious infection that results in an abnormal body temperature and white blood cell count.

subepidermal bulla
A large blister that extends beneath the epidermis.

synthetic process
A constructive metabolic process that builds complex substances from simpler components.

thrombus (plural thrombi)
A clot that forms within a blood vessel and remains attached to the location where it originates. A thrombus that gets loose may become lodged in one of the blood vessels of the brain and cause a stroke.

vasculature
The disposition or arrangement of blood vessels within an organ or region of the body.

Bibliography

[1] T. Agner, *Ultrasound A-Mode Measurement Of Skin Thickness*, in *Handbook of Non-invasive Methods and the Skin*, CRC Press, Ann Arbor, MI, 1995, pp. 289-292

[2] D. Anthony, J. Barnes & J. Unsworth, *An Evaluation Of Current Risk Assessment Scales For Decubitus Ulcer In General Inpatients And Wheelchair Users*, Clinical Rehabilitation, 12(2): 136-42 (1998)

[3] N. Agarwal, *The Role Of Nutrition In The Management Of Pressure Sores* in *Surgical Management Of Cutaneous Ulcers And Pressure Sores*, Chapman & Hall, New York, NY, 1998, pp. 60-70

[4] C. Bansal, R. Scott, D. Stewart & C. Cockerell, *Decubitus Ulcers: A Review Of The Literature*, International Journal of Dermatology, 44(10):805-810 (2005)

[5] J. Barbenel, F. Gibson & F. Turnbull, *Optical Assessment Of Skin Blood Content And Oxygenation* in *Bedsore Biomechanics*, University Park Press, Baltimore, MD, 1975, pp. 83-93

[6] N. Bergstrom, B. Braden, A. Laguzza & V. Holman, *The Braden Scale For Predicting Pressure Sore Risk*, Nursing Residence, 36: 205-210 (1987)

[7] N. I. Bergstrom, *Strategies for Preventing Pressure Ulcers*, Clinics in Geriatric Medicine 13(3):437-453 (1997)

[8] P. J. Besl and N. D. McKay, *A Method for Registration of 3-D Shapes*, IEEE Transactions on Pattern Analysis and Machine Intelligence, 14(2): 239-256 (1992)

[9] K. Bogie, I. Nuseibeh & D. Bade, *Early Progressive Changes In Tissue Viability In The Seated Spinal Cord Injured Subject*, Paraplegia 33: 141-147 (1995)

[10] S. Bridal, P. Fornes, P. Bruneval & G. Berger, *Parametric (Integrated Backscatter And Attenuation) Images Constructed Using Backscattered Radio Frequency Signals (25- 56 MHz) From Human Aortae In Vitro*, Ultrasound in Medicine & Biology, 23(2): 215-229 (1997)

[11] D. Brienza, R. Inigo, K.C. Chung & C. Brubaker, *Seat Support Surface Optimization Using Force Feedback*, IEEE Transactions On Biomedical Engineering, 40(1): 95-104 (1993)

[12] D. Brienza, K. C. Chung, C. E. Brubaker, J. Wang, T. E. Karg & C. T. Lin, *A System For The Analysis Of Seat Support Surfaces Using Surface Shape Control And Simultaneous Measurement of Applied Pressures*, IEEE Transactions on Rehabilitation Engineering 4(2): 103-133 (1996)

[13] D. Brienza, P. Karg & C. E. Brubaker, *Seat Cushion Design for Elderly Wheelchair Users Based On Minimization of Soft Tissue Deformation Using Stiffness And Pressure Measurements*, IEEE Transactions on Rehabilitation Engineering 4(4): 320-327 (1996)

[14] D. Brienza & P. Karg, *A Comparison Of Interface Pressure And Tissue Stiffness Characteristics For Spinal Cord Injured And Elderly Patients*, Archives Of Physical Medicine and Rehabilitation, 79:388-94 (1998)

[15] D. Brienza & L. Ostrander, *Mechanical Loading And Pressure Ulcers* in *Surgical Management Of Cutaneous Ulcers And Pressure Sores*, Chapman & Hall, New York, NY, 1998, pp. 116-128

[16] J. Carison, M. Payette & L. Vervena, *Seating Orthosis Design For Prevention Of*

Decubitus Ulcers, Journal Of Prosthetics And Orthotics, 7(2): 51-60 (1995)
[17] J. F. Chen & J. Zagzebski, *Tests of Backscatter Coefficient Measurement Using Broadband Pulses*, IEEE Transactions on Ultrasonics, Ferroelectrics, and Frequency Control, 40(5): 603-607 (1993)
[18] W. W. Chow and E. Odell, *Deformations And Stresses In Soft Body Tissues Of A Sitting Person*, Journal Of Biomechanical Engineering, 100: 79-87 (1978)
[19] M. Clark, L. Rowland, H. Wood & R. Crow, Measurement Of Soft Tissue Thickness Over the Sacrum Of Elderly Hospital Patients Using B-Mode Ultrasound, Journal Of Biomedical Engineering, 11: 202 (1989)
[20] L. Clifford, P. Fitzgerald & D. James, *Non-Rayleigh First-Order Statistics Of Ultrasonic Backscatter From Normal Myocardium*, Ultrasound in Medicine & Biology, 19(6): 487-95 (1993)
[21] C. Daly, J. Chomoskey, G. Holloway & D. Kennedy, *The Effect Of Pressure Loading On The Blood Flow Rate In Human Skin* in *Bedsore Biomechanics*, University Park Press, Baltimore, MD, 1975, pp. 69-77
[22] R. Daniel, D. Priest, D. Wheatley, *Etiologic Factors In Pressure Sores: An Experimental Model*, Archives Of Physical Medicine and Rehabilitation, 62: 492-498 (1981)
[23] G. Davidson, C. Hall, J. Miller, M. Scott & S. Wickline, *Ultrasonic Tissue Characterization Of End-Stage Dilated Cardiomyopathy*, Ultrasound in Medicine & Biology, 21(7): 853-60 (1995)
[24] S. Dinsdale, *Mechanical Factors in the Pathogenesis of Ischemic Skin Ulcers in Swine*, Ph.D. Thesis, University of Minnesota (1970)
[25] S. Dinsdale, *Decubitus Ulcers: Role Of Pressure And Friction In Causation*, Archives of Physical Medicine and Rehabilitation, 55:147-152 (1974)
[26] K. Donohue, J. Bressler, T. Varghese & N. Bilgutay, *Spectral Correlation In Ultrasonic Pulse Echo Signal Processing*, IEEE Transactions on Ultrasonics, Ferroelectrics, and Frequency Control, 40(4): 330-7 (1993)
[27] D, Fawcett, *A Textbook Of Histology (11th Edition)*, W.B. Saunders Company, Philadelphia (1986)
[28] P. Fitzgerald, M. MacDaniel, E. Rolett, D. James & J. Strohbehn, *Two-Dimensional Ultrasonic Variation In Myocardium Throughout The Cardiac Cycle*, Ultrasonic Imaging, 1986 8(): 241-251
[29] F. Forsberg, E. Conant, K. Russell & J. Moore Jr., *Quantitative Ultrasonic Diagnosis Of Silicone Breast Implant Rupture: An In Vivo Feasiblity Study*, Ultrasound in Medicine & Biology, 22(1): 53-60 (1996)
[30] Y.C. Fung, *Biomechanics: Mechanical Properties Of Living Tissue*, Springer-Verlag, New York, NY, 1993
[31] M. Geyer, D. Brienza, P. Karg, E. Treffler & S. Kelsey, A Randomized Trial To Evaluate Pressure Reducing Seat Cushions For Elderly Wheelchair Users, Advances In Skin And Wound Care, May/June (2001)
[32] B. Goldstein & J. Sanders, *Skin Response To Reptitive Mechanical Stress: A New Experimental Model In Pig*, Archives of Physical Medicine and Rehabilitation, 79: 265-272 (1998)
[33] H. Gray, *Gray's Anatomy*, Gramercy Books, NY (1977)
[34] K. Groth, *Klinische Beobachtungen Und Experimentelle Studien Uber Die*

Entstehung Des Dekubitus, Acta Chirugica Scandinavia 87:1-209 (1942)

[35] A. Hyodo, S. Reger, S. Negami, H. Kambic, E. Reyes & E. Browne, *Evaluation Of a Pressure Sore Model Using Monoplegic Pigs*, Plastic and Reconstructive Surgery, 96: 421-428 (1995)

[36] B. Hete & K Shung, *Scattering Of Ultrasound From Skeletal Muscle Tissue*, IEEE Transactions on Ultrasonics, Ferroelectrics, and Frequency Control, 40(4): 354-365 (1993)

[37] B. Hete & K. Shung, *A Study Of The Relationship Between Mechancial And Ultrasonic Properties of Dystrophics And Normal Skeletal Muscle*, Ultrasound in Medcine & Biology, 21(3): 343-52 (1995)

[38] H. Huisman, J. Thijssen, D. Th. Wagener & G. Rosenbusch, Quantitative *Ultrasonic Analysis Of Liver Metastases*, Ultrasound in Medicine & Biology, 24(1): 67-77 (1998)

[39] J. Hunt, A. Worthington & A. Kerr, *The Subtleties Of Ultrasound Images Of An Ensemble Of Cells: Simulation From Regular And More Random Distributions Of Scatterers*, Ultrasound in Medicine & Biology, 21(3): 329-41 (1995)

[40] T. Husain, *An Experimental Study Of Some Pressure Effects On Tissue With Reference To The Bed-Sore Problem*, Journal of Pathological Bacteria, LXVI: 347-358 (1953)

[41] M. Insana, R. Wagner, B. Garra, D. Brown & T. Shawker, *Analysis Of Ultrasound Image Texture Via Generalized Rician Statistics*, Optical Engineering 25(6):743-748 (1986)

[42] L. Kanj, S. Van B. Wilking & T. Phillips, Pressure Ulcers, Journal of the American Academy of Dermatology, 38(4): 517-536 (1998)

[43] P. Karg, D. Brienza, C. Brubaker, J. Wang, C.T. Lin, *A System For The Design And Analysis Of Seat Support Surfaces*, Proceedings of the 19th Annual RESNA Conference, Salt Lake City, Utah, June 7-12, 1996

[44] P.Karg, D. Brienza, K.-C. Chung, C. Brubaker, *Evaluation Of A Surface Optimization Technique For Custom Contoured Cushion Design*, Proceedings of the 19th Annual RESNA Conference, Salt Lake City, Utah, June 7-12, 1996

[45] G. Kawchuk & P. Elliott, *Validation Of Displacement Measurements Obtained From Ultrasonic Images During Indentation Testing*, Ultrasound in Medicine and Biology, 24(1): 105-111 (1998)

[46] W. Kapit & L. Elson, *The Anatomy Coloring Book*, Harper-Collins, New York, NY (1993)

[47] A. Keller and R. Feingold, *Technique In The Surgery Of Pressure Sores* in *Surgical Management Of Cutaneous Ulcers And Pressure Sores*, Chapman & Hall, New York, NY, 1998, pp. 239-245

[48] H. Kimitsuki, R. Parsons, B. Sigel, E. Feleppa, R. Golub, J. Justin, J. Machi, M. Rorke, J. Sokil-Melgar, I. Kodama, T. Kurohiji, T. Kakegawa & H. Zaren, *Effect Of Perfusion And Blood Content On Ultrasonic Backscattering Of Liver Tissue*, 19(1): 39-43 (1993)

[49] B. Klaus & P. Horn, *Robot Vision*, The MIT Press, Cambridge, MA and McGraw-Hill, New York, NY, 1986

[50] J. Kokate, K. Leland, A. Held, G. Hansen, G. Kveen, B. Johnson, M. Wilke, E. Sparrow & P. Iazzo, *Temperature-Modulated Pressure Ulcers: A Porcine Model*,

Archives of Physical Medicine and Rehabilitation, 76(7): 666-673 (1995)
[51] M. Kosiak, *Etiology And Pathology Of Ischemic Ulcers*, Archives of Physical Medicine and Rehabilitation, 40:62-69 (1959)
[52] T. Krouskop, D. Dougherty & F. Vinson, *A Pulsed Doppler Ultrasonic System For Making Noninvasive Measurements Of The Mechanical Properties Of Soft Tissue*, Journal of Rehabilitation Research and Development, 24(2):1-8 (1987)
[53] T. Krouskop, N. Reddy, W. Spencer & J. Secor, *Mechanisms of Decubitus Ulcer Formation*, Medical Hypotheses, 4: 37-39 (1978)
[54] J. Kuffner, *Effective Sampling And Distance Metrics For 3D Rigid Body Path Planning*, Proceedings of the IEEE Converence on Robotics and Automation, New Orleans, LA (2004)
[55] A. Landsman, D. Meaney, R. Cargill II, E. Macarak & L. Thibault, *High Strain Rate Tissue Deformation: A Theory On The Mechanical Etiology Of Diabetic Foot Ulcerations*, Journal of the American Podiatric Medical Association, 85(10):519- 527 (1995)
[56] K. M. Le, B. Madsen, P. Barth, G. Ksander, J. Angell & L. Vistnes, *An In-Depth Look At Pressure Sores Using Monolithic Silicon Pressure Sensors*, Plastic and Reconstructive Surgery, 74(6):745-56 (1984)
[57] B. Lee, V. Guerra, and B. Herz, *Role Of Antimicrobial Agents In Infected Decubitus Ulcers* in *Surgical Management Of Cutaneous Ulcers And Pressure Sores*, Chapman & Hall, New York, NY, 1998, pp. 129-140
[58] B. Lee and M. Karmakar, *Pressure Ulcers: An Overview* in *Surgical Management Of Cutaneous Ulcers And Pressure Sores*, Chapman & Hall, New York, NY, 1998, pp. 86-115
[59] B. Lee, & L. Ostrander, *Noninvasive Evaluation Of The Cutaneous Circulation* in *Surgical Management Of Cutaneous Ulcers And Pressure Sores*, Chapman & Hall, New York, NY, 1998, pp. 14-26
[60] N. M. Lalonde, J. Dansereau, R. Aissaoui, and M. Lacoste, *Effect Of Different Tilt And Seat-To-Back Angles On Trunk, Pelvic And Hip Orientations*, Proceedings of the 22nd Annual RESNA Conference, June 25-29, 1999
[61] R. Lerner, S. R. Huang & K. Parker, *"Sonoelasticity" Images Derived From Ultrasound Signals In Mechanically Vibrated Tissues*, Ultrasound in Medicine & Biology, 16(3): 231-239 (1990)
[62] J. Levine, M. Simpson & R. MacDonald, *Pressure Sores: A Plan For Primary Care Prevention*, Geriatrics, 44:75-90 (1989)
[63] S. Levine, R. Kett & M. Ferguson-Pell, *Tissue Shape And Deformation Versus Pressure As A Characterization Of The Seating Interface*, Assistive Technology 2:93-99 (1991)
[64] C. Li & C. Lee, *Minimum Cross Entropy Thresholding*, Pattern Recognition, 26: 617-625 (1993)
[65] F. Li & Y. Yang, *A Loss Function Analysis For Classification Methods In Text Categorization*, Proceedings of the 20th International Conference On Machine Learning (ICML'03) pp. 472-479 (2003)
[66] Y. Li, R. Aissaoui, D. Brienza & J. Dansereau, *Determination Of Generic Seat Interface Shapes By Cluster Analysis*, Proceedings of the 22nd Annual RESNA Conference, June 25-29, 1999

[67] R. Lim, R. Sirett, T. Conine & D. Daechsel, Clinical Trial Of Foam Cushions In The Prevention Of Decubitus Ulcers In Elderly Patients, Journal of Rehabilitation Research and Development, 25(2): 19-26 (1988)
[68] L.C. Lin, C.C. Wu, Y.L. Ho, M.F. Chen, C.S. Liau & Y.T. Lee, *Ultrasonic Tissue Characterization In Predicting Residual Ischemia And Myocardial Viability For Patients With Acute Myocardial Infarction*, Ultrasound in Medicine & Biology, 24(8): 1107-1120 (1998)
[69] L.C. Lin, C.C. Wu, Y.L. Ho, C.W. Lin, W.J. Chen, M.F. Chen, C.S. Liau & Y.T. Lee, *Ultrasonic Tissue Characterization For Coronary Care Unit Patients With Acute Myocardial Infarction*, Ultrasound In Medicine & Biology, 24(2): 187-96 (1998)
[70] F. Lizzi, M. Greenbaum, E. Feleppa & M. Elbaum, Theoretical Framework For Spectrum Analysis In Ultrasonic Tissue Characterization, Journal of the Acoustic Society of America 73(4): 1366-1372 (1983)
[71] F. Lizzi, M. Ostromogilsky, E. Feleppa, E. Rorke & M. Yaremko, *Relationship Of Ultrasonic Spectral Parameters Of Features Of Tissue Microstructure*, IEEE Transactions on Ultrasonics, Ferroelectrics and Frequency Control 34:319-329 (1987)
[72] F. Lizzi, D. King & M. Rorke, *Comparison Of Theoretical Scattering Results And Ultrasonic Data From Clinical Liver Examinations*, Ultrasound in Medicine and Biology 14:377-385 (1988)
[73] F. Lizzi, M. Astor, E. Feleppa, M. Shao & A. Kalisz, *Statistical Framework For Ultrasonic Spectral Parameter Imaging*, Ultrasound in Medcine & Biology, 23(9): 1371-1382 (1997)
[74] P. Lowthian, *Notes On The Pathogenesis Of Serious Pressure Sores*, British Journal of Nursing, 6(16):907-12 (1997)
[75] A. Mak, L. Huang & Q. Wang, *A Biphasic Poroelastic Analysis Of The Flow Dependent Subcutaneous Tissue Pressure And Compaction Due To Epidermal Loadings: Issues In Pressure Sore*, Journal of Biomechancial Engineering, 116:421-429 (1994)
[76] K. Martin, W. Schroeder, B. Lorensen, *The Visualization Toolkit*, Kitware, Inc., *http://www.vtk.org*
[77] W. McDicken, *Diagnostic Ultrasonics: Principles And Use Of Instruments (Third Edition)*, Churchill Livingstone, New York (1991)
[78] M. Meehan, *Multisite Pressure Ulcer Prevelence Survey*, Advances in Wound Care, 7(3):27-38 (1994)
[79] J. Meunier & M. Bertrand, *Echographic Image Mean Gray Level Changes With Tissue Dynamics: A System-Based Model Study*, IEEE Transactions on Biomedical Engineering, 42(4): 403-410 (1995)
[80] J. Meunier, *Tissue Motion Assessment From 3D Echographic Speckle Tracking*, Physics in Medicine & Biology, 43: 1241-1254 (1998)
[81] C. Michel and H. Gillot, *Microvascular Mechanisms In Statis And Ischaemia* in *Pressure Sores: Clinical Practice and Scientific Approach*, MacMillan Press, London, 1990, pp. 153-163
[82] S. Milton, *Experimental Studies On Island Flaps II: Ischemia And Delay*, Plastic and Reconstructive Surgery, 49:444-447 (1972)
[83] R. Molthen, V. Narayanan,P. Shankar, J. Reid, V. Genis, F. Forsberg, E. Halpern & B.

Goldberg, *Using Phase Information In Ultrasonic Backscatter For In Vivo Liver Analysis*, Ultrasound in Medicine & Biology, 24(1):79-91 (1998)

[84] R. Molthen, P. Shankar & J. Reid, *Characterization Of Ultrasonic B-Scans Using Non-Rayleigh Statistics*, Ultrasound in Medicine & Biology, 21(2): 161-170 (1995)

[85] R. Molthen, P. Shankar, J. Reid, F. Forsberg, E. Halpern, C. Piccoli & B. Goldberg, *Comparisons Of The Rayleigh And K-Distribution Models Using In Vivo Breast And Liver Tissue*, Ultrasound in Medicine & Biology, 24(1): 93-100 (1998)

[86] S. Monstrey, *Pressure Sores*, Acta Chirurgica Belgica, 97: 6-12 (1997)

[87] A. Montauban van Swijndregt, H. Elbers, F. Moll, J. de Letter & R. Ackerstaff, *Ultrasonographic Characterization Of Carotid Plaques*, Ultrasound in Medicine & Biology, 24(4): 489-93 (1998)

[88] V. M. Narayanan, P. Shankar & J. Reid, *Non-Rayleigh Statistics Of Ultrasonic Backscattered Signals*, IEEE Transactions On Ultrasonics, Ferroelectrics, and Frequency Control, 41(6): 845-52 (1994)

[89] National Pressure Ulcer Advisory Panel, *Pressure Ulcer Research: Etiology, Asssessment and Early Intervention* (1995)

[90] National Spinal Cord Injury Statistical Center, *Spinal Cord Injury: Facts And Figures At A Glance*, Birmingham, AL (2005)

[91] Z. Niazi and C. Salzberg, *Surgical Management Of Difficult Recurrent Pressure Ulcers* in *Surgical Management Of Cutaneous Ulcers And Pressure Sores*, Chapman & Hall, New York, NY, 1998, pp. 246-252

[92] F. Netter, *Atlas Of Human Anatomy*, Novartis, East Hanover, NJ (1997)

[93] T. Noritomi, J. Machim, E. Feleppa, E/ Yamagohara & K. Shirouzu, *In Vitro Investigation Of Lymph Node Metastatis Of Colorectal Cancer Using Ultrasonic Spectral Parameters*, Ultrasound in Medicine & Biology, 24(2): 235-43 (1998)

[94] T. Noritomi, B. Sigel, V. Swami, J. Justin, V. Gahtan, X. Chen, E. Feleppa, A. Roberts & K. Shirouzu, *Carotid Plaque Typing By Multiple-Parameter Ultrasonic Tissue Characterization*, Ultrasound in Medicine & Biology, 23(5): 643-50 (1997)

[95] D. Norton, R. McLaren & A. Exton-Smith, An Investigation Of Geriatric Nursing Problems In Hospital. London: Churchil Livingstone (1975)

[96] B. Oosterveld, J. Thijssen, P. Hartman & G. Rosenbusch, *Detection Of Diffuse Liver Disease By Quantitative Echography: Dependence On A Priori Choice Of Parameters*, Ultrasound in Medicine & Biology, 19(1): 21-25 (1993)

[97] A. Oppenheim & R. Schafer, *Discrete-Time Signal Processing*, Prentice Hall, NJ, 1989

[98] T. Ota, D. Craig & J. Kisslo, *Influences Of Ultrasonic Machine Settings, Transducer Frequency and Placement Of Region Of Interest On The Measurement Of Integrated Backscatter And Cyclic Variation*, Ultrasound in Medicine & Biology, 23(7): 1059-70 (1997)

[99] L. Pan, L. Zan & F. Foster, *Ultrasonic And Viscoelastic Properties Of Skin Under Transverse Mechanical Stress In Vitro*, Ultrasond in Medicine & Biology, 24(7): 995-1007 (1998)

[100] J. Parkinnen, K. Selkainaho & E. Oja, *Detecting Texture Peroidicity From The Co-occurence Matrix*, Pattern Recognition Letters 11:43-50 (1990).

[101] R. Parsons, B. Sigel, E. Feleppa, R. Golub, J. Justin, V. Swami, M. Rorke, A. Kalisz, C. Long, *A. Can, F. Lizzi & H. Kitamura, Ultrasonic Tissue Characterization Of*

Experimental Venous Intimal Hyperplasia, Ultrasound in Medicine & Biology, 19(4): 299-308 (1993)

[102]N. Petersen & S. Bittman, *The Epidemiology Of Pressure Sores In The Greater Glasgow Health Board Area*, Lancet 2: 548 (1977)

[103]D. Recchia, J. Miller & S. Wickline, *Quantification Of Ultrasonic Anisotropy In Normal Myocardium With Lateral Gain Compensation Of Two-Dimensional Integrated Backscatter Images*, Ultrasound in Medicine & Biology, 19(6): 497-505 (1993)

[104]N. Reddy, G. Cochran & T. Krouskop, *Interstitial Fluid Flow As A Factor In Decubitus Ulcer Formation,* Journal of Biomechanics, 14(12): 879-881 (1981)

[105]N. Reddy, V. Palmieri & G. Cochran, S*ubcutaneous Interstitial Fluid Pressure During External Loading,* American Journal of Physiology, 240(5): R327-9 (1981)

[106]N. Reddy, Effects Of Mechanical Stresses On Lymph And Interstitial Fluid Flows in Pressure Sores: Clinical Practice And Scientific Approach, The MacMillian Press, London, pp. 203-220 (1990)

[107]S. Reger et al., *Deformation And Stiffness Of Soft Tissues By Magnetic Resonance Imaging*, The 8th Annual IEEE/Engineering In Medicine And Biology Society Conference (1986)

[108]J Reswick and J Rodgers, *Experience at Rancho Los Amigos Hospital With Devices and Techniques to Prevent Pressure Sores* in *Bedsore Biomechanics*, University Park Press, Baltimore, MD, 1975, pp.301-310

[109]H. Rijsterborgh, F. Mastik, C. Lancee, P. Verdouw, J. Roelandt & N. Bom, *Ultrasound Myocardial Integrated Backscatter Signal Processing: Frequency Domain Versus Time Domain*, Ultrasound in Medicine & Biology, 19(3): 211-9 (1993)

[110]M. Rosenthal, R. Felton, D. Hileman, M. Lee, M. Friedman & J. Navach, *A Wheelchair Cushion Designed To Redistribute Sites Of Sitting Pressure*, Archives of Physical Medicine & Rehabilitation, 77: 278-82 (1996)

[111]J. Sanders, B. Goldstein, D. Leotta, *Skin Response To Mechanical Stress: Adaption Rather Than Breakdown- A Reiview Of The Literature*, Journal of Rehabilitation Research and Development, 32(3): 214-226 (1995)

[112]B. Sangeorzan, R. Harrington, C. Wyss, J. Czerniecki & F. Matsen, *Circulatory And Mechanical Response Of Skin To Loading*, Journal Of Orthopedic Research 7(3): 425-341 (1989)

[113]V. Schubert, J. Heraud, *The Effects Of Pressure And Shear On Skin Microcirculation In Elderly Stroke Patients Lying In Supine or Semi-Recumbent Positions*, Age and Aging, 23(5): 405-10 (1994)

[114]P. Shankar, R. Molthen, V. Narayanan, J. Reid, V. Genis, F. Forsberg, C. PIccoli, A. Lindenmayer & B. Goldberg, *Studies On The Use Of Non-Rayleigh Statistics For Ultrasonic Tissue Characterization*, Ultrasound in Medicine & Biology, 22(7): 873-882 (1996)

[115]M. Siegel & T. Ault, *Measurement Issues in Quantitative Ultrasonic Imaging*, Proceedings of the International Measurement Technology Conference, pg. 16-19 (1997)

[116]R. Silverman, R. Folberg, H. Boldt, H. Lloyd, M. Rondeau, M. Mehaffey, F. Lizzi & D. Coleman, *Correlation Of Ultrasound Parameter Imaging With Microcirculatory*

Patterns In Uveal Melanomas, Ultrasound in Medicine & Biology, 23(4): 573-581 (1997)

[117]D. Simon, *Fast And Accurate Shape Based Registration*, Ph.D. Thesis, Carnegie Mellon University (1996)

[118]T. Spencer, M. Ramo, D. Salter, T. Anderson, P. Kearney, G. Sutherland, K. Fox & W. N. McDicken, *Characterization Of Atherosclerotic Plaque By Spectral Analysis Of Intravascular Ultrasound: An In Vitro Methodology*, Ultrasound in Medicine & Biology, 23(2): 191-203 (1997)

[119]A. Stefanovska, L. Vodovnik, H. Benko, M. Malezic, R. Turk, A. Kolenk and S. Rebersek, *Enhancement Of Ulcerated Tissue Healing By Electrical Stimulation*, Proceedings of the RESNA 10th Annual Conference, San Jose, Califorina, pp. 585- (1987)

[120]P. Stetson & G. Sommer, *Ultrasonic Characterization Of Tissues Via Backscatter Frequency Dependence*, Ultrasound in Medicine & Biology, 23(7): 989-96 (1997)

[121]C. Sumi, A. Suzuki & K. Nakayama, *Estimation Of Shear Modulus Distribution In Soft Tissue From Strain Distribution*, IEEE Transactions on Biomedical Engineering, 42(2): 193-202 (1995)

[122]T. Tateishi, J. Machi, E. Feleppa, R. Oishi, J. Jucha, E. Yanagihara, L. McCarthy, T. Noritomi & K. Shirouzo, *In Vitro Diagnosis Of Axillary[sic] Lymph Node Metastates In Breast Cancer By Spectrum Analysis Of Radio Frequency Echo Signals*, Ultrasound in Medicine & Biology, 24(8): 1151-9 (1998)

[123]J. Thijssen, B. Oosterveld, P. Hartman & G. Rosenbusch, *Correlations Between Acoustic And Texture Parameters From RF And B-Mode Liver Echograms*, Ultrasound in Medicine & Biology, 19(1):13-20 (1993)

[124]B. Todd & J. Thacker, *Three Dimensional Computer Model Of The Human Buttocks In-Vivo*, Hournal of Rehabilitation Research and Development, 31(2): 1994: 111-119 (1994)

[125]E. Torai & B. Chung, *The Management Of Pressure Sores*, Journal of Dermatological Surgical Oncology, 3: 507-516 (1977)

[126]D. Turnbull, J. Ramsay, G. Shivji, T. Bloomfield, L. From, D. Sauder & F. Foster, *Ultrasound Backscatter Microscope Analysus Of Mouse Melanoma Progression*, Ultrasound in Medicine & Biology, 22(7): 845-854 (1996)

[127]F. Valckx & J. Thijssen, *Characterization Of Echographic Image Texture By Cooccurrence matrix Parameters*, Ultrasound in Medicine & Biology, 23(4): 559-71 (1997)

[128]W. Vannah & D. Childress, *Indentor Tests And Finite Element Modeling Of Bulk Muscular Tissue In Vivo*, Journal of Rehabilitation Research and Development, 33(3): 239- 252 (1996)

[129]T. Varghese & J. Ophir, *Estimating Tissue Strain From Signal Decorrelation Using The Correlation Coefficient*, Ultrasound in Medicine & Biology, 22(9): 1249-1254 (1996)

[130]R. Wagner, M. Insana & D. Brown, *Statistical Properties Of Radio-Frequency And Envelope-Detected Signals With Applications To Medical Ultrasound*, Journal of the Optical Society of America A, 4(5): 910-922 (1987)

[131]J. Wang, D. Brienza, C. Brubaker, Y. W. Yuan, *Design Of An Ultrasound Soft Tissue Characterization System For The Computer-Aided Seating System*, Proceedings of

the 19th Annual RESNA Conference, June 7-12, 1996
[132]J. Wang, D. Brienza, Y. W. Yuan, P. Kang & C. Brubaker, *A Compound Sensor For Biomechanical Analysis Of Load-Bearing Soft Tissue*, Proceedings of the 20th Annual RESNA Conference, June 20-24, 1997
[133]J. Wang, *Development Of A Compound Ultrasonic Device And In Vivo Biomechanical Assessment Of Buttock Soft Tissue*, Ph.D. Thesis, University Of Pittsburgh (2000)
[134]J. Wang, D. Brienza, G. Bertocci, V. Chib, P. Karg & Y. W. Yuan, *Reliability Of The In Vivo Protocol For Measuring Indentation Properties Of Buttock Soft Tissue*, Proceedings of the 23rd Annual RESNA Conference, June 28-July 2, 2000
[135]J. Wang, D. Brienza, Y. W. Yuan, P. Karg & Q. Xue, *A Compound Sensor For Biomechanical Analyses Of Buttock Soft Tissue In Vivo*, Journal of Rehabilitation Research and Development, 37(4): 433-443 (2000)
[136]J. Wang, D. Brienza, G. Bertocci & P. Karg, *Stress Relaxation Properties Of Buttock Soft Tissues: In Vivo Indentation Test*, Proceedings of the 24th Annual RESNA Conference, June 22-26, 2001
[137]J. Ward, *Hierarchical Grouping To Optimize An Objective Function, Journal of the American Statistical Assocation* 58: 234-244 (1963)
[138]J. Waterlow, *A Risk Assessment Card*, Nursing Times, 49:49-55 (1987)
[139]K. Wear & B. Garra, *Assessment Of Bone Density Using Ultrasonic Backscatter*, Ultrasound in Medicine & Biology, 24(5): 689-95 (1998)
[140]K. Wear, R. Wagner, M. Insana & T. Hall, *Application of Autoregressive Spectral Analysis To Cepstral Estimation Of Mean Scatterer Spacing*, IEEE Transactions on Ultrasonics, Ferroelectrics, and Frequency Control, 40(1): 50-58 (1993)
[141]Y. Yang, *An Evaluation Of Statistical Approaches To Text Categorization*, Journal Of Information Retrieval 1(1):67-88 (1999)
[142]F. Yeung, S. Levinson & K. Parker, *Multilevel And Motion Model-Based Ultrasonic Speckle Tracking Algorithms*, Ultrasound in Medicine & Biology 24(3): 427-441 (1998)
[143]A. Zeltwanger, J. Wang, G. Bertocci, D. Brienza & V. Chib, *Effective Modulus Of Buttocks Soft Tissue*, Proceedings of the 23rd Annual RESNA Conference, June 28-July 2, 2000
[144]A. Zeltwanger, J. Wang, G. Bertocci, D. Brienza, P. Karg & V. Chib, *Repeatability Of Determining Effective Young's Modulus Of Buttocks Soft Tissue Across Multiple Subjects*, Proceedings of the 24th Annual RESNA Conference, June 22-26, 2001
[145]Y. P. Zheng & A. Mak, *An Ultrasound Indentation System For Biomechanical Properties Assessment of Soft Tissues In-Vivo*, IEEE Transactions on Biomedical Engineering, 43(9): 912-918 (1996)
[146]Y. P. Zheng & A. Mak, *Extraction Of Quasi-Linear Viscoelastic Parameterts From Manual Indentation Experiment, Journal of Biomechanical Engineering* 121(6): 330-339
[147]J. D. Zhang, A. Mak & L. D. Huang, *A Large Deformation Biomechanical Model For Pressure Ulcers*, Journal of Biomechanical Engineering, 119:406-408 (1997)
[148]Q. Zhu & B. Steinberg, *Wavefront Amplitude Distribution In The Female Breast*, Journal of the Acoustical Society of America, 66: 1-9 (1994)
[149]Y. Zimmer, S. Akselrod & R. Tepper, *The Distribution Of The Local Entropy In*

Ultrasound Images, Ultrasound in Medicine & Biology, 22(4): 431-9 (1996)

[150]Y. Zimmer, R. Tepper & S. Akselrod, *A Two-Dimensional Extension Of Minimum Cross Entropy Thresholding For The Segmentation Of Ultrasound Images*, Ultrasound in Medicine & Biology, 22(9): 1183-90 (1996)